Methods in Molecular Biology 2722

Springer Protocols



Javier Agusti *Editor*

Xylem

Methods and Protocols

Second Edition

Humana Press

METHODS IN MOLECULAR BIOLOGY

Series Editor
John M. Walker
School of Life and Medical Sciences
University of Hertfordshire
Hatfield, Hertfordshire, UK

For further volumes:
http://www.springer.com/series/7651

For over 35 years, biological scientists have come to rely on the research protocols and methodologies in the critically acclaimed *Methods in Molecular Biology* series. The series was the first to introduce the step-by-step protocols approach that has become the standard in all biomedical protocol publishing. Each protocol is provided in readily-reproducible step-by-step fashion, opening with an introductory overview, a list of the materials and reagents needed to complete the experiment, and followed by a detailed procedure that is supported with a helpful notes section offering tips and tricks of the trade as well as troubleshooting advice. These hallmark features were introduced by series editor Dr. John Walker and constitute the key ingredient in each and every volume of the *Methods in Molecular Biology* series. Tested and trusted, comprehensive and reliable, all protocols from the series are indexed in PubMed.

Xylem

Methods and Protocols

Second Edition

Edited by

Javier Agusti

UPV-CSIC, Universitat Politècnica de València, Valencia, Spain

Humana Press

Editor
Javier Agusti
UPV-CSIC
Universitat Politècnica de València
Valencia, Spain

ISSN 1064-3745 ISSN 1940-6029 (electronic)
Methods in Molecular Biology
ISBN 978-1-0716-3476-9 ISBN 978-1-0716-3477-6 (eBook)
https://doi.org/10.1007/978-1-0716-3477-6

© The Editor(s) (if applicable) and The Author(s), under exclusive license to Springer Science+Business Media, LLC, part of Springer Nature 2024
This work is subject to copyright. All rights are solely and exclusively licensed by the Publisher, whether the whole or part of the material is concerned, specifically the rights of translation, reprinting, reuse of illustrations, recitation, broadcasting, reproduction on microfilms or in any other physical way, and transmission or information storage and retrieval, electronic adaptation, computer software, or by similar or dissimilar methodology now known or hereafter developed.
The use of general descriptive names, registered names, trademarks, service marks, etc. in this publication does not imply, even in the absence of a specific statement, that such names are exempt from the relevant protective laws and regulations and therefore free for general use.
The publisher, the authors, and the editors are safe to assume that the advice and information in this book are believed to be true and accurate at the date of publication. Neither the publisher nor the authors or the editors give a warranty, expressed or implied, with respect to the material contained herein or for any errors or omissions that may have been made. The publisher remains neutral with regard to jurisdictional claims in published maps and institutional affiliations.

Cover photo: Cover photograph by Marta-Marina Perez Alonso

This Humana imprint is published by the registered company Springer Science+Business Media, LLC, part of Springer Nature.
The registered company address is: 1 New York Plaza, New York, NY 10004, U.S.A.

Paper in this product is recyclable.

Preface

How do plants transport water from the soil? How do plants sustain themselves? These are two fundamental questions that have intrigued plant scientists for centuries. Although at first glance these questions may not seem conceptually related, in reality they are. In the seventeenth century, Marcello Malpighi identified a tissue made of cells with special properties in the stem of plants and, in the nineteenth century, the anatomical studies of Carl Wilhelm von Nägeli led to the conclusion that this tissue constitutes wood of trees. For this reason, the tissue received the name "xylem," derived from the Greek word "xylon," which means wood. A century and a half later, we know that xylem plays a pivotal role in plant physiology because it is the tissue that (i) is responsible for the long-distance transport of water and mineral nutrients from the soil to all plant organs, and (ii) provides the mechanical support and stability that plants need to sustain themselves and expand their growth. Both functions are tightly linked because, in order to maintain the hydraulic pressure that water transport entails, xylem cells develop thick and lignified secondary cell walls, which in turn provide mechanical support and robustness.

Fundamental research on xylem biology has provided a comprehensive understanding of the physiology and the hydraulics behind water flow throughout the plant, the biochemistry of xylem secondary cell walls, and the genetic and molecular mechanisms governing xylem proliferation, differentiation, and maturation. Ecophysiology research has also highlighted the importance of xylem plasticity, which enables plants to adjust their growth and physiological programs to their surrounding environment. Furthermore, evolutionary studies have revealed how xylem morphology changed and adapted to suit different environmental conditions, and how it played a crucial role in one of the largest radiations in evolution, making it a significant aspect of our planet's history.

From an applied perspective, it is worth noting that wood represents a key material for industry such as paper, fiber, pulp energy or construction. Furthermore, in species developing storage roots, xylem parenchyma is the edible tissue.

Given xylem's relevance in plant physiology, evolution, ecology, industry, nutrition, and forest sciences, there is great excitement surrounding research on xylem biology. This book is focused on technological and methodological advances to study four main aspects of xylem biology. As a result, the book is organized into four parts:

Part I: Xylem Transport, Functional Dynamics and Modelling (Chaps. 1, 2, 3, and 4)

This part provides a compilation of methods aimed at understanding how transport is carried out by xylem cells and how alterations in transport dynamics due to environmental conditions can lead to xylem vulnerability through physical phenomena such as embolism. Additionally, it describes strategies for implementing computational modeling on xylem activity. The information presented in this part can be valuable for studies aimed at understanding novel questions about xylem functionality and the impact of the environment on it.

Part II: Xylem Development and Evolution (Chaps. 5, 6, and 7)

The essential molecular aspects of xylem biology have only recently been unraveled, and the development of new techniques aimed at studying xylem cell biology in detail has been key to this process. This part provides methodology to isolate xylem cells and study fundamental cellular aspects of their biology in detail. In addition, this part covers evolutionary aspects of xylem based on the observation of fossil records.

Part III: Xylem Diseases (Chaps. 8 and 9)

Plant diseases affecting xylem formation and/or activity have been the focus of research in many species, as their impact can be significant on agriculture. Detecting xylem pathogens and studying the effect of diseases on xylem cells is critical to implementing new strategies to mitigate the impact of such diseases on plant production. This part presents examples on these crucial aspects of plant disease research.

Part IV: Xylem Composition and Imaging (Chaps. 10, 11, 12, 13, 14, and 15)

Imaging and determining the composition of xylem accurately can be challenging tasks since xylem is usually the innermost tissue in most organs. This part contains new technologies and methodologies developed in recent years to make such tasks more affordable.

Target audience: Plant physiologists, ecophysiologists, cell biologists, biochemists, developmental biologists, computer scientists.

Valencia, Spain *Javier Agusti*

Contents

Preface . . . . . *v*
Contributors . . . . . *ix*

PART I XYLEM TRANSPORT, FUNCTIONAL DYNAMICS AND MODELLING

1 Monitoring Xylem Transport in *Arabidopsis thaliana* Seedlings Using Fluorescent Dyes 3
Kai Bartusch, Noel Blanco-Touriñán, Antia Rodriguez-Villalón, and Elisabeth Truernit

2 Modeling and Analyzing Xylem Vulnerability to Embolism as an Epidemic Process 17
Anita Roth-Nebelsick and Wilfried Konrad

3 Modeling Xylem Functionality Aspects 35
Alex Tavkhelidze, Gerhard Buck-Sorlin, and Winfried Kurth

4 Detecting and Quantifying Xylem Embolism by Synchrotron-Based X-Ray Micro-CT 51
Martina Tomasella, Francesco Petruzzellis, Sara Natale, Giuliana Tromba, and Andrea Nardini

PART II XYLEM DEVELOPMENT AND EVOLUTION

5 Analysis of Xylem Cells by Nucleus-Based Transcriptomics and Chromatin Profiling 67
Dongbo Shi, Laura Luzzietti, Michael Nodine, and Thomas Greb

6 Quantification of Xylem-Specific Thermospermine-Dependent Translation of *SACL* Transcripts with Dual Luciferase Reporter System 79
Anna Solé-Gil, Cristina Úrbez, Alejandro Ferrando, and Miguel A. Blázquez

7 Fossil Wood Analyses: Several Examples from Five Case Studies in the Area of Central and NW Bohemia, Czech Republic 89
Jakub Sakala

PART III XYLEM DISEASES

8 Isolation and Reproductive Structures Induction of Fungal Pathogens Associated with Xylem and Wood Necrosis in Grapevine 107
Ana López-Moral and Carlos Agustí-Brisach

9 Determination of De Novo Suberin-Lignin Ferulate Deposition in Xylem Tissue Upon Vascular Pathogen Attack 117
Weiqi Zhang, Álvaro Jiménez-Jiménez, Montserrat Capellades, Jorge Rencoret, Anurag Kashyap, and Núria S. Coll

Part IV Xylem Composition and Imaging

10 Quantification of Tracheary Elements Types in Mature Hypocotyl of *Arabidopsis thaliana* 131
Paula Brunot-Garau, Cristina Úrbez, and Francisco Vera-Sirera

11 Histochemical Detection of Peroxidase and Laccase Activities in Populus Secondary Xylem 139
Marta-Marina Pérez Alonso, Àngela Carrió-Seguí, and Hannele Tuominen

12 Lignin Analysis by HPLC and FTIR: Spectra Deconvolution and S/G Ratio Determination 149
Jorge Reyes-Rivera and Teresa Terrazas

13 Inducible Pluripotent Suspension Cell Cultures (iPSCs) to Study Plant Cell Differentiation 171
Delphine Ménard, Henrik Serk, Raphael Decou, and Edouard Pesquet

14 Bulk and In Situ Quantification of Coniferaldehyde Residues in Lignin 201
Edouard Pesquet, Leonard Blaschek, Junko Takahashi, Masanobu Yamamoto, Antoine Champagne, Nuoendagula, Elena Subbotina, Charilaos Dimotakis, Zoltan Bascik, and Shinya Kajita

15 Clearing of Vascular Tissue in *Arabidopsis thaliana* for Reporter Analysis of Gene Expression 227
Antonio Serrano-Mislata and Javier Brumós

Index *241*

Contributors

Carlos Agustí-Brisach • *Department of Agronomy (DAUCO, Unit of Excellence María de Maeztu 2020-24), University of Cordoba, Cordoba, Spain*

Kai Bartusch • *Group of Phloem Development and Function, Institute of Molecular Plant Biology, Department of Biology, ETH Zürich, Zürich, Switzerland*

Zoltan Bascik • *Department of Materials and Environmental Chemistry (MMK), Stockholm University, Stockholm, Sweden*

Noel Blanco-Touriñán • *Group of Plant Vascular Development, Institute of Molecular Plant Biology, Department of Biology, ETH Zürich, Zürich, Switzerland*

Leonard Blaschek • *Department of Ecology, Environment and Plant Sciences (DEEP), Stockholm University, Stockholm, Sweden*

Miguel A. Blázquez • *Instituto de Biología Molecular y Celular de Plantas (CSIC-Universitat Politècnica de València), Valencia, Spain*

Javier Brumós • *Instituto de Biología Molecular y Celular de Plantas (CSIC-Universitat Politècnica de València), Valencia, Spain*

Paula Brunot-Garau • *Instituto de Biología Molecular y Celular de Plantas (CSIC-Universitat Politècnica de València), Valencia, Spain*

Gerhard Buck-Sorlin • *IRHS, INRAE, Institut Agro Rennes-Angers, Université d'Angers, SFR 4207 QUASAV, Beaucouzé, France*

Montserrat Capellades • *Centre for Research in Agricultural Genomics (CRAG), CSIC-IRTA-UAB-UB, Bellaterra, Spain; Consejo Superior de Investigaciones Científicas (CSIC), Barcelona, Spain*

Àngela Carrió-Seguí • *Umeå Plant Science Centre, Department of Forest Genetics and Plant Physiology, Swedish University of Agricultural Sciences, Umeå, Sweden*

Antoine Champagne • *Department of Ecology, Environment and Plant Sciences (DEEP), Stockholm University, Stockholm, Sweden*

Núria S. Coll • *Centre for Research in Agricultural Genomics (CRAG), CSIC-IRTA-UAB-UB, Bellaterra, Spain; Consejo Superior de Investigaciones Científicas (CSIC), Barcelona, Spain*

Raphael Decou • *Umeå Plant Science Centre (UPSC), Department of Plant Physiology, Umeå University, Umeå, Sweden*

Charilaos Dimotakis • *Department of Ecology, Environment and Plant Sciences (DEEP), Stockholm University, Stockholm, Sweden*

Alejandro Ferrando • *Instituto de Biología Molecular y Celular de Plantas (CSIC-Universitat Politècnica de València), Valencia, Spain*

Thomas Greb • *Department of Developmental Physiology, Centre for Organismal Studies (COS), Heidelberg University, Heidelberg, Germany*

Álvaro Jiménez-Jiménez • *Centre for Research in Agricultural Genomics (CRAG), CSIC-IRTA-UAB-UB, Bellaterra, Spain*

Shinya Kajita • *Graduate School of Bio-Applications and Systems Engineering, Tokyo University of Agriculture and Technology, Tokyo, Japan*

Anurag Kashyap • *Centre for Research in Agricultural Genomics (CRAG), CSIC-IRTA-UAB-UB, Bellaterra, Spain; Department of Plant Pathology, Assam Agricultural University, Jorhat, Assam, India*
Wilfried Konrad • *Department of Geosciences, University of Tübingen, Tübingen, Germany; Institute of Botany, Technical University of Dresden, Dresden, Germany*
Winfried Kurth • *Georg-August-Universität Göttingen, Göttingen, Germany*
Ana López-Moral • *Department of Agronomy (DAUCO, Unit of Excellence María de Maeztu 2020-24), University of Cordoba, Cordoba, Spain*
Laura Luzzietti • *Department of Developmental Physiology, Centre for Organismal Studies (COS), Heidelberg University, Heidelberg, Germany*
Delphine Ménard • *Department of Ecology, Environment and Plant Sciences (DEEP), Stockholm University, Stockholm, Sweden; Umeå Plant Science Centre (UPSC), Department of Plant Physiology, Umeå University, Umeå, Sweden*
Andrea Nardini • *Dipartimento di Scienze della Vita, Università di Trieste, Trieste, Italy*
Sara Natale • *Dipartimento di Scienze della Vita, Università di Trieste, Trieste, Italy*
Michael Nodine • *Laboratory of Molecular Biology, Cluster of Plant Developmental Biology, Wageningen University, Wageningen, PB, the Netherlands*
Nuoendagula • *Graduate School of Bio-Applications and Systems Engineering, Tokyo University of Agriculture and Technology, Tokyo, Japan*
Marta-Marina Pérez Alonso • *Umeå Plant Science Centre, Department of Forest Genetics and Plant Physiology, Swedish University of Agricultural Sciences, Umeå, Sweden*
Edouard Pesquet • *Department of Ecology, Environment and Plant Sciences (DEEP), Stockholm University, Stockholm, Sweden; Umeå Plant Science Centre (UPSC), Department of Plant Physiology, Umeå University, Umeå, Sweden; Bolin Centre for Climate Research, Stockholm University, Stockholm, Sweden*
Francesco Petruzzellis • *Dipartimento di Scienze della Vita, Università di Trieste, Trieste, Italy*
Jorge Rencoret • *Institute of Natural Resources and Agrobiology of Seville (IRNAS), CSIC, Seville, Spain*
Jorge Reyes-Rivera • *UMIEZ, FES-Zaragoza, UNAM, Batalla 5 de mayo S/N, Mexico City, Mexico*
Antia Rodriguez-Villalón • *Group of Plant Vascular Development, Institute of Molecular Plant Biology, Department of Biology, ETH Zürich, Zürich, Switzerland*
Anita Roth-Nebelsick • *State Museum of Natural History Stuttgart, Stuttgart, Germany*
Jakub Sakala • *Institute of Geology and Palaeontology, Faculty of Science, Charles University, Prague, Czech Republic*
Henrik Serk • *Umeå Plant Science Centre (UPSC), Department of Plant Physiology, Umeå University, Umeå, Sweden*
Antonio Serrano-Mislata • *Instituto de Biología Molecular y Celular de Plantas (CSIC-Universitat Politècnica de València), Valencia, Spain*
Dongbo Shi • *Department of Developmental Physiology, Centre for Organismal Studies (COS), Heidelberg University, Heidelberg, Germany; Department of Genetics, Institute of Biochemistry and Biology, University of Potsdam, Potsdam-Golm, Germany; Japan Science and Technology Agency (JST) PRESTO Researcher, Tokyo, Japan*
Anna Solé-Gil • *Instituto de Biología Molecular y Celular de Plantas (CSIC-Universitat Politècnica de València), Valencia, Spain*
Elena Subbotina • *Department of Organic Chemistry, Stockholm University, Stockholm, Sweden*

Junko Takahashi • *Department of Forest Genetics and Plant Physiology, Umeå Plant Science Centre, Swedish University of Agricultural Sciences, Umeå, Sweden*
Alex Tavkhelidze • *Georg-August-Universität Göttingen, Göttingen, Germany*
Teresa Terrazas • *Departamento de Botánica, Instituto de Biología, UNAM, Circuito Exterior S/N, Ciudad Universitaria, Mexico City, Mexico*
Martina Tomasella • *Dipartimento di Scienze della Vita, Università di Trieste, Trieste, Italy*
Giuliana Tromba • *Elettra-Sincrotrone Trieste, Trieste, Italy*
Elisabeth Truernit • *Group of Phloem Development and Function, Institute of Molecular Plant Biology, Department of Biology, ETH Zürich, Zürich, Switzerland*
Hannele Tuominen • *Umeå Plant Science Centre, Department of Forest Genetics and Plant Physiology, Swedish University of Agricultural Sciences, Umeå, Sweden*
Cristina Úrbez • *Instituto de Biología Molecular y Celular de Plantas (CSIC-Universitat Politècnica de València), Valencia, Spain*
Francisco Vera-Sirera • *Instituto de Biología Molecular y Celular de Plantas (CSIC-Universitat Politècnica de València), Valencia, Spain*
Masanobu Yamamoto • *Graduate School of Bio-Applications and Systems Engineering, Tokyo University of Agriculture and Technology, Tokyo, Japan*
Weiqi Zhang • *Centre for Research in Agricultural Genomics (CRAG), CSIC-IRTA-UAB-UB, Bellaterra, Spain*

Part I

Xylem Transport, Functional Dynamics and Modelling



Chapter 1

Monitoring Xylem Transport in *Arabidopsis thaliana* Seedlings Using Fluorescent Dyes

Kai Bartusch, Noel Blanco-Touriñán, Antia Rodriguez-Villalón, and Elisabeth Truernit

Abstract

Fluorescent dyes are often used to observe transport mechanisms in plant vascular tissues. However, it has been technically challenging to apply fluorescent dyes on roots to monitor xylem transport in vivo. Here, we present a fast, noninvasive, and high-throughput protocol to monitor xylem transport in seedlings. Using the fluorescent dyes 5(6)-carboxyfluorescein diacetate (CFDA) and Rhodamine WT, we were able to observe xylem transport on a cellular level in *Arabidopsis thaliana* roots. We describe how to apply these dyes on primary roots of young seedlings, how to monitor root-to-shoot xylem transport, and how to measure xylem transport velocity in roots. Moreover, we show that our protocol can also be applied to lateral roots and grafted seedlings to assess xylem (re)connection. Altogether, these techniques are useful for investigating xylem functionality in diverse experimental setups.

Key words *Arabidopsis thaliana*, Vasculature, Xylem transport, Root, Grafting, Fluorescent dyes, CFDA, Rhodamine WT

1 Introduction

The high plasticity of xylem development is important for adapting plant growth to the environment [1, 2]. To understand the physiological consequences of these adaptations, there is a clear need for monitoring xylem transport. For this, several invasive and noninvasive methods have been developed over time (reviewed in [3]), but most of these techniques were designed for trees [3, 4]. Recently, water fluxes could be monitored in *Arabidopsis thaliana* (Arabidopsis) roots on a cellular level in real time. Deuterated water was supplied to root tips, and its shootward transport was tracked by Raman micro-spectroscopy [5]. In addition, the usage of xylem-transported dyes has become a popular in vivo approach to assess xylem functionality, since using dyes is rather straightforward and plants can be analyzed in high throughput. For instance, Basic

Javier Agusti (ed.), *Xylem: Methods and Protocols*, Methods in Molecular Biology, vol. 2722,
https://doi.org/10.1007/978-1-0716-3477-6_1,
© The Author(s), under exclusive license to Springer Science+Business Media, LLC, part of Springer Nature 2024

Fuchsin was used as a mobile dye to show that grapes are hydraulically connected to the shoot [6], and 5(6)-carboxyfluorescein diacetate (CFDA) was utilized as a long-distance transport tracer in xylem regions in branches of *Acer* and *Populus* [7]. Furthermore, Texas Red (sulforhodamine 101 acid chloride) xylem transport between the parasitic plant *Cuscuta* spec and its host plants could confirm intact xylem connections [8].

Arabidopsis has become a popular model system for studying vascular development and regeneration [9, 10]. Especially the Arabidopsis primary root of young seedlings is an ideal system to study xylem differentiation and function. The xylem in Arabidopsis roots is easily accessible by microscopy, and the xylem axis consists of only three central metaxylem cell files flanked by two protoxylem cell files [1, 9]. Important genetic regulators of Arabidopsis xylem development are already known. While their knockout or overexpression leads to anatomical changes, such as undifferentiated proto- and/or metaxylem cells, we have barely any information about the resulting physiological consequences of these mutant phenotypes. One of the first physiological attempts to monitor Arabidopsis xylem transport using dyes was applying ink containing agar to roots and studying the shootward transport of ink in Arabidopsis seedlings [11]. However, the ink transport from roots to shoots took several hours, even in small seedlings, and it is unclear whether ink is exclusively transported by the xylem [11]. Recently, Rhodamine B and fluorescein sodium salt were used to track xylem flow from Arabidopsis roots to leaves. This also enabled transport velocity measurements. When the dye was applied to the lower primary root region in 14-day-old plants, the fluorescent signal was detectable in the upper root region after a few minutes already. Here, the roots needed to be cut at the dye application site to facilitate dye penetration [12]. Alternatively, CFDA was used to investigate xylem transport in Arabidopsis. The advantage of using CFDA is that it only fluoresces strongly once it enters living tissue [13]. CFDA has been applied to confirm the restoration of xylem transport after grafting [10, 14, 15]. In one approach, the roots were cut off and the hypocotyl bases were pinched in dye-containing agar [10, 16, 17]. In another approach, the seedlings were transferred horizontally on a moist surface. A piece of Parafilm was positioned under the root, a dye drop was pipetted on the root, and the roots were then cut with scalpels to ensure fast dye entering [14–16]. If the fluorescent signal of CFDA can be detected in the cotyledons (above the graft junction), this confirms xylem reconnection and functionality. Usually, the grafted seedlings were assessed 1 h after dye application [14, 15]. However, these methods have clear limitations: (i) The roots need to be wounded by cutting, and (ii) the xylem transport can only be monitored in the shoot and upper root part of the seedling. In addition, although a reasonable assumption, it was never shown that the dye was indeed moving in xylem cells.

Here, we present a detailed protocol for monitoring xylem transport in Arabidopsis seedlings suitable for high throughput experiments. In principle, we pipette a dye-containing solution to the root region of interest, which must be locally supported by a Parafilm piece to avoid spreading of the dye drop across the moist surface. The plants can be positioned on moist Whatman paper or on agar-containing media. Xylem transport of the dye can be monitored with a dissecting microscope in real time, enabling xylem transport velocity measurements. Utilizing the adjuvant Adigor in our dye solution, we do not need to cut roots as in the previously described protocols [14–16]. Hence, the dye solution can be pipetted to any region of interest in the root system. We are using CFDA or Rhodamine WT as fluorescent xylem tracers. Both of these dyes have also been used as phloem tracers when applied to leaves [18], but we confirmed by confocal microscopy that when applied to roots, they are exclusively transported via xylem cells in roots. Therefore, the xylem transport can be assessed from an unwounded root system to the shoot on a cellular level. Additionally, we present further potential applications of our protocol, such as how to apply our protocol to lateral roots and grafted seedlings to assess xylem (re)connection.

2 Materials

2.1 Applying Fluorescent Dye Solutions to Arabidopsis Seedling Roots

1. Arabidopsis plants (*see* **Note 1**).
2. 1.5 mL microcentrifuge tubes.
3. Adigor (Syngenta, *see* **Note 2**).
4. Aluminum foil.
5. CFDA dye solution: Prepare a 100 mM 5(6)-Carboxyfluorescein diacetate (CFDA) stock solution in a 1.5 mL microcentrifuge tube by dissolving 46 mg CFDA in 1 mL DMSO. Transfer 100 μL of the CFDA stock to a new microcentrifuge tube, add 5 μL Adigor and 895 μL DMSO. This results in a working solution of 10 mM CFDA with 0.5% (v/v) Adigor (*see* **Note 2**). It is also possible to work with a lower CFDA concentration (*see* **Note 3**). Wrap tube in aluminum foil and store in the fridge.
6. Rhodamine WT dye solution (as an alternative to CFDA solution, *see* **Note 4**): Prepare a working solution of 100 mM Rhodamine WT with 0.5% (v/v) Adigor in a 1.5 mL microcentrifuge tube by pipetting 283 μL Rhodamine WT (20% in water) and 5 μL Adigor into 712 μL sterile ddH_2O. Wrap tube in aluminum foil and store in the fridge.
7. Parafilm.
8. Fine forceps.

9. Pipettes and tips.
10. Plates containing standard growth medium with 1.2% agar, for example, ½× Murashige and Skoog (MS) (*see* **Note 5**).
11. Fine scalpels (only if no adjuvant is used, *see* **Note 2**).
12. Whatman 3MM CHR filter paper, 46 × 57 cm (only if no adjuvant is used, *see* **Note 2**).
13. 9 cm round Petri dishes (only if no adjuvant is used, *see* **Note 2**).

2.2 Monitoring Xylem Root-to-Shoot Transport

1. Epifluorescence dissecting microscope equipped with a digital camera and a GFP or YFP filter to detect CFDA, or an RFP or mCherry filter to detect Rhodamine WT. We used a Leica M205 FA and an ET GFP filter (excitation 470/40 nm, emission 525/50 nm) for CFDA. For Rhodamine WT, we used an mCherry filter (excitation 560/40 nm, emission 630/75 nm).
2. ImageJ software (https://imagej.net/software/imagej/) to measure xylem transport velocity (*see* **Note 6**).

2.3 Monitoring Xylem-Transported Fluorescent Dyes on the Cellular Level

1. 1× Phosphate-buffered saline solution (PBS).
2. 4% (w/v) Paraformaldehyde (PFA) solution in PBS.
3. ClearSee solution: 10% (w/v) xylitol; 15% (w/v) sodium deoxycholate; 25% (w/v) urea in H_2O, as described in [19].
4. Basic Fuchsin (*see* **Note 4**).
5. Calcofluor White.
6. Six-well plates.
7. Microscope slides and cover slips.
8. Confocal laser-scanning microscope. We used a Zeiss LSM 780.

3 Methods

3.1 Applying Fluorescent Dyes to Arabidopsis Seedlings

1. Cut the Parafilm in 1 × 10 cm strips, and position one strip on a fresh media plate leaving space above and below the strip. If the plants are still small and two rows of plants fit onto one plate, two strips of Parafilm can be used per agar plate (Figs. 1a and 2a).
2. Select the Arabidopsis seedlings of interest for investigating xylem transport. Our protocol allows for the analysis of a wide range of developmental stages (*see* **Note 7**). We recommend using plants grown vertically on sterile growth media with an agar concentration higher than 1% (*see* **Note 1**).
3. Transfer carefully the selected Arabidopsis seedlings to the fresh media plate by using fine forceps. The root region

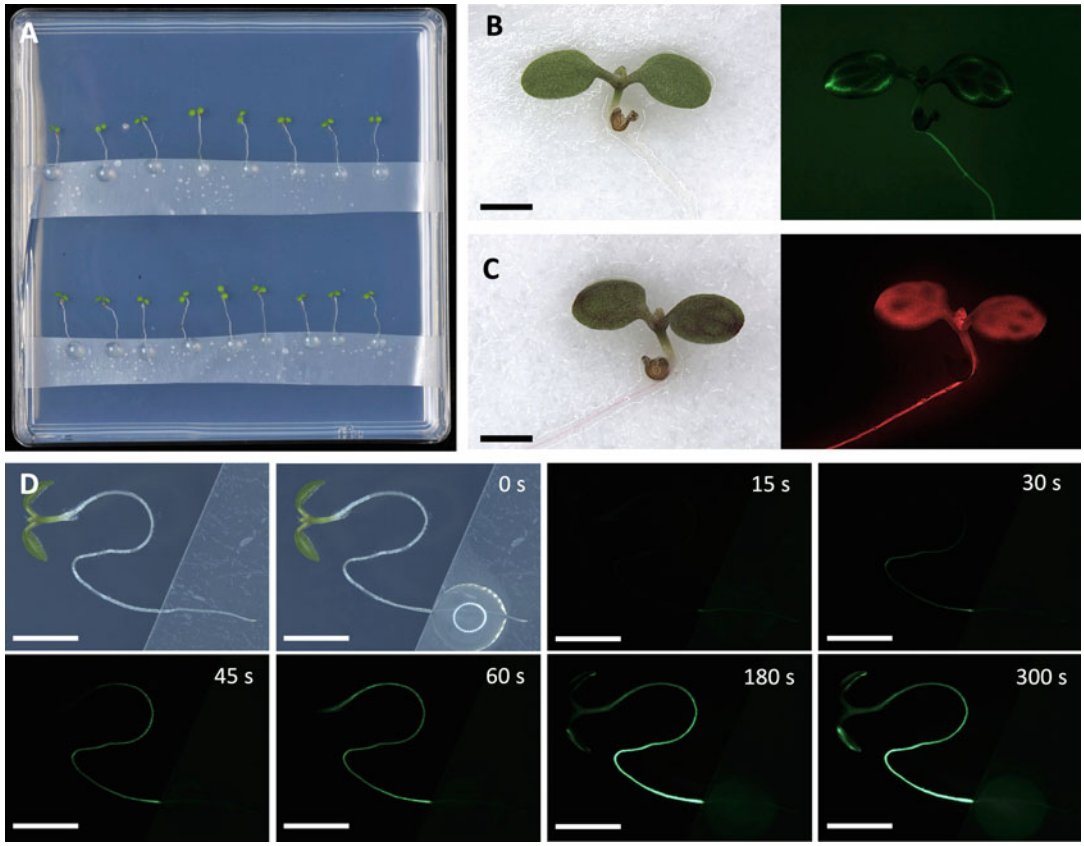


Fig. 1 Xylem transport assay in primary roots of *Arabidopsis thaliana* seedlings. (**a**) Xylem transport can be studied directly on agar medium using an Adigor containing dye solution (containing CFDA in this example) which is pipetted on the root tip. A parafilm strip is placed under the root tip to avoid spreading of the dye drop. After application to primary root tips, (**b**) CFDA or (**c**) Rhodamine WT signals are equally visible in cotyledons, demonstrating rapid root-to-shoot transport of both dyes. In contrast to CFDA, the red color of Rhodamine WT is also visible in bright field. (**d**) The xylem transports CFDA within a minute from the primary root tip region to the hypocotyl. Three minutes after dye application, the fluorescence signal is already detectable in the cotyledons. Shown are 7-day-old seedlings grown in a 12 h light/12 h dark regime. In **b**–**c** bright field images and the corresponding epifluorescence light images are shown. Scale bars **b**–**c** = 1 mm, **d** = 2 mm

where the dye shall be loaded should be positioned on the Parafilm strip, while most of the root system should be kept on the moist agar medium to ensure water supply. If the dye shall be loaded to the primary root, keep just the root tips on Parafilm (Figs. 1a and 3a, b). If the dye shall be loaded to the lateral root, keep the lateral root on the Parafilm and the upper and lower part of the primary root should be in contact with the agar medium (Fig. 2a).

4. Pipette 1 μL of the dye solution to the root region of interest, for example, close to the primary (Fig. 1a) or lateral root tip (Fig. 2a). Depending on your scientific question, continue with Subheading 3.2 or 3.3.

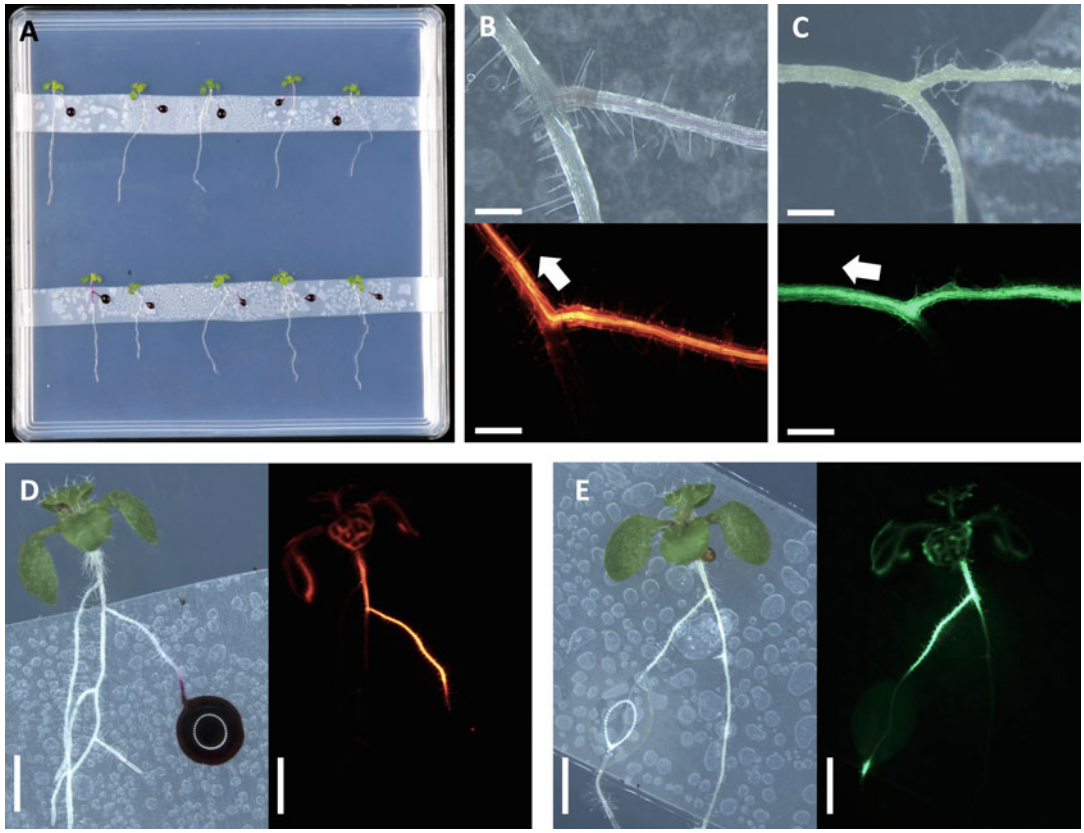


Fig. 2 Xylem transport assay in lateral roots of *Arabidopsis thaliana* seedlings. (**a**) Monitoring xylem transport in lateral roots. A parafilm strip is placed under the lateral roots of interest, and the dye solution (containing Rhodamine WT in this example) is applied to the lateral root tips. (**b**, **d**) Rhodamine WT and (**c**, **e**) CFDA are transported from the lateral root to the primary root where they are transported shootward – indicating exclusive xylem transport. (**b**, **c**) The junction of the lateral and primary root in detail. White arrows mark the direction of xylem transport. (**d**, **e**) After a few minutes, the fluorescent signal is detectable in the shoots and the venation pattern in the leaves is visible. Shown are 12-day-old seedlings grown in a 12 h light/12 h dark regime. In **b**–**e** bright field images and the corresponding epifluorescence light images are shown. Scale bars **b**–**c** = 250 μm, **d**–**e** = 2 mm

3.2 Monitoring Xylem Root-to-Shoot Transport

1. Xylem transport can be monitored directly with an epifluorescence dissecting microscope.
2. After a few minutes, the fluorescent signal should be detectable in the vascular network of the cotyledons of young seedlings (Fig. 1b–d). Any alterations of xylem transport in mutant plants or treatments of interest may be observed at this stage. For instance, the observation of rapid root-to-shoot transport is particularly useful to assess successful restoration of xylem transport in grafted plants (Fig. 3; *see* **Note 8**). It is also possible to assess xylem transport velocity (Fig. 1d, *see* **Note 6**).

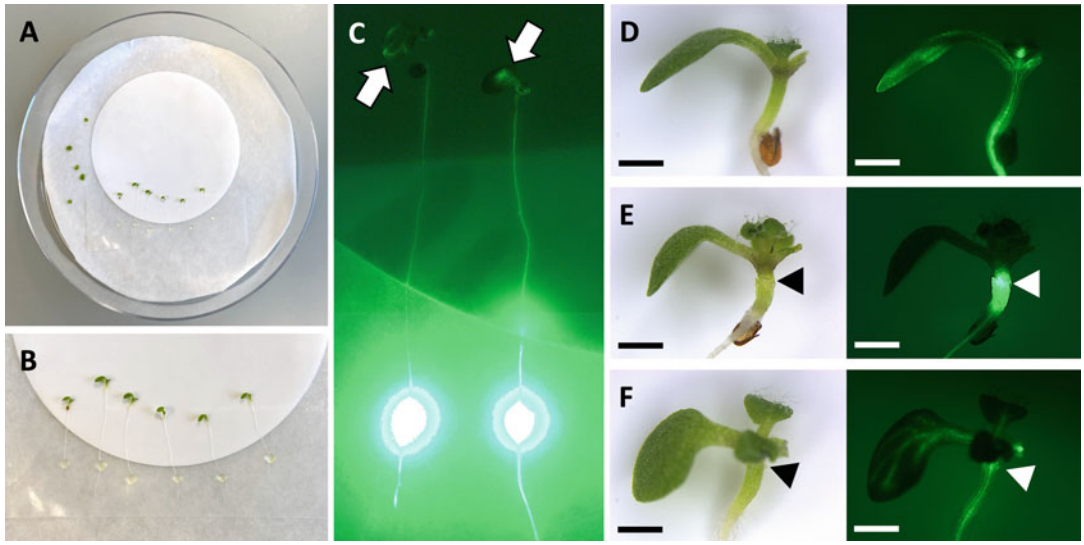


Fig. 3 Applying CFDA to root tips to monitor xylem transport recovery in grafted plants. (**a**) By adding Parafilm directly to grafting plates, xylem reconnection can be assessed in this setup: Two moist Whatman paper circles, one Parafilm rectangle and one MF-Millipore™ membrane filter are positioned in a Petri dish with grafted seedlings on top. (**b**) Close-up of (**a**) after CFDA application to seedlings. (**c**) The CFDA solution is applied to the root and the fluorescence signal is monitored in the grafted shoots (white arrows). (**d**) Ungrafted control plants display the CFDA signal in the cotyledons. (**e**) If the fluorescence signal is not detectable in the cotyledon of the grafted shoot and CFDA is accumulating at the graft junction, the xylem is not reconnected. (**f**) If the fluorescence signal is detectable in the cotyledon of the grafted shoot, the xylem is reconnected, and the xylem transport is restored across the graft junction. The graft junctions are indicated by white triangles. Fluorescence signals were detected 1 h after dye application. Shown are 14-day-old seedlings grown in a 12 h light/12 h dark regime (grafted at day 7). In **d**–**f** bright field images and the corresponding epifluorescence light images are shown. Scale bars = 500 μm

3. Depending on your scientific question, take pictures of whole seedlings (Figs. 1d and 3c), shoots (Figs. 1b, c, 2d, e, 3d–f), or specific root regions (Fig. 2b, c) for documentation.

3.3 Monitoring Xylem Transported CFDA on the Cellular Level

To visualize xylem transport on the cellular level, the protocol by Ursache et al. [19] was used with minor modifications. Carry out all incubation steps in six-well plates at room temperature on a horizontal shaker with gentle agitation. Adjust the volume of the used solutions to the number of seedlings used. Seedlings should be fully immersed in the used solutions.

1. Move whole seedlings (*see* **Note 9**) 5 min after CFDA application into fixative (4% (w/v) PFA in 1× PBS), and incubate for 1 h. Several seedlings can be put into one well (depending on seedling size).
2. Remove the fixing solution, and wash the seedlings twice for 5 min in 1× PBS.
3. Clear seedlings in ClearSee for 1 day.

4. For double staining with Basic Fuchsin and Calcofluor White, remove the ClearSee solution and incubate seedlings first with 0.2% (w/v) of Basic Fuchsin in ClearSee solution overnight. Wrap the six-well plates in aluminum foil to avoid exposing the staining solution to light. Seedlings assessed with Rhodamine WT dye solution cannot be stained with Basic Fuchsin (*see* **Note 4**). In this case, go directly to **Step 6**.
5. Remove the staining solution, rinse seedlings 3× for 15 min in 1× PBS solution, and incubate once more in ClearSee overnight.
6. Remove the ClearSee solution and stain seedlings with 0.1% (w/v) Calcofluor White in ClearSee solution for 1 h.
7. Remove the Calcofluor White solution, and wash the roots in ClearSee for 1 h.
8. Mount the seedlings in ClearSee on slides for imaging with a confocal laser-scanning microscope. Basic Fuchsin was excited with 561 nm and detected at 600–650 nm, while Calcofluor White was excited with 405 nm and detected at 425–475 nm. CFDA was excited with 488 nm and detected at 500–550 nm (Fig. 4a, b). Rhodamine WT was excited with 561 nm and detected at 550–600 nm (Fig. 4c, d).

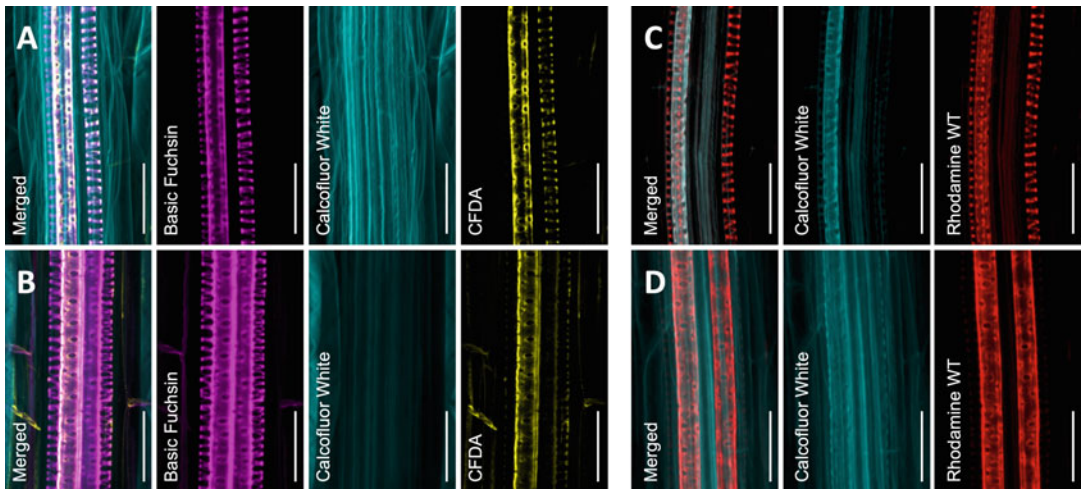


Fig. 4 CFDA and Rhodamine WT applied to root tips are specifically transported in xylem tissue. Confocal laser-scanning microscope images of fixed and stained primary root xylem tissue. (**a**, **b**) CFDA and (**c**, **d**) Rhodamine WT fluorescence can be specifically seen in xylem cells. Calcofluor White (staining cell wall cellulose) and Basic Fuchsin (staining the lignified secondary cell wall of xylem cells – only used in the CFDA experiment) were used as counter stains. (**a**) CFDA and (**c**) Rhodamine WT are transported by both protoxylem (spiral cell wall pattern) and metaxylem (pitted cell wall pattern) close to the dye application site, while approximately 1 cm above the dye application site (**b**) CFDA and (**d**) Rhodamine WT are primarily transported by metaxylem. Shown are longitudinal optical root sections of 7-day-old seedlings grown in a 12 h light/12 h dark regime. Scale bars = 20 μm

4 Notes

1. We recommend growing the plants vertically in sterile conditions on agar containing growth media (e.g., ½ Murashige and Skoog (MS) medium, pH 5.7). The agar concentration should be between 1% and 2% (w/v) so that the roots do not grow into the agar. Entire plants are then easily transferrable to the Parafilm. If there is still sufficient space for placing Parafilm and transferring plants, it is also possible to perform the whole xylem assay directly on the original growth plate. In principle, diverse developmental stages of young Arabidopsis plants can be analyzed in our plate setup. We successfully tested xylem transport in primary roots of 7-day-old seedlings (Fig. 1), in lateral roots of 12-day-old seedlings (Fig. 2), and in 14-day-old grafted seedlings (Fig. 3).
2. Adigor was already used successfully in phloem transport assays [18, 20]. We recommend using adjuvants, such as Adigor (Syngenta), since they facilitate dye penetration into roots. In a small trial, we applied CFDA solution with and without 0.5% (v/v) Adigor to seedling roots. In the Adigor-treated plants, the dye entered the root within seconds and was quickly transported to the shoot (see Fig. 1d). Without Adigor, on the other hand, CFDA signals in the shoots were only detectable in 40% of the plants ($N = 20$) 1 h after application. In most of the plants, the dye could not enter the root vasculature. While we assume that Adigor mostly influences dye penetration into root tissue, we cannot rule out that it also has an effect on xylem transport properties. Without adjuvant, however, the roots need to be cut using scalpels, as previously described [12, 14–16]. In this case, instead of working on an agar medium plate, we recommend working on moist Whatman papers to facilitate precise cuts. Cut two pieces of Whatman paper so that they fit into a Petri dish, and soak them in ddH_2O. Transfer the two moist Whatman papers to the Petri dish, and place the Parafilm strip on top. Position the selected plants with the root region of interest on the Parafilm. Perform the cut within the dye drop so that the dye can directly enter the root tissue.
3. It is also fine to work with lower CFDA concentrations, such as 1 mM. In our experience, a higher CFDA concentration (10 mM) helps to easily detect the fluorescence signal in the cotyledons. The 100 mM CFDA stock solution (in DMSO) and the 10 mM working solution are not fluorescing. If the 10 mM CFDA solution gets further diluted in water, the solution starts fluorescing weakly. This fluorescence got even stronger when the diluted solution was used several times (Fig. 5). It is still fine to work with this "old" solution for

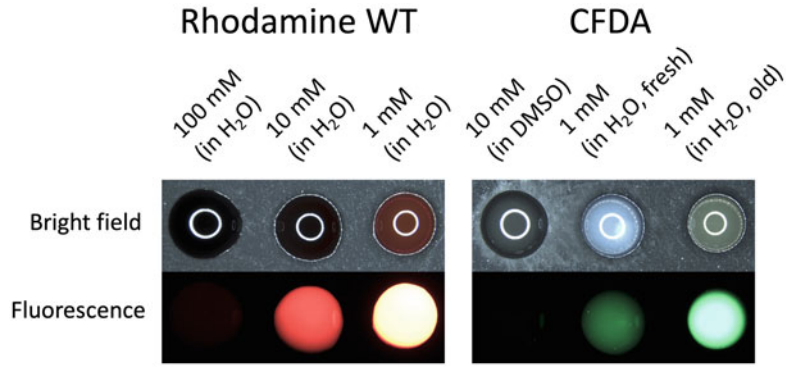


Fig. 5 Fluorescence of Rhodamine WT and CFDA dye solutions depends on different parameters. 100 mM Rhodamine WT (in water) and freshly prepared 10 mM CFDA (in DMSO) are not fluorescing, but the corresponding dilutions (in water) display fluorescence. 'Old' (e.g., 14 days after preparation) CFDA dilutions display stronger fluorescence

monitoring xylem root-to-shoot transport (Subheading 3.2, Fig. 3c) or xylem transported CFDA on a cellular level (Subheading 3.3, Fig. 4). For measuring xylem transport velocity (*see* **Note 6**), we would avoid using autofluorescencing drops to observe clearly where CFDA enters the root tissue (Fig. 1d). Note that CFDA usually starts fluorescing strongly when entering living tissue and getting into contact with intracellular esterases [13]. Besides, we observed that the rapid shootward transport of CFDA is exclusive to the xylem tissue (Fig. 4a, b).

4. To our knowledge, Rhodamine WT has not been used before in xylem transport assays. We observed that, like CFDA, this dye is rapidly transported shootward from primary or lateral roots and was detectable in leaves after a few minutes (Figs. 1c and 2d). Moreover, Rhodamine WT was exclusively transported in xylem cells (Fig. 4c, d). We noticed that highly concentrated Rhodamine WT is not fluorescing, but the corresponding dilutions are (Fig. 5). To take advantage of this self-quenching effect, we recommend using a 100 mM working solution (in ddH_2O) including 0.5% (v/v) Adigor. In this setting, the applied drop is not fluorescing, but once the dye enters the plant tissue, it gets diluted and, therefore, starts fluorescing (Fig. 2d). In contrast to CFDA, Rhodamine WT transport in roots can also be detected in bright field mode if a highly concentrated solution is used (Fig. 1c). However, Rhodamine WT-treated plants cannot be stained with Basic Fuchsin, as both dyes have very similar excitation and emission spectra. A combination with Calcofluor White, however, works well (Fig. 4c, d).

5. The agar concentration should not be higher than 2% to ensure sufficient water supply for the seedlings. Nutrients are not required in the medium, as xylem transport can be studied within several minutes. Thus, a pure agar medium works as well. See also **Note 1**.
6. To measure xylem transport velocity, using an epifluorescence dissecting microscope take a picture every 10–15 s directly after CFDA application. The dye will be transported from root tips to cotyledons within a few minutes (Fig. 1d). The resulting time series of images will give a detailed picture of xylem transport in an individual plant, and with this, the xylem transport velocity can be measured. Continue pipetting the CFDA solution and time series imaging for every seedling individually. Approximately, 20 seedlings can be imaged per hour when images are taken until 5 min after dye application (Fig. 1d). When all seedlings are analyzed, choose from each time series two successively taken pictures where the dye already entered the root xylem but has not reached the hypocotyl yet (e.g., time point 30 s and 45 s after dye application in Fig. 1d). Open the two selected images in ImageJ, set the scale, and measure in both images the distance between the start of the CFDA signal in the root tip and the CFDA front in the upper part of the root. Carefully follow the waves of the root using the "Freehand Line" tool in ImageJ. The xylem transport velocity can be calculated by dividing the resulting difference of both measured lengths by the time taken.
7. As the time needed for root-to-shoot transport could vary depending on the genotype, developmental stage, and region of dye application (total distance from the application site to the leaves), we recommend setting the optimal conditions to assess the root-to-shoot transport in your process/condition of interest.
8. If xylem transport restoration after grafting should be tested, the xylem transport assay can be performed directly on the grafting plate (Fig. 3a). The usual setup for grafting Arabidopsis seedlings consists of a round Petri dish, two moist layers of Whatman paper and a membrane with the grafted seedlings on top [21]. For a xylem assay, we recommend positioning the seedlings with the shoots on the membrane and with the root tips on the Whatman paper directly before grafting. In the following, the whole membrane can be transferred with all grafted seedlings at once to the Parafilm (Fig. 3a, b). To save time, we recommend working with the 10 mM CFDA solution containing 0.5% (v/v) Adigor. However, it is also possible to work without Adigor in this setup (*See* **Note 2**), which was done already in hypocotyl [15] and cotyledon micrografting [14]. In these studies, the shootward xylem transport was

assessed 1 h after CFDA application, assuming rapid root-to-shoot transport is xylem specific. Here, we undoubtedly confirm that the dye transport is in fact mediated by xylem cells (see Subheading 3.3; Fig. 4). If the fluorescent dye is not detectable in the cotyledons and accumulates at the graft junction instead, the xylem transport is not restored (Fig. 3e). If the fluorescent dye signal is detectable in the cotyledons, the xylem transport is restored (Fig. 3f). We recommend also testing a few ungrafted control plants in parallel (Fig. 3d).

9. We used whole seedlings for all incubation steps, since 7-day-old plants are easily transferrable (Fig. 1). If the seedlings are older (Fig. 2), it is also possible to cut off the roots or root sections of interest to facilitate easier transfer into the six-well plates.

Acknowledgment

We thank Thomas Assinger for advice about adjuvants, Orlando Maciel Rodrigues Junior for discussions about our protocol, and Simona Crivelli for critical reading of the manuscript. This work was supported by the Swiss National Science Foundation (Projects 184762 and 179551).

References

1. Cornelis S, Hazak O (2022) Understanding the root xylem plasticity for designing resilient crops. Plant Cell Environ 45:664–676. https://doi.org/10.1111/pce.14245
2. Agustí J, Blázquez MA (2020) Plant vascular development: mechanisms and environmental regulation. Cell Mol Life Sci 77:3711–3728. https://doi.org/10.1007/s00018-020-03496-w
3. Brodersen CR, Roddy AB, Wason JW et al (2019) Functional status of xylem through time. Annu Rev Plant Biol 70:407–433. https://doi.org/10.1146/annurev-arplant-050718-100455
4. Konrad W, Katul G, Roth-Nebelsick A et al (2019) Xylem functioning, dysfunction and repair: a physical perspective and implications for phloem transport. Tree Physiol 39:243–261. https://doi.org/10.1093/treephys/tpy097
5. Pascut FC, Couvreur V, Dietrich D et al (2021) Non-invasive hydrodynamic imaging in plant roots at cellular resolution. Nat Commun 12:4682. https://doi.org/10.1038/s41467-021-24913-z
6. Keller M (2006) Ripening grape berries remain hydraulically connected to the shoot. J Exp Bot 57:2577–2587. https://doi.org/10.1093/jxb/erl020
7. Sokołowska K, Zagórska-Marek B (2012) Symplasmic, long-distance transport in xylem and cambial regions in branches of Acer pseudoplatanus (Aceraceae) and Populus tremula × P. tremuloides (Salicaceae). Am J Bot 99:1745–1755. https://doi.org/10.3732/ajb.1200349
8. Birschwilks M, Sauer N, Scheel D et al (2007) Arabidopsis thaliana is a susceptible host plant for the holoparasite Cuscuta spec. Planta 226:1231–1241. https://doi.org/10.1007/s00425-007-0571-6
9. De Rybel B, Mähönen AP, Helariutta Y et al (2016) Plant vascular development: from early specification to differentiation. Nat Rev Mol Cell Biol 17:30–40. https://doi.org/10.1038/nrm.2015.6
10. Melnyk CW, Schuster C, Leyser O et al (2015) A developmental framework for graft formation and vascular reconnection in Arabidopsis thaliana. Curr Biol 25:1306–1318. https://doi.org/10.1016/j.cub.2015.03.032

11. Li S, Chen M, Yu D et al (2013) EXO70A1-mediated vesicle trafficking is critical for tracheary element development in Arabidopsis. Plant Cell 25:1774–1786. https://doi.org/10.1105/tpc.113.112144
12. Endo S, Iwai Y, Fukuda H (2019) Cargo-dependent and cell wall-associated xylem transport in Arabidopsis. New Phytol 222:159–170. https://doi.org/10.1111/nph.15540
13. Breeuwer P, Drocourt JL, Bunschoten N et al (1995) Characterization of uptake and hydrolysis of fluorescein diacetate and carboxyfluorescein diacetate by intracellular esterases in Saccharomyces cerevisiae, which result in accumulation of fluorescent product. Appl Environ Microbiol 61:1614–1619. https://doi.org/10.1128/aem.61.4.1614-1619.1995
14. Bartusch K, Trenner J, Melnyk CW, Quint M (2020) Cut and paste: temperature-enhanced cotyledon micrografting for Arabidopsis thaliana seedlings. Plant Methods 16:12. https://doi.org/10.1186/s13007-020-0562-1
15. Serivichyaswat PT, Bartusch K, Leso M et al (2022) High temperature perception in leaves promotes vascular regeneration and graft formation in distant tissues. Development 149: dev200079. https://doi.org/10.1242/dev.200079
16. Jiang M, Deng Z, White RG et al (2019) Shootward movement of CFDA tracer loaded in the bottom sink tissues of Arabidopsis. J Vis Exp 59606. https://doi.org/10.3791/59606
17. Melnyk CW (2017) Monitoring vascular regeneration and xylem connectivity in Arabidopsis thaliana. In: de Lucas M, Etchhells JP (eds) Xylem. Springer, New York, pp 91–102
18. Knoblauch M, Vendrell M, de Leau E et al (2015) Multispectral phloem-mobile probes: properties and applications. Plant Physiol 167: 1211–1220. https://doi.org/10.1104/pp.114.255414
19. Ursache R, Andersen TG, Marhavý P et al (2018) A protocol for combining fluorescent proteins with histological stains for diverse cell wall components. Plant J 93:399–412. https://doi.org/10.1111/tpj.13784
20. Knox K, Paterlini A, Thomson S et al (2018) The coumarin glucoside, esculin, reveals rapid changes in phloem-transport velocity in response to environmental cues. Plant Physiol 178:795–807. https://doi.org/10.1104/pp.18.00574
21. Bartusch K, Melnyk CW (2020) Insights into plant surgery: an overview of the multiple grafting techniques for Arabidopsis thaliana. Front Plant Sci 11:613442. https://doi.org/10.3389/fpls.2020.613442



Chapter 2

Modeling and Analyzing Xylem Vulnerability to Embolism as an Epidemic Process

Anita Roth-Nebelsick and Wilfried Konrad

Abstract

Xylem vulnerability to embolism can be quantified by "vulnerability curves" (VC) that are obtained by subjecting wood samples to increasingly negative water potential and monitoring the progressive loss of hydraulic conductivity. VC are typically sigmoidal, and various approaches are used to fit the experimentally obtained VC data for extracting benchmark data of vulnerability to embolism. In addition to such empirical methods, mechanistic approaches to calculate embolism propagation are epidemic modeling and network theory. Both describe the transmission of "objects" (in this case, the transmission of gas) between interconnected elements. In network theory, a population of interconnected elements is described by graphs in which objects are represented by vertices or nodes and connections between these objections as edges linking the vertices. A graph showing a population of interconnected xylem conduits represents an "individual" wood sample that allows spatial tracking of embolism propagation. In contrast, in epidemic modeling, the transmission dynamics for a population that is subdivided into infection-relevant groups is calculated by an equation system. For this, embolized conduits are considered to be "infected," and the "infection" is the transmission of gas from embolized conduits to their still water-filled neighbors. Both approaches allow for a mechanistic simulation of embolism propagation.

Key words Xylem, Embolism, Vulnerability curves, Model, Epidemic model, SIR model, Network theory

1 Relevance of Xylem Embolism and Its Quantification

Water transport in the xylem to transpiring leaves is driven by the pressure (or water potential) gradient generated by evaporation at the leaf tissue [36, 59]. This has the inevitable consequence that the xylem sap comes under negative pressure, which means that the water columns inside the xylem conduits are under tension. This widely accepted transport mechanism is remarkable since water under tension is a thermodynamically metastable state and

Electronic supplementary material: The online version of this chapter (https://doi.org/10.1007/978-1-0716-3477-6_2) contains supplementary material, which is available to authorized users.

Javier Agusti (ed.), *Xylem: Methods and Protocols*, Methods in Molecular Biology, vol. 2722,
https://doi.org/10.1007/978-1-0716-3477-6_2,
© The Author(s), under exclusive license to Springer Science+Business Media, LLC, part of Springer Nature 2024

therefore prone to disturbances leading to the collapse of the water column into a stable state (cavitation) and subsequent filling of the conduit with air (embolism) [59]. It is generally acknowledged that embolism occurs mostly via air seeding, meaning gas entering a functional conduit through the pits [11, 14, 16, 23, 53, 56]. In fact, it was observed that embolism occurs preferentially close to already embolized conduits or other gas-filled spaces [1, 5].

Studying embolism, its formation, and propagation within the xylem has gained much attention because the resulting loss of conductive capacity upon increasing water stress is ecologically relevant as it is related to species-specific environmental demands, ecophysiological strategies, functional wood anatomy, and drought-induced plant mortality [19, 29–31, 35, 36, 38, 58]. Studies in which the accumulating loss of hydraulic conductivity of the xylem during increasing dehydration (or decreasing water potential) is monitored have been conducted for decades [54, 59].

During the last years, various methods were developed to facilitate the determination of xylem vulnerability to embolism (quantified in terms of xylem conductivity as a function of water potential) and to make the results more reliable and reproducible. Originally, such "vulnerability curves" (VC) were produced by subjecting wood samples to dehydration, by just leaving these to dry in the lab, and recording a series of pressure/conductivity pairs [54, 59, 60]. An alternative method to decrease the water potential in wood samples is to use centrifugal force and was introduced by [9] ("Cavitron method"). Because embolism spread occurs by air seeding, meaning that the pressure difference between embolized and still functional conduits has to exceed a critical limit, also air injection into the xylem was used to generate VC [23, 57]. This method is, however, prone to cause artifacts [64].

Additionally, different methods to quantify embolism were described. Embolism can be monitored either by determining the loss of hydraulic conductivity via flow experiments [54, 59] or by observing the number of embolized conduits. Embolized conduits can be identified by staining [4] or by imaging methods, such as μCT [5, 10], nuclear magnetic resonance imaging [8], neutron imaging [61], or the "optical method" that is based on the circumstance that embolism alters visual light transmission [2]. Because hydraulic conductivity of a conduit rises with the fourth power of its radius, large conduits contribute much more to hydraulic conductivity than smaller conduits. Therefore, to convert the number of embolized vessels correctly to the loss of xylem conductivity, the radius distribution of the embolized vessels has to be known.

Meanwhile, a huge amount of data on the relationship between pressure and embolism propagation have been accumulated. The available resource of VC shows first that the vulnerability of the xylem to embolism is species-specific as well as organ-specific, and, second, point clouds of recorded pressure/conductivity pairs can often be approximated by curves that follow a sigmoidal shape

[62]. It became common practice to characterize water stress sensitivity of the xylem via parameters that are based on VC, such as the pressure P_{50}, which means that pressure under which a loss of 50% of the total hydraulic conductivity of a sample occurs. These values are used to quantify the xylem vulnerability to embolism for a certain species and organ [37, 58].

2 Vulnerability Curves and Functions Suited for Fitting Them

Usually, vulnerability curves depict the "percent loss of conductivity" against the water potential ψ or against

$$p = p_{atm} - \psi, \tag{1}$$

that is, the difference between atmospheric pressure p_{atm} (that prevails in a conduit embolized via air seeding) and the xylem water potential ψ. In what follows, we use the latter convention because conduits embolized via air seeding are then characterised by p=0. The "percent loss of conductivity" (PLC) is defined in terms of xylem hydraulic conductivity $K(p)$ as

$$PLC(p) = 1 - \frac{K(p)}{K_{max}} \tag{2}$$

with K_{max} denoting the maximum value of $K(p)$.

The typical sigmoidal shape of VC as well as their potential for ecophysiological analysis (particularly with respect to prediction of sensitivity to drought) has incited various approaches to fit experimentally obtained data that form point clouds in the pressure/conductivity plane to suitable curves. Characterizing the obtained data in this way simplifies the extraction of ecophysiological information, such as the above-mentioned pressure P_{50}, from the data. Notice that curve fitting merely facilitates data handling and interpretation; it does not provide *per se* insights into the mechanisms that produce these data. It is, nonetheless, reasonable to use fitting functions that have proven helpful in structurally similar problems.

One such natural candidate is the logistic function [44]

$$PLC(p) = \frac{1}{1 + e^{-a(p - P_{50})}}, \tag{3}$$

which is able to fit the sigmoidal "S" shape very nicely, if the data points lie symmetric with respect to the point $(p, PLC) = (P_{50}, 0.5)$. The slope of the function $PLC(p)$ at $p = P_{50}$ amounts to $a/4$.

The logistic shape of a VC consists of three parts (Fig. 1): a flat initial phase (a "lag" phase), followed by a more or less steep slope and a final flat part. The steep incline indicates a fast accumulation of embolized conduits once a certain pressure has been exceeded. The steepness of this incline is considered to reflect vulnerability to embolism [1].

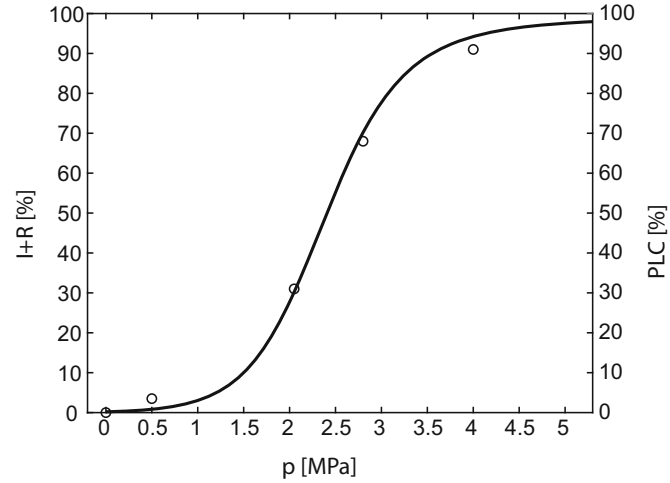


Fig. 1 Vulnerability curve calculated with the SIR model applied to data of *Sequoia sempervirens* [5]. The ordinate represents the percentage $I + R$ of embolized conduits as a function of xylem pressure p. Circles: experimental determination of embolized conduits obtained via the μCT image method [5]. Selected parameters: $\sigma = 7$, $V_{con} = 1.6$ MPa [47]. Native embolism (I_0) was selected according to the μCT images [5]. This example was calculated by using Matlab. The corresponding script (in Live Code File Format) can be found in the Supplement (Supplement_homogeneous_model). Image from [47]

If the (p, PLC) -point cloud does not show the symmetry exhibited by the logistic function, functions with more than one undeterminate parameter (a, in the case of the logistic function) have to be used. Candidates are the Weibull distribution function [15, 43]

$$PLC(p) = 1 - e^{-ap^b} \tag{4}$$

with undeterminate parameters a and b, or the Gompertz function

$$PLC(p) = ae^{-e^{b-cp}} \tag{5}$$

with open parameters a, b, and c. The application of both functions to xylem failure is probably motivated from their successful usage in the fields of reliability engineering, failure analysis, and calculation of mortality rates. In fact, they provide enough flexibility to represent the so-called r-shaped VC, or other and even more complex shapes [3, 10, 55]. The reasons for these "non-sigmoidal" shapes and whether these are due to artifacts are still under discussion [3, 51, 55].

While empirical VC fitting provides information on the susceptibility to embolism for a specific wood, it does not indicate any mechanistic explanation for the specific VC shape. Benchmark data of xylem vulnerability to embolism derived from VC, such as P_{50} or the slope of the steep part of a VC, are expected to depend on

various anatomical key parameters. Analyzing the role of specific anatomical traits that are supposed to be involved in air seeding requires mechanistic theoretical approaches. In this contribution, two methods will be considered and discussed: epidemic modeling and network theory. Both methods describe the transmission of "objects" between interconnected elements.

3 Mechanistic Approaches to Describe Xylem Vulnerability for Embolism

Various traits are considered to be important for xylem vulnerability to embolism and therefore for the specific shapes of VCs. Of particular interest is the pit structure. For angiosperms, mainly the nanostructure of the pit membrane is considered, as it dictates the pressure gradient that is necessary to drive gas from a dysfunctional conduit to its still functioning neighbor. There are ongoing efforts to obtain a detailed picture of the pit membrane structure, its porosity, and the impact of pit traits on xylem vulnerability to embolism [25, 28, 31, 45, 65] and also of the physical processes of air seeding [22, 48]. Likewise, pit and torus structure in conifers are studied with respect to their role in embolism propagation [50, 52].

On a higher level, the total pit area of a conduit, represented by the number and size of pits, is considered to be important because it was suggested that the probability for air seeding along a conduit would increase with pit membrane area [6, 63]. The rare-pit hypothesis suggests that all species have a small fraction of exceptionally "leaky" pits (the leakiness caused, for instance, by an unusually wide opening in the nanostructure of the pit membrane). Although this hypothesis is currently under debate [6, 7, 24, 25, 49], it is reasonable to assume that the probability for a conduit to show in at least one of its pits an exceptionally large pit membrane pore rises with pit membrane area [39].

Another crucial parameter for embolism spread is the number of conduits with which a given conduit is connected (by one or more pits): a multi-connected conduit can potentially initiate embolism in more neighbors than a conduit with fewer connections. This parameter leads on to the next scale level, from the characteristics of single conduits to characteristics of the conduit population making up a wood sample. In the end, propagation of embolism depends on the "collective" behavior of many interconnected conduits. To describe and analyze collective processes within populations of interconnected entities, various tools are available, which have similarities as well as fundamental differences. Two of them were applied to xylem embolism and will be described in the next sections: network analysis and epidemic modeling.

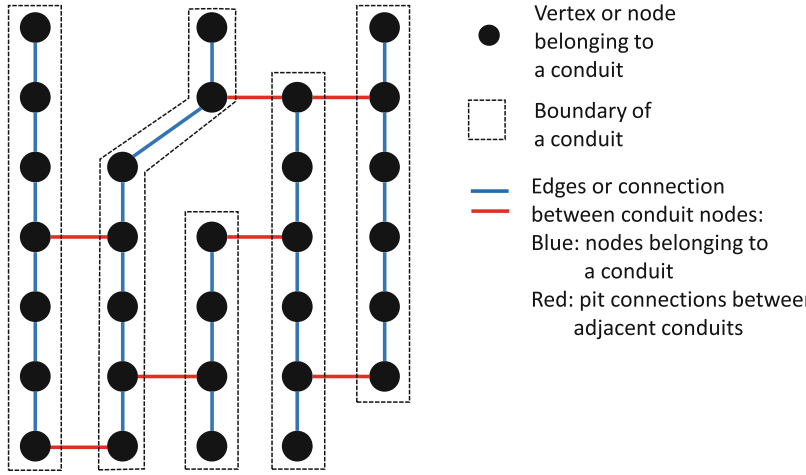


Fig. 2 Example for a graph that is used in network theory. Graphs consist of vertices that are interconnected, with the connections represented by edges. This graph is suitable to represent xylem structure because it is a lattice-like structure with mostly adjacent vertices being interconnected (for instance, Loepfe et al. [33]). Different kinds of connections are possible, indicated by blue and red edges. The vertices interconnected by blue edges may represent conduits, whereas the red edges represent pits connecting adjacent conduits

3.1 Modeling Embolism by Graphs and Network Theory

Graphs describe the relations between objects (or entities) and consist of vertices (or nodes) and edges linking the vertices (Fig. 2). Graphs allow for representing any kinds of relations, such as in physics, computer sciences, biology, or sociology. The analysis of graph systems is network theory [12]. Network theory was applied to embolism propagation in the xylem by Loepfe et al. [33] and Mrad et al. [39, 40].

The first step for analyzing embolism propagation patterns in a model of interconnected conduits is to design the conduit network. To create a xylem model, [33] generated a three-dimensional population of conduits that are aligned parallel along the flow direction, with a "lower" end (the inlet) and an "upper" end (the outlet). The geometry of the conduits (including length, diameter, and the number of pits) and the geometry of the pits in the model were—based on data of real conduit geometry—randomly distributed.

In a second step, the overall hydraulic resistance of the conduit network was calculated: the resistance of individual conduits can be inferred from the law of Hagen–Poiseuille, and the resistance provided by the openings in the pit membrane follows via the law of Darcy and the continuity equation. Combining these basic elements according to the network design provides the overall hydraulic resistance of the network. This result allows to express the flow through the (functioning) conduit network as a function of the pressure difference between inlet and outlet.

In a third step, embolism propagation is calculated: the Young–Laplace equation is used to predict if an embolized conduit remains "hydraulically isolated" or if gas can enter and embolize a still

functioning neighboring conduit. This depends: (i) on the pressure difference between gas- and water-filled conduit and (ii) the radii of the gas/water interfaces forming around the membrane pores. Since the sizes of the membrane pores are supposed to follow some distribution, embolism may propagate along the whole distance between the inlet and outlet or it may stop at some point. When the pressure difference between inlet and outlet is varied, embolism propagation also varies.

Based on this network model of xylem, Loepfe et al. [33] conducted "virtual experiments," meaning a large number of single model runs in which the effects of parameter variations on the resulting flow and embolism were evaluated. The results demonstrated the influence of the various xylem anatomical parameters on xylem vulnerability and also conductivity. Increasing conduit diameter, conduit length, connectivity, pit pore size, or pit area all promoted hydraulic conductivity. Increasing connectivity, however, enhanced also vulnerability to embolism, as did the rising size of pit membrane pores (as expected) and conduit length.

The model devised and studied by [33] impressively demonstrated how various xylem traits affect hydraulic conductivity and embolism in a different way and provided a theoretical basis for interpreting the relationships between xylem anatomy and embolism spread. The latter process was represented by vulnerability curves that were obtained from the calculation results by performing a series of runs with increasing pressure load.

In a recent study, Mrad et al. [39] modified the original network model approach of Loepfe et al. [33] to include additional parameters, particularly pit membrane traits, such as thickness, pit aperture, and depth of the pit chamber. The aim was to include the mechanical behavior of pit membranes under mechanical load because it is assumed that pit membranes bulge under the pressure difference between embolized and water-filled conduits. This bulging is expected to enlarge the pit membrane pores, depending on pit membrane thickness, and is limited by the size of the stomatal chamber (Tixier et al. 2014). The results of [39] supported these assumptions and provided further evidence for the influence of pit structure and conduit connectivity on embolism propagation (the network model is publicly available at https://github.com/mradassaad/Xylem_Network_Matlab).

Network models provide valuable insights into the influence that xylem anatomy has on susceptibility to embolism and on its propagation that can be tracked by series of model runs. The effect of spatial structure can be observed, such as clustering of interconnected conduits, because graphs represent topologies with a finite number of objects. A xylem model represented by a graph is therefore an "individual" sample, very much like a physical wood sample. Network models of graphs represent therefore a discrete mathematical approach, similar to finite-element modeling

that is based on subdividing a concrete problem setting into a mesh and solving the related mathematical approach numerically for this defined computational domain. To change the "anatomical" structure of the modeled xylem sample, it is necessary to generate a new graph. A network model run represents therefore an *in silico* experiment performed on virtual xylem samples, providing data on embolism spread.

3.2 Modeling Embolism by Epidemic Theory

3.2.1 The Classic SIR Model

Embolism propagation by air seeding occurs by transmission of air from embolized conduits to their neighbors and resembles therefore an epidemic that is the spreading of an infection within a population by direct contact between infected and uninfected individuals. In fact, network theory and epidemiology are linked in many ways [26]. The "standard models" in epidemic theory are compartment models, that is, a population is subdivided into infection-relevant groups ("classes") whose interaction and temporal evolution are described by first-order differential equations (with respect to time).

One basic approach is the SIR model that consists of three classes: S means the individuals who are susceptible to the infection, I are the individuals who are infected and transmit the infection, and R are those individuals who are "removed" from the epidemic process by having recovered (and acquired immunity) or died [17]. S, I, and R mean the number of individuals (with $N = S + I + R$ denoting the total population size) or—another often chosen convention—the proportion of individuals with respect to the total population size, i.e., $S + I + R = 1$. The temporal evolution of a spreading infection is described in the SIR model by the following system of three ordinary, non-linear, differential equations:

$$dS/dt = -\beta IS \tag{6a}$$

$$dI/dt = \beta IS - \gamma I \tag{6b}$$

$$dR/dt = \gamma I. \tag{6c}$$

The parameters β and γ control the interaction that evolves between S, I, and R.

The left-hand sides of Eqs. (6a) to (6c) represent the slopes of the curves in Fig. 3, while the right-hand sides specify the interactions between the classes S, I, and R. The product βIS in Eqs. (6a) and (6b) represents the contacts between infectious (I) and susceptible (S) individuals that result in an infection and the transfer of the infected from S to I, whereupon class S decreases and I increases. The parameter β—the mean number of infections caused by one

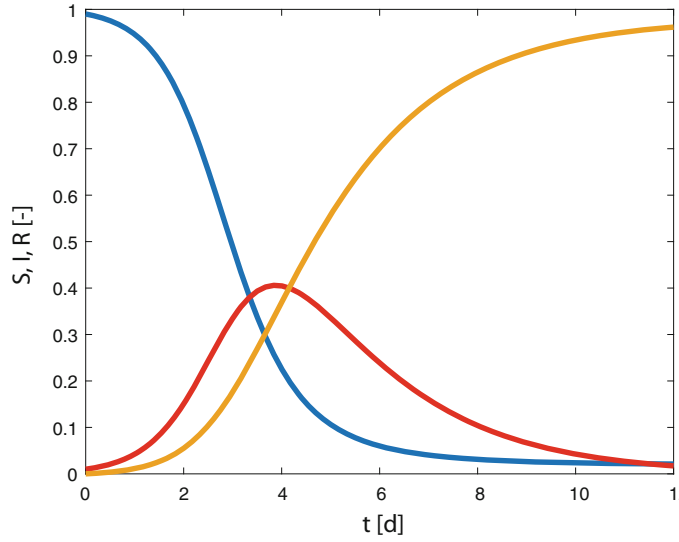


Fig. 3 Solution curves $S(t)$, $I(t)$, and $R(t)$ of the SIR model, according to Eq. (6) for the parameter values $\beta = 3\ d^{-1}$ and $\gamma = 1\ d^{-1}$. Blue: $S(t)$, red: $I(t)$, Yellow: $R(t)$. This example was calculated by using Matlab. The corresponding script (in Live Code File Format) can be found in the Supplement (Supplement_basic_model)

infective person per time unit—contains information on the intensity of the contact and on the infectiousness of the pathogen.

The parameter γ in Eqs. (6b) and (6c) denotes the mean value of the rate of removal, i.e., the average number of individuals transferred from class I to R per time unit, with obvious consequences for both classes. The reciprocal of γ can be understood as the time an individual remains infectious. Since γ represents a mean value, the time that an individual remains in class I scatters around the value $1/\gamma$. It has been shown [18] that the fraction of individuals that is still in the infective class Δt time units after entering class I is exponentially distributed, according to

$$P(\Delta t) = \exp(-\gamma \Delta t). \tag{7}$$

The definitions of β and γ imply that the fraction

$$\sigma = \frac{\beta}{\gamma} \tag{8}$$

is the mean number of individuals infected by one infectious person.

In order to obtain a definite solution of the system Eq. (6), initial values $S_0 = S(t=0)$, $I_0 = I(t=0)$, and $R_0 = R(t=0)$ have to be prescribed (in addition to β and γ). Solutions of Eq. (6) provide the temporal course of the three classes; an example is shown in Fig. 3.

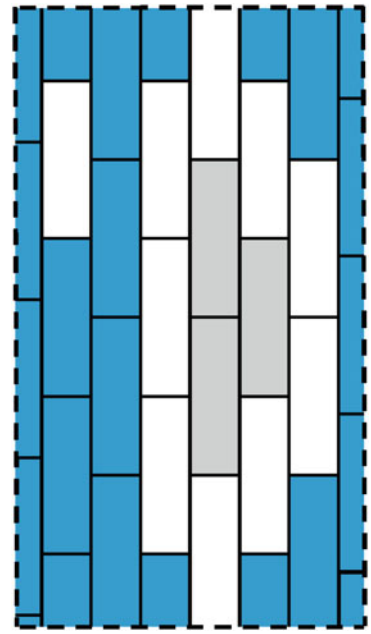


Fig. 4 Schematic representation illustrating the application of the SIR model to the xylem. The three conduit classes are: *S* (susceptible), which are functional water-filled conduits (blue), *I* (infective) embolized conduits (white), and *R* (removed) conduits (grey). The difference between *I* conduits and *R* conduits lies in the capacity to "air-seed" neighbors. Conduits in the class *R* do no longer participate in the embolism process because they have already infected all of their neighbors

3.2.2 Application of the SIR Model to Xylem Embolism and Air Seeding

In terms of embolism, air seeding can be regarded as the transmission of an infection, and all functional conduits can be regarded as susceptible to air seeding (class *S*). Embolized conduits that are able to transmit air to neighbors can be regarded as being both "infected" (with air) and "infectious" and belong therefore to class *I*. If, however, an air-filled conduit has transmitted air to all of its neighbors, it has exhausted its infective potential and is removed from the propagation process. Therefore, these isolated embolized conduits belong to class *R* (Fig. 4).

The structural similarity between an epidemic and embolism spreading in the xylem can be concretized as follows:

- Originally, SIR models refer to time as independent variable. Crucial for embolism is, however, not time but the difference $p = p_{atm} - \psi$ between the gas pressure in the infective (already embolized) conduit and the water potential in the still functioning conduit. The value of p is decisive for the occurrence of air seeding and thus for conduits becoming dysfunctional. Therefore, if a classic SIR model as in Eq. (6) is used to describe the spreading of xylem embolism, the pressure p defined in Eq. (1) instead of time t should be chosen as the independent variable.

- If t is replaced by p, consistency requires that β and γ have units of 1/pressure. The pressure $V_{con} = 1/\gamma$ may then be considered to represent the mean value of the "critical" difference between the pressure in an embolized conduit (which can be expected after air seeding to be close to atmospheric pressure p_{atm}) and the xylem water potential ψ in an adjacent conduit (see Eq. (1)) that leads to air seeding. If p exceeds V_{con}, air seeding occurs and a functioning conduit becomes embolized. Therefore, a high V_{con} means a low vulnerability because the conduit can withstand a high pressure difference $p = p_{atm} - \psi$. In contrast, a low V_{con} means a high vulnerability for a conduit, meaning that it becomes embolized already for smaller pressure differences p than a conduit with a high V_{con}.
- The analogue of Eq. (7), if t is replaced by p, is

$$P(\Delta p) = \exp\left(-\frac{\Delta p}{V_{con}}\right), \tag{9}$$

  i.e., it gives the fraction of infected conduits that is still able to spread air seeding if the pressure difference has been increased by Δp since the conduit was embolized (i.e., after having entered class I).
- The parameter σ, defined in Eq. (8), represents now the conduit interconnectedness, that is, the number of neighbors with which a conduit shares connective pits.

To summarize, the SIR model with its parameters β and γ can principally be translated to air seeding by the replacement

$$\gamma = \frac{1}{V_{con}}, \tag{10}$$

and the reinterpretation of σ as the conduit interconnectedness. The value of the parameter β is then obtained via

$$\beta = \sigma\gamma. \tag{11}$$

Besides σ and V_{con}, initial values S_0, I_0, and R_0 for $p = 0$ have to be prescribed. Assigning a certain initial number I_0 to the class I means to start embolism propagation by "seeding" a preexisting amount of embolized (= infected) individuals. High I_0 shortens or even "cuts off" the lag phase of the $I(p) + R(p)$ curves (cf. Fig. 1), that is, increasing I_0 promotes embolism propagation [47]. Higher R_0 values lead to flatter slopes of the $I(p) + R(p)$ curves [47].

In its basic form, as given in Eq. (6), the SIR model is applied to a "homogeneous" population of conduits, meaning that all conduits show the same mean values of interconnectedness σ and vulnerability V_{con}. Such a structure appears to be particularly appropriate for coniferous wood consisting of tracheids. Figure 1 shows the result of an SIR model for *Sequoia sempervirens*. The initial size

I_0 of the infected group was based on μCT analysis of [5]. Interconnectedness σ was estimated from various anatomical studies ([5], see also the discussion in [47]). No data, however, existed for V_{con}, which were tuned in such a way that the SIR curve matched experimental vulnerability data. To obtain maximum fitting of the SIR result with the measured VC, a $V_{con} = 1.6$ MPa was suitable.

It is important to emphasize that the influence of both V_{con} and σ means that similarly shaped VC can be obtained with different combinations of both parameters. The effects of the two parameters on a VC are, however, different. As can be shown with SIR parameter variations, P_{50} decreases approximately linearly with increasing conduit vulnerability (= decreasing V_{con}) for a defined value of interconnectivity σ, whereas for a fixed V_{con} the P_{50} declines with increasing σ in a non-linear way [47].

3.2.3 Differences and Links Between the SIR Approach and Network Models—the Relevance and Role of Spatial Structure and Probability

For both approaches, the probability of a functional conduit for becoming "infected with air" depends on, first, the probability of being a neighbor of an already embolized conduit and, second, the probability that the pit membrane area that separates the functional conduit from the infected neighbor fails and allows gas to be transmitted.

In contrast to the network model, the "classic" epidemic approach as exemplified by Eq. (6) does not include a spatial analysis of the propagation of an infection (it is possible, however, to complement Eq. (6) by spatial components in the form of diffusional terms, *see* Noble [42] or Murray [41]). For instance, the exact location of the infected part of the population with respect to the non-infected part cannot be obtained via an analysis based on SIR. The underlying concept of the SIR is that the epidemic is driven by the contacts and not by the exact spatial structure of the population: what counts, apart from I_0, the initial number of infected individuals, are the infectious contacts between infected and non-infected individuals. In other words, spatial structures are only indirectly considered if they reflect contact conditions. The classic SIR model appears therefore to be particularly apt for xylem because the interconnectivity between conduits is—once the xylem is ontogenetically mature—static.

The influence of spatial structure of contacts between the conduits is, however, relevant for xylem with different conduit classes and therefore particularly for angiosperms. Here, long and wide vessels can potentially contribute to air seeding dispersal stronger than shorter vessels if connectivity to other conduits is expected to increase with conduit size. Also, a longer vessel can potentially infect neighbors over a longer distance. These effects were visible in the network models [33]. There are, however, also other structural details that influence embolism propagation, such as vessel

grouping. Also, interconnectivity can be higher in conduits of the same age, leading to circumferential embolism patterns [46].

Such spatial heterogeneities can, however, be considered by dividing a SIR population into different subpopulations that show different properties with respect to infection transmission [13, 34]. To account for such heterogeneous populations, "stratified populations" can be defined, that is, groups of conduits that show different values of the pressure V_{con} and of the interconnectivity between conduits, σ. Also, the interconnectivity between the different groups can be specified. The general form for a stratified SIR population consisting of m subpopulations of conduits is (for m subpopulations, $j = 1 \ldots m$)

$$\begin{aligned} dS_j/dp &= -S_j\left(\beta_{1j}I_1 + \ldots + \beta_{mj}I_m\right) \\ dI_j/dp &= S_j\left(\beta_{1j}I_1 + \ldots + \beta_{mj}I_m\right) - \gamma_j I_j \\ dR_j/dp &= \gamma_j I_j \end{aligned} \tag{12}$$

with σ generalized to $\sigma_{kj} = \beta_{kj}/\gamma_j$. For example, a SIR population consisting of two subpopulations, SP 1 and SP 2, shows four interconnectivities $(\sigma_{11}, \sigma_{12}, \sigma_{21}, \sigma_{22})$ and two pressure thresholds $(V_{con,1}, V_{con,2})$ (Fig. 5). Notice that the latter are simply subpopulation-specific, while the interconnectivities connect a given conduit with conduits of the same subpopulation (SP 1 $\overset{\sigma_{11}}{\leftrightarrow}$ SP 1 and SP 2 $\overset{\sigma_{22}}{\leftrightarrow}$ SP 2) and with conduits of the other subpopulation (SP 1 $\overset{\sigma_{12}}{\leftrightarrow}$ SP 2 and SP 2 $\overset{\sigma_{21}}{\leftrightarrow}$ SP 1).

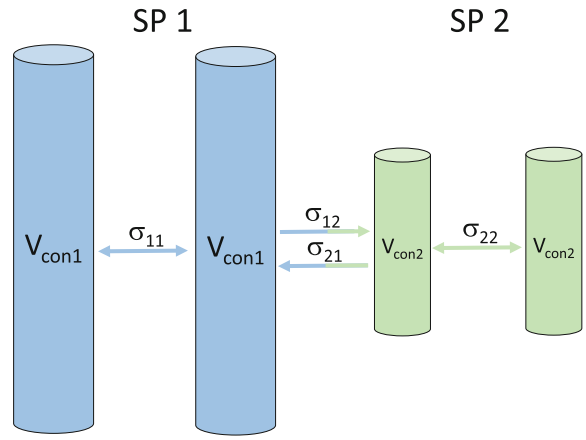


Fig. 5 The SIR model allows the considered population to consist of different groups with different interconnectivities and vulnerabilities. This sketch shows a conduit population composed of two subpopulations (SP), SP 1 and SP 2: longer vessels (SP 1, blue) and shorter vessels (SP 2, green). Four different connectivities are possible: one connectivity between SP 1 vessels, one connectivity between SP 2 vessels, and two connectivities between SP 1 and SP 2 vessels. Also, different V_{con} can be assigned to the subpopulations

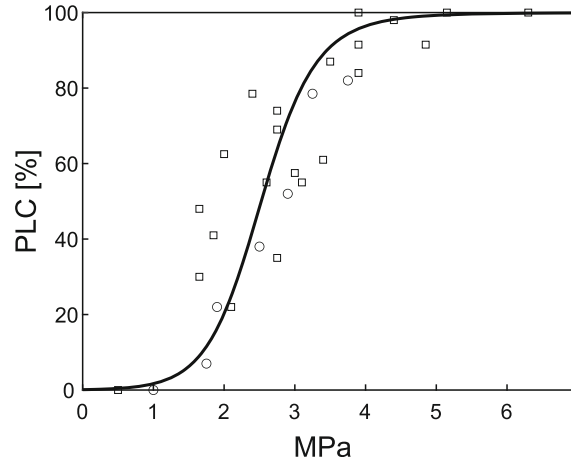


Fig. 6 VC calculated by the two-group SIR model for two groups of vessels, applied to *Fraxinus excelsior* showing earlywood vessels (diameter = 100 μm) and latewood vessels (diameter = 40 μm). Input parameters: $\sigma = 7$ for and between latewood vessels, $\sigma = 9$ for and between earlywood vessels, $\sigma = 0.3$ between both vessel types, $V_{con} = 3$ MPa for both earlywood and latewood vessels, native embolism $I_0 = 0.1\%$, $R_0 = 0\%$. The percent loss of hydraulic conductivity (PLC) was calculated by using the Hagen–Poiseuille law, according to [4]. The points represent experimental data by [66], obtained by two different methods. Circles: Bench dehydration data. Squares: Pneumatic method. This example was calculated by using Matlab. The corresponding script (in Live Code File Format) can be found in the Supplement (Supplement_two_group_model)

As an exemplary case, a two-group model will be applied considering the data set of [66] for xylem vulnerability in *Fraxinus excelsior* that shows two vessel types: wider earlywood vessels and narrower latewood vessels. The wider earlywood vessels were assumed to be shorter than the latewood vessels [20, 21, 32] and therefore to show more connections [33]. Connectivity between earlywood vessels and latewood vessels was assumed to be low [27]. A combination of $\sigma = 7$ between latewood vessels, $\sigma = 9$ between earlywood vessels, and $\sigma = 0.3$ between both vessel types as well as $V_{con} = 3$ MPa for both earlywood and latewood vessels lead to a decrease in hydraulic conductivity fitting the experimental VC quite well (Fig. 6) [47]. It should be emphasized that the PLC data of [66] can in fact be matched by other combinations of vulnerability and connectivity. Increasing V_{con} requires a higher connectivity and vice versa, to maintain the fit between calculated PLC and the PLC data obtained by [66].

The epidemic curves presenting the I + R fraction separated into earlywood and latewood vessels (Fig. 7) show that the latewood vessels are more resistant to embolism compared to the earlywood vessels. Since identical V_{con} was assigned to both vessel types, the higher resistance of the latewood vessels is caused by their lower interconnectivity.

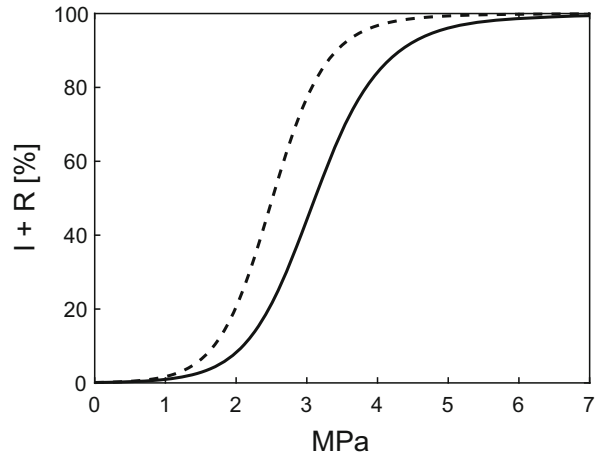


Fig. 7 Epidemic curves of the two-group SIR model applied to earlywood and latewood vessels in *Fraxinus excelsior* (VC see Fig. 6). The graph shows I + R curves of larger earlywood vessels (100 μm diameter) and narrower latewood vessels (40 μm diameter). Input parameters: $\sigma = 7$ for and between latewood vessels, $\sigma = 9$ for and between earlywood vessels, $\sigma = 0.3$ between both vessel types, $V_{con} = 3$ MPa for both earlywood and latewood vessels, native embolism $I_0 = 0.1\%$, $R_0 = 0\%$. Dashed line: earlywood vessels. Solid line: latewood vessels This example was calculated by using Matlab. The corresponding script (in Live Code File Format) can be found in the Supplement (SIR_Supplement_two_group_model). Image from [47]

The possibility of defining different subpopulations with different interconnectivities and different "air seeding vulnerability" allows for constructing quite complex xylem structures and to analyze the impact of the considered anatomical key parameters [47]. The results are provided directly in the form of VC because the SIR equation system calculates the fractions of the conduits as belonging to the three "embolism states" S (water-filled), I (embolized and capable to propagate embolism), and R (embolized and no longer propagating embolism). Particularly, interconnectivity σ and V_{con} can be assigned independently from each other, allowing separate analysis of these two crucial traits.

4 Conclusions

Modeling embolism propagation by network models and epidemic models allows us to analyze the influence of the two key parameters, conduit interconnectivity, and conduit vulnerability on vulnerability curves. Particularly, the possibility to evaluate the effect of both parameters separately is valuable and contributes to our understanding of embolism propagation and the reasons for different VC shapes. Available results of embolism modeling by network

models and epidemic modeling illustrate how both parameters, conduit interconnectivity and conduit vulnerability, interact in producing VC. Whereas the possibility of a mechanistic analysis of embolism propagation therefore exists, there is a lack of data on conduit interconnectivity and conduit vulnerability, which requires the tuning of input data in embolism modeling to match experimental VC data. To fully exploit the possibility of mechanistic modeling of embolism propagation, more data on xylem conduit structure and conduit vulnerability are desirable.

References

1. Avila RT, Guan X, Kane CN, Cardoso AA, Batz TA, DaMatta FM, Jansen S, McAdam SAM (2022) Xylem embolism spread is largely prevented by interconduit pit membranes until the majority of conduits are gas-filled. Plant Cell Environ 45(4):1204–1215. https://doi.org/10.1111/pce.14253
2. Brodribb TJ, Carriqui M, Delzon S, Lucani C (2017) Optical measurement of stem xylem vulnerability. Plant Physiol 174(4):2054–2061
3. Cai J, Li S, Zhang H, Zhang S, Tyree MT (2014) Recalcitrant vulnerability curves: methods of analysis and the concept of fibre bridges for enhanced cavitation resistance. Plant Cell Environ 37(1):35–44
4. Cai J, Tyree MT (2010) The impact of vessel size on vulnerability curves: data and models for within-species variability in saplings of aspen, *Populus tremuloides* Michx. Plant Cell Environ 33(7):1059–1069
5. Choat B, Brodersen CR, McElrone AJ (2015) Synchrotron X-ray microtomography of xylem embolism in *Sequoia sempervirens* saplings during cycles of drought and recovery. New Phytol 205(3):1095–1105. https://doi.org/10.1111/nph.13110
6. Christman MA, Sperry JS, Adler FR (2009) Testing the 'rare pit' hypothesis for xylem cavitation resistance in three species of *Acer*. New Phytol 182(3):664–674
7. Christman MA, Sperry JS, Smith DD (2012) Rare pits, large vessels and extreme vulnerability to cavitation in a ring-porous tree species. New Phytol 193(3):713–720
8. Clearwater M, Clark C (2003) In vivo magnetic resonance imaging of xylem vessel contents in woody lianas. Plant Cell Environ 26:1205–1214
9. Cochard H (2002) Xylem embolism and drought-induced stomatal closure in maize. Planta 215(3):466–471
10. Cochard H, Delzon S (2013) Hydraulic failure and repair are not routine in trees. Ann For Sci 70(7):659–661
11. Cochard H, Holtta T, Herbette S, Delzon S, Mencuccini M (2009) New insights into the mechanisms of water-stress-induced cavitation in conifers. Plant Physiol 151(2):949–954
12. Costa LdF, Oliveira ON, Travieso G, Rodrigues FA, Villas Boas PR, Antiqueira L, Viana MP, Correa Rocha LE (2011) Analyzing and modeling real-world phenomena with complex networks: a survey of applications. Adv Phys 60(3):329–412. https://doi.org/10.1080/00018732.2011.572452
13. Daley DJ, Gani J (2001) Epidemic modelling: an introduction, vol 15. Cambridge University Press, Cambridge
14. Delzon S, Douthe C, Sala A, Cochard H (2010) Mechanism of water-stress induced cavitation in conifers: bordered pit structure and function support the hypothesis of seal capillary-seeding. Plant Cell Environ 33(12):2101–2111
15. Hacke U, Sperry J, Wheeler J, Castro L (2006) Scaling of angiosperm xylem structure with safety and efficiency. Tree Physiol 26:689–701
16. Hacke UG, Sperry JS, Pittermann J (2004) Analysis of circular bordered pit function II. Gymnosperm tracheids with torus-margo pit membranes. Am J Bot 91(3):386–400
17. Hethcote HW (2000) The mathematics of infectious diseases. SIAM Rev 42(4):599–653
18. Hethcote HW, Stech HW, van den Driessche P (1981) Periodicity and stability in epidemic models: a survey, pp 65–82. Elsevier, Amsterdam
19. Jacobsen AL, Ewers FW, Pratt RB, Paddock WA, Davis SD (2005) Do xylem fibers affect vessel cavitation resistance? Plant Physiol 139(1):546–556
20. Jacobsen AL, Pratt RB, Tobin MF, Hacke UG, Ewers FW (2012) A global analysis of xylem vessel length in woody plants. Am J Bot 99(10):1583–1591. https://doi.org/10.3732/ajb.1200140
21. Jacobsen AL, Valdovinos-Ayala J, Rodriguez-Zaccaro FD, Hill-Crim MA, Percolla MI,

Venturas MD (2018) Intra-organismal variation in the structure of plant vascular transport tissues in poplar trees. Trees 32(5):1335–1346. https://doi.org/10.1007/s00468-018-1714-z

22. Jansen S, Klepsch M, Li S, Kotowska M, Schiele S, Zhang Y, Schenk H (2018) Challenges in understanding air-seeding in angiosperm xylem. Acta Horticulturae, Belgium
23. Jarbeau J, Ewers F, Davis S (1995) The mechanism of water-stress-induced embolism in two species of chaparral shrubs. Plant Cell Environ 18:189–196
24. Kaack L, Altaner CM, Carmesin C, Diaz A, Holler M, Kranz C, Neusser G, Odstrcil M, Schenk HJ, Schmidt V (2019) Function and three-dimensional structure of intervessel pit membranes in angiosperms: a review. IAWA J 40(4):673–702
25. Kaack L, Weber M, Isasa E, Karimi Z, Li S, Pereira L, Trabi CL, Zhang Y, Schenk HJ, Schuldt B (2021) Pore constrictions in intervessel pit membranes provide a mechanistic explanation for xylem embolism resistance in angiosperms. New Phytol 230(5):1829–1843
26. Keeling MJ, Eames KT (2005) Networks and epidemic models. J Roy Soc Interface 2(4):295–307. https://doi.org/10.1098/rsif.2005.0051
27. Kitin PB, Fujii T, Abe H, Funada R (2004) Anatomy of the vessel network within and between tree rings of *Fraxinus lanuginosa* (Oleaceae). Am J Bot 91(6):779–788. https://doi.org/10.3732/ajb.91.6.779
28. Klepsch MM, Schmitt M, Paul Knox J, Jansen S (2016) The chemical identity of intervessel pit membranes in acer challenges hydrogel control of xylem hydraulic conductivity. AoB Plants 8:plw052. https://doi.org/10.1093/aobpla/plw052
29. Lens F, Sperry JS, Christman MA, Choat B, Rabaey D, Jansen S (2011) Testing hypotheses that link wood anatomy to cavitation resistance and hydraulic conductivity in the genus *Acer*. New Phytol 190(3):709–723
30. Lens F, Tixier A, Cochard H, Sperry JS, Jansen S, Herbette S (2013) Embolism resistance as a key mechanism to understand adaptive plant strategies. Curr Opin Plant Biol 16(3):287–292
31. Li S, Lens F, Espino S, Karimi Z, Klepsch M, Schenk HJ, Schmitt M, Schuldt B, Jansen S (2016) Intervessel pit membrane thickness as a key determinant of embolism resistance in angiosperm xylem. IAWA J 37(2):152–171
32. Liu M, Pan R, Tyree MT (2017) Intra-specific relationship between vessel length and vessel diameter of four species with long-to-short species-average vessel lengths: further validation of the computation algorithm. Trees 32(1):51–60. https://doi.org/10.1007/s00468-017-1610-y
33. Loepfe L, Martinez-Vilalta J, Pinol J, Mencuccini M (2007) The relevance of xylem network structure for plant hydraulic efficiency and safety. J Theor Biol 247(4):788–803
34. Magal P, Seydi O, Webb G (2016) Final size of an epidemic for a two-group sir model. SIAM J Appl Math 76(5):2042–2059
35. Maherali H, Pockman WT, Jackson RB (2004) Adaptive variation in the vulnerability of woody plants to xylem cavitation. Ecology 85:2184–2199
36. Manzoni S, Katul G, Porporato A (2014) A dynamical system perspective on plant hydraulic failure. Water Resour Res 50(6):5170–5183
37. Martinez WL, Martinez AR (2001) Computational statistics handbook with MATLAB. Chapman and Hall/CRC, Boca Raton
38. Meinzer FC, Johnson DM, Lachenbruch B, McCulloh KA, Woodruff DR (2009) Xylem hydraulic safety margins in woody plants: coordination of stomatal control of xylem tension with hydraulic capacitance. Funct Ecol 23(5):922–930
39. Mrad A, Domec J, Huang C, Lens F, Katul G (2018) A network model links wood anatomy to xylem tissue hydraulic behaviour and vulnerability to cavitation. Plant Cell Environ 41(12):2718–2730
40. Mrad A, Johnson DM, Love DM, Domec JC (2021) The roles of conduit redundancy and connectivity in xylem hydraulic functions. New Phytol. https://doi.org/10.1111/nph.17429
41. Murray JD (2002) Mathematical biology: I. An introduction. Interdisciplinary applied mathematics. Mathematical biology. Springer, New York
42. Noble JV (1974) Geographic and temporal development of plagues. Nature 250(5469):726–729
43. Ogle K, Barber JJ, Willson C, Thompson B (2009) Hierarchical statistical modeling of xylem vulnerability to cavitation. New Phytol 182(2):541–554
44. Pammenter N, Vander Willigen C (1998) A mathematical and statistical analysis of the curves illustrating vulnerability of xylem to cavitation. Tree Physiol 18:589–593
45. Pesacreta TC, Groom LH, Rials TG (2005) Atomic force microscopy of the intervessel pit membrane in the stem of *Sapium sebiferum* (Euphorbiaceae). IAWA J 26(4):397–426

46. Pritzkow C, Brown MJ, Carins-Murphy MR, Bourbia I, Mitchell PJ, Brodersen C, Choat B, Brodribb TJ (2022) Conduit position and connectivity affect the likelihood of xylem embolism during natural drought in evergreen woodland species. Ann Bot 130(3):431–444
47. Roth-Nebelsick A (2019) It's contagious: calculation and analysis of xylem vulnerability to embolism by a mechanistic approach based on epidemic modeling. Trees 33(5):1519–1533. https://doi.org/10.1007/s00468-019-01891-w
48. Schenk HJ, Steppe K, Jansen S (2015) Nanobubbles: a new paradigm for air-seeding in xylem. Trends Plant Sci 20(4):199–205
49. Scholz A, Rabaey D, Stein A, Cochard H, Smets E, Jansen S (2013) The evolution and function of vessel and pit characters with respect to cavitation resistance across 10 *Prunus* species. Tree Physiol 33(7):684–694
50. Schulte PJ, Hacke UG (2021) Solid mechanics of the torus–margo in conifer intertracheid bordered pits. New Phytol 229(3):1431–1439. https://doi.org/10.1111/nph.16949
51. Sergent AS, Segura V, Charpentier JP, Dalla-Salda G, Fernandez ME, Rozenberg P, Martinez-Meier A (2020) Assessment of resistance to xylem cavitation in cordilleran cypress using near-infrared spectroscopy. For Ecol Manage 462:117943
52. Song Y, Poorter L, Horsting A, Delzon S, Sterck F (2021) Pit and tracheid anatomy explain hydraulic safety but not hydraulic efficiency of 28 conifer species. J Exp Bot 73(3):1033–1048. https://doi.org/10.1093/jxb/erab449
53. Sperry J, Donelly J, Tyree M (1988) A method for measuring hydraulic conductivity and embolism in xylem. Plant Cell Environ 11: 35–40
54. Sperry JS (1986) Relationship of xylem embolism to xylem pressure potential, stomatal closure, and shoot morphology in the palm Rhapis Excelsa. Plant Physiol 80(1):110–116
55. Sperry JS, Christman MA, Torres-Ruiz JM, Taneda H, Smith DD (2012) Vulnerability curves by centrifugation: is there an open vessel artefact, and are 'r' shaped curves necessarily invalid? Plant Cell Environ 35(3):601–610
56. Sperry JS, Hacke UG (2004) Analysis of circular bordered pit function I. angiosperm vessels with homogenous pit membranes. Am J Bot 91(3):369–385
57. Sperry JS, Tyree M (1990) Water-stress-induced xylem embolism in three species of conifers. Plant Cell Environ 13:427–436
58. Trueba S, Pouteau R, Lens F, Feild TS, Isnard S, Olson ME, Delzon S (2017) Vulnerability to xylem embolism as a major correlate of the environmental distribution of rain forest species on a tropical island. Plant Cell Environ 40(2):277–289
59. Tyree M, Sperry J (1989) Vulnerability of xylem to cavitation and embolisms. Annu Rev Plant Physiol 40:19–38
60. Tyree MT, Dixon MA (1986) Water stress induced cavitation and embolism in some woody plants. Physiol Plant 66(3):397–405. https://doi.org/10.1111/j.1399-3054.1986.tb05941.x
61. Tötzke C, Miranda T, Konrad W, Gout J, Kardjilov N, Dawson M, Manke I, Roth-Nebelsick A (2013) Visualization of embolism formation in the xylem of liana stems using neutron radiography. Ann Bot 111:723–730
62. Venturas MD, Sperry JS, Hacke UG (2017) Plant xylem hydraulics: What we understand, current research, and future challenges. J Integr Plant Biol 59(6):356–389
63. Wheeler JK, Sperry JS, Hacke UG, Hoang N (2005) Inter-vessel pitting and cavitation in woody Rosaceae and other vesselled plants: a basis for a safety versus efficiency trade-off in xylem transport. Plant Cell Environ 28(6):800–812
64. Yin P, Meng F, Liu Q, An R, Cai J, Du G (2018) A comparison of two centrifuge techniques for constructing vulnerability curves: insight into the 'open-vessel' artifact. Physiol Plant 165(4):701–710
65. Zhang Y, Carmesin C, Kaack L, Klepsch MM, Kotowska M, Matei T, Schenk HJ, Weber M, Walther P, Schmidt V, Jansen S (2020) High porosity with tiny pore constrictions and unbending pathways characterize the 3d structure of intervessel pit membranes in angiosperm xylem. Plant Cell Environ 43(1):116–130. https://doi.org/10.1111/pce.13654
66. Zhang Y, Lamarque LJ, Torres-Ruiz JM, Schuldt B, Karimi Z, Li S, Qin DW, Bittencourt P, Burlett R, Cao KF, Delzon S, Oliveira R, Pereira L, Jansen S (2018) Testing the plant pneumatic method to estimate xylem embolism resistance in stems of temperate trees. Tree Physiol 38(7):1016–1025. https://doi.org/10.1093/treephys/tpy015



Chapter 3

Modeling Xylem Functionality Aspects

Alex Tavkhelidze, Gerhard Buck-Sorlin, and Winfried Kurth

Abstract

Depending on the questions to be answered, water flow in the xylem can be modelled following different approaches with varying spatial and temporal resolution. When focussing on the influence of hydraulic architecture upon flow dynamics, distribution of water potentials in a tree crown or questions of vulnerability of the hydraulic system, functional-structural plant models, which link representations of morphological structure with simulated processes and with a virtual environment, can be a promising tool. Such a model will then include a network of idealized xylem segments, each representing the conducting part of a stem or branch segment, and a numerical machinery suitable for solving a system of differential equations on it reflecting the hydrodynamic laws, which are the basis of the broadly accepted cohesion-tension theory of water flow in plants. We will discuss functional-structural plant models, the simplifications that are useful for hydraulic simulations within this framework, the deduction of the used differential equations from basic physical conservation laws, and their numerical solution, as well as additional necessary models of radiation, photosynthesis, and stomatal conductance. In some supplementary notes, we are shortly addressing some related questions, for example, about root systems or about the relation between macro-scale hydraulic parameters and fine-grained (anatomical) xylem structure.

Key words Xylem, Functional-structural plant modeling, GroIMP, Fluid dynamics, Water flow, Darcy's law, Hagen-Poiseuille equation

1 Introduction

1.1 Previous Approaches to Describe Xylem Functionality

More than five hundred years ago, Leonardo da Vinci wrote in his notebooks that the cross-section area of a tree branch is (approximately) equal to the sum of the cross-section areas of all its daughter branches at any higher level [1, 2], thus stating what can be seen as the first model of hydraulic architecture of plants. Much later, Shinozaki et al. [3] refined this approach by taking the mortality of conducting vessels into account and by associating each chain of vessels, which they conceptualized as "unit pipes," with a fixed number of water-uptaking (fine roots, *see* **Note 1**) and water-transpiring organs (leaves). Hence, their model conceived plant

Javier Agusti (ed.), *Xylem: Methods and Protocols*, Methods in Molecular Biology, vol. 2722,
https://doi.org/10.1007/978-1-0716-3477-6_3,
© The Author(s), under exclusive license to Springer Science+Business Media, LLC, part of Springer Nature 2024

shape as the result of functional requirements in terms of uptake and plant-internal movement of water (and nutrients solved therein).

The pipe model and its numerous refinements, most of them based on empirically derived allometric relationships, provide, however, only static descriptions of plant architecture and are not able to predict the dynamics of water uptake, xylem sap flow and transpiration. Moreover, they cannot be helpful for assessing the vulnerability of the hydraulic system under stress conditions. To address such tasks, hydrodynamic models have been developed, capable to simulate the flow of water and solutes through the vessel system and its diurnal and seasonal changes. Among the first models of this sort were those proposed by Hatheway and Winter [4], Edwards et al. [5], Tyree [6], and Früh [7]. Hölttä et al. [8] extended this approach even further by including the flow dynamics in the phloem and its linkage to the xylem. In the rest of this chapter, we will give an overview of the theoretical foundations and numerical considerations necessary for such a simulation model of plant-internal flows.

1.2 The Plant Hydraulic System

According to a widely accepted theoretical frame describing the transport of water in plants, known as "Cohesion-Tension" theory [9, 10], the sun, by creating a gradient in humidity between the air and the leaf, provides the energy for transpiration, which latter (predominantly from substomatal cavities) induces suction (tension) that fuels spontaneous (passive) bulk flow of water through a plant (its xylem conduit network) within the so-called soil-plant-atmosphere continuum. The backbone of this flow is made up of highly cohesive water molecules.

We will not recur here to a detailed description of the thermodynamics of the processes involved. Put simply, the driving force of water movement can be attributed to a negative gradient of xylem water potential. More specifically, water flows from regions of higher water potential toward those of lower one (Fig. 1).

From the anatomical perspective, the xylem water-conducting network is predominantly composed of bundles of tracheid cells (e.g. for conifers) or vessels (e.g. for angiosperms) tapered to both ends. Both tracheids and vessel elements (the latter forming vessels by fusing their ends into axially located perforation plates) are dead pipe-like cells, which possess numerous pairs of bordered pits (valved perforations) on their walls that allow for convective water flow between adjacent conduits. Tracheids and vessel elements exhibit great variation in length and diameter, ranging from 0.5 to 5 mm in length [11] and 5 to 30 μm in diameter [12], with radial pit diameters ranging from 0.5 to 7 μm in a number of temperate tree species [13].

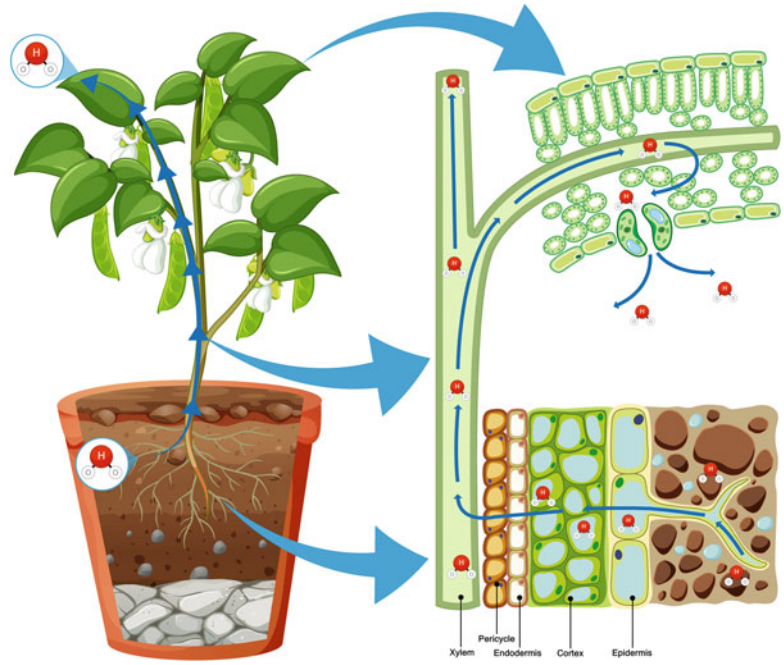


Fig. 1 Schematic diagram illustrating the xylem transport pathway (designed by brgfx/Freepik)

1.3 Plant Architecture

Aerial plant architecture is the result of the rhythmic activity (growth and development) of a shoot apical meristem (SAM), which is most often embedded within protective structures (leaf primordia and scales), the latter referred to as buds. Buds are located at the tip of an exisiting shoot and in the axils of most leaves and scales, that is, on each node. Unlike their aerial analogs, root meristems will rhythmically produce only root segments. The behavior of buds in time (growth, dormancy, death), which is subject to the environment (microclimate) surrounding the plant and gradients induced by the production and transport of growth hormones, will thus result in the observed crown and root architecture of a tree (*see* **Note 1**). A multitude of further factors affect this architecture, among them mechanical stresses, which can lead to the formation of so-called reaction wood, and the mortality of tissues, organs, or whole branches. A special case of mortality is the transformation of xylem vessels into heartwood in older woody plants.

At the organ scale, a tree consists of a multitude (hundreds to thousands) of leaves, internodes, root segments, and a number of fruits. These organs are connected to each other via an elaborate system of xylem and phloem vessels, which form during the primary growth of a new shoot or root segment, due to the activity of cellular descendents of the aforementioned SAMs, and which

become enlarged by secondary growth, at the heart of which is the activity of a ring of stem cells in between the phloem and xylem, the cambium. It has to be noted that a young bud, newly formed in the axil of a leaf or scale, will not yet have a connection to the exisiting vascular system, but it has to establish this connection itself, thanks to an elaborate hormonal regulation system (involving auxins, cytokinins, and strigolactones: for reviews, *see* [14–16]).

2 Materials and Methods

2.1 Governing Equations and Physical Laws

From a coarse fluid-mechanical perspective, the entire ramified network of xylem vascular bundles could be treated as an isolated physical system of conduits, and mechanical laws such as energy, momentum, and mass conservation would apply to it. These are indispensable for setting up a solvable system of what generally turns out to be differential-algebraic equations, possibly mixed with a set of inequalities. In order to resolve the trade-off between accuracy and complexity, simplifying assumptions along with ad hoc approaches need to be accommodated, since there is no rule of thumb on how to make the processing of such complex systems feasible.

2.1.1 Conservation of Energy

The causal principle triggering a net flow of fluid and determining its direction is the conservation of energy. Exact direction of flow between any two distinct points along a selected path is then determined by gradients of total energy. To put in a nutshell, fluid flows from point A to point B of a given streamline if and only if the total energy at A exceeds the total energy at B. Lastly, following the lines of Bernoulli's theory, we additively compose total energy from pressure energy (akin to hydrostatic pressure) and potential energy (also known as datum energy). For xylem, this sum essentially coincides with water potential.

Taking into account the fact that rather low velocities of water flow were observed in xylem bundles [17, 18], the conditions of a laminar incompressible creeping flow are well realized. Particularly, this setup allows us to neglect the impact of flow velocity on changes in static pressure. This simplification effectively avoids unnecessary complexity when modeling flow and keeps the focus on major constituents.

2.1.2 Conservation of Momentum

We accommodate the conservation of momentum by employing Darcy's law, which describes the convective flow of a fluid (in our case, water in liquid form) in porous media. In the light of the previously described xylem hydraulic system (*see* Subheading 1.2, last paragraph), simplification of its detailed geometry is well reasoned and treating it as a porous medium is well justified.

Although originally an empirical law, Darcy's equation received some sound theoretical treatment in recent decades [19, 20] and is considered as being theoretically well derived [21]. For simplicity, we deal with homogeneous and isotropic porous media. This assumption effectively reduces a (symmetric) permeability tensor K to a single constant (*see* **Note 2**) scalar k (*see* Eq. 1).

According to Darcy's equation, assuming (without loss of generality) that a volume $V\,(\mathrm{m}^3)$ with transverse-sectional area A_{transv} (m^2) and longitudinal length L_{long} (m) discharges water into an adjacent volume (cylindrically shaped volumes standing for xylem vascular bundles are considered for simplicity), the mass flow rate dM_{ax}/dt (kg/s) of water is then given by the following differential equation with respect to time t (where the rightmost equation is the essential proposition):

$$\frac{dM_{ax}}{dt} = \frac{d(\rho \cdot V)}{dt} = \rho \cdot \frac{dV}{dt} = \rho \cdot \frac{A_{\mathrm{transv}} \cdot k}{L_{\mathrm{long}} \cdot \mu} \cdot \Delta p \tag{1}$$

Here, dV/dt stands for the volumetric flow rate $(\mathrm{m}^3/\mathrm{s})$, ρ denotes water density $(\mathrm{kg}/\mathrm{m}^3)$, μ is its dynamic viscosity (Pa · s) (*see* **Note 3**), and Δp represents the properly signed gradient of total energy between the discharging and receiving volumes.

Furthermore, the representation of each single tracheid or vessel in a model (*see* **Note 4**) will normally be far too expensive in terms of computational resources, particularly in the case of trees. Hence, it will be a meaningful simplification to work with effective values of hydraulic variables over the whole cross section of an internode or annual shoot.

2.1.3 Conservation of Mass

For the last of conservation laws involved, namely, the mass continuity, we rely on the mass balancing part of the Saint-Venant equations, widely used for modeling hydrological systems [22], which can be stated in the following form:

$$M(t + \Delta t) - M(t) = \int_{t}^{t+\Delta t} \left[\frac{dM_{\mathrm{in}}}{dt} - \frac{dM_{\mathrm{out}}}{dt} \right] dt \tag{2}$$

Here, for any given elementary volume, the left-hand side (LHS) stands for the change in the total mass of fluid in consideration (water in liquid form), measured over some duration Δt and starting at any time t. The right-hand side (RHS) represents the integral of the net mass flow rate of fluid per unit period over the same time margin Δt.

While treating volumes as linearly elastic thin-walled (that is, $\tau/r \leq 10\%$) fluid-filled cylindrical pressure vessels with modulus of elasticity E (Pa), internal pressure p (Pa), internal radius r (m), and wall thickness τ (m), we consider only the largest of two principal stresses for simplicity, namely, the circumferential (hoop) stress

$\sigma_h = p \cdot r/\tau$. Changes in pressure dp occurring over unit time period dt correspond to changes in radius dr, and we quantify this interplay between stress and strain using Hooke's law:

$$\frac{dp}{dt} = E \cdot \frac{\tau}{r^2} \cdot \frac{dr}{dt} \tag{3}$$

Now, applying the simple geometric relation [23] between changes in radius of a cylinder with longitudinal length L_{long} and corresponding changes in mass of enclosed incompressible fluid $dM/dt = \rho \cdot 2\pi r L_{\text{long}} \cdot dr/dt$ to the RHS of Eq. 3 yields:

$$\frac{dp}{dt} = E \cdot \frac{\tau}{M \cdot 2r} \cdot \frac{dM}{dt} \tag{4}$$

Finally, using the mean value theorem of integral calculus for the RHS of Eq. 2 and taking $\Delta t \to 0$, we land at:

$$\frac{dM}{dt} = \frac{dM_{\text{in}}}{dt} - \frac{dM_{\text{out}}}{dt} \tag{5}$$

Equations 3–5 demonstrate how we can accommodate distensibility of ducts in the mass balance equation.

2.2 Implementation Framework

2.2.1 Representing and Encoding Plant Architecture

When we want to simulate water flow in a tree crown, we need to represent the topology and geometry of the branching system (see [24] for an overview of structural representations of plants). Such a representation, which – for our purpose – must also include the hydraulic properties of all constituents, can be the result of extensive manual measurements covering a single real tree [25], semi-automatic measurements using an electromagnetic digitizer [26], or using a remote method, e.g. by a laser scanner [27]. The three-stem alder tree from the historical Branitz Park (*see* Fig. 2 (left)) is an example of a visualization of such a reconstruction coming close to the very unique habit of the original tree. The 3D structure can also be the result of simulated development and growth, for example, based on a functional-structural plant model (see next subsection), like the "artificial" pine tree (*see* Fig. 2 (right)). In either case, the data structure offering itself for such a representation is a graph (in the sense of graph theory), that is, a network of nodes and edges, where the nodes stand for the basic elements or modules of the plant (cf. [31]), like internodes, leaves, buds, and fruits, and the edges connect neighboring elements, thus encoding the topology of the branching system. The nodes will then carry information about geometry, like length and diameter, and – for our purposes – also hydraulic parameters of the included xylem, like hydraulic resistance and capacitance. An extension of this graph representation allows for a simultaneous simulation of plant structure at several scales of spatial resolution (multiscaled tree graphs – MTG, [32]). Dedicated "decomposition edges" specify here which fine-scale organs are part of an element at the next-higher scale level.



Fig. 2 Examples of 3D reconstructions of above-ground tree architecture. Left-hand side: Black alder tree from the Branitz Park near Cottbus, Germany [28, 29]. Right-hand side: Scots pine tree simulated by the FSPM LIGNUM at the ages of 10, 20, 30, and 40 years [30]

2.2.2 Functional-Structural Plant Modeling

One major aim of simulation models of the functioning and growth of plants is to represent and explore complex interactions between plant architecture and the physical and biological processes that drive plant development at several temporal and spatial scales. Research during the last 30 years led to the emergence of functional-structural plant models (FSPMs), also called virtual plants. They are characterized by explicitly describing the development over time of the 3D architecture or structure of plants as governed by physiological processes which, in turn, depend on environmental factors [33]. FSPMs typically couple a selection of physiological processes with a geometrical representation of 3D plant architecture (structural model [34]), often supplied with a mutual feedback between physiology and structure [35]. Such FSPMs have been developed for many types of plants and production systems, such as annual crops (e.g., ADEL-maize [36], ADEL-wheat [37], barley [38], and rice [39, 40]), forest trees (e.g., Lignum [41, 42]), ornamentals like rose [43], grapevine [44], palms [45, 46], and fruit trees (L-Peach [47–49]; MAppleT [50, 51]). Depending on the application domain, FSPMs have integrated several physical and physiological processes and varied in the level of detail considered for the spatial representation of the plant (considering different hierarchical scales: individual organs, sets of organs, entire plants or plant stands). They can also help to characterize genetic differentiation as well as the effects of genotype

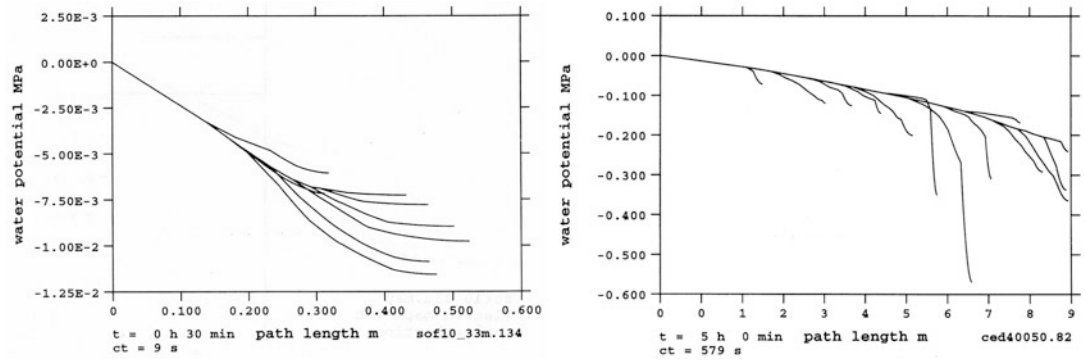


Fig. 3 Simulated patterns of water potential [7] based on spatially explicit representations of branching systems of a *Picea abies* (**left**) and a *Thuja occidentalis* (**right**; structural data from [6])

by environment interactions. One genotype can be considered as the equivalent of one set of model parameters in a range of environmental conditions [52–55].

At the example of hydraulic architecture [56], we demonstrate the analytical value of linking structural information with the simulation of water relations within the branching systems of tree crowns at two different species. Figure 3 shows the simulated water potential profiles, obtained with the software HYDRA [7, 57, 58], which is based on the aforementioned physical laws, along selected paths from the root collar to branch tips in the crown, on the left-hand side for a 40 cm high spruce (*Picea abies L. (Karst.)* [7]) and on the right-hand side for a 9.6 m high *Thuja occidentalis L.*, which has been geometrically mapped by Tyree [6]. The patterns differing between the two trees can be interpreted as indications for different strategies to organize water flow within the crowns.

2.2.3 *Numerical Solvers*

Processes of continuum mechanics encompassing xylem water transport are governed by differential equations (*see* Eqs. 1–5). Although even quite complicated physical phenomena could be described by rather simple (from a mathematical perspective) differential equations, the need for numerical methods and thus in their implementations as numerical solvers emerges almost inevitably when attempting to model compound physical processes in complex architectures somewhat realistically.

Furthermore, not only the differential constituent of an underlying differential-algebraic system (*see* Subheading 2.1) could have cumbersome analytic solutions or have none of such at all, but also even a polynomial equation or an easiest transcendental one would immensely benefit from iterative methods for finding a reasonable approximation to the solution.

When mentioning numerical solutions for differential equations, the process of discretization, both spatial and temporal,

draws a major attention as the conrnerstone of replacing a continuous problem by a discrete one. For the network of xylem conduits, one could always adopt a coarse but natural spatial discretization based on branching points and endpoints of branches [58] or a finer one by introducing more types of discrete elements, such as nonbranched and terminal parts of xylem pathways [59]. When employing this sort of naturalism, it is worth bearing in mind that, due to the characteristic uneven and non-minimized distance pattern of such discretizations, the drawback of untolerable steplike profiles (e.g., of water potential or water content) would likely arise in the course of simulations, and this lack in smoothness might, as a consequence, lead to blowing up solutions (also known as *instability*).

From a practical point of view, other cases of particular interest that are inherently exposed to the risk of instability revolve around perturbations of initial conditions and triggers of sudden stress scenarios, the latter essentially determined by superimposed abrupt changes, usually applied to the model parameters, such as environmental factors, physiological properties of a plant, or hydraulic characteristics of its xylem.

It is, therefore, of vital importance, and the responsibility of a modeler, to carry out a stability analysis, as well as to choose and implement an efficient and stable numerical solver with a tolerable degree of inaccuracy (*see* **Note 5**).

2.2.4 Auxiliary Models

Radiation

One of the major hypostases of plant/environment interactions is the interception of electromagnetic radiation (such as solar energy or radiant energy of artificial light sources). Being the driving force for photosynthesis and an effector of transpiration (*see* Subheading "Stomatal conductance and photosynthesis"), light interception [60, 61] should be an indispensable part of any modeling framework for xylem water transport.

Along with the quantified absorption, reflectance and transmittance characteristics for every surface element of the plant geometry in question (*see* Subheading 2.2.1), accurate description of light sources and their dynamics constitutes another pivotal cornerstone of light interception.

If we take the sun as an example of a light source, incorporating one of widely used solar position algorithms (SPA) would come in handy for setting up its dynamics on the celestial sphere, centered on the targeted plant. Furthermore, light scattering needs to be taken into account, which ultimately gives rise to the dichotomy of direct (solar beam) and diffuse (sky) radiation, the latter describing the sunlight scattered by various atmospheric constituents. Moreover, there is evidence [62] underpinning the importance of segregating direct and diffuse components of global radiation for modeling photosynthesis.

Lastly, implementing any physically accurate sky radiation distribution model [63] that accommodates various (CIE-adopted) sky conditions from overcast to clear would complete the radiation model.

Stomatal Conductance and Photosynthesis

Photosynthesis, and associated with it, stomatal conductance, is one of the most investigated and best-known physiological processes, both with respect to experimentation and modeling. It is, therefore, beyond the scope of this subchapter, to deal with this fundamental process other than with respect to its immediate importance for xylem and phloem transport. For more information on the modeling of photosynthesis, the reader is referred to the numerous works by Thornley [64, 65] and the excellent review on photosynthesis models by Yin and Struik [66]. Photosynthesis rate, stomatal conductance, and leaf transpiration are closely coupled and interdependent processes. The plant needs to open leaf stomata to let water vapour escape, leading to transpirational cooling. As stated above, the latter is a physical process fueled by solar energy. At the same time, carbon dioxide from the surrounding air will enter the leaves via the opened stomata and eventually be available for photosynthesis. The global and local rates at which water vapour and CO_2 are transported out of, and into, the leaf, are loosely referred to as stomatal conductance. The rates of in- and efflux may vary among molecule types and depend on a number of physiological and environmental factors, such as the resistances for the molecules to traverse specific tissues and layers surrounding the leaf (boundary layer, stomatal, mesophyll etc.), CO_2 concentration in the surrounding air, and in the different compartments of the leaf, wind speed, or the CO_2 assimilation rate (which, itself, depends on the stomatal conductance). They also depend on the temperature within the leaf, which is itself a function of air temperature, stomatal conductance, and photosynthesis rate. Open stomata will, thus, guarantee transpirational cooling and a sufficient supply with carbon dioxide for photosynthesis – if water supply from the soil or substrate is sufficiently met. As drought stress can frequently occur, even in temperate regions during the vegetation period, plants have evolved to control the opening of their stomata, as a compromise between closed stomata, ensuring conservation of water during drought stress periods, yet at the risk of starvation due to CO_2 shortage, and opened stomata, ensuring CO_2 influx and, thus, carbon assimilation, yet with the risk of a runaway transpiration, in which water loss by the leaves is not matched by water supply by the roots (*see* **Note 1**), potentially leading to sometimes irreversible structural damage, such as vascular embolisms and withering.

3 Notes

1. Tree roots, though hidden from sight, are of enormous importance for the tree, as they provide, among others, anchorage of the tree in the soil; water and mineral absorption and transport, and storage; and synthesis of hormones controlling aboveground activities of the tree [67]. Distribution of roots in the soil, and root architecture, in general, depends on the presence or absence of a taproot. Generally, it is highly plastic and depends on species, soil type, water and mineral availability, and on competition with other roots. The plasticity of roots is illustrated by their rapid growth into wet zones (e.g., by drip irrigation) of a partially wet soil [67]. As already outlined above, roots, like stems, contain xylem and phloem bundles, although here they are found in the centre of the root to protect them from stretching forces.
2. More realistic modeling requires treating hydraulic conductivity, conveniently expressed as flow rate per gradient of total energy, as varying with xylem conduit diameter [6], pit characteristics [68] and water potential [69], the latter assessable using so-called vulnerability curves, which show the percent decrease in xylem hydraulic conductivity versus xylem water potential. These curves are obtained specieswise by experimentally exposing excised parts of targeted plants to increasing levels of xylem tension [70]. In such experiments, xylem water (in condensed phase) is being stretched by generating negative pressure [71]. Upon reaching some critical tension (depending on numerous factors, such as species, xylem sap composition, etc.), this metastable state begins to collapse due to cavitation, which, in turn, leads to reduction of xylem hydraulic conductivity and, finally, hydraulic dysfunction (embolism). Cavitation is triggered by forming sufficiently large gas-filled voids within water-conducting xylem conduits and/or induced by air-seeding, when air-water menisci in the capillaries of interconduit pit pores (separating an embolized conduit from a functional one) reach radii of curvature small enough for air passage [9].
3. Taking into account substantial variations in diurnal air temperatures, a modeler is advised to reflect viscosity's dependence on temperature by employing a computationally inexpensive empirical model for liquid water [72], which is sufficiently accurate for xylem-specific value ranges of intensive thermodynamical properties (temperature, pressure). On the other hand, due to negligible solute concentration of the xylem sap [9], dependence of viscosity on solute content could be safely ignored here.

4. Another empirically discovered and theoretically derived (from the Navier-Stokes equations) physical law, named after Gotthilf Hagen and Jean Léonard Marie Poiseuille, is widely used for modeling the flow of water through xylem conduits, generally seen as smooth-walled cylinders [9]. In a nutshell, this law states that the flow rate is proportional to the fourth power of the duct radius, thus making its output highly sensitive to even rather small variations in diameter of xylem capillaries. Furthermore, a modification of the Hagen-Poiseuille equation exists that computes the hydraulic conductivity of xylem, represented as a bundle of cylindrical conduits [73].
5. In the context of ordinary differential equations (ODEs), examples of solver properties are whether the ODE solver is multistep or not, with adaptive timestepping or not, explicit or implicit (the latter providing better numerical stability, being a better choice for stiff problems, but doing more work per step). Some noteworthy open-source implementations are the latest stable releases of the Apache Commons Math library (mainly for nonstiff problems), written in Java, and CVODE (part of the SUNDIALS suite), written predominantly in C.

Acknowledgments

The first author wants to thank Meri Chorgolashvili for her insightful discussions on theoretical arguments and experimental evidence of absolute negative pressure regimes for condensed phases.

References

1. Richter JP (1970) The notebooks of Leonardo da Vinci (1452–1519), compiled and edited from the original manuscripts. Dover, New York (Reprint of a work originally published by Sampson Low, Marston Searle and Rivington, London 1883), p 367
2. Eloy C (2011) Leonardo's rule, self-similarity, and wind-induced stresses in trees. Phys Rev Lett 107(25):258101
3. Shinozaki K, Yoda K, Hozumi K et al (1964) A quantitative analysis of plant form – the pipe model theory. I basic analysis. Jpn J Ecol 14(3): 97–105
4. Hatheway WH, Winter DF (1981) Water transport and storage in Douglas-fir: a mathematical model. Mitteil Forstl BVA Wien 142: 193–222
5. Edwards WRN, Jarvis PG, Landsberg JJ et al (1986) A dynamic model for studying flow of water in single trees. Tree Physiol 1:309–324
6. Tyree MT (1988) A dynamic model for water flow in a single tree: evidence that models must account for hydraulic architecture. Tree Physiol 4:195–217
7. Früh T (1995) Entwicklung eines Simulationsmodells zur Untersuchung des Wasserflusses in der verzweigten Baumarchitektur. In: Ber FZW Göttingen, ser A, vol 131. Dissertation, University of Göttingen
8. Hölttä T, Vesala T, Sevanto S et al (2006) Modeling xylem and phloem water flows in trees according to cohesion theory and Münch hypothesis. Trees 20(1):67–78
9. Tyree MT, Zimmermann MH (2002) Xylem structure and the ascent of sap. Springer, Berlin
10. Tyree MT (1997) The cohesion-tension theory of sap ascent: current controversies. J Exp Bot 48:1753–1765
11. Bailey IW (1920) The cambium and its derivative tissues. II size variations of cambial initials

in gymnosperms and angiosperms. Am J Bot 7: 355–367
12. Sperry JS, Hacke UG, Pittermann J (2006) Size and function in conifer tracheids and angiosperm vessels. Am J Bot 93(10): 1490–1500. https://doi.org/10.3732/ajb.93.10.1490. PMID:21642096
13. Sano Y, Jansen S (2006) Perforated pit membranes in imperforate tracheary elements of some angiosperms. Ann Bot 97(6): 1045–1053. https://doi.org/10.1093/aob/mcl049
14. Hajný J, Tan S, Friml J (2022) Auxin canalization: from speculative models toward molecular players. Curr Opin Plant Biol 65:102174. https://doi.org/10.1016/j.pbi.2022.102174
15. Hwang I, Sheen J, Müller B (2012) Cytokinin signaling networks. Annu Rev Plant Biol 63: 353–380
16. Waters MT, Gutjahr C, Bennett T et al (2017) Strigolactone signaling and evolution. Annu Rev Plant Biol 68:291–322. https://doi.org/10.1146/annurev-arplant-042916-040925
17. Köckenberger W, Pope J, Xia Y et al (1997) A non-invasive measurement of phloem and xylem water flow in castor bean seedlings by nuclear magnetic resonance microimaging. Planta 201:53–63
18. Peuke AD, Rokitta M, Zimmermann U et al (2001) Simultaneous measurement of water flow velocity and solute transport in xylem and phloem of adult plants of Ricinus communis over a daily time course by nuclear magnetic resonance spectrometry. Plant Cell Environ 24: 491–503
19. Neuman SP (1977) Theoretical derivation of Darcy's law. Acta Mech 25:153–170
20. Whitaker S (1986) Flow in porous media I: a theoretical derivation of Darcy's law. Transp Porous Media 1:3–25
21. Di Nucci C (2014) Theoretical derivation of the conservation equations for single phase flow in porous media: a continuum approach. Meccanica 49:2829–2838
22. Litrico X, Fromion V (2009) Modeling and control of hydrosystems. Springer, London
23. Sevanto S, Hölttä T, Holbrook N (2011) Effects of the hydraulic coupling between xylem and phloem on diurnal phloem diameter variation. Plant Cell Environ 34(4):690–703
24. Godin C (2000) Representing and encoding plant architecture: a review. Ann For Sci 57(5):413–438
25. Kurth W, Lanwert D (1995) Biometrische Grundlagen für ein dynamisches Architekturmodell der Fichte (*Picea abies* (L.) KARST.). Allg Forst Jagdztg 166(9–10):177–184
26. Sinoquet H, Rivet P (1997) Measurement and visualization of the architecture of an adult tree based on a three-dimensional digitising device. Trees 11(5):265–270
27. Balduzzi M, Boudon F, Godin C (2013) Optimal 3D reconstruction of plants canopy from terrestrial laser scanner data by fusion of the 3D point information and the intensity value. In: 7th international conference on functional-structural plant models, pp 58–60
28. Kniemeyer O (2008) Design and implementation of a graph grammar based language for functional-structural plant modelling. Doctoral dissertation, University of Technology at Cottbus
29. Rogge S (2008) Generierung von Baumdarstellungen in VRML für den Branitzer Park. Bachelor's thesis, BTU Cottbus
30. Sievänen R, Perttunen J, Nikinmaa E et al (2009) Invited talk: functional structural plant models – case LIGNUM. In: 2009 third international symposium on plant growth modeling, simulation, visualization and applications, pp 3–9
31. White J (1979) The plant as a metapopulation. Annu Rev Ecol Syst 10:109–145
32. Godin C, Caraglio Y (1998) A multiscale model of plant topological structures. J Theor Biol 191(1):1–46
33. Vos J, Evers JB, Buck-Sorlin GH et al (2010) Functional-structural plant modelling: a new versatile tool in crop science. J Exp Bot 61: 2101–2115. https://doi.org/10.1093/jxb/erp345
34. Kurth W (1994) Morphological models of plant growth: possibilities and ecological relevance. Ecol Model 75/76:299–308
35. Buck-Sorlin GH (2013) Functional-structural plant modeling. In: Dubitzky W, Wolkenhauer O, Cho K, Yokota H (eds) Encyclopedia of systems biology. Springer, New York, pp 778–781
36. Fournier C, Andrieu B (1999) ADEL-maize: an L-system based model for the integration of growth processes from the organ to the canopy. Application to regulation of morphogenesis by light availability. Agronomie 19:313–327
37. Fournier C, Andrieu B, Ljutovac S et al (2003) Adel-wheat: a 3D architectural model of wheat development. In: Hu B-G, Jaeger M (eds) Plant growth modeling and applications. Tsinghua University Press/Springer, Beijing, pp 54–66
38. Buck-Sorlin GH, Hemmerling R, Kniemeyer O et al (2008) A rule-based model of barley morphogenesis, with special respect to shading

and gibberellic acid signal transduction. Ann Bot 101:1109–1123

39. Luquet D, Dingkuhn M, Kim H et al (2006) EcoMeristem, a model of morphogenesis and competition among sinks in rice. 1. Concept, validation and sensitivity analysis. Funct Plant Biol 33:309–323
40. Xu L, Henke M, Zhu J et al (2011) A functional–structural model of rice linking quantitative genetic information with morphological development and physiological processes. Ann Bot 107:817–828. https://doi.org/10.1093/aob/mcq264
41. Perttunen J, Sievänen R, Nikinmaa E et al (1996) LIGNUM: a tree model based on simple structural units. Ann Bot 77:87–98
42. Sievänen R, Nikinmaa E, Nygren P et al (2000) Components of functional-structural tree models. Ann For Sci 57:399–412
43. Buck-Sorlin GH, de Visser PHB, Henke M et al (2011) Towards a functional-structural plant model of cut-rose – simulation of light environment, light absorption, photosynthesis and interferences with the plant structure. Ann Bot 108:1121–1134
44. Pallas B, Christophe A, Cournède PH et al (2009) Using a mathematical model to evaluate the trophic and non-trophic determinants of axis development in grapevine. Funct Plant Biol 36:156–170
45. Pallas B, Soulié JC, Aguilar G et al (2013) X-palm, a functional structural plant model for analysing temporal, genotypic and inter-tree variability of oil palm growth and yield. In: Sievänen R, Nikinmaa E, Godin C, Lintunen A, Nygren P (eds) Proceedings of the 7th international conference on functional structural plant model. Finnish Society of Forest Science, Vantaa, pp 319–321
46. Pallas B, Clément-Vidal A, Rebolledo MC et al (2013) Using plant growth modelling to analyze C source-sink relations under drought: inter and intra specific comparison. Front Plant Sci 4:437
47. Allen MT, Prusinkiewicz P, DeJong TM (2005) Using L-systems for modeling source-sink interactions, architecture and physiology of growing trees: the L-PEACH model. New Phytol 166:869–880
48. Lopez G, Favreau RR, Smith C et al (2008) Integrating simulation of architectural development and source-sink behaviour of peach trees by incorporating Markov chains and physiological organ function sub-models into L-PEACH. Funct Plant Biol 35:761–771
49. Da Silva D, Favreau RR, Auzmendi I et al (2011) Linking water stress effects on carbon partitioning by introducing a xylem circuit into L-PEACH. Ann Bot 108:1135–1145
50. Smith C, Costes E, Favreau RR et al (2008) Improving the architecture of simulated trees in L-PEACH by integrating Markov chains and pruning. Acta Hortic 803:201–208
51. Costes E, Smith C, Renton M et al (2008) MAppleT: simulation of apple tree development using mixed statistical and biomechanical models. Funct Plant Biol 35:936–950
52. Buck-Sorlin GH, Bachmann K (2000) Simulating the morphology of barley spike phenotypes using genotype information. Agron Plant Genet Breed 20:691–702
53. Tardieu F (2003) Virtual plant: modelling as a tool for the genomics of tolerance to water deficit. Trends Plant Sci 8:9–14
54. Hammer GL, Cooper M, Tardieu F et al (2006) Models for navigating biological complexity in breeding improved crop plants. Trends Plant Sci 11:587–593
55. Lecoeur J, Poiré-Lassus R, Christophe A et al (2011) Quantifying physiological determinants of genetic variation for yield potential in sunflower. SUNFLO: a model-based analysis. Funct Plant Biol 38:246–259
56. Cruiziat P, Cochard H, Améglio T (2002) Hydraulic architecture of trees: main concepts and results. Ann For Sci 59:723–752
57. Früh T (1997) Simulation of water flow in the branched tree architecture. Silva Fennica 31: 275–284
58. Früh T, Kurth W (1999) The hydraulic structure of trees: theoretical framework and numerical simulation. J Theor Biol 201:251–270
59. Lacointe A, Minchin PEH (2008) Modelling phloem and xylem transport within a complex architecture. Funct Plant Biol 35(10):772–780
60. Da Silva D, Boudon F, Godin C et al (2008) Multiscale framework for modeling and analyzing light interception by trees. Multiscale Model Simul 7(2):910–933
61. Johnson RS, Lakso AN (1991) Approaches to modeling light interception in orchards. HortScience 26(8):1002–1004
62. Spitters CJT, Toussaint HAJM, Goudriaan J (1986) Separating the diffuse and direct component of global radiation and its implications for modeling canopy photosynthesis part I. Components of incoming radiation. Agric For Meteorol 38(1):217–229
63. Perez R, Seals R, Michalsky J (1993) All-weather model for sky luminance distribution – preliminary configuration and validation. Sol Energy 50(3):235–245

64. Thornley JHM (1976) Mathematical models in plant physiology. Academic Press, London
65. Thornley JHM (1998) Dynamic model of leaf photosynthesis with acclimation to light and nitrogen. Ann Bot 81(3):421–430
66. Yin X, Struik PC (2009) C3 and C4 photosynthesis models: an overview from the perspective of crop modelling. NJAS-Wageningen J Life Sci 57(1):27–38
67. Faust M (1989) Physiology of temperate zone fruit trees. Wiley Intersciences, New York, p 338
68. Hacke U (ed) (2015) Functional and ecological xylem anatomy. Springer, Cham
69. Holbrook NM, Zwieniecki MA (eds) (2005) Vascular transport in plants. Elsvier, Amsterdam
70. Taiz L, Zeiger E, Møller IM et al (2018) Fundamentals of plant physiology. Oxford University Press, New York
71. Alder NN, Pockman WT, Sperry JS et al (1997) Use of centrifugal force in the study of xylem cavitation. J Exp Bot 48(308):665–674
72. Pátek J, Hrubý J, Klomfar J et al (2009) Reference correlations for thermophysical properties of liquid water at 0.1 MPa. J Phys Chem Ref Data 38:21–29
73. Tyree MT, Ewers FW (1991) The hydraulic architecture of trees and other woody plants. New Phytol 119:345–360



Chapter 4

Detecting and Quantifying Xylem Embolism by Synchrotron-Based X-Ray Micro-CT

Martina Tomasella, Francesco Petruzzellis, Sara Natale, Giuliana Tromba, and Andrea Nardini

Abstract

The vulnerability to xylem embolism is a key trait underlying species-specific drought tolerance of plants, and hence is critical for screening climate-resilient crops and understanding vegetation responses to drought and heat waves. Yet, accurate determination of embolism in plant's xylem is challenging, because most traditional hydraulic techniques are destructive and prone to artefacts. Hence, direct and in vivo synchrotron-based X-ray micro-CT observation of xylem conduits has emerged as a key reference technique for accurate quantification of vulnerability to xylem embolism. Micro-CT is nowadays a fundamental tool for studies of plant hydraulic architecture, and this chapter describes the fundamentals of acquisition and processing of micro-CT images of plant xylem.

Key words X-ray, Micro-CT, Xylem vulnerability, Xylem embolism, PLC, Stem, Leaf

1 Introduction

X-ray micro-computed tomography (micro-CT) is a powerful non-destructive imaging technique that allows obtaining information on the internal structure of different samples via the detection of the attenuation or the phase shift of the X-rays transmitted through the sample itself. During a micro-CT scan, the X-ray beam, after passing through the object, is collected by a detector. While the sample is rotating, a sequence of bidimensional projections is taken, usually at a fixed angular increment.

After application of adequate reconstruction algorithms and filtering functions, 3D virtual volumes or virtual cuts (slices) of the sample can be visualized. In the specific case of plants, this technique allows to clearly distinguish gas-filled from water-filled spaces, thus allowing analysing hydraulic integrity and embolism patterns of the xylem conduits [e.g. 1, 2]. So far, micro-CT has been widely used to visualize and quantify xylem embolism because

Javier Agusti (ed.), *Xylem: Methods and Protocols*, Methods in Molecular Biology, vol. 2722,
https://doi.org/10.1007/978-1-0716-3477-6_4,
© The Author(s), under exclusive license to Springer Science+Business Media, LLC, part of Springer Nature 2024

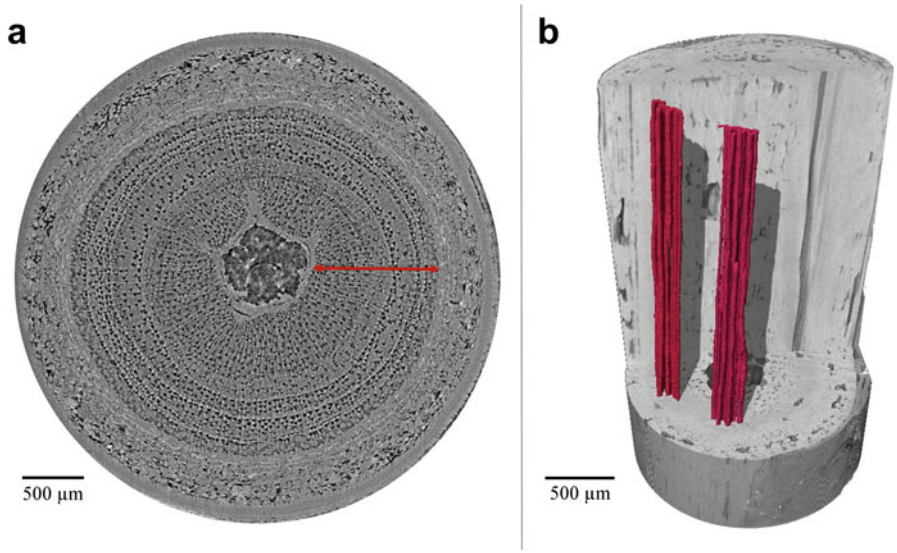


Fig. 1 2D and 3D in vivo visualization by synchrotron-based X-ray Micro-CT of xylem emboli in stems: (**a**) 2D transverse image of a *Populus nigra* L. stem, and (**b**) 3D reconstruction of a *Helianthus annuus* L. stem in drought-stressed potted plants. In (**a**), gas-filled xylem conduits are shown in black in the sapwood region delimited by the red double arrow. In (**b**), two bundles of reconstructed empty xylem vessels are marked in red

of its high spatial resolution (down to ca. 1 µm pixel size), high signal-to-noise ratio and fast scan times [3–9]. Most importantly, micro-CT allows direct observation of xylem embolism in vivo on intact plants, thus offering significant advantages over classical destructive hydraulic techniques that are potentially prone to artefacts [10–12]. However, it should be noted that X-rays could cause severe damage to living cells [13], and depending on the purpose of the study, special attention should be paid to reduce the delivered radiation dose and sample exposure time and to avoid multiple scans on the same sample.

Micro-CT allows obtaining both transverse two-dimensional (2D) images and three-dimensional (3D) reconstructions of stems, petioles, leaf portions (including veins), and roots. Examples of a 2D and a 3D reconstruction of stems are shown in Fig. 1. While both image types allow detecting xylem embolism, 3D reconstructions provide important information on structural connectivity and heterogeneity of the xylem network [14, 15]. Reconstructed slices offer a simple and reliable tool to detect gas-filled conduits, while also allowing easy measurements of conduit size. Thus, these images are used to estimate the theoretical xylem hydraulic conductivity and percentage loss of hydraulic efficiency due to embolism accumulation. By observing the xylem in plants or plant samples of the same species at different hydration levels, it is also possible to relate the percentage of embolized conduits to the xylem pressure, thus constructing xylem vulnerability curves to estimate hydraulic vulnerability parameters (e.g., the water potential inducing 50% loss

of hydraulic conductivity, Ψ_{50}) that can also be estimated with classical hydraulic methods [4]. This allows to validate the classical hydraulic measurements, which are potentially prone to artefacts.

In this chapter, we illustrate a method to analyse xylem embolism using 2D images acquired by synchrotron-based X-ray micro-CT. We describe how this method can be applied to different plant organs both in vivo (intact plants) and ex vivo (cut plant portions).

2 Materials

2.1 Synchrotron-Based Micro-CT Facility

1. Synchrotron radiation laboratory with phase contrast imaging (PCI) approach (see Subheading 3.1 for detailed description). *See* **Note 1** for information on facilities availability.

2.2 Plant Material

1. Intact plants/cut plant portions (*see* **Note 2**).

2.3 Sample Preparation

1. Wooden sticks with a screw at the bottom that can be mounted on the sample holder are required to keep eventual bending-prone samples in a vertical position (*see* **Note 3**) (Fig. 2).
2. Parafilm.
3. Cling film.
4. Adhesive tape (e.g., American tape).
5. Plastic bags to contain eventual pots, root systems, and soil to avoid soil particles loss.
6. Razor blades and scissors.

2.4 Additional Measurements

1. A Scholander pressure chamber (alternatively a dewpoint hygrometer or a leaf/stem psychrometer) to measure leaf or stem water potential (Ψ_{leaf} and Ψ_{stem}, respectively).
2. A razor blade to cut the petiole/base of the leaf.
3. Cling film to wrap the leaf used for Ψ_{leaf} or Ψ_{stem} determination.
4. A light source and a stereoscope/magnifying lens to examine the cut section of the leaf blade/petiole/stem and to detect sap appearance during progressive pressurization of the sample.

2.5 Reconstruction Software

1. Reconstruction software for X-ray micro-CT data (see Subheading 3.5 for explanations).

2.6 Image Analysis Software for Xylem Embolism Quantification

1. ImageJ [16] (a free and complete tool for image visualization, but also commercial image analysis software are available).

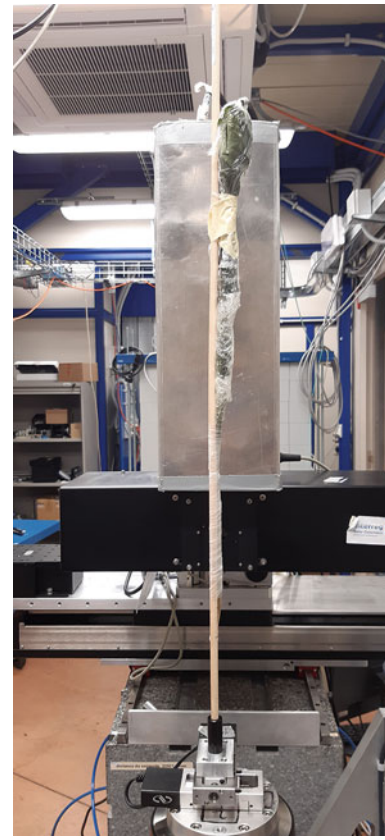


Fig. 2 Example of a cut plant shoot mounted on the sample holder in the X-ray micro-CT setup at the SYRMEP beamline of the Elettra synchrotron facility. In this setup, the sample holder consists of a ca. 1 m wooden stick fixed at the base to a plastic cylinder, directly screwed on the rotator

3 Methods

3.1 Technical Specification

Conventional micro-CT facilities are based on micro-focus X-ray generators. Like all X-ray tubes, these sources produce X-rays when highly energetic electrons are stopped in a solid metal anode. A polychromatic conic beam is generated, from which a conical solid angle is selected. Many benchtop micro-CT systems are nowadays able to reach very high-resolution level, in the range of 1 μm with a voxel size even below 1 μm. The position of the sample with respect to the source and the detector can be changed to adjust the magnification and the resolution. However, as the sample must stay inside the field of view, the optimal position is always a compromise between sample size and spatial resolution. The mainly used technique is the absorption modality as the produced beam is not always enough coherent to obtain phase contrast.

A new generation of X-ray sources based on the liquid-metal-jet anode (MetalJet) technology has been recently implemented to improve the limitations of conventional systems with an important increase in the brightness. With these systems, a sufficient grade of spatial coherence is achieved, allowing the use of phase-contrast imaging techniques. However, for these sources the available X-ray fluxes are still far below the ones available at synchrotron labs. As a consequence, the time required to complete a CT scan in phase contrast modality is much longer.

Synchrotron radiation (SR) is generated by an electron traveling at relativistic speed when it changes movement direction. SR covers a large spectrum of electromagnetic waves, from infrared to hard X-rays. SR is produced in large accelerator-based facilities equipped with different magnetic structures (bending magnets and insertion devices) optimized to maximize radiation production for the different experimental purposes and user requirements. SR is extracted from the accelerators and transported to the experimental stations through so-called *beamlines*.

The peculiar properties of SR, such as the high spatial coherence of the source, the monochromaticity, and the high available fluxes, have opened unprecedented opportunities in the field of hard X-ray imaging. In this framework, the phase contrast imaging (PCI) techniques have been developed with the aim of improving the image quality available from conventional sources, and overcoming their main limitations in the study of soft biological tissues. Image contrast, which in conventional imaging is due to differences in the X-ray absorption, has been overcome by the information of phase shifts occurring to the coherent X-rays crossing the sample and determining the phase contrast in the image. This implied a real revolution in biomedical and biological X-ray imaging that involved wide application areas at different resolution scales. For imaging plants vascular system, the use of PCI approach is fundamental as it allows to easily visualize a gas phase even in very narrow xylem conduits, thus facilitating image segmentation and a quantitative assessment of embolism.

Before mounting the sample on the sample holder placed in the hutch, the user must set the following technical details related to the observation and acquisition procedure.

Based on the specific research question, the user has first to define the average X-ray source energy, and thus apply proper filters between the beam exit point and the sample to eventually decrease beam's energy to the desired level. As an example, in Savi et al. [5], two filters (1 mm of aluminium and 1 mm of silicon) were used to obtain an average X-ray source energy of 22 keV. Common energy levels used to image xylem embolism range from 20 to 25 keV.

In a second step, the sample-to-detector distance and the zoom of the detector must be set up according to the desired pixel size, which must consider xylem conduit diameter and the sample size (*see* **Note 4**), as well as the available field of view (FOV).

3.2 How to Prepare Plant Samples

While observation of different organs in intact plants provide a reliable estimate of xylem embolism, the use of cut plant portions can lead to experimental artefacts similar to those observed in some classical hydraulic techniques. In this case, care should be taken during sample preparation to avoid "open vessel artefacts" when using stem/branch segments shorter than maximum vessel length [12, 17] and spurious embolism generation when cutting xylem under tension [10, 11], as both can potentially lead to embolism overestimation. The size of intact plants that can be observed at the beamline is often limited by the design and features of the sample holder and of the detector. While some facilities allow observations of relatively big plants rooted in large and heavy pots (up to 60 kg), most commonly the reasonable plant size is limited to about 1 m height. A new setup optimized for the study of heavy samples has been recently implemented at the SYRMEP beamline [18] and will allow to perform accurate microCT studies on plants with bigger stem sizes (5–10 cm).

1. Roots/pots are tightly enclosed in plastic bags to avoid soil losses to the mechanisms of the rotator/sample holder. In this way, the plant can also be mounted upside-down, allowing scanning of apical vs basal parts. For intact plants, it could be necessary to partially remove the soil before the scan when the available sample holder cannot sustain the weight of the pot. The stem and, most importantly, the leaves must be also wrapped in cling film to avoid water loss during the scan. Parafilm and tape are used to properly attach the sample to the wooden/plastic stick, in order to avoid sample's swinging during the sample rotation.
2. The scanned portion is attached to the wooden stick with parafilm.
3. The stick is fixed to the sample holder on the rotator. The plant (with the stick) is mounted on the sample holder taking care that the stem is vertically oriented, and when rotating, the part to be scanned remains on the rotation axis and perpendicular to the beam.

3.3 Acquisition Procedure

The image acquisition is performed using a specific software controlling the detector and all the motion stages for sample positioning. Before launching the acquisition, it is necessary to select the X-ray energy, the exposure time, and the number of projections. In the nearby parallel geometry of the SR X-ray beam, the CT scan is performed with a total rotation angle of 180°. A rotation over 360° can be used to extend the detector field of view. Indeed, in the so-called half acquisition mode, an off-center rotation over 360° is performed to almost double the width of the available field-of-view [19].

The total exposure time determines the entrance dose delivered to the sample. The dose has to be carefully evaluated in order to reduce the sample damage and must be set according to the specific research question (*see* **Note 5**). For example, in Secchi et al. [9], 1800 projections were acquired at an exposure time of 100 ms with a 360°-degree rotation angle, resulting in a total acquisition time of 3 min and in an entrance dose rate in water of 47 mGy s^{-1}. Typical scan times for different studies performed at synchrotron facilities range from 75 s to 4 min.

Dark and flat images must be acquired prior to sample scanning (*see* **Note 6**). For dark images, it is necessary to launch an acquisition while the beam is off. For flat images, acquisition must be launched after the beam is turned on and after moving the sample outside the FOV.

After these preliminary acquisitions, the sample is placed in the centre of the FOV and the acquisition can start (*see* **Note 7**).

Additionally, according to the research question, the above steps could be repeated after cutting the samples few mm above the scanned area to induce embolism in all functional conduits. This is often necessary as water-filled conduits cannot be easily recognized against the background of hydrated parenchyma and mechanical cells of the wood, so that it might be impossible to calculate the embolism rate as a percentage of embolized conduits over the total number of conduits. Furthermore, this final cutting procedure allows to distinguish mature and functional conduits from immature ones, thus improving the accuracy of embolism estimation (see Subheading 3.6).

After saving sample's acquisition, the sample is removed from the sample holder and used for eventual additional measurements.

3.4 Additional Measurements

The quantification of xylem embolism is usually coupled with measurement of leaf or stem water potential (Ψ_{leaf} and Ψ_{stem}, respectively). For each sample, Ψ_{leaf} is measured on mature and fully expanded leaves. For Ψ_{stem} determination using the pressure chamber, leaves must be wrapped in cling film to equilibrate Ψ_{leaf} with Ψ_{stem} at least 30 min before measurement. Here, below, are the procedures to be applied for each of the instruments for water potential determination:

1. Pressure chamber: Excise the leaf from the stem and wrap it immediately in plastic film (*see* **Note 8**). Remove few mm of the petiole with a razor blade, making a couple of close and perpendicular cuts. Place the leaf in the pressure chamber, and apply gas pressure inside the chamber until sap emerges from xylem [20]. For best procedures, see methodological tests performed by Rodriguez-Dominguez et al. [21].
2. Dewpoint hygrometer: After calibrating the instrument (check instrument manual for the calibration procedure), cut leaf discs

or stem segments according to the size of the sample holder and place them in the measurement chamber. For some leaves, it could be necessary to punch the blades with a needle to favour water potential equilibration during measurements. In the case of stems, split them longitudinally before inserting them in the chamber.

3. Leaf/stem psychrometer: Calibrate the instrument according to the calibration procedure of the specific instrument. Leaf/stem surface must be cleaned and dried prior sealing the portion of the sample in the psychrometer. Abrade surface of leaf/stem, apply some silicon grease around psychrometer surface, place the sample into a sealed chamber, and allow it to equilibrate.

3.5 Image Reconstruction

The reconstruction workflow of X-ray micro-CT data is based on multiple computational steps, from flat fielding and the application of conventional filtered back projection (FBP) algorithm [22] to more refined image processing to compensate artefacts, enhance the quality of the reconstructed images and improve the identification of the different structures. To this aim, additional preprocessing algorithms are used in phase contrast imaging to decouple phase from absorption effects and improve image contrast [23]. In this light, an open-source software package, namely, SYRMEP Tomo Project (STP) [24], has been developed to allow the users of SYRMEP beamline at Elettra synchrotron designing custom CT reconstructions. The software is free to use, and its releases can be downloaded at the Elettra Scientific Computing group GitHub repository https://github.com/ElettraSciComp/STP-Gui. Commercial software is also available on the market.

Generally, the output of the acquisition process is a file under a format (e.g., TDF, Tomo Data Format) that allows handling a large dataset consisting in a sequence of 2D image files (usually a TIFF file for each acquired projection as well as flat/dark images). Thus, a software is required to extract and reconstruct the acquired projections in a sequence of 2D images that can be further analysed using image analysis software (see below). The choice of the software depends on the algorithm used for the reconstruction. The simplest one, namely, the filtered back projection (FBP) algorithm after the flat fielding of the projection data, can be run by most of the computing software tools (e.g., MATLAB, IDL) [24]. However, thanks to the coherence of the synchrotron radiation, phase-contrast imaging can be applied on synchrotron-derived data, as it allows differentiating between two materials of similar electron density or with negligible X-ray absorption (i.e., phase objects) so as to ease the image segmentation step and the subsequent analyses [24]. In this light, STP software reconstructs 2D images sequence from TDF files by implementing phase-contrast imaging algorithms.

The framework implemented in the software includes the following steps:

- Preprocessing: In this step, it is possible to apply dark/flat correction, as well as ring removal method;
- Phase-retrieval: In this step, a phase retrieval algorithm [23] can be applied to separate phase from absorption effects and accounting for pixel size, detector-to-sample distance, X-ray energy, and the different attenuation properties of the elements composing the imaged object (i.e., by tuning δ and β coefficients).
- Image reconstruction: This is the step leading to the final reconstruction of the 2D images sequence. Here, the centre of rotation could be automatically calculated or manually inserted if known and the reconstruction algorithm can be specified.
- Postprocessing: This step allows to set several features of the reconstructed 2D image sequences, such as rescaling images to 8- or 16-bit quality or to select a region of interest to be reconstructed.

3.6 Image Analysis

Reconstructed 2D transverse section images are analysed via an image analysis software. Hereafter, the procedure for ImageJ is described. The proper scale is set based on pixel size (image -> set scale). The sapwood area on which performing the measurements (from vascular cambium to pith excluded) is selected with the polygon selection tool (*see* **Note 9**) and measured (analyze -> measure).

In the selected sapwood area, a proper pixel threshold is selected to clearly identify gas-filled conduits shown in dark grey (Image -> Adjust -> Threshold). Preprocessing adjustments (brightness, contrast) or manual cleaning of the image can be applied to improve the analysis (*see* **Note 10**).

With the particle analysis tool (image -> analyse particles), the single embolized conduits are identified and counted and their area is measured. The equivalent circle diameter (d) is calculated from single conduit surface areas. Different parameters can be used as an estimate of the amount of xylem embolism.

1. Theoretical percentage loss of hydraulic conductance (PLC_t). Theoretical hydraulic conductance of gas-filled conduits (k_{gf}) is calculated according to the Hagen-Poiseuille Equation from d values, as $(\pi\rho/128\,\mu)\Sigma d^4$, where ρ and μ are the density of the fluid and the viscosity of water, respectively [25]. The sum of gas-filled and water-filled conduit conductance gives the maximum hydraulic conductance (k_{max}), when it is possible to clearly identify water-filled conduits. Alternatively, k_{max} is calculated from all empty conduits of the transverse section obtained from a second scan done after cutting the stem closely

above the previously scanned area (see Subheading 3.3). k_{gf} and k_{max} can be divided by the cross-sectional xylem area to obtain the theoretical specific hydraulic conductance of gas filled conduits (k_s) and theoretical specific maximum hydraulic conductance (k_{s_max}), respectively. PLC_t is finally calculated as $k_s/k_{s_max} \times 100$ (*see* **Note 11**).

2. Embolized conduit fraction. This is the number of empty xylem conduits divided by total number of conduits.
3. Embolized sapwood area (A_{embol}). This is calculated by dividing the total embolized pixel area by the mature sapwood area, in percentage. If the reconstructed image of the sample after cutting the stem above the scanned area is available, it is possible to calculate the embolized vessel area (EVA), calculated dividing A_{embol} by the embolized sapwood area, after the final cut made above the scanned region (namely, A_{embol_cut}, see Subheading 3.3), expressed in percentage.

3.7 Xylem Vulnerability Curve (VC) Estimation

Xylem vulnerability curves can be obtained by plotting PLC_t versus the corresponding Ψ_{leaf} or Ψ_{stem} and fitting sigmoidal or Weibull functions using a data analysis software (e.g., MATLAB, Sigmaplot, R) (*see* **Note 12**). Alternatively, A_{embol} can be used instead of PLC_t, given that the resulting VCs typically show good agreement with those obtained with PLC_t [9]. Depending on the function used, several parameters are obtained. The most important ones from an agronomical and ecophysiological point of view are the water potential at 12, 50, and 88% PLC_t (or A_{embol}, or EVA), namely, Ψ_{12}, Ψ_{50} and Ψ_{88}, respectively.

4 Notes

1. Several synchrotron radiation laboratories are available in Europe, Asia, Australia, and the Americas. The access to imaging beamlines in these laboratories is free of charge and subject to submission of a specific proposal, where the scientific case is presented, the need for SR is justified and a given number of beamtime hours is requested according to the number of samples to be scanned and an estimate of total exposure time needed for each scan. The proposals are evaluated by independent review panels twice a year, and beamtime is assigned according to a merit score. As an example, access to the SYRMEP imaging beamline at the Elettra synchrotron source (https://www.elettra.eu/) is performed through the so called Virtual User Office (https://vuo.elettra.eu/). Useful suggestions on how to write a successful proposal are reported in https://www.elettra.eu/userarea/apbt.html.

2. Xylem embolism can be quantified on intact plants or cut plant portions, as well as on different plant organs (stems, leaves, petioles, roots), according to the specific research question and to the beamline's technical characteristics (e.g. sample holder, pixel size, field of view). We suggest carefully assessing the size and the weight of intact plants or cut plant portions to be scanned prior the experiments, and in particular to check:
   (a) Size of the hutch: Very long samples might not fit in the hutch.
   (b) Characteristics of the sample holder, making sure that the sample's weight can be sustained by the sample holder.
   (c) Field of view, making sure that at least half of the cross-section of the scanned samples lies within the available field.
3. Wooden sticks are recommended because of their low X-ray absorption and should be adequately tall and hard enough to avoid sample swinging during image acquisition. To easily distinguish the stick from the stem of the sample, a thin metal wire can be rolled around the stem, right above or below the region to be scanned (*see* also **Note 7**).
4. Pixel size must be lower than xylem conduit diameter. For example, in Losso et al. [6], the pixel size was set to 2 μm and conduit diameter of the study species ranged between 15 and 25 μm.
5. Carefully choose exposure time: not too fast to avoid plant movement or oscillations during rotation, and not too slow to prevent samples receiving an excessive X-ray dose.
6. The number of projections and the exposure time could be reduced for dark and flat acquisition, in order to reduce the total acquisition time.
7. Make sure that samples (or the region that must be acquired) during the rotation are centred and do not move out of the FOV. The centre of rotation could be checked during sample preparation by placing 1 mm long metal wire few millimetres above the scanning area. In live mode, it will be clearly visible by the detector. To assess whether the sample is centred in the FOV, let it rotate by 180° and be sure that the steel wire remains in the centre of rotation.
8. This is fundamental to prevent water loss during sample preparation.
9. If stem sapwood is larger than the field of view and, therefore, only a part of the sapwood is imaged, analyses are done on a smaller portion.

10. Manual selection of conduits may be necessary. In this case, the ROI menu in ImageJ is a helpful tool.
11. Note that here k_s is the theoretical specific hydraulic conductance of gas filled conduits, so the formula differs from that used for classic hydraulic measurements, where the initial (native) k is the specific hydraulic conductance of water filled conduits.
12. "fitplc" R package [26] is widely used.

References

1. Brodersen CR, McElrone AJ, Choat B et al (2013) In vivo visualizations of drought-induced embolism spread in *Vitis vinifera*. Plant Physiol 161:1820–1829
2. Choat B, Brodersen CR, McElrone AJ (2015) Synchrotron X-ray microtomography of xylem embolism in *Sequoia sempervirens* saplings during cycles of drought and recovery. New Phytol 205:1095–1105
3. Cochard H, Delzon S, Badel E (2015) X-ray microtomography (micro-CT): a reference technology for high-resolution quantification of xylem embolism in trees. Plant Cell Environ 38:201–206
4. Nardini A, Savi T, Trifilò P, Lo Gullo MA (eds) (2017) Drought stress and the recovery from xylem embolism in woody plants, Progress in botany, vol 79. Springer, Cham, pp 197–231
5. Savi T, Miotto A, Petruzzellis F et al (2017) Drought-induced embolism in stems of sunflower: a comparison of in vivo micro-CT observations and destructive hydraulic measurements. Plant Physiol Biochem 120:24–29
6. Losso A, Bär A, Dämon B et al (2019) Insights from in vivo micro-CT analysis: testing the hydraulic vulnerability segmentation in *Acer pseudoplatanus* and *Fagus sylvatica* seedlings. New Phytol 221:1831–1842
7. Peters JMR, Gauthey A, Lopez R et al (2020) Non-invasive imaging reveals convergence in root and stem vulnerability to cavitation across five tree species. J Exp Bot 71:6623–6637
8. Tomasella M, Casolo V, Natale S et al (2021) Shade-induced reduction of stem nonstructural carbohydrates increases xylem vulnerability to embolism and impedes hydraulic recovery in *Populus nigra*. New Phytol 231: 108–121
9. Secchi F, Pagliarani C, Cavalletto S et al (2021) Chemical inhibition of xylem cellular activity impedes the removal of drought-induced embolisms in poplar stems – new insights from micro-CT analysis. New Phytol 229: 820–830
10. Wheeler JK, Huggett BA, Tofte AN et al (2013) Cutting xylem under tension or supersaturated with gas can generate PLC and the appearance of rapid recovery from embolism. Plant Cell Environ 36:1938–1949
11. Trifilò P, Raimondo F, Lo Gullo MA et al (2014) Relax and refill: xylem rehydration prior to hydraulic measurements favours embolism repair in stems and generates artificially low PLC values. Plant Cell Environ 37: 2491–2499
12. Torres-Ruiz JM, Jansen S, Choat B et al (2015) Direct X-ray microtomography observation confirms the induction of embolism upon xylem cutting under tension. Plant Physiol 167:40–43
13. Petruzzellis F, Pagliarani C, Savi T et al (2018) The pitfalls of in vivo imaging techniques: evidence for cellular damage caused by synchrotron X-ray computed micro-tomography. New Phytol 220:104–110
14. Brodersen CR, Lee EF, Choat B et al (2011) Automated analysis of three dimensional xylem networks using high-resolution computed tomography. New Phytol 191:1168–1179
15. Wason J, Bouda M, Lee EF et al (2021) Xylem network connectivity and embolism spread in grapevine (*Vitis vinifera* L.). Plant Physiol 186: 373–387
16. Schneider CA, Rasband WS, Eliceiri KW (2012) NIH image to ImageJ: 25 years of image analysis. Nat Methods 9:671–675
17. Martin-StPaul NK, Longepierre D, Huc R et al (2014) How reliable are methods to assess xylem vulnerability to cavitation? The issue of "open vessel" artifact in oaks. Tree Physiol 34: 894–905
18. Dullin C, D'Amico L, Saccomano G et al (2023) Novel setup for rapid phase contrast CT imaging of heavy and bulky specimens. J

Synchrotron Rad 30:650. https://doi.org/10.1107/S1600577523001649

19. Buzug TM (2008) Computed tomography: from photon statistics to modern cone-beam CT. Springer, Berlin/Heidelberg
20. Brown PW, Tanner CB (1981) Alfalfa water potential measurement: a comparison of the pressure chamber and leaf dew-point hygrometers. Crop Sci 21:240–244
21. Rodriguez-Dominguez CM, Forner A, Martorell S et al (2022) Leaf water potential measurements using the pressure chamber: synthetic testing of assumptions towards best practices for precision and accuracy. Plant Cell Environ 45:2037. https://doi.org/10.1111/pce.14330
22. Kak AC, Slaney M (1988) Principles of computerized tomographic imaging. IEEE Press, New Brunswick
23. Paganin D, Mayo SC, Gureyev TE et al (2002) Simultaneous phase and amplitude extraction from a single defocused image of a homogeneous object. J Microsc 206:33–40
24. Brun F, Pacilè S, Accardo A et al (2015) Enhanced and flexible software tools for X-ray computed tomography at the Italian synchrotron radiation facility Elettra. Fundamenta Informaticae 141:233–243
25. Tyree MT, Zimmermann MH (2002) Xylem structure and the ascent of sap. Springer, Berlin/Heidelberg
26. Duursma R, Choat B (2017) fitplc – an R package to fit hydraulic vulnerability curves. J Plant Hydraul 4:e002

Part II

Xylem Development and Evolution



Chapter 5

Analysis of Xylem Cells by Nucleus-Based Transcriptomics and Chromatin Profiling

Dongbo Shi, Laura Luzzietti, Michael Nodine, and Thomas Greb

Abstract

Nuclei contain essential information for cell states, including chromatin and RNA profiles – features which are nowadays accessible using high-throughput sequencing applications. Here, we describe analytical pipelines including nucleus isolation from differentiated xylem tissues by fluorescence-activated nucleus sorting (FANS), as well as subsequent SMART-seq2-based transcriptome profiling and assay for transposase-accessible chromatin (ATAC)-seq-based chromatin analysis. Combined with tissue-specific expression of nuclear fluorescent reporters, these pipelines allow obtaining tissue-specific data on gene expression and on chromatin structure and are applicable for a large spectrum of cell types, tissues, and organs. Considering, however, the extreme degree of differentiation found in xylem cells with programmed cell death happening during vessel element formation and their role as a long-term depository for atmospheric CO_2 in the form of wood, xylem cells represent intriguing and relevant objects for large-scale profilings of their cellular signatures.

Key words FANS, Nucleus sorting, RNA-seq, ATAC-seq, SMART-seq2, Flow cytometry

1 Introduction

Plant tissues are generally composed of many different types of cells. To gain insight into the physiology and development of those cell types, collecting information from crude mixed samples is often not sufficient as cell type-specific features are masked by surrounding tissues. By labelling of specific cell types, fluorescence-based isolation of protoplasts, and subsequent genome-wide transcriptome analyses, gene expression atlases were generated, which considerably accelerated plant science [1, 2]. However, these approaches have been only applied to a limited number of tissues so far. One of the obstacles is protoplast isolation, which is challenging in certain tissues like xylem cells due to their tight embedment into internal tissues and the heterogeneous size of the resulting protoplasts. Moreover, protoplasting itself affects cell state and, thus, gene expression [2]. In contrast, nuclei can be

Javier Agusti (ed.), *Xylem: Methods and Protocols*, Methods in Molecular Biology, vol. 2722,
https://doi.org/10.1007/978-1-0716-3477-6_5,
© The Author(s), under exclusive license to Springer Science+Business Media, LLC, part of Springer Nature 2024

isolated relatively easily [3] and, at the same time, applied to transcriptome and chromatin landscape analysis [4–6]. Here, we described methods for isolating plant nuclei using FANS and further analysis by RNA-seq and ATAC-seq. Due to the large size of targeted cells, the methods are especially suited for differentiated cells like cells from the xylem or any other vascular tissue.

2 Material

2.1 Plant Material

The amount of plant material should be determined in preparatory experiments. In case of Arabidopsis, for example, this can be 2 g of internodes [7] or 1 g of 3-week-old seedlings grown on agar plates [8] (*see* **Note 1**). Prepare enough plant material for replicates and controls (e.g., nonstained samples and nontransgenic lines).

2.2 Nucleus Isolation Using a Centrifuge

1. Nucleus resuspension buffer: 20 mM Tris-HCl pH 7.5 (stock 1 M), 40 mM sodium chloride (stock 5 M), 90 mM potassium chloride (stock 3 M), 2 mM ethylenediaminetetraacetic acid (EDTA) pH 8.0 (stock 0.5 M), 0.5 mM ethylene glycol-bis (β-aminoethyl ether)-N,N,N′,N′-tetraacetic acid (EGTA) (stock 0.1 M), 0.5 mM spermidine (stock 1 M to be kept at −20 °C), 0.2 mM spermine (stock in 1 M kept kept at −20 °C), 15 mM 2-mercaptoethanol, 0.5 mM phenylmethylsulfonylfluorid (PMSF) (stock 0.1 M to be kept at −20 °C), cOmplete Protease Inhibitor Cocktail [Roche, #11697498001] (1 tablet/50 mL).
2. Nucleus isolation buffer: 2 mL nucleus resuspension buffer supplemented with 10 μL RiboLock RNase inhibitor (40 U/μL) (ThermoFisher, #EO0381) and 0.05% Triton-X (stock 10%) for each sample.
3. Staining solution: 300 μL nucleus resuspension buffer supplemented with 10 μg/mL Hoechst 33342 (or DAPI) and 5 μL of RiboLock RNase inhibitor.
4. Razor blades (Wilkinson, Classic or Feather, #FA-10). Clean the surface before use.
5. Petri dishes, 60 mm diameter.
6. CellTrics filter. 50 μm (Sysmex, #04-004-2327) and/or 30 μm (Sysmex, #04-004-2326).
7. 5 mL test tube for sorting and filtering (Falcon, #352235).
8. Low protein binding tube (2 mL) (Eppendorf, #0030108132).
9. Nuclease-free water.
10. Conventional centrifuge with cooling function.

2.3 Nucleus Isolation Without Using a Centrifuge

1. 1× NIB buffer: Included in CelLytic™ PN Isolation/Extraction Kit (MilliporeSigma #CELLYTPN1) (stock Nucleus Isolation Buffer 4× (NIB)).
2. 1× NIB+ buffer: 1× NIB buffer 2 mL, supplemented with 10 μg/mL Hoechst 33342 (or DAPI) and 10 μL of RiboLock RNase inhibitor per sample.
3. Same material as in **items 4–10** in Subheading 2.2.

2.4 Nucleus Sorting

1. Cell sorter (e.g., BD FACSAriaTM IIIu cell sorter (Becton Dickinson)) with laser to excite nucleus staining (405 nm laser for Hoechst 33342 or DAPI staining).
2. PBS (pH 7.4, flow cytometry grade, ThermoFisher #A1286301).
3. Fluorescence microscope [optional].

2.5 RNA Extraction and SMART-seq2 Amplification

1. Low DNA binding tube (1.5 mL) (Eppendorf, # 0030108051).
2. Trizol reagent (Thermo Fisher, #15596026).
3. 5 mg/mL Glycogen (Thermo Fisher, #AM9510).
4. 100% isopropanol and 75% ethanol.
5. Conventional centrifuge with cooling function.
6. Conventional thermal cycler.
7. 5 M Betaine (Sigma, #B0300-1VL).
8. 0.1 M $MgCl_2$ (Sigma, #00457-1ML-F).
9. 10 μM Template switching oligo (TSO).
   5′- AAGCAGTGGTATCAACGCAGAGTAC rGrG+G-3′ can be purchased from QIAGEN, IDT or others, where rG stands for riboguanosines and + G stands for locked nucleic acid (LNA)-modified guanosine.
10. Nuclease-free water.
11. Ribolock RNase inhibitor.
12. 0.1 M Superscript II first-strand buffer, Dithiothreitol (DTT), Superscript II Reverse Transcriptase in SuperScript™ II Reverse Transcriptase kit (ThermoFisher, #18064022).
13. 10 or 100 μM Anchored olig-dT primer.

    5′-AAGCAGTGGTATCAACGCAGAGTACT_{30}VN-3′.
14. 10 or 100 mM dNTP mix.
15. KAPA HiFi Hotstart ReadyMix (Roche, #KK2601).
16. 10 μM ISPCR primers.

    5’-AAGCAGTGGTATCAACGCAGAGT-3′.

17. AMPure XP beads (Beckman Coulter, #A63880).
18. Magnetic stand.
19. 80% ethanol.
20. 10 mM Tris-Cl, pH 8.5 (or Buffer EB from Qiagen).

2.6 Tagmentation for ATAC-seq Analysis

1. Collection buffer: 15 mM Tris-HCl pH 8.0, 20 mM sodium chloride, 80 mM potassium chloride, 0.05% Triton-X.
2. Tris-Mg buffer: 10 mM Tris-HCl pH 8.0, 5 mM magnesium chloride.
3. Low DNA binding tube (1.5 mL) (Eppendorf, #0030108051).
4. Tagment DNA (TD) Enzyme and Buffer Small Kit (Illumina, #20034197).
5. Transposase reaction mix (enzyme from **step 4**. Illumina kit):

2x TD buffer	25 μL
Nuclease-free water	22.5 μL[a]
Transposase	2.5 μL

[a]The amount of water can be adjusted depending on the amount of microliters left after the second wash

6. Monarch® PCR & DNA Cleanup Kit (NEB, #T1030L).
7. Conventional centrifuge with cooling function.
8. Conventional thermal cycler or incubator.
9. PCR master mix:

NEB Next High Fidelity 2× PCR Master Mix (NEB, #M0541)	25 μL
25 μM custom Nextera PCR primer 1[a]	2.5 μL
25 μM custom Nextera PCR primer 2[a]	2.5 μL
Nucleus-free water	8 μL
Total	38 μL

[a]Choose the sequence in Buenrostro et al. [12], based on how you want to pool the sample for sequencing

10. AMPure XP beads (Beckman Coulter, #A63880).
11. Magnetic stand.
12. 15 mM Tris (pH 8.0).

3 Methods

3.1 Nucleus Isolation Using Centrifuges

1. Freshly prepare nucleus resuspension buffer and nucleus isolation buffer, and keep on ice.
2. Precool the centrifuge.
3. Collect plant material and keep in a petri dish on ice. Cover to avoid drying.
4. Add adequate volume of chilled nucleus isolation buffer so that the collected plant samples are just soaked in (*see* **Note 2**).
5. Chop the samples manually with a new razor blade on ice (*see* **Note 2**). Chopping time can be up to 5 min. If the size of chopped pieces does not get smaller, chopping may be terminated earlier.
6. Collect all the material and transfer it to a low protein binding tube through a CellTrics filter. Use a pipet with the tip cut if necessary. Add additional nucleus isolation buffer (total 2 mL/sample) to wash the dish, and transfer the washing buffer with remaining plant material onto the filter as well. The same pipet tip can be continuously used without renewal if nucleus isolation buffer is added in small aliquots to increase the nucleus collection efficiency.
7. Discard the filter and spin for 10 min at 1000 *g* at 4 °C.
8. Carefully remove the supernatant using a pipet.
9. Add 2 mL of nucleus resuspension buffer and resuspend the pellet. Gently rotate the tube manually several times. There is no need to completely dissolve the pellet.
10. Spin for 10 min at 1000 *g* and 4 °C.
11. Repeat **steps 8**–**10** once.
12. Carefully remove the supernatant using a pipet. A cotton bud can be used to additionally absorb the supernatant. Add 300 μL of staining solution and gently resuspend the pellet.
13. Transfer the solution to a 5 mL test tube for sorting and filtering. Keep on ice (*see* **Note 3**).

3.2 Nucleus Isolation Without Using Centrifuges (See Note 4)

1. Freshly prepare 1× NIB and 1× NIB+ buffer and keep on ice.
2. Collect plant material and keep it in a petri dish on ice. Cover to avoid drying.
3. Add adequate volume of chilled 1× NIB+ buffer so that the collected plant samples are just soaked in (*see* **Note 2**).
4. Chop the samples manually with a new razor blade on ice (*see* **Note 2**). Chopping time can be up to 5 min. If the size of chopped pieces does not get smaller, chopping may be terminated earlier. Make sure not to over-process the samples as this could damage the nuclei [14].

5. Incubate the dish on ice (or in a cold room at 4 °C) in the dark for 15 min. Gently shake dishes with an orbital or a tilting shaker, if available.
6. Prewet the CellTrics filter by 1× NIB buffer just before sample application. Make sure that the buffer fully penetrates the filter.
7. Collect all the material and transfer it to a low protein binding tube through a CellTrics 50 μm filter mounted on a CellTrics 30 μm filter, both prewet (adjusted) [14]. Use a pipet with the tip cut if necessary. Add additional 1× NIB+ buffer (total 2 mL/sample) to wash the dish, and transfer the washing buffer with the remaining plant material onto the filter as well. The same tip can be continuously used without renewal if nucleus isolation buffer is prepared in small aliquots to increase the nucleus collection efficiency.
8. Prewet the nylon mesh filter of a 5 mL test tube for sorting and filtering, and transfer the filtered solution on the test tube. Keep the tube on ice and in darkness.

3.3 Nucleus Sorting Using Cell Sorters

The detailed method for the usage of a cell sorter is out of the scope of this chapter. Cell sorters should be set up and calibrated before plant sampling (*see* **Note 5**).

3.4 RNA Extraction, Smart-seq2 [9, 10] Amplification and Purification (See Note 6)

1. Sort 5000–15,000 nuclei for one sample to a low DNA binding tube containing 750 μL TRIzol™ inside.
2. Follow TRIzol™ instructions to extract RNA using glycogen as an indicator. Dissolve by 7 μL of RNase-free water, and store eluate at −70 °C (*see* **Note 7**).
3. Prepare first-strand reaction mix as following and keep on ice.

5 M Betaine	2 μL
0.1 M MgCl2	0.9 μL
10 μM TSO	1 μL
Nuclease-free water	0.1 μL
Ribolock RNase inhibitor	0.25 μL
Superscript II first-strand buffer	2 μL
0.1 M DTT	0.25 μL
Superscript II reverse transcriptase	0.5 μL
Total	7 μL/sample

4. Prepare annealing mix as following and denature at 72 °C for 3 min. Place immediately on ice.

10 μM Anchored olig-dT primer	1 μL
10 mM dNTP mix	1 μL
Dissolved sample RNA	1 μL

Alternatively, we could also increase the volume of template RNA as following in case a lower number of nuclei (e.g., 5000–7000) is used as a sample.

100 μM Anchored olig-dT primer	0.1 μL
100 mM dNTP mix	0.1 μL
Dissolved sample RNA	2.8 μL

5. Add 7 μL of first-strand reaction mix, and mix by pipetting up and down 10 times.
6. Incubate in a thermal cycler using the following cycling program: 42 °C for 90 min, 10 cycles of 50 °C for 2 min and 42 °C for 2 min, 70 °C for 15 min.
7. Prepare PCR master mix freshly as following, and add 40 μL to the reaction from **step 6**.

Nuclease-free water	14 μL
KAPA HiFi Hotstart ReadyMix	25 μL
10 μM ISPCR primers	1 μL
Total	40 μL

Incubate in a thermal cycler at 98 °C for 3 min, for 20 cycles at 98 °C for 15 s, 68 °C for 20 s, 72 °C for 6 min, and at 72 °C for 5 min.

8. Incubate AMPure XP beads at room temperature by placing them on a bench for around 30 min.
9. Vortex beads two times for 2 s, and add 50 μL beads to each sample. Pipet up and down 10 times, and incubate for 8 min at room temperature.
10. Place on a magnetic stand for 5 min, and then remove the supernatant by pipetting.
11. Keep samples on the magnetic stand, and add 200 μL of fresh 80% ethanol. Wait for 30 s and remove the supernatant. Repeat once.
12. Use a smaller pipet (e.g. 2 μL) to remove all the supernatant. Incubate for 5 min at room temperature and remove from stands.

13. Add 15 μL of 10 mM Tris-Cl, pH 8.5 (or Buffer EB from Qiagen), pipet up and down 10 times, and incubate tubes on a magnetic stand for 2 min.
14. Collect the supernatant in a Low DNA binding tube, and store the DNA at −20 °C (*see* **Note 8**).

3.5 Tagmentation for ATAC-seq Analysis [8, 11, 12]

1. Sort 500–15,000 nuclei for one sample to a low DNA binding tube containing 300 μL collection buffer (Subheading 2.6, **item 1**) inside (*see* **Note 9**).
2. Spin for 10 min at 3000 *g* and 4 °C using a swinging bucket centrifuge.
3. Discard the supernatant by pipetting without touching the walls (the pellet is invisible). Leave ≈ 10 μL to avoid removing nuclei, and wash using 300 μL Tris-Mg buffer.
4. Spin for 10 min at 1000 *g* at 4 °C using a swinging bucket centrifuge.
5. Prepare transposase reaction mix freshly and keep on ice.
6. Carefully remove the supernatant without touching the walls (the pellet is invisible). Leave ≈ 10 μL to avoid removing nuclei, and immeadiately add reaction mix to resuspend the nuclei.
7. Incubate the sample at 37 °C for 30 min while gently shaking (300 rpm).
8. Purify the DNA with Monarch DNA purification kit, and elute in 15 μL of Monarch® DNA Elution Buffer.
9. Prepare PCR master mix, and then add 12 μL of eluted DNA sample to 38 μL of PCR master mix.
10. Incubate in a thermal cycler using the following cycling program: 72 °C for 5 min and 98 °C for 30 s, 16 cycles of 98 °C for 10 s, 63 °C for 30 s, and 72 °C for 1 min (*see* **Note 10**).
11. Clean up the library by using AMPure XP beads (make sure to shake the AMPure XP bottle before using to resuspend any magnetic particles).
12. Apply 50 μL of the PCR reaction to 50 μL of PCR beads, (1:1 volume), mix througly by pipetting for 10 times, and incubate 10 min.
13. Place on magnetic stand for 5 min, and carefully remove the supernatant by pipetting.
14. Keep the samples on the magnetic stand, and add 200 μL of fresh 80% ethanol. Wait 30 s and remove the supernatant. Repeat once.

15. Use a smaller pipet (e.g. 2 μL) to remove all the supernatant. Incubate for 5 min at room temperature and remove from stands.
16. Add 15 μL of 15 mM Tris-HCl, pH 8.0 (or Buffer EB from Qiagen), pipet up and down 10 times and incubate tubes on a magnetic stand for 2 min.
17. Remove and keep the eluate, collecting it in a Low DNA binding tube, and store the DNA at −20 °C (*see* **Note 8**).
18. Sequence the library using compatible Illumina system (e.g., NextSeq 550) with paired-end mode.

4 Notes

1. It depends on the density of cells, isolation efficiency by chopping, and the population of interested cells if a fluorescence marker is used. Avoid soil contaminations as much as possible. In case of generating fluorescence markers, we recommend using histone tagged fluorescent proteins as we experienced certain difficulties in sorting nuclei with fluorescent proteins carrying only a nuclear localization signal (NLS). Although we usually use fresh plant material, frozen material should also be applicable upon certain protocol modification [13].
2. Efficient chopping is important for efficient nucleus isolation. Make sure that the blade can hit the sample efficiently. Do not flood the sample with too much buffer [14] as it is not necessary to cover the whole surface of the petri dish with the buffer containing the plant sample. In case of 1 g of 3-week-old Arabidopsis seedlings, the volume of buffer should be around 350 μL. Keep the sample in the centre of the dish and tilt the dish often using the blade to hold the plant material so that the excess buffer can drain off the plant sample and accumulate in a corner of the dish.
3. Here, it is possible to interrupt the procedure and collect multiple samples at this point. We prefer to limit the exposure time to the detergent in the nucleus isolation buffer. Ideally, samples should be immediately passed to the next step if the nucleus isolation buffer is applied.
4. We recommend using the protocol described in Subheading 3.2 rather than in Subheading 3.1 for nucleus isolation as it is faster, easier, and suitable for both RNA-seq and ATAC-seq analysis. Centrifugation is also reported to be a cause for nucleus loss [14]. The idea is to use a cell sorter to identify nuclei from a crude sample, instead of using a centrifuge. However, nuclei can be difficult to be detected in the Subheading 3.2 protocol due to abundant non-nucleus particles remaining in the sample solution.

5. We strongly recommend contacting staff working in local core facilities and running preliminary experiments to set the gates for the nucleus isolation and to check how much plant material is needed for a particular experimental setup. As a reference, we currently use BD FACSAria IIIu or FACSAria fusion, with a 100 μm nozzle and a 405 nm laser. We use PBS instead of FACSFlow as a sheath fluid. Gates are first set with FSC-A and SSC-A, and then FSC-H and DAPI-H, and lastly DAPI-W and DAPI-A for doublet removal. We use the 405 nm laser signal (DAPI-H) as a threshold to remove non-nucleus particles. The gate settings depend on the source of plant material and species [14]. We often prepare a test sample of Arabidopsis leaves to check the integrity of nucleus preparation based on the sharpness of multiple peaks derived from endoduplication on a histogram of DAPI-A. In the case of using GFP or other fluorescence markers, it is always recommended to prepare a sample without that fluorescence signal to set the gate. Sorted nuclei can be checked and counted by (1) re-sorting, (2) microscopy or (3) fluorescence automatic cell counter. For example, Countess™ 3 FL (Thermo Fisher, #AMQAF2000) is suitable for convenient fluorescence imaging. However, we manually count nuclei based on the captured pictures because automated counting based on fluorescent imaging is currently not available. RNase inhibitor can be omitted for preliminary experiments to reduce costs.
6. Here, we described the protocol for original Smart-seq2 protocols [9, 10]. Adding biotin as a 5′ tag to TSO, anchored oligo dT, and ISPCR primers is recommended to reduce multiple template switching and unwanted reactions and to increase purification efficiency, together with using streptavidin beads [15–17]. Alternatively, commercial kits for Smart-seq (e.g., SMART-Seq® v4 Ultra® Low Input RNA Kit for Sequencing, TaKaRa Bio, #634888 – #634892) or other kits designed for low input RNA are also available.
7. Due to the low concentration and low volume of eluted RNA, we normally skip the quality control of RNA at this stage.
8. Now, the sample is ready for quality check, fragmentation and subsequent library preparation using a conventional kit for subsequent next generation sequencing (e.g., NEBNext Ultra II DNA prep kit with NEBNext Multiplex Oligos for Illumina sequencing (New England Biolabs, #7645)). Due to the low amount of starting material, reads can contain a certain amount of oligo sequence. These can be removed by the Cutadapt software [7, 18] before mapping reads to the genome.
9. We recommend using the nucleus isolation described in Subheading 3.2 without using centrifuges for ATAC-seq application. If available, we prefer to collect 15,000 nuclei as we

obtain more reproducible results than for a lower number of nuclei. A lower number of nuclei may deliver noisy results probably due to the loss of nuclei during subsequent processing steps. As a control, naked DNA can be purified from another sample with the same number of nuclei using a commercial kit (e.g., QIAGEN, #69104).

10. Cycle number can be changed depending on the initial number of nuclei. Quantitative PCR can be used for determining cycle number [11].

Acknowledgments

We would like to thank Daniel Schubert (Freie Universität Berlin, Germany) for providing reagents. Library preparation and next-generation sequencing were carried out by David Ibberson (The CellNetworks Deep Sequencing Core Facility, Heidelberg University, Germany). Nucleus sorting was carried out by Monika Langlotz (Flow Cytometry and FACS Core Facility, ZMBH, Heidelberg University, Germany). We also thank Pablo Sanchez (GMI, Vienna, Austria) and Virginie Jouannet (Heidelberg University, Germany) for developing protocols. This work was supported by the European Research Council (ERC) through an ERC Consolidator grant [647148, PLANTSTEMS to T.G.], the Deutsche Forschungsgemeinschaft [DFG, through a Heisenberg Professorship GR2104/5-2 and the SFB1101 to T.G.], a postdoctoral fellowship of the Alexander von Humboldt-Stiftung [3.5-JPN −1164674-HFST-P to D.S.], the Japan Society for the Promotion of Science [JSPS Overseas Research Fellowships 201960008 to D. S.], a Japan Science and Technology Agency grant [PRESTO: JPMJPR2046 to D.S.].

References

1. Brady SM, Orlando DA, Lee JY et al (2007) A high-resolution root spatiotemporal map reveals dominant expression patterns. Science 318(5851):801–806
2. Birnbaum K, Shasha DE, Wang JY et al (2003) A gene expression map of the Arabidopsis root. Science 302(5652):1956–1960
3. Galbraith DW, Harkins KR, Maddox JM et al (1983) Rapid flow cytometric analysis of the cell cycle in intact plant tissues. Science 220(4601):1049–1051
4. Deal RB, Henikoff S (2010) A simple method for gene expression and chromatin profiling of individual cell types within a tissue. Dev Cell 18(6):1030–1040
5. Zhang C, Gong FC, Lambert GM et al (2005) Cell type-specific characterization of nuclear DNA contents within complex tissues and organs. Plant Methods 1(1):7
6. Bajic M, Maher KA, Deal RB (2018) Identification of open chromatin regions in plant genomes using ATAC-Seq. Methods Mol Biol 1675:183–201
7. Shi D, Jouannet V, Agusti J et al (2021) Tissue-specific transcriptome profiling of the Arabidopsis thaliana inflorescence stem reveals local cellular signatures. Plant Cell 33(2):200–223
8. Wallner E-S, Tonn N, Shi D et al (2023) OBERON3 and SUPPRESSOR OF MAX2 1-LIKE proteins form a regulatory module

driving phloem development. Nat Commun 14:2128.

9. Picelli S, Bjorklund AK, Faridani OR et al (2013) Smart-seq2 for sensitive full-length transcriptome profiling in single cells. Nat Methods 10(11):1096–1098
10. Picelli S, Faridani OR, Bjorklund AK et al (2014) Full-length RNA-seq from single cells using Smart-seq2. Nat Protoc 9(1):171–181
11. Buenrostro JD, Giresi PG, Zaba LC et al (2013) Transposition of native chromatin for fast and sensitive epigenomic profiling of open chromatin, DNA-binding proteins and nucleosome position. Nat Methods 10(12): 1213–1218
12. Buenrostro JD, Wu B, Chang HY et al (2015) ATAC-seq: a method for assaying chromatin accessibility genome-wide. Curr Protoc Mol Biol 109:21 29 21–21 29 29
13. Sunaga-Franze DY, Muino JM, Braeuning C et al (2021) Single-nucleus RNA sequencing of plant tissues using a nanowell-based system. Plant J 108(3):859–869
14. Thibivilliers S, Anderson D, Libault M (2020) Isolation of plant root nuclei for single cell RNA sequencing. Curr Protoc Plant Biol 5(4):e20120
15. Picelli S (2017) Single-cell RNA-sequencing: the future of genome biology is now. RNA Biol 14(5):637–650
16. Islam S, Zeisel A, Joost S et al (2014) Quantitative single-cell RNA-seq with unique molecular identifiers. Nat Methods 11(2):163–166
17. Misra CS, Santos MR, Rafael-Fernandes M et al (2019) Transcriptomics of Arabidopsis sperm cells at single-cell resolution. Plant Reprod 32(1):29–38
18. Martin M (2011) Cutadapt removes adapter sequences from high-throughput sequencing reads. EMBnet.journal 17(1):10–12



Chapter 6

Quantification of Xylem-Specific Thermospermine-Dependent Translation of *SACL* Transcripts with Dual Luciferase Reporter System

Anna Solé-Gil, Cristina Úrbez, Alejandro Ferrando, and Miguel A. Blázquez

Abstract

Thermospermine (Tspm) is a polyamine found to play a crucial role in xylem development in *Arabidopsis thaliana*. Tspm promotes the translation of the *SACL* genes by counteracting the activity of a *cis* element in their 5′-leader region that suppresses the translation of the main ORF. Here we describe a method to test the Tspm-dependent translational regulation of the 5′-leader of the *SACL* mRNAs in *Nicotiana benthamiana* leaves and *A. thaliana* mesophyll protoplasts with a dual luciferase assay. The dual luciferase reporter system is used to assess gene expression and is based on the detection of the *Firefly* luciferase luminescence driven by a specific promoter. However, it can also be used to evaluate the *cis* elements found in 5′-leader that influence the translation of the main ORF in a transcript. We have used a modified version of the pGreenII 0800 LUC plasmid carrying a double 35S promoter, followed by a poly-linker sequence in phase with the *Firefly* luciferase gene (pGreen2x35SLUC) where the full 5′-leader sequence of *SACL3* was cloned. This construct was used for *Agrobacterium tumefaciens* infiltration of *N. benthamiana* leaves and for transfection *of A. thaliana* mesophyll protoplasts, followed by mock or Tspm treatments. The resulting translation of the *Firefly* luciferase in these organisms and conditions was then tested by measuring luminescence with the dual luciferase assay and a luminometer. These experiments have allowed us to quantify the positive effect of Tspm in the translation of *SACL3* transcripts.

Key words Thermospermine, Xylem vessel element, 5′-leader region (5′-leader), Upstream open reading frame (uORF), Posttranscriptional regulation, Dual luciferase reporter system, SACL group-XIV bHLH transcription factors, Protoplast, *Arabidopsis thaliana*, *Nicotiana benthamiana*

1 Introduction

Thermospermine is a tetraamine involved in the regulation of xylem cell proliferation and differentiation in *Arabidopsis thaliana* [1], widely present in the whole plant lineage [2, 3]. It is synthesized by the Tspm synthase encoded by *ACAULIS5 (ACL5)* in the precursor cells of vessel elements, where it has been proposed to prevent premature cell death [4]. Tspm also regulates cell proliferation at the vascular cambium by promoting the translation of a group XIV

Javier Agusti (ed.), *Xylem: Methods and Protocols*, Methods in Molecular Biology, vol. 2722,
https://doi.org/10.1007/978-1-0716-3477-6_6,
© The Author(s), under exclusive license to Springer Science+Business Media, LLC, part of Springer Nature 2024

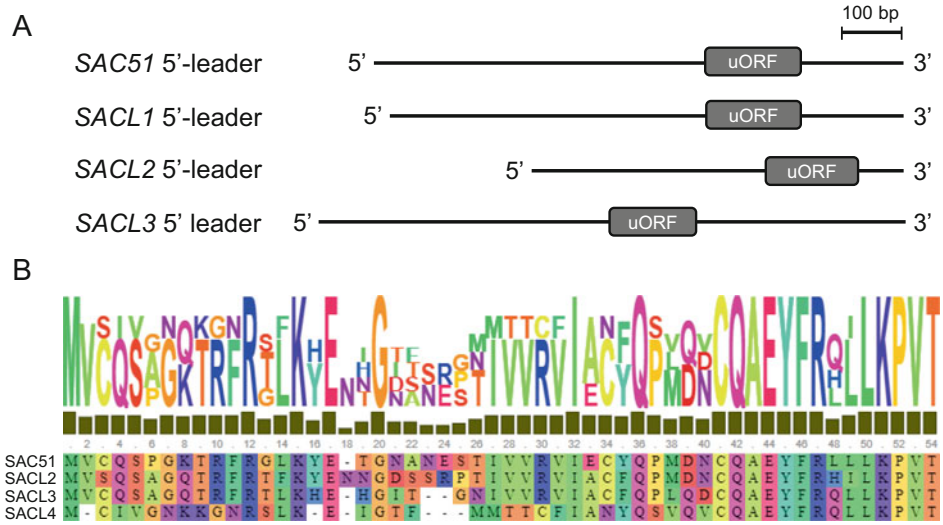


Fig. 1 5′-leader sequences of group XIV bHLH transcription factors of *A. thaliana*. (**a**) Schematic representation of the structure and size of the 5′-leader of the four *SACL* genes, indicating the position of the uORF. (**b**) Putative peptides encoded by the uORFs of the four *SACL* genes and consensus sequence. Note the conservation of the terminal third of the peptide

bHLH transcription factors of the SUPRESSOR OF ACAULIS LIKE (SACL) family through the interaction with a *cis* element in the *SACL* transcript's 5′-leader sequence [5–8].

The *cis* element that regulates the translation of *SACL* consists of an upstream open reading frame (uORF), which operates as other previously identified uORFs [9]. Some uORFs have stalling sequences that prevent the ribosome from scanning the rest of the transcript and, therefore, inhibit the translation of the main ORF (mORF). This is probably the type of uORF present in the 5′--leader region of *SACL* transcripts, where a very highly conserved sequence can be found in the C-terminal end of the putative peptide encoded by the uORF. *A. thaliana* harbors 4 *SACL* genes in its genome that belong to the clade XIV of bHLH transcription factors: *SAC51, SACL1, SACL2,* and *SACL3*, all carrying a conserved uORF in their 5′-leader sequences [8] (*see* Fig. 1). Here we describe a method for the quantification of the Tspm-dependent translation using a fusion of the 5′-leader of *SACL* transcripts to a dual luciferase reporter system using two Angiosperm species with two different approaches: transient expression using *Agrobacterium tumefaciens* in *Nicotiana benthamiana* leaves and protoplast transfection of *Arabidopsis thaliana* mesophyll cells.

Dual luciferase reporter system relies on the activity of two different enzymes, *Renilla* and *Firefly* luciferases, with different evolutionary origins and dissimilar substrates to be used upon the luminescent reaction [10]. For this protocol, we constructed the pGreen2x35SLUC plasmid (Addgene plasmid #108228), by

introducing a *Pst*I-blunt fragment including the 2x35S promoter sequence derived from plasmid pGJ1425 [11] and subcloned into plasmid backbone pGreenII0800-LUC [12] digested with *Pst*I-*Sma*I. The 35S promoter was introduced at the 5′ of the *Firefly* luciferase gene and separated by a window of 62 nucleotides with a polylinker sequence where the 5′-leader of the *AtSACL3* was cloned. This vector allowed us to quantify the translation of the *Firefly* luciferase upon Tspm treatments using as reference the *Renilla* luciferase under a constitutive 35S promoter, which was insensitive to Tspm treatments.

To perform the Tspm treatments, we used two different transient expression techniques. Transient expression can be easily achieved in *N. benthamiana* through agroinfiltration. However, Tspm treatments might be influenced by the Tspm produced in the leaves, where Tspm might be synthesized in continuously forming vascular bundles, as it is known to occur in *A. thaliana* leaves [13]. Alternatively, transient expression can also be achieved in protoplasts derived from *A. thaliana* mesophyll cells. With this approach, different mutant backgrounds of *A. thaliana* can also be tested, such as the *acl5-1* mutant with no Tspm production [14], to ensure a Tspm-free environment. The duration of Tspm treatments was established empirically to be optimal after 18 h in darkness at 23 °C.

After the treatments, translation efficiency can be estimated by measuring *Firefly* luciferase activity, normalized by *Renilla* luciferase activity (*see* Fig. 2).

2 Materials

Prepare all solutions using ultrapure water with a sensitivity of f 18 MΩ-cm at 25 °C and analytical grade reagents. All the solutions can be prepared and stored at room temperature (unless specified otherwise). Please note that some solutions must be prepared fresh.

2.1 Agroinfiltration of N. benthamiana Leaves and Tspm Treatment

1. Infiltration solution: 10 mM MES (prepared from stock solution of 1 M MES pH 5.6, adjusted with KOH), 10 mM $MgCl_2$ (prepared from stock solution of 1 M $MgCl_2$.), 1× acetosyringone (prepared from 500× stock solution. To prepare 1 mL: 20 mg/1 mL 100% Et0H and stored at −20 °C in darkness).
2. Liquid half-strength Gamborg's B5 medium with vitamins (to prepare 1 L solution: 1.58 g of Gamborg B5 medium including vitamins, 0.5 g MES, pH 5.7 adjusted with KOH), autoclaved, and complemented with either sterile water (for mock treatment) or 100 μM thermospermine (from 100 mM stock solution, diluted in sterile water).

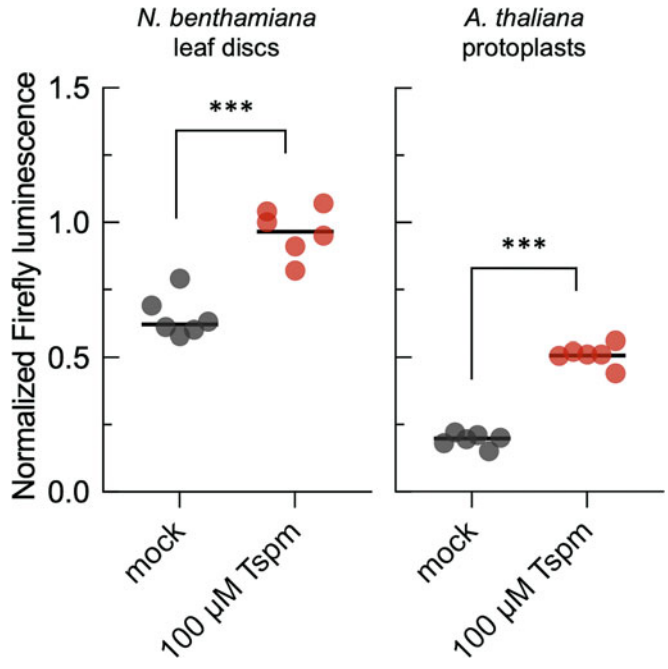


Fig. 2 Increase in translation of *Firefly* luciferase transcripts fused to the 5′-leader sequence of *SACL3* induced by Tspm treatments in *N. benthamiana* leaf discs and *A. thaliana* mesophyll protoplasts. A significant increase in luciferase activity after Tspm treatments was observed with both techniques. (***), *p*-value < 0.001

2.2 Protoplast PEG-Calcium Transfection

1. Enzyme solution: 20 mM MES (pH 5.7), 1.5% (w/v) cellulase R10, 0.4% (w/v) macerozyme R10, 0.5 M mannitol, and 1 mM KCl. Before adding the enzyme powder, warm the solution at 70 °C for 5 min. Warm the solution at 55 °C for 10 min to inactivate the DNAse and proteases, and enhance enzyme solubility. Cool it to room temperature and add 10 mM $CaCl_2$ and 0.1% of BSA. This solution must be prepared fresh.
2. WI solution: 4 mM MES (pH 5.7), 0.5 M mannitol, 20 mM KCl. For Thermospermine treatment, add either mock treatment (distilled water) or 100 µM Thermospermine (from stock solution 100 mM, diluted in sterile water).
3. W5 solution: 2 mM MES (pH 5.7), 154 mM NaCl, 125 mM $CaCl_2$, 5 mM KCl.
4. MMG solution: 4 mM MES (pH 5.7), 0.4 M mannitol, 15 mM $MgCl_2$.
5. PEG-calcium transfection solution: 40% (w/v) PEG4000 in distilled water, 0.2 M mannitol, 100 mM $CaCl_2$. Prepare this solution fresh 1 h in advance before utilizing.
6. 1% BSA solution in distilled water.

2.3 Luciferase Assay

1. Passive lysis buffer: From stock solution at 5× (Promega) diluted with distilled water.
2. Dual-Glo Luciferase solution: 10 mL Dual-Glo ® Luciferase buffer, 1 g Dual-Glo ® Luciferase Substrate and kept at −80 °C (*see* **Note 1**).
3. Dual-Glo Stop & Glo Solution: Dual-Glo® Stop & Glo® Buffer and Dual-Glo ® Stop & Glo® Substrate at 100×.

3 Methods

3.1 Agroinfiltration of N. benthamiana Leaves and Tspm Treatments

1. Pick one colony and prepare a 2-day old 5 mL culture in a 50 mL Falcon tube of *Agrobacterium* C58 carrying the pSOUP helper plasmid and the pGreen2x35SLUC plasmid with your 5′-leader sequence and another 5 mL culture of *Agrobacterium* C58 carrying a plasmid expressing the p19 silencing suppressor with antibiotics (*see* **Note 2**).
2. Centrifuge the liquid cultures for 10 min at 2500 rpm.
3. Discard the supernatant and resuspend the pellet with 10 mL of infiltration solution.
4. Leave in gentle sake at 28 °C in the dark for 2 h.
5. Measure the O.D. at 600 nm, and dilute your *A. tumefaciens* cultures at O.D. 0.5.
6. Leave in gentle sake at 28 °C in the dark for 1 h.
7. Prepare *A. tumefaciens* culture combinations with a final O.D. of 0.05 (for p19) and 0.1 (for the pGreen2x35SLUC plasmid and the pSOUP).
8. Agroinfiltrate the induced bacteria in the abaxial side of fully expanded *N. benthamiana* leaves creating various 2 cm diameter "infiltration spots" per leaf with a 1 mL syringe (*see* **Note 3**).
9. Let the infiltrated *N. benthamiana* plants rest for 2 days under continuous light at room temperature.
10. Prepare the treatment solutions with ½ strength Gamborg's B5 media containing either Mock treatment (water) or 100 μM thermospermine (*see* **Note 4**). The treatment is performed in a 12-well sterile plate, each well with 2 mL of treatment solution.
11. Collect 1 cm diameter leaf discs of the infiltration spots with the help of a puncher and introduce one single leaf disc per well, making sure that the abaxial part of the leaf touches the treatment solution.
12. Vacuum the 12-well plates for 15 min at room temperature.
13. Keep in dark for 18 h at 23 °C.

14. Collect the tissue in safe-lock 2 mL tubes containing 3–4 stainless steel beads and freeze in liquid nitrogen.
15. Grind the tissue in cold conditions with a sample miller (2× 30 s at 30,000 rpm) and keep the grinded sample at −80 °C until further analysis.

3.2 Protoplast PEG-Calcium Transfection and Tspm Treatments (This Protocol Has Been Adapted from [15])

1. Grow Arabidopsis plants for 3 weeks under short day conditions (13 h light at 23 °C and 11 h dark at 20 °C).
2. Select between 10–20 well-expanded leaves from plants that have not undergone flowering per treatment (six biological replicates are recommended).
3. Cut 0.5–1 mm leaf strips using a fresh sharp razor blade and transfer them quickly and gently into 4 mL of enzyme solution in a 30 mm diameter clean petri dish.
4. Vacuum the leaf strips for 30 min in the dark using a desiccator.
5. Continue the digestion, without shaking, in the dark for 2.5 h at room temperature.
6. Check the efficiency of protoplast production by analyzing 10 μL of the cell suspension under the microscope.
7. Add 4 mL of W5 solution to the protoplast solution.
8. Wash a 75 μm nylon mesh with water to remove ethanol (*see* **Note 5**), and filter the enzyme solution containing protoplasts into a 50 mL conical tube.
9. Centrifuge the flow-through at 100 *g* for 2 min.
10. Remove as much supernatant as possible, and resuspend the protoplasts with W5 solution (100 μL per biological replicate) with gentle swirling.
11. Maintain the protoplasts on ice for 30 min.
12. Remove the W5 solution as much as possible without disturbing the protoplast pellet that has been settled during the previous 30 min.
13. Resuspend the pellet with MMG solution (same as Subheading 3.2, **step 10**, 100 μL per replicate).
14. Add 10 μg of the pGreen2x35SLUC constructs (up tp 10 μL) in a 2 mL microfuge tube.
15. Add 100 μL protoplasts and mix gently.
16. Add 100 μL of PEG solution, and mix completely by gently tapping the tube.
17. Incubate the transfection mixture at room temperature for 15 min.
18. Dilute the mixture with 420 μL of W5 solution at room temperature and mix gently.

19. Centrifuge at 100 *g* for 2 min at room temperature and remove the supernatant.
20. Resuspend the protoplasts gently with 0.5 mL of WI solution, and transfer to a 12-well that has been previously coated with 1% BSA solution.
21. Add mock and Tspm 100 μM treatments (from 1000× stock solutions).
22. Incubate the protoplasts in the dark at 23 °C for 18 h.
23. Resuspend the protoplasts and harvest by centrifugation in 1.5 microfuge tubes at 100 *g* for 2 min.
24. Remove the supernatant and freeze samples with liquid nitrogen. Keep at −80 °C until further analysis.

3.3 Dual Glo Luciferase Assay

1. Add passive lysis buffer to the samples (for *N. benthamiana* 150 μL, for *A. thaliana* protoplasts 100 μL) and vortex vigorously until the sample is completely resuspended in the buffer. Keep the samples on ice until all the samples are processed.
2. Centrifuge in a microcentrifuge at 13,500 rpm for 5 min at 4 °C.
3. Thaw the Dual-Glo Luciferase solution on ice in the dark, and add 40 μL per sample into a white 96 well microplate for luminometer reading.
4. Add 5 μL of the supernatant into the well containing 40 μL of Dual-Glo Luciferase solution per sample.
5. Let the 96 well microplate sit in the dark for 10 min at room temperature.
6. Record the *Firefly* luminescence of the plate (3 readings; Integration time, 10 s; Period, 3 min).
7. Calculate the amount of the Dual-Glo Stop & Glo solution needed (40 μL per sample), and prepare it fresh.
8. Add 40 μL Dual-Glo Stop & Glo solution to every well containing the Dual-Glo luciferase solution.
9. Let the 96-well microplate sit in the dark for 10 min at room temperature.
10. Read the *renilla* luminescence of the plate (3 readings, integration time 10 s, period 3 min).
11. Calculate the translation of the *Firefly* luciferase by normalizing the luminescence value of the *Firefly* luciferase with the *renilla* value.

4 Notes

1. Prepare small aliquots of the Dual Glo Luciferase solution and store at −80 °C. This solution degrades easily with thawing, so avoid reusing this solution more than 2 times.
2. Only use fresh cultures started from single colonies in solid plates; otherwise, the efficiency of the agroinfiltration will decrease significantly.
3. Only use fully expanded leaves for agroinfiltration. One leaf can be used for several biological replicates with independent infiltration points. When collecting the replicates, avoid collecting tissues with a high density of veins. The optimal number of biological replicates per treatment and combination is 12.
4. Tspm is degraded quickly, so keep the Tspm stock solution on ice during the whole time required for the preparation of the treatment solutions, and keep it at −20 °C as soon as the solutions are made. Prepare small aliquots of stock solutions to prevent damage by freezing and thawing.
5. The 75 μm nylon mesh can be washed with distilled water and kept in 70% ethanol for future uses.

Acknowledgments

We thank Javier Agustí (IBMCP, Valencia) for critical input on the manuscript and useful suggestions. MAB also acknowledges grant PID2019-110717GB-I00, funded by Spanish MCIN/AEI/10.13039/501100011033. ASG is the recipient of the Fellowship of the Spanish Ministry of Science, Innovation and Universities (BES-2017-080387).

References

1. Vera-Sirera F, Minguet EG, Singh SK et al (2010) Role of polyamines in plant vascular development. Plant Physiol Biochem 48:534–539
2. Minguet EG, Vera-Sirera F, Marina A et al (2008) Evolutionary diversification in polyamine biosynthesis. Mol Biol Evol 25:2119–2128
3. Solé-Gil A, Hernández-García J, López-Gresa MP et al (2019) Conservation of thermospermine synthase activity in vascular and non-vascular plants. Front Plant Sci 10:663
4. Muñiz L, Minguet EG, Singh SK et al (2008) ACAULIS5 controls *Arabidopsis* xylem specification through the prevention of premature cell death. Development 135:2573–2582
5. Vera-Sirera F, De Rybel B, Urbez C et al (2015) A bHLH-based feedback loop restricts vascular cell proliferation in plants. Dev Cell 35:432–443
6. Imai A, Hanzawa Y, Komura M et al (2006) The dwarf phenotype of the *Arabidopsis acl5* mutant is suppressed by a mutation in an upstream ORF of a bHLH gene. Development 133:3575–3585
7. Cai Q, Fukushima H, Yamamoto M et al (2016) The *SAC51* family plays a central role in thermospermine responses in Arabidopsis. Plant Cell Physiol 57:1583–1592

8. Ishitsuka S, Yamamoto M, Miyamoto M et al (2019) Complexity and conservation of thermospermine-responsive uORFs of *SAC51* family genes in angiosperms. Front Plant Sci 10:564
9. Morris DR, Geballe AP (2000) Upstream open reading frames as regulators of mRNA translation. Mol Cell Biol 20:8635–8642
10. Sherf BA, Navarro SL, Hannah RR et al (1996) Dual-luciferase reporter assay: an advanced co-reporter technology integrating firefly and Renilla luciferase assays. Promega Notes 57:02
11. Jach G, Binot E, Frings S, Luxa K et al (2001) Use of red fluorescent protein from *Discosoma* sp. (dsRED) as a reporter for plant gene expression. Plant J 28:483–491
12. Hellens R, Allan A, Friel EN et al (2005) Transient expression vectors for functional genomics, quantification of promoter activity and RNA silencing in plants. Plant Methods 1:13
13. Baima S, Forte V, Possenti M, Peñalosa A et al (2014) Negative feedback regulation of auxin signaling by ATHB8/ACL5-BUD2 transcription module. Mol Plant 7:1006–1025
14. Kakehi J, Kuwashiro Y, Niitsu M et al (2008) Thermospermine is required for stem elongation in *Arabidopsis thaliana*. Plant Cell Physiol 49:1342–1349
15. Yoo SD, Cho YH, Sheen J (2013) *Arabidopsis* mesophyll protoplasts: a versatile cell system for transient gene expression analysis. Nat Protoc 2:1565–1572



Chapter 7

Fossil Wood Analyses: Several Examples from Five Case Studies in the Area of Central and NW Bohemia, Czech Republic

Jakub Sakala

Abstract

In the area of the Central and NW Bohemia, Czech Republic, the fossil wood is quite abundant, found in different states of preservation and present from Paleozoic (Pennsylvanian), through Mesozoic (Upper Cretaceous), to Cenozoic (upper Eocene to lower Miocene). So, this small area is ideal to demonstrate various aspects of the fossil wood analyses, including anatomy (*unifacial vs. bifacial cambium*, *formation of tyloses and its significance*, *early vs. late wood*, *unambiguity of scientific terminology*, *stem vs. root wood*), taphonomy (*completeness of fossil record*, *influence of environment on mode of preservation*, *influence of preservation on wood anatomy and preservation potential*, *discrepancy between the record of wood and other organs*), systematics (*stem vs. crown group*, *wide concept of fossil wood genera*, "*mosaic" species*, *wood of extinct plants*), and palaeoclimatic reconstruction (*definition of "wood type," subjective vs. objective methods*). The majority of the studied woods were thin-sectioned following the standard techniques and observed with a compound light microscope.

Key words Fossil wood, Paleozoic, Mesozoic, Cenozoic, Bohemian Massif, Czech Republic

1 Introduction

Fossil wood, thanks to its robust nature, is both abundant and numerous in the fossil record, and it represents an important component of the plant fossils [1]. Its significance in the development of the palaeobotany is well illustrated by the fact that even Count Kaspar Maria von Sternberg in 1820 dealt intensively with the so-called "tree of the deluge" from Jáchymov/*Joachimsthal* [2] on the very first page of his monumental work *Flora der Vorwelt* [3], which is considered today as the starting point of modern palaeobotany [4]. Sternberg mainly underlines the importance of the wood from Jáchymov for understanding of the fossilization process as such. Palaeoxylotomy, as we can label the science study-

Javier Agusti (ed.), *Xylem: Methods and Protocols*, Methods in Molecular Biology, vol. 2722,
https://doi.org/10.1007/978-1-0716-3477-6_7,
© The Author(s), under exclusive license to Springer Science+Business Media, LLC, part of Springer Nature 2024

ing the fossil wood, becomes progressively, thanks to its brilliant representatives as, for example, professors Heinrich Göppert (1800–1884), Richard Kräusel (1890–1966), or Édouard Boureau (1913–1999), an integral part of the palaeobotany [5]. Nowadays, besides purely systematical studies, the fossil wood is often used for the palaeoclimate reconstruction, for example, [6], or to get other more general pieces of information from the geological history.

The area of the Central and NW Bohemia, Czech Republic has been intensively explored. The first palaeobotanical data were published already by Sternberg, but the overall systematic research started there in the second half of the nineteenth century and has continued until present. Palaeobotanical data are based there on different plant organs as fossil leaves, fruits and seeds, or wood. Concerning the fossil wood, it is found in different states of preservation; it is quite abundant and also present from Paleozoic (Pennsylvanian), through Mesozoic (Upper Cretaceous), to Cenozoic (upper Eocene to lower Miocene). Hence, this rather small area seems to be ideal to demonstrate various, sometimes unexpected, aspects of the fossil wood analyses, based on personal experience during standard palaeobotanical research. The present chapter summarizes my scientific trajectory over the last 25 years, including unpublished results [7, 8]. Majority of woods presented hereafter were thin-sectioned following the standard techniques and observed with a compound light microscope, which remains practically unchanged for almost 200 years from the times of Henry T. M. Witham [9]. A small part of the woods, mainly xylitic and charcoalified ones, were then observed under SEM.

2 Paleozoic Woods

Paleozoic is probably the most important era regarding the evolution of the wood and different growth forms in general. The first wood (secondary xylem) appears already in Early Devonian [10], but the plants with tree habit came only later. The oldest representatives of arborescent forms are members of Pseudosporochnales from Middle Devonian (*Gilboa tree*); they are systematically close to the ferns, but they had no leaves yet, only branches with 3D terminal appendages and limited root system. The first modern trees with leaves, long-lived branches, and roots and bifacial cambium appeared in Middle/Late Devonian, and they are connected with "progymnosperms" and the genus *Archaeopteris* [11, 12]. Generally, the main growth forms in plants are present already in Mississippian [13].

2.1 Case Study 1: Kladno-Rakovník Basin

Kladno-Rakovník Basin belongs to the upper Paleozoic of the Central and Western Bohemia. Recently, the fossil wood was described there by J. Holeček in his Master Thesis and the consecutive publications [14–16], partly also by J. Bureš from the systematic point of view [17, 18] and P. Matysová in her PhD Thesis from mineralization perspective [19]. Traditionally, the lithological content is divided into four Formations, two of them are "Grey" ("Lower Grey" Kladno Fm., "Upper Grey" Slaný Fm.) and two "Red" ("Lower Red" Týnec Fm., "Upper Red" Líně Fm.), which alternate mutually [20]. The most recent overview, within the European context, with modified dating and stratigraphy [21], shows that the youngest Líně Formation, where the fossil woods are the most abundant, crosses the Carboniferous/Permian boundary. The silicified calamitalean stems, which are discussed in the following part, are then found in the Týnec Formations, and partly also in Líně Formation [14, 15].

2.1.1 Completeness of Fossil Record

The fact that the fossil record is incomplete is emphasized from Darwin's times till now as the main limitation of the palaeontology when reconstructing the evolution of life and the systematic relations between different organisms, for example, [5, 22]. In spite of this objective fact, the incompleteness of the fossil record is sometimes overestimated and the paucity of own finds is often used as an excuse for lack of any new research. A good opportunity how to get a unique material, which was proved in Kladno-Rakovník Basin and also elsewhere, is to establish a close cooperation with collectors. Thanks to such a relation, full of mutual respect, it was possible for Holeček [14] and also for Mencl [15] to confirm that the fossil wood is generally present in all four formations, but mainly to get and describe calamitalean stems, which would otherwise remain unknown to the broad scientific community.

2.1.2 Unifacial vs. Bifacial Cambium

Contrary to the modern trees and shrubs (lignophytes) with bifacial cambium and indeterminate secondary growth, see in [23–25], the arborescent calamitaleans belongs to the group of secondary growing plants with unifacial cambium, that is, anticlinal divisions add no new initials to the cambium, which is closed, so the tree diameter is limited producing only a small amount of wood. Despite this apparent restriction, the calamitalean stems from Kladno-Rakovník Basin reach diameter of several decimeters or even more than 0.6 m (F. Jech, pers. comm. 2015), which exceeds the largest diameter recorded so far in *Arthropitys ezonata* [26]. This finding follows up the results of R. Rößler's team from Chemnitz [26, 27], which mentioned great amount of wood or unusual type of branching in early Permian members of the fossil species *Arthropitys ezonata* and *A. bistriata*. This only faces the traditional "textbook" perception of life and architecture of arborescent calamitaleans, which must partially be revised (compare in [28], p. 399).

2.1.3 Influence of Environment on Mode of Preservation

Almost all (per)mineralized Paleozoic woods of the Bohemian Massif, maybe with the exception of several unique layers as silicified peats, originated in fluvial or lacustrine environment without any influence of volcanism sensu [29] and they were somehow transported. As a result, no extraxylary tissue, outside of the cambium, is preserved, so the samples are chiefly decorticated, formed by secondary xylem alone. This phenomenon, which also concerns the above-described calamitaleans, represents some limitation regarding the potential interpretation of branching and other details of the trunk architecture. On the other hand, such generally long and resistant logs can be correlated for long distances and more general conclusions on tectonics, sedimentation, and palaeoclimate can be established based on them, for example, [30].

3 Mesozoic Woods

Concerning the evolution of plants, the Mesozoic represents a transitional period, when the "pteridophytes" decline and many extant and extinct groups among "gymnosperms," the wood of which has often an unusual combination of features from today's point of view, for example, [31], are in progress. We can cite here several examples as the problematical fossil genus *Xenoxylon* [32, 33], artificial group of conifers Protopinaceae [34, 35], or extinct family Cheirolepidiaceae [36]. At the end of Mesozoic, throughout Cretaceous, a new group originated and diversified to take complete control over the following period – angiosperms.

3.1 Case Study 2: Bohemian Cretaceous Basin

Bohemian Cretaceous Basin is the largest intracontinental basin of the Bohemian Massif, Late Cretaceous in age, originated in one sedimentary cycle (Cenomanian to Santonian), forming a narrow Seaway between the North Sea Basin and the Tethys Ocean during that time [37]. In the lower part, in the Peruc-Korycany Formation, there is some terrestrial influence with the well-known Cenomanian flora; for summary, see [38]. As for the fossil wood, probably the first detailed anatomical description was that of the angiosperm genus *Bridelioxylon* from the middle Turonian locality Bílé Horky near Louny [39]. A similar type of wood was described from the Cenomanian of the locality Pecínov as *Paraphyllanthoxylon* [40]. There are also charcoalified woods, both conifers and angiosperms, for example, [41–43], and several anatomically undescribed silicified woods, related either to coniferous *Cupressinoxylon* [41], angiosperm *Paraphyllanthoxylon* or bennettitalean trunks of *Cycadeoidea*-type [44].

3.1.1 Formation of Tyloses and Its Significance

Tyloses represent a standard physiological process, typically in the angiosperm heartwoods, related to low water content or injury [45]. The abundance of tyloses in *Paraphyllanthoxylon* was already

discussed [46], and the tyloses are present in *Paraphyllanthoxylon* from Pecínov in all anatomical sections as well. The tyloses are formed not only in standing living tree in heartwood, but also in samples taken from sapwood, for example, [47] for *Quercus rubra*, depending on the moment of sampling and temperature of storing, or they can also be formed in felled trees without "true coloured" heartwood, as observed in *Fagus sylvatica* under slow desiccation and specific temperature 15–40 °C [48]. Given the specificity of fossil record, it is hard to say whether our fossil wood represented heartwood or sapwood, but we think, thanks to a big amount of tyloses formed, that our fossil represents true heartwood. A nice summary on tylosis formation, including the oldest fossil evidence in permineralized wood of the (pro)gymnosperm, was recently presented [49].

3.1.2 Stem vs. Crown Group

The woods of *Paraphyllanthoxylon* correspond systematically to several botanical families; compared in [40]. Our Cenomanian wood is close to the Lauraceae; moreover, in Pecínov, there are more representatives of this family [50], including some charcoalified woods, which were thought to be also lauraceous [42]. However, an important feature typical of Lauraceae is lacking: there are no idioblasts in the wood, that is, inflated oil or mucilage cells; see in [51]. Alternative explication of the absence of idioblasts, supported also by J. A. Doyle (pers. comm. 2008), lies in the possibility that the Cenomanian lauraceous plants belonged to the stem lineage, which does not show yet all features typical of the modern representatives of Lauraceae, from the so-called crown group, for example, [52], p. 176. This conceptual framework can explain the systematical position of other problematic taxa, which are not unambiguously attributable to any of the modern families, for example, *Doliostrobus* Marion; for summary, see [53].

3.1.3 Wide Concept of Fossil Wood Genera

Today, from the *Melbourne Code* [54] on, all taxa (including wood, but diatom taxa excepted), the name of which are based on fossil types, are recognized as "fossil-taxa." According to the European palaeoxylotomical tradition, the names of fossil wood genera are mainly created using the suffix *–xylon*, when the prefix mostly points to a family, sometimes even to one single genus, for example, *Laurinoxylon* is a wood of Lauraceae, *Quercoxylon* corresponds to an oak (*Quercus*). Concerning *Paraphyllanthoxylon* I. W. Bailey, it represents a typical example of the widely defined fossil genus, for example, [55], Table 4, which indicated 14 families with features of this genus. As a result, this fossil genus cannot be attributed to one single family, which is a kind of unusual situation in the hierarchical classification. It is also interesting that the generic diagnosis of *Paraphyllanthoxylon* completely overlaps the two younger generic diagnoses: *Burseroxylon* Prakash & Tripathi, see in [46], and

Canarioxylon Prakash et al., which was defined in [56] from the Lipnice Formation in Southern Bohemia; see discussion in [40]. These two fossil generic names can thus be considered as synonyms of the name *Paraphyllanthoxylon*.

4 Cenozoic Woods

In Cenozoic, mainly from Neogene onwards, the main part of woods recorded, conifers or angiosperms, present already the modern features and are comparable to extant genera, for example, [57] for "dicots". Beside the systematical research, in which we proceed, thanks to the comparison with the nearest living relatives (*NLR*), it is possible to use the fossil wood for reconstruction of palaeoclimate. There are mainly Wiemann et al.'s statistical model, based on physiognomy for "dicot" woods [6, 58, 59], and the so-called *Coexistence approach*, based on precise systematical attribution and depiction of the corresponding *NLR*s, for example, [60].

4.1 Case Study 3: Most Basin

The Tertiary of northwestern Bohemia is spread in the northwestern part of the Czech Republic as a continuous zone of magmatic and sedimentary complexes, parallel to the Czech-German boundary, linked to the Ohře Rift system. This zone is formed, from west to east, of the Cheb and Sokolov Basins, the Doupovské hory Mountains, the Most Basin, the České středohoří Mountains, and the Žitava Basin. The following three case-studies will progressively deal with Most Basin, České středohoří and Doupovské hory Mountains. The Most Basin, limited by Doupovské hory in W, Krušné hory in N and České středohoří in SE, is the largest from the so-called Krušné hory Piedmont Basins. The evolution of the Most Basin can be subdivided into six distinct phases related to tectonic and palaeoenvironmental changes: (1) the Central River, (2) the Floodplain and First Moors, (3) the Whole Basin Swamp, (4) the Local Lakes, (5) the Whole Basin Lake, and (6) the Swamp Rehabilitation phases [61]. The first phase started at the end of the Oligocene, and then the sedimentation continued throughout the early Miocene when the main fill of the basin, including the "Main Seam" and the richly fossiliferous overlying clays and sands, was deposited. The final stage occurred during the onset of the so-called Mid-Miocene Climatic Optimum [62], that is, during the end of the early Miocene [61]. Concerning the fossil wood research and palaeobotany in general, there is mainly locality Bílina with a unique combination of well-studied area with easy access, rich co-occurring plant remains [63], and, finally, also good scientific and personal cooperation. As a consequence, there are recently several publications, which deal with the fossil wood in a broader context [64–66].

4.1.1 Influence of Preservation on Wood Anatomy and Preservation Potential

Influence of environment on mode of the preservation was already discussed above (see Subheading 2.1.3). The influence of different types of preservation on the wood anatomy has been demonstrated in Bílina: The two specimens studied, (1) one mineralized by limonite and the other (2) coalified (xylitic), were very different from each other at first sight, especially in cross section [64], Fig. 2A vs. 2D. However, they have been interpreted as a single species of elm wood after a more detailed analysis. Another example is shrinkage; for general summary, see [67], or even qualitative change, for example, cross-field pitting; see [68], during (3) charcoalification, typical of the charcoals from Bílina [69] and elsewhere. Concerning the preservation potential in Most Basin, there is a clear impoverishment of fossil angiosperm wood. Almost all woods found in last decades belong to conifers; the hardwoods are represented by 2–3 types; for summary, see [7, 8], even though there must be over 100 species only in Bílina based on foliage and reproductive structures, many of them with secondary growth [63]. This discrepancy is to a great extent linked to the fact the plants often lived on acidic peat soils, where the conifer woods, mainly coalified ones, are more suitable to be preserved [70]. There is also a different preservation potential of particular organs of the same plant, for example, the lauraceous wood is more likely to enter the fossil record; see [71], p. 62. On the other hand, the lauraceous pollen disintegrates, so it practically does not enter the fossil record (R. Zetter, pers. comm. 2003).

4.1.2 "Mosaic" Species

In Bílina, the fossil wood is related to the elm foliage and samaras of *Ulmus pyramidalis* Goeppert [64]. This species is characteristic of riparian forests on *levées* along rivers. The same autecology is, in analogy, supposed for the fossil wood. On the other hand, the botanical affinities of the fossil wood, labelled as *Ulmoxylon marchesonii* Biondi, are not exactly the same as those of *U. pyramidalis*. In fact, the fossil elm of Bílina must be considered as a particular extinct species, a kind of "mosaic" where each part of the plant shows relationship to a different living relative and consequently as a specific fossil elm, which is, as a whole, different from all modern elms. This is a typical situation for Tertiary plants, which makes the search for the exact *NLR*s difficult.

4.1.3 Early vs. Late Wood

Identification of many (per)mineralized [65] and practically all xylitic [66, 72] conifer woods was obscured by the fact that the part of early wood was deformed. As a result, we could observe only the features in late wood, which, thanks to narrower tracheids, has different radial bordered pits, see [73], p. 239, and also cross-field pits [74]. Consequently, such (late) wood parts are not suitable for comparison with the typical published descriptions in atlases, etc, as usually published, based on the features from early wood.

Comparative studies of anatomical features, as they change within growth-ring among similar taxa, are rather rare, for example, [75], so the identification was accompanied by certain caution and some degree of uncertainty.

4.2 Case Study 4: České středohoří Mountains

The České středohoří Mountains is a complex of alkaline volcanites and intravolcanic deposits, such as diatomites, marls and volcanoclastics, which are often fossiliferous. A general summary, including the main literal sources, can be found in [76]. The age of České středohoří ranges from late Eocene to early Miocene, with the main activity in Oligocene. In 2003, a new subdivision into six levels was offered [77], reflecting the ecosystem change; in every level, it was proposed to regroup corresponding localities with typical floral elements and members of the ichthyofauna. The most recent overview of the fossil wood described so far both from České středohoří and Doupovské hory Mountains was recently published [78] with many fossiliferous localities, but the following part will only concern two of them: Kučlín and Divoká Rokle. The first locality of Kučlín is a relic of the volcanogenic complex on the top of the Trupelník Hill near Bílina. The deposit contains a richly fossiliferous diatomite with flora, fossil insects, crayfish, fish, and other vertebrates; see [79] and other papers in the same issue; and it represents a volcanic facies coeval with the fluvial settings of the Staré Sedlo Formation, late Eocene in age. I will focus on the unique 7.5-m-tall trunk, discovered in 1976 by F. Holý. This conifer wood was comprehensively studied [80]; later on, I studied that wood from the systematical point of view alone [81, 82]. The second locality, Divoká Rokle near the regional capital of Ústí nad Labem, was proposed as a parastratotype of the Ústí Formation [83], early Oligocene in age, and its origin is interpreted as a mud-flow deposit [84], with numerous small pieces of fossil wood. They were studied [85] and then published [86]. Most recently, two types of woods were reinterpreted as stem and root wood of the single fossil species [87].

4.2.1 Discrepancy Between the Record of Wood and Other Organs

The big, silicified trunk from Kučlín, originally identified as *Podocarpoxylon helmstedtianum* Gottwald and associated with extinct conifer *Doliostrobus* [80], was later reinterpreted as *Tetraclinoxylon vulcanense* Privé, related to the modern genus *Tetraclinis* Masters [81]. In the Tertiary of Europe, there are only two species of *Tetraclinis*, well defined by cones, seeds, and foliage: *T. brachyodon* (Brongniart) Mai & Walther and *T. salicornioides* (Unger) Z. Kvaček, the latter extending to western North America [88]. On the other hand, there are six species of *Tetraclinoxylon* Grambast, see in [89]. This discrepancy evokes the question if the species based on wood really represent natural species of *Tetraclinis*. Parallelly, the true botanical affinity of *Podocarpoxylon helmstedtianum* and several other species of *Podocarpoxylon* Gothan described

from the European Cenozoic, see in [90], Table 1, remains also uncertain: they are often compared to Podocarpaceae, for example, [60], but the only reliable macroscopic record of Podocarpaceae in the Cenozoic of Europe, other than wood, is the leaves of *Prumnopitys* Philippi, described from the Eocene of England [91].

4.2.2 Unambiguity of Scientific Terminology

When describing the anatomy of conifer woods, I always try to start with the generally accepted terminology, concretely [92], to avoid any potential misunderstanding. Unfortunately, some anatomical features, which are commonly used in the fossil wood description, are not defined there. As an example, we can cite the type of cross-field pitting "glyptostroboid" or "podocarpoid," with the latter being important for interpretation and comparison of the trunk from Kučlín [82]. Moreover, the existing definition of the podocarpoid type is ambiguous and it seems there are differences in interpretation between different xylotomical schools, specifically between German and French ones [93]; it is interesting that [94] came independently to the same conclusion.

4.2.3 Stem vs. Root Wood

A new find of an angiosperm wood from the locality Divoká rokle was related to another one, described earlier from the same locality as *Manilkaroxylon* sp. [86], and both samples were identified as a new fossil genus/species *Paradiospyroxylon kvacekii* Koutecký and Sakala, as its stem and root form, respectively [87]. A similar philosophy has already been applied in the case of two wood specimens from the Eocene of Dangu (France). They were also interpreted as two forms (stem vs. root) of the same species [95]. Such a general approach, which reflects individual variability, avoids artificial splitting of taxa and promotes a more natural concept in fossil wood classification.

4.3 Case Study 5: Doupovské Hory Mountains

The volcanic complex of the Doupovské hory Mountains is similarly to České středohoří linked to the activity of the Ohře Rift system and its today appearance is strongly influenced by denudation. Recently, a popular overviewing book was published [96], but there is no modern scientific synthesis, only separated papers, for example, [97–99]. Due to the presence of the military base in the central part of the Doupovské hory, the fossil record has mostly been studied in the peripheral part. There are interesting records of Oligocene mammals in the southern region, in the calcareous tuffites of Dvérce, Dětaň, and Valeč; see in [96]. Concerning the fossil wood, there are several papers published [78, 86, 100–102]. It is worth mentioning that the eastern part of the Doupovské hory, more specifically, the town of Kadaň and its nearest vicinity, which is Oligocene in age, represents the richest site for fossil wood in former Czechoslovakia as regards the diversity [103].

4.3.1 Wood of Extinct Plants

In Kadaň – Zadní vrch Hill, eight different types of angiosperm wood were recognized [100], including *Cercidiphylloxylon kadanense* Prakash et al., which has been later reviewed in detail [101]. The wood of *C. kadanense* represents the oldest record of the fossil wood of true *Cercidiphyllum* Siebold & Zuccarini because of its Oligocene age and the parallel occurrence of leaves, fruits, seeds, staminate inflorescences, and pollen of *Cercidiphyllum* in northwestern Bohemia, for example, [104]. All older cercidiphyllaceous woods, described so far, do not represent the wood of *Cercididiphyllum*, but most probably extinct *Cercidiphyllum*-like plants with similar leaves of *Trochodendroides* Berry emend. Crane, but different fruits of the *Nyssidium*-type. So, in other words, even if the vegetative organs as wood or foliage look the same in extinct and extant plant, the reproductive structures are always of primary importance in order to distinguish them. It is also difficult to depict the exact *NLR* in the case of an extinct type [105].

4.3.2 Definition of "Wood Type"

"*Wood type*" was delimited as the main operational unit for their palaeoclimatic model based on statistical evaluation of anatomical features of "dicot" woods, as "*. . .most often a genus, but it was occasionally a species or group of species if wood anatomical differences permitted such a separation*" [58]. Rather than an unambiguous definition, the authors offered the example for better understanding: 30 temperate North American species of the genus *Quercus* can be recognized as three "*wood types*": live, red, and white oaks; see [58], p. 85. In the systematical study of the woods from the Doupovské hory, I used that category as well [102], mainly for joining the wood that, as I supposed, belonged to one botanical type despite their original systematical attributions [100]. As a result, eight different types of angiosperm wood defined originally [100] were transformed into five wood types [102].

4.3.3 Subjective vs. Objective Methods of Palaeoclimatic Reconstruction

Methods of palaeoclimatic reconstruction based on fossil plants can be separated in two groups: those, which require the systematical attribution of the plants as, for example, *Coexistence approach* using *NLR* and those, which do not require it, mainly various types of physiognomic methods as *CLAMP* for leaves, or Wiemann et al.'s model cited above for wood [103]. Concerning the first type of methods, the scientific skill and experience of an investigator are really necessary for their correct application, so these methods are greatly "subjective." On the other hand, the physiognomic methods should rather be independent from the person, who does the palaeoclimatic reconstruction, so they can be classified as "objective." However, during the application of the "objective" Wiemann et al.'s statistical model, it seems there is still an important first "subjective" step, which requires an experienced xylotomist, that is, choice of the wood types. For instance, in German locality Rauscheröd, I choose 16 wood types, see [103], Table 1, from

22 described fossil species, see in [60], but another colleague can perform a different choice, which will subsequently change the calculated values, so a different palaeoclimate will be reconstructed. Unfortunately, in the richest site for fossil angiosperm wood in the Czech Republic (Kadaň) and its vicinity, there are only six well-defined *wood types* of fossil "dicots" [102], which is not sufficient for a correct application of that statistical model. A possible solution to get more wood types might be the use of a set of ecologically similar and coeval localities [106].

5 Conclusions

The ultimate objective of palaeobotany is to understand the entire organism – the whole fossil plant – and its evolution in time and space. However, in fossil record, the plants are present mostly disarticulated in isolated organs. The approach known today as the "whole plant" concept combines the detached organs in order to reconstruct the whole plant as it really looked like and lived in the past. I chose the area of the Central and NW Bohemia as the ideal one to illustrate the fossil wood analysis within the frame of this "whole plant" concept. In five case studies corresponding to five geological regions, ranging from Paleozoic to Cenozoic, I showed step by step fifteen practical aspects of palaeoxylotomical scientific work. In fact, my main goal was to introduce the specificity of the fossil wood analysis to the readers, who are not familiar with it.

References

1. Poole I, van Bergen PF (2006) Physiognomic and chemical characters in wood as palaeoclimate proxies. In: Rozema J, Aerts R, Cornelissen H (eds) Plants and climate change. Tasks for vegetation science, vol 41. Springer, Dordrecht. https://doi.org/10.1007/978-1-4020-4443-4_12
2. Dupéron J, Dupéron-Laudoueneix M, Sakala J, De Franceschi D (2008) *Ulminium diluviale* Unger: historique de la découverte et nouvelle étude. Ann Paléontol 94:1–12. https://doi.org/10.1016/j.annpal.2007.12.003
3. Sternberg KM (1820) Versuch einer geognostisch-botanischen Darstellung der Flora der Vorwelt I, 1. F. Fleischer, Leipzig
4. Kvaček Z (1982) Against the newly proposed starting point in palaeobotany. Taxon 31:319. https://doi.org/10.2307/1219999
5. Taylor TN, Taylor EL, Krings M (2009) Paleobotany: the biology and evolution of fossil plants, 2nd edn. Academic Press, Burlington
6. Wiemann MC, Manchester SR, Wheeler EA (1999) Paleotemperature estimation from dicotyledonous wood anatomical characters. PALAIOS 14:459–474. https://doi.org/10.2307/3515397
7. Sakala J (2004) The 'Whole-Plant' concept in palaeobotany with examples from the Tertiary of northwestern Bohemia, Czech Republic with particular reference to fossil wood. PhD thesis, Université Pierre-et-Marie Curie (Paris 6) and Charles University. http://web.natur.cuni.cz/ugp/main/staff/sakala/01-PhD_Thesis/
8. Sakala J (2015) Fossil wood and its importance in palaeobotanical research: case studies from the area of Central and NW Bohemia. Habilitation thesis, Charles University. (in Czech with English summary). http://web.natur.cuni.cz/ugp/main/staff/sakala/02-habilitace/

9. Noll R, Rössler R, Wilde V (2005) 150 Jahre *Dadoxylon* – Zur Anatomie fossiler Koniferen- und Cordaitenhölzer aus dem Rotliegend des euramerischen Florengebietes. Veröff Museum für Naturkunde Chemnitz 28:29–48
10. Strullu-Derrien C, Kenrick P, Badel E, Cochard H, Tafforeau P (2013) An overview of the hydraulic systems in early land plants. IAWA J 34:333–351. https://doi.org/10.1163/22941932-00000029
11. Meyer-Berthaud B, Decombeix A-L (2007) A tree without leaves. Nature 446:861–862. https://doi.org/10.1038/446861a
12. Meyer-Berthaud B, Decombeix A-L (2009) L'évolution des premiers arbres: les stratégies dévoniennes. C R Palevol 8:155–165. https://doi.org/10.1016/j.crpv.2008.08.002
13. DiMichele WA, Bateman RM (2005) Evolution of land plant diversity: major innovations and lineages through time. In: Krupnick GA, Kress WJ (eds) Plant conservation. A natural history approach. Chicago University Press, Chicago
14. Holeček J (2011) Late carboniferous silicified wood from the western part of Kladno-Rakovník Basin. Master thesis, Charles University. (in Czech with English abstract)
15. Mencl V, Holeček J, Rößler R, Sakala J (2013) First anatomical description of silicified calamitalean stems from the upper Carboniferous of the Bohemian Massif (Nová Paka and Rakovník areas, Czech Republic). Rev Palaeobot Palynol 197:70–77. https://doi.org/10.1016/j.revpalbo.2013.05.001
16. Mencl V, Bureš J, Sakala J (2013) Summary of occurrence and taxonomy of silicified *Agathoxylon*-type of wood in late Paleozoic basins of The Czech Republic. Folia Mus Rerum Nat Bohemiae Occid, Geol et Paleobiol 47:14–26
17. Bureš J (2011) Silicified cordaite and conifers wood in the sediments of the Líně formation of the Pilsen Carboniferous Basin. Erica 18:179–198. (in Czech with English abstract)
18. Bureš J (2013) Morphological-anatomical research of two large trunks of pycnoxylic woods (cordaitalean plants) from the Stephanian of Pilsen basin. Erica 20:179–190. (in Czech with English abstract)
19. Matysová P (2016) Study of fossil wood by modern analytical methods: case studies. PhD thesis, Charles University
20. Pešek J, Holub V, Jaroš J, Malý L, Martínek K, Prouza V, Spudil J, Tásler R (2001) Geology and deposits of the Upper Paleozoic limnic basins of The Czech Republic. Czech Geological Survey, Prague. (in Czech)
21. Opluštil S, Schmitz M, Cleal CJ, Martínek K (2016) A review of the Middle-Late Pennsylvanian west European regional substages and floral biozones, and their correlation to the Global Time Scale based on new U-Pb ages. Earth Sci Rev 154:301–335. https://doi.org/10.1016/j.earscirev.2016.01.004
22. Kutschera U, Niklas KJ (2004) The modern theory of biological evolution: an expanded synthesis. Naturwissenschaften 91:255–276. https://doi.org/10.1007/s00114-004-0515-y
23. Donoghue MJ (2005) Key innovations, convergence, and success: macroevolutionary lessons from plant phylogeny. Paleobiology 31:77–93. https://doi.org/10.1666/0094-8373(2005)031[0077:KICASM]2.0.CO;2
24. Spicer R, Groover A (2010) Evolution of development of vascular cambia and secondary growth. New Phytol 186:577–592. https://doi.org/10.1111/j.1469-8137.2010.03236.x
25. Hoffman LA, Tomescu AMF (2013) An early origin of secondary growth: *Franhueberia gerriennei* gen. et sp. nov. from the Lower Devonian of Gaspé (Quebec, Canada). Am J Bot 100:754–763. https://doi.org/10.3732/ajb.1300024
26. Rößler R, Noll R (2006) Sphenopsids of the Permian (I): the largest known anatomically preserved calamite, an exceptional find from the petrified forest of Chemnitz, Germany. Rev Palaeobot Palynol 140:145–162. https://doi.org/10.1016/j.revpalbo.2006.03.008
27. Rößler R, Feng Z, Noll R (2012) The largest calamite and its growth architecture – *Arthropitys bistriata* from the Early Permian Petrified Forest of Chemnitz. Rev Palaeobot Palynol 185:64–78. https://doi.org/10.1016/j.revpalbo.2012.07.018
28. Decombeix A-L, Boura A, Tomescu AMF (2019) Plant hydraulic architecture through time: lessons and questions on the evolution of vascular systems. IAWA J 40:387–420. https://doi.org/10.1163/22941932-40190254
29. Matysová P, Rössler R, Götze J, Leichmann J, Forbes G, Taylor EL, Sakala J, Grygar T (2010) Alluvial and volcanic pathways to silicified plant stems (Upper Carboniferous–Triassic) and their taphonomic and palaeoenvironmental meaning. Palaeogeogr Palaeoclimatol Palaeoecol 292:127–143. https://doi.org/10.1016/j.palaeo.2010.03.036

30. Trümper S, Mencl V, Opluštil S, Niemirowska S, Rößler R (2022) Large woody debris accumulations in the Late Pennsylvanian tropics—evolutionary signal or tectono-climatic archive? PALAIOS 37: 251–291. https://doi.org/10.2110/palo.2022.003
31. Philippe M, Bamford MK (2008) A key to morphogenera used for Mesozoic conifer-like woods. Rev Palaeobot Palynol 148:184–207. https://doi.org/10.1016/j.revpalbo.2007.09.004
32. Marynowski L, Philippe M, Zatoń M, Hautevelle Y (2008) Systematic relationships of the Mesozoic wood genus *Xenoxylon*: an integrative biomolecular and palaeobotanical approach. Neues Jahrb Geol Palaontol Abh 247:177–189. https://doi.org/10.1127/0077-7749/2008/0247-0177
33. Oh C, Philippe M, Kim K (2015) *Xenoxylon* synecology and palaeoclimatic implications for the Mesozoic of Eurasia. Acta Palaeontol Pol 60:245–256. https://doi.org/10.4202/app.2012.0132
34. Miller CN Jr (1977) Mesozoic conifers. Bot Rev 43:217–280
35. Philippe M (1992) Un déterminisme architectural pour les bois de conifères à ponctuation mixte (Protopinaceae Kraüsel, 1917)? Canad J Bot 70:1834–1839. https://doi.org/10.1139/b92-227
36. Alvin KL (1982) Cheirolepidiaceae: biology, structure and paleoecology. Rev Palaeobot Palynol 37:71–98. https://doi.org/10.1016/0034-6667(82)90038-0
37. Čech S (2011) Palaeogeography and stratigraphy of the bohemian cretaceous basin (Czech Republic) – an overview. Geol Res Moravia Silesia 18(1):18–21
38. Kvaček J, Uličný D, Svobodová M, Špičáková L (2006) Cretaceous of Central Bohemia. In: Fatka O, Kvaček J (eds) 7th European palaeobotany and palynology conference, Prague, excursions guide book. National Museum, Prague
39. Prakash U, Březinová D (1970) Wood of *Bridelia* from the cretaceous of Bohemia. Palaeobotanist 18(1969):173–176.
40. Gryc V, Vavrčík H, Sakala J (2009) Cenomanian angiosperm wood from the Bohemian Cretaceous Basin, Czech Republic. IAWA J 30:319–329. https://doi.org/10.1163/22941932-90000221
41. Falcon-Lang HJ, Kvaček J, Uličný D (2001) Fire-prone plant communities and palaeoclimate of a Late Cretaceous fluvial to estuarine environment, Pecínov quarry, Czech Republic. Geol Mag 138:563–576. https://doi.org/10.1017/S0016756801005714
42. Oakley D, Falcon-Lang HJ (2009) Morphometric analysis of Cretaceous (Cenomanian) angiosperm woods from The Czech Republic. Rev Palaeobot Palynol 153:375–385. https://doi.org/10.1016/j.revpalbo.2008.10.006
43. Greguš J, Kvaček J, Sakala J (2020) Charcoalified homoxylous woods from the Cenomanian of the Bohemian Cretaceous Basin (Czech Republic). Rev Palaeobot Palynol 282:104311. https://doi.org/10.1016/j.revpalbo.2020.104311
44. Novotný T (2022) Geological history of the Nové Strašecí area. Bílinská přírodovědná společnost z.s., Bílina. (in Czech)
45. Panshin AJ, de Zeeuw C (1980) Textbook of wood technology: structure, identification, properties, and uses of the commercial woods of the United States and Canada. McGraw-Hill, New York
46. Wheeler EA (1991) Paleocene dicotyledonous trees from Big Bend National Park, Texas: variability in wood types common in the Late Cretaceous and Early Tertiary, and ecological inferences. Am J Bot 78:658–671. https://doi.org/10.2307/2445087
47. Murmanis L (1975) Formation of tyloses in felled *Quercus rubra* L. Wood Sci Technol 9: 3–14
48. Jurášek L (1956) The origin of tyloses in beech wood. Drevársky výskum 1:7–15. (in Czech with English abstract)
49. Decombeix A-L, Harper CJ, Galtier J, Meyer-Berthaud B, Krings M (2022) Tyloses in fossil plants: new data from a Mississippian tree, with a review of previous records. Bot Lett 169:510–526. https://doi.org/10.1080/23818107.2022.2099461
50. Eklund H, Kvaček J (1998) Lauraceous inflorescences and flowers from the Cenomanian of Bohemia (Czech Republic, Central Europe). Int J Plant Sci 159:668–686. https://doi.org/10.1086/297585
51. Mantzouka D, Karakitsios V, Sakala J, Wheeler EA (2016) Using idioblasts to group *Laurinoxylon* species: case study from the Oligo-Miocene of Europe. IAWA J 37: 459–488. https://doi.org/10.1163/22941932-20160147
52. Judd WS, Campbell CS, Kellogg EA, Stevens PF, Donoghue MF (2007) Plant systematics: a phylogenetic approach, 3rd edn. Sinauer Associates, Inc, Sunderland
53. Kvaček Z (2002) Novelties on *Doliostrobus* (Doliostrobaceae), an extinct conifer genus

of the European Palaeogene. J Nat Mus Nat Hist Ser 171:131–175

54. McNeill J, Barrie FR, Buck WR, Demoulin V, Greuter W, Hawksworth DL, Herendeen PS, Knapp S, Marhold K, Prado J, Prud'homme van Reine WF, Smith GF, Wiersema JH, Turland NJ (eds) (2012) International code of nomenclature for algae, fungi, and plants (Melbourne Code): adopted by the Eighteenth International Botanical Congress Melbourne, Australia, July 2011, Regnum Vegetabile 154. Koeltz Scientific Books, Königstein
55. Thayn GF, Tidwell WD (1984) A review of the genus *Paraphyllanthoxylon*. Rev Palaeobot Palynol 43:321–335. https://doi.org/10.1016/0034-6667(84)90003-4
56. Prakash U, Březinová D, Awasthi N (1974) Fossil woods from the Tertiary of South Bohemia. Palaeontogr Abt B 147:107–123
57. Wheeler EA, Baas P (1993) The potentials and limitations of dicotyledonous wood anatomy for climatic reconstructions. Paleobiology 19:487–498. https://doi.org/10.1017/S009483730001410X
58. Wiemann MC, Wheeler EA, Manchester SR, Portier KM (1998) Dicotyledonous wood anatomical characters as predictors of climate. Palaeogeogr Palaeoclimatol Palaeoecol 139:83–100. https://doi.org/10.1016/S0031-0182(97)00100-4
59. Wiemann MC, Dilcher DL, Manchester SR (2001) Estimation of mean annual temperature from leaf and wood physiognomy. For Sci 47:141–149. https://doi.org/10.1093/forestscience/47.2.141
60. Böhme M, Bruch AA, Selmeier A (2007) The reconstruction of Early and Middle Miocene climate and vegetation in Southern Germany as determined from the fossil wood flora. Palaeogeogr Palaeoclimatol Palaeoecol 253:91–114. https://doi.org/10.1016/j.palaeo.2007.03.035
61. Mach K, Teodoridis V, Matys Grygar T, Kvaček Z, Suhr P, Standke G (2014) An evaluation of palaeogeography and palaeoecology in the Most Basin (Czech Republic) and Saxony (Germany) from the late Oligocene to the early Miocene. Neues Jahrb Geol Palaontol Abh 272:13–45. https://doi.org/10.1127/0077-7749/2014/0395
62. Mosbrugger V, Utescher T, Dilcher DL (2005) Cenozoic continental climatic evolution of Central Europe. PNAS 102:14964–14969. https://doi.org/10.1073/pnas.0505267102
63. Kvaček Z, Dvořák Z, Mach K, Sakala J (2019) Tertiary plants of the North-Bohemian brown-coal basin, 2nd edn. Bílinská přírodovědná společnost z.s. and Granit s.r.o, Bílina and Prague. (in Czech with English/German abstracts)
64. Sakala J (2002) First record of fossil angiosperm wood (*Ulmoxylon*, Ulmaceae) from the famous locality of Bílina (Czech Republic, Early Miocene). CR Palevol 1:161–166. https://doi.org/10.1016/S1631-0683(02)00025-8
65. Teodoridis V, Sakala J (2008) Early Miocene conifer macrofossils from the Most Basin (Czech Republic). Neues Jahrb Geol Palaontol Abh 250:287–312. https://doi.org/10.1127/0077-7749/2008/0250-0287
66. Havelcová M, Sýkorová I, Bechtel A, Mach K, Trejtnarová H, Žaloudková M, Matysová P, Blažek J, Boudová J, Sakala J (2013) "Stump horizon" in the Bílina Mine (Most Basin, Czech Republic)—GC–MS, optical and electron microscopy in identification of wood biological origin. Int J Coal Geol 107:62–77. https://doi.org/10.1016/j.coal.2012.09.008
67. Rößler R, Trümper S, Noll R, Hellwig A, Niemirowska S (2021) Wood shrinkage during fossilisation and its significance for studying deep-time lignophytes. Rev Palaeobot Palynol 292:104455. https://doi.org/10.1016/j.revpalbo.2021.104455
68. Gerards T, Damblon F, Wauthoz B, Gerrienne P (2007) Comparison of cross-field pitting in fresh, dried and charcoalified softwoods. IAWA J 28:49–60. https://doi.org/10.1163/22941932-90001618
69. Fischlová K (2012) Floristic associations of Miocene mires based on fuzite clasts study. Master thesis, Charles University. (in Czech)
70. Březinová D (1970) An overview of the fossil wood record from the territory of Czechoslovakia on the basis of the literature. Manuscript in National Museum, Prague. (in Czech)
71. Wheeler EA, Manchester SR (2002) Woods of the Middle Eocene Nut Beds Flora, Clarno Formation, Oregon, USA. IAWA J Suppl 3:1–188
72. Boudová J (2012) Study of xylitic wood of the Most Basin using the electron microscopy: systematics and palaeoenviroment. Master thesis, Charles University. (in Czech)
73. Bailey IW, Faull AF (1934) The cambium and its derivative tissues. IX. Structural variability in the redwood, *Sequoia sempervirens*, and its significance in the identification of fossil woods. J Arnold Arbor 15:233–254

74. Gromyko DV (1990) Comparative anatomical study of pits on the crossfields of wood of the Taxodiaceae family using scanning electron microscopy. Bot Zhurn 75:973–978. (in Russian)
75. Gromyko DV (1982) A comparative-anatomical study of wood in the family Taxodiaceae. Bot Zhurn 67:898–906. (in Russian with English abstract)
76. Kopecký L (2010) České středohoří Mts and ambient young alkaline volcanic complexes in the Ohře Rift, Czech Republic: volcanology, petrology and rift evolution. Czech Geological Survey, Prague
77. Kvaček Z, Walther H (2003) Reconstruction of vegetation and landscape development during the volcanic activity in the České středohoří mountains. Andean Geol 15:60–64
78. Koutecký V, Teodoridis V, Čáp P, Mantzouka D, Sakala J (2019) Fossil wood from the Doupovské hory and České středohoří volcanic complexes: latest overview and new angiosperms from the locality Dvérce. Neues Jahrb Geol Palaontol Abh 293:283–306. https://doi.org/10.1127/njgpa/2019/0842
79. Kvaček Z, Teodoridis V (2011) The Late Eocene flora of Kučlín near Bílina in North Bohemia revisited. Acta Mus Nat Pragae Ser B Hist Nat 67:83–144
80. Březinová D, Holý F, Kužvartová A, Kvaček Z (1994) A silicified stem of *Podocarpoxylon helmstedtianum* Gottwald, 1966 from the Paleogene site Kučlín (NW Bohemia). J Czech Geol Soc 39:221–234
81. Sakala J (2003) *Podocarpoxylon helmstedtianum* Gottwald from Kučlín (Late Eocene, Czech Republic) reinterpreted as *Tetraclinoxylon vulcanense* Privé. Feddes Repert 114:25–29. https://doi.org/10.1002/fedr.200390015
82. Sakala J (2011) Silicified stem from the Late Eocene fossil locality of Kučlín (Czech Republic): overview and new remarks. Acta Mus Nat Pragae, Ser B Hist Nat 67:145–148
83. Cajz V (2000) Proposal of lithostratigraphy for České středohoří Mts. volcanics. Bull Czech Geol Surv 75:7–16
84. Kratochvíl M (2007) Reconstruction of sedimentary processes and environment of volcanoclastic material of the Ústí Formation of the Českého středohoří Mts. Master thesis, Charles University. (in Czech)
85. Koutecký V (2014) Paleogene woods from the Doupovské hory and České středohoří Mts.: overview and new research. Master thesis, J E Purkyně University. (in Czech)
86. Koutecký V, Sakala J (2015) New fossil woods from the Paleogene of Doupovské hory and České středohoří Mts. (Bohemian Massif, Czech Republic). Acta Mus Nat Pragae Ser B Hist Nat 71:377–398
87. Koutecký V, Sakala J, Chytrý V (2023) *Paradiospyroxylon kvacekii* gen. et sp. nov. from the Paleogene of The Czech Republic: a case study of individual variability and its significance for fossil wood systematics. Hist Biol 35:1186–1196. https://doi.org/10.1080/08912963.2022.2084694
88. Kvaček Z, Manchester SR, Schorn HE (2000) Cones, seeds, and foliage of *Tetraclinis salicornioides* (Cupressaceae) from the Oligocene and Miocene of western North America: a geographic extension of the European Tertiary species. Int J Plant Sci 161:331–344. https://doi.org/10.1086/314245
89. Iamandei S, Iamandei E, Dumitrescu MS (2011) Petrified wood of *Tetraclinoxylon* from Căprioara Valley, Feleac, Cluj (Middle Miocene, Romania). Acta Palaeontol Roman 7:219–224
90. Pujana RR, Ruiz DP (2017) *Podocarpoxylon* Gothan reviewed in the light of a new species from the Eocene of Patagonia. IAWA J 38:220–244. https://doi.org/10.1163/22941932-20170169
91. Greenwood DR, Hill CR, Conran JG (2013) *Prumnopitys anglica* sp. nov. (Podocarpaceae) from the Eocene of England. Taxon 62:565–580. https://doi.org/10.12705/623.15
92. IAWA Committee (2004) IAWA list of microscopic features for softwood identification. IAWA J 25:1–70. https://doi.org/10.1163/22941932-90000349
93. Dolezych M, Sakala J (2007) Wood of *Doliostrobus* – *Podocarpoxylon* versus *Doliostroboxylon*. In: Dašková J, Kvaček J (eds) Palaeobotany – contributions to the evolution of plants and vegetation (recognizing the contribution of Zlatko Kvaček on the occasion of his 70th year). National Museum, Prague
94. Bamford MK, Philippe M (2001) Jurassic–Early Cretaceous Gondwanan homoxylous woods: a nomenclatural revision of the genera with taxonomic notes. Rev Palaeobot Palynol 113:287–297. https://doi.org/10.1016/S0034-6667(00)00065-8
95. Sakala J, Privé-Gill C, Koeniguer J-C (1999) Silicified angiosperm wood from the Dangu locality (Ypresian of the Gisors region, Eure, France): the problem of root wood. CR Acad Sci Ser IIA 328:553–557. https://doi.org/10.1016/S1251-8050(99)80138-4

96. Matějů J, Hradecký P, Melichar V (eds) (2016) Doupovské hory. Czech Geological Survey and Museum Karlovy Vary, Prague and Karlovy Vary. (in Czech)
97. Hradecký P (2003) New data on the Doupovské hory Cenozoic formations. Geosci Res Rep 36:21–22. (in Czech with English abstract)
98. Cajz V, Rapprich V, Radoň M (2006) Volcanics on the periphery of the Doupovské hory Mts. – a volcanological study of the Dětaň paleontological site. Geosci Res Rep 39:13–16. (in Czech with English abstract)
99. Rapprich V (2011) N-1 Valeč borehole: a searcher into the initial phase of the Doupovské hory Volcanic Complex. Geosci Res Rep 44:41–45. (in Czech with English abstract)
100. Prakash U, Březinová D, Bůžek Č (1971) Fossil woods from the Doupovské hory and České středohoří Mountains in Northern Bohemia. Palaeontogr Abt B 133:103–128
101. Sakala J, Privé-Gill C (2004) Oligocene angiosperm woods from northwestern Bohemia, Czech Republic. IAWA J 25:369–380. https://doi.org/10.1163/22941932-90000372
102. Sakala J, Rapprich V, Pécskay Z (2010) Fossil angiosperm wood and its host deposits from the periphery of a dominantly effusive ancient volcano (Doupovské hory Volcanic Complex, Oligocene-Lower Miocene, Czech Republic): systematics, volcanology, geochronology and taphonomy. Bull Geosci 85:617–629. https://doi.org/10.3140/bull.geosci.1196
103. Sakala J (2007) The potential of the fossil angiosperm wood to reconstruct the palaeoclimate in the Tertiary of Central Europe (Czech Republic, Germany). Acta Palaeobot 47:127–133
104. Kvaček Z, Konzalová M (1996) Emended characteristics of *Cercidiphyllum crenatum* (Unger) R. W. Brown based on reproductive structures and pollen in situ. Palaeontogr Abt B 239:147–155
105. Kvaček Z (2007) Do extant nearest relatives of thermophile European Cenozoic plant elements reliably reflect climatic signal? Palaeogeogr Palaeoclimatol Palaeoecol 253:32–40. https://doi.org/10.1016/j.palaeo.2007.03.032
106. Sakala J (2000) Silicified angiosperm wood from the Dangu locality (Ypresian of the Gisors region, Eure, France) – final part: the problem of palaeoclimate reconstruction based on fossil wood. Geodiversitas 22:493–507

Part III

Xylem Diseases



Chapter 8

Isolation and Reproductive Structures Induction of Fungal Pathogens Associated with Xylem and Wood Necrosis in Grapevine

Ana López-Moral and Carlos Agustí-Brisach

Abstract

Grapevine (*Vitis vinifera* L.) trunk diseases (GTDs) are considered a disease complex including five diseases: esca, Petri disease, black-foot disease, Botryosphaeria dieback, and Eutypa dieback. The main symptom is a general decline in affected plants, which show xylem necrosis and discoloration or sectorial necrosis in the wood. Their diagnosis is tedious due to four main reasons: (*i*) the wide diversity of internal symptoms that we can find; (*ii*) the great diversity of fungi that are associated with them; (*iii*) the high frequency of co-infections in the same plant; and (*iv*) the different behavior that the fungal species associated with GTDs show in vitro. Here, we describe a detailed protocol to isolate the different fungal trunk pathogens associated with GTDs as well as methods to induce sporulation and formation of fruiting bodies (pycnidia) to make easier their morphological characterization.

Key words Culture media, Diagnosis, Fungi, Morphology, *Vitis vinifera*

1 Introduction

Grapevine (*Vitis vinifera* L.) trunk diseases (GTDs) suppose one of the main limiting factors of this crop worldwide [1–3]. GTDs are considered a disease complex including five diseases that can occur alone or co-infecting the same plant: esca, Petri disease, black-foot disease, Botryosphaeria dieback, and Eutypa dieback. All of them cause general decline as unspecific external symptom, while each GTD develops specific internal symptoms in the trunk or roots of affected plants. In particular, esca shows white wood rot mainly in older vines; Botryosphaeria dieback and Eutypa dieback show sectorial wood necrosis on the arms and trunk; Petri disease results in necrosis and discoloration of xylem vessels; and black-foot disease causes root rot, showing black-brown areas in the rootstock [4]. In addition, a broad diversity of fungi has been described associated with each disease. Esca sensu stricto (*s.s.*) is caused by

Javier Agusti (ed.), *Xylem: Methods and Protocols*, Methods in Molecular Biology, vol. 2722,
https://doi.org/10.1007/978-1-0716-3477-6_8,
© The Author(s), under exclusive license to Springer Science+Business Media, LLC, part of Springer Nature 2024

basidiomycetous, with *Fomitiporia mediterranea* being the main causal agent. Botryosphaeria dieback is associated mainly with species belonging to the genera *Botryosphaeria*, *Diplodia*, *Dothiorella*, and *Neofusicoccum* (Ascomycota: Botryosphaeriaceae). *Eutypa lata* (Ascomycota: Diatrypaceae) is the main causal agent of Eutypa dieback. Petri disease is associated with *Cadophora luteo-olivacea*, *Phaeomoniella chlamydospora*, and a wide diversity of *Phaeoacremonium* species (Ascomycota). Petri disease pathogens are also associated with Esca complex disease co-infecting with basidiomycetes. Finally, "*Cylindrocarpon*" anamorphs (Ascomycota), that is, *Dactylonectria* spp. and *Ilyonectria liriodendri*, are the main fungi associated with black-foot disease [2, 4–7].

The diagnosis of GTDs is tedious for four main reasons: (*i*) the wide diversity of internal symptoms that can be found; (*ii*) the great diversity of fungi that are associated with GTDs; (*iii*) the high frequency of co-infections in the same plant; and (*iv*) the different behavior that the fungal species associated with GTDs show in vitro, including a wide range of mycelial growth rate (MGR; mm/day). The exploration of internal wood symptoms can serve as a first approach on the diagnosis. However, the isolation of all the fungi that could be causing the infection is difficult because co-infections of several fungal species associated with different GTDs often occur in the same plant. Consequently, valuable information for the diagnosis of GTDs can be lost if the fungal isolation protocol being carried out is not well-monitored. Therefore, here we describe a protocol to isolate trunk pathogens fungi from wood samples with the initial assumption that co-infections may be found in the processed samples. In addition, we describe methods to induce sporulation and formation of fruiting bodies (pycnidia) to make the morphological characterization of the main fungal family and genera associated with GTDs easier. An overview of the protocol described below is shown in Fig. 1. It is worth considering that the methods described here are also useful for fungal isolation and morphological characterization of fungal trunk pathogens from all woody plants, as they belong to the same families and genera regardless of the host.

2 Materials

2.1 Preparation of Culture Media

1. Laminar flow hood.
2. Distilled water.
3. Erlenmeyer flasks (2 L and 50 mL vol.)
4. Diverse solid media to isolate microorganisms: Prepared potato dextrose agar (PDA), malt extract agar (MEA) and agar (e.g., Sigma-Aldrich).

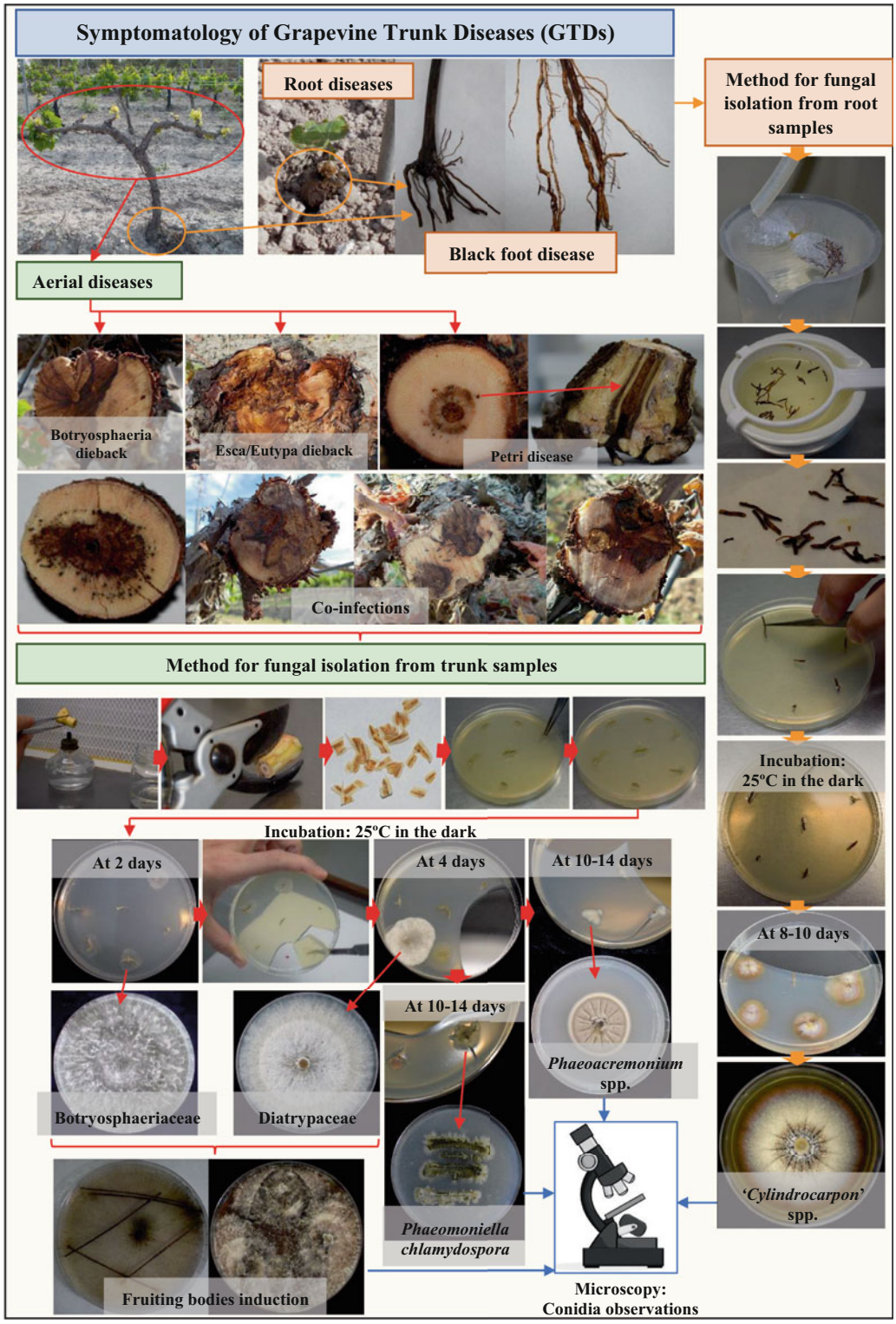


Fig. 1 Overview of the protocol for isolation of fungal trunk pathogens

5. Aluminum foil.
6. Autoclave.
7. Streptomycin sulfate (Sigma-Aldrich) to avoid bacterial contaminations (*see* **Note 1**).
8. Water bath.
9. Plastic Petri dishes (9 mm in diameter).
10. Fresh pine (*Pinus* spp.) needles (*see* **Note 2**).
11. Fresh pistachio (*Pistacia vera* L.) leaves (*see* **Note 3**).

2.2 Plant Material Preparation and Fungal Isolation

1. Laminar flow hood.
2. Lab tweezers.
3. Lab Scalpel.
4. Incubator (set at 23 ± 2 °C).
5. Parafilm®.
6. Labeled plastic bags (*see* **Note 4**).

Specific material to process trunk samples:

1. Knife.
2. Ethanol (70% solution in distilled water).
3. Lab burner for surface disinfection of trunk (wood) samples.
4. Pruning shears.

Specific material to process root samples:

1. Cheesecloth.
2. Plastic or glass beaker.
3. Mortar.
4. Metal or plastic strainer.
5. Sodium hypochlorite for surface disinfection of root tissues (20% solution in distilled water).
6. Sterile filter paper (sterilize using a Lab oven at 90 °C for 2 h).

3 Methods

3.1 Preparation of Culture Media for Fungal Isolation

Herein, two culture media for fungal isolation are described: antibiotic MEA and PDA. Carry out all procedures at room temperature into the laminar flow hood unless otherwise specified.

1. Introduce 1 L of distilled water into the 2 L Erlenmeyer flask.
2. Introduce the appropriate amount of each prepared solid media (PDA or MEA) into the Erlenmeyer flasks, and seal them with aluminum foil in the top.

3. For antibiotic solution preparation, add 10 mL of distilled water into a 50 mL Erlenmeyer flask, and seal with aluminum foil in the top.
4. Sterilize all the Erlenmeyer flasks at 120 °C for 20 min.
5. Incubate the Erlenmeyer flaks containing the culture media in the water bath (previously preconditioned at 45 °C) for 30 min.
6. Add the streptomycin sulphate (0.5 g/L of culture media) into the 50 mL Erlenmeyer flask, shake for 5 s (*see* **Note 5**), and pour it into the Erlenmeyer flask containing the culture media.
7. Homogenize the solution contained in the Erlenmeyer flask, and pour it into plastic Petri dishes.
8. After culture media solidification, store at 4 °C in the dark until use.

3.2 Fungal Isolation from Trunk Samples

1. Remove the bark from the wood cross sections with a knife, wash under running tap water, hold the wood section with tweezers, spray the sample with a 70% (vol/vol) ethanol solution in distilled water, and burn it.
2. Once inside the laminar flow hood, spray the pruning shears with the ethanol solution, burn, and use the disinfected shears to cut the wood section to access to the discolored tissues.
3. Cut small pieces of wood from the margin of the discolored tissues using a sterile scalpel.
4. Use sterile tweezers to collect the wood samples, and place them onto a Petri dish filled with antibiotic MEA (*see* **Notes 6** and **7**).
5. Incubate the inoculated Petri dishes at 23 ± 2 °C in the dark for 2–16 days.
6. The target fungi for isolation show different MGR. Thus, it is recommended to check the Petri dishes at 2, 4, 8, 12, and 16 days after plating. At each check, replate the growing colonies to fresh Petri dishes with PDA only to obtain pure cultures and seal them with Parafilm®. Subsequently, remove all similar colonies by cutting the agar around 1 cm beyond the colony margin (*see* **Notes 8** and **9**).
7. After each check, store the Petri dishes in the same conditions as described in **step 5** until the next check.
8. Incubate pure cultures on PDA at 23 ± 2 °C in the dark.

3.3 Fungal Isolation from Root Samples

1. Remove soil remains from the roots with pressurized water.
2. Select root samples showing necrotic tissues, place them in a cheesecloth, and keep under running tap water (low flow) into a plastic or glass beaker for at least 1 h.

3. Once in the laminar flow hood, cut small root fragments (0.5–1.0 cm in length) using a sterile scalpel, and place them in a 20% hypochlorite solution for 2 min (*see* **Note 10**).
4. Keep the disinfected root fragments on sterile filter paper for 5 min.
5. Use sterile tweezers to collect the root samples, and place them onto a Petri dish filled with antibiotic PDA. It is recommended not to place more than seven root pieces per Petri dish. At least three replicate Petri dishes per wood sample should be generated.
6. Incubate the inoculated Petri dishes at 23 ± 2 °C in the dark for 7–14 days.
7. Check periodically the Petri dishes (*see* **Note 11**), and maintain them in the same conditions as described in **step 6** until the next check.
8. Incubate pure cultures on PDA at 23 ± 2 °C in the dark.

3.4 Fruiting Bodies (Pycnidia) Induction in Specific Culture Media

Herein, two culture media for inducing pycnidia in vitro are described: agar with pine needles [8] and pistachio leaf agar (PLA) [9, 10]. Carry out all procedures at room temperature into the laminar flow hood unless otherwise specified.

1. Place a Teflon bar magnetic stirrer and 1 L of sterile water into the 2 L Erlenmeyer flask (*see* **Note 12**).
2. To prepare the pine needle agar base, weigh the appropriate amount of agar according to the manufacturer instructions, and place it into the Erlenmeyer flasks. To prepare the PLA base, mix PDA, agar at 10 g/L each, and place them in the Erlenmeyer flask.
3. Seal the Erlenmeyer flask with cotton and aluminum foil in the top.
4. Sterilize the culture media in the autoclave at 120 °C for 20 min.
5. Place the Erlenmeyer flaks with culture media for 30 min into the water bath previously conditioned at 45 °C.
6. Homogenize the culture media by means of a magnetic stirrer for 5 min.
7. Carefully fill plastic Petri dishes with the culture media. For PLA, place a sterilized pistachio leaf on the surface of culture medium by using two sterile tweezers just after pouring the culture medium into the Petri dishes. The pistachio leaf must be kept embedded in the culture medium (*see* Fig. 2d).
8. After pouring, keep them in the laminar flow hood overnight.

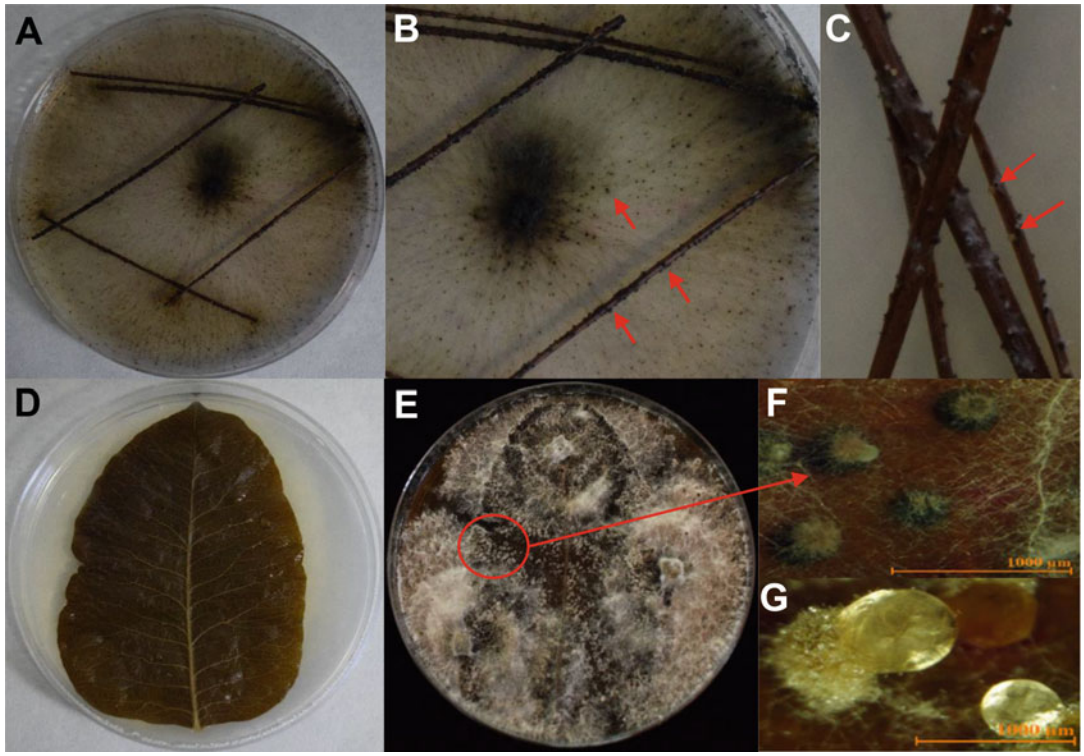


Fig. 2 Culture media to induce fruiting bodies (pycnidia) of fungal trunk pathogens in vitro. (**a**–**c**) Pycnidia of Botryosphaeriaceae (red arrows) developed onto water agar and in pine needles. (**d**) Petri dish with pistachio leaf agar (PLA) just after preparation. (**e**–**g**) Pycnidia of Botryosphaeriaceae developed on PLA

9. Store in a fridge at 4 °C in the dark until use.
10. Both culture media described above can be used to induce pycnidia formation (*see* **Note 13**). If you decide to use agar with pine needles, place a mycelial agar plug from the fungal isolate in the center of the Petri dish filled with agar and then insert 3–4 pine needles on the agar surface (*see* Fig. 2a–c). If PLA is used, place 2–3 mycelial agar plugs from the fungal isolate at the interface of pistachio leaf and agar (*see* Fig. 2e and **Note 14**).
11. Incubate the Petri dishes at 23 ± 2 °C under continuous fluorescent light for 2–3 weeks.
12. After 2–3 weeks of incubation, the pycnidia can be collected by scraping the pine needles or the entire PLA surface (*see* Fig. 2 and **Note 15**).

4 Notes

1. We recommend the use of the antibiotic streptomycin sulphate to avoid bacterial contaminations in the culture media, but it can be replaced by lactic acid [0.1% (vol/vol); pH = 4.0–4.5].
2. Collect pine needles just before processing in the laboratory, regardless of the season. Before preparing the media, wash the pine needles under running tap water, place them in aluminum foil, sterilize in autoclave at 120 °C for 20 min, and dry in lab oven at 60 °C overnight.
3. Collect pistachio leaflets in mid-late spring, and carefully separate the leaves of each leaflet. Then the leaves can be used immediately or stored in plastic bags at −20 °C. Before preparing the culture medium, place fresh or defrosted leaves in aluminum foil (10–15 leaves per package), sterilize them by double turn in autoclave at 120 °C, for 20 min each turn (allow 24 h between turns), and dry in Lab oven at 60 °C overnight.
4. We recommend to keep the processed samples in labeled plastic bags at 4 °C in the dark until the end of the fungal isolation process in case that the fungal isolation needs to be repeated (i.e., due to contamination) during the process.
5. Wait at least 20 min after sterilization before adding the streptomycin sulphate to the glass tube filled with sterile distilled water.
6. We recommend not sealing the Petri dishes used for fungal isolation with Parafilm®, as it is necessary to check them every 2 days.
7. We recommend seven pieces of wood per Petri dish and at least three replicate Petri dishes per wood sample.
8. Consider that fungi belonging to Botryosphaeriaceae (high MGR) develop colonies between 2 and 4 days after plating; Diatrypaceae (moderate MGR) between 4 and 8 days after plating; and Petri disease pathogens (slow MGR) need from 10 to 16 days to develop small colonies.
9. We strongly recommend removing the growing colonies of each fungal group as they grow. Otherwise, there is a high risk that they will grow overlapping the remaining isolation attempts (pieces of wood). Consequently, it will not be possible to isolate fungi with lower MGR such as Petri disease pathogens.
10. We recommend using a standard strainer to deepen the root segments in the sodium hypochlorite solution because this makes it easier to remove all root segments after the disinfection process.

11. It is recommended that Petri dishes are checked at 2 and 4 days after plating to remove them as described before. From 4 days after plating, we were able to visualize orange-brown colonies that match with "*Cylindrocarpon*" anamorphs, which are the main fungal pathogens that we expect to collect from root tissues. Then replate them to PDA.
12. We recommend using 1 L Erlenmeyer flasks with 0.5 L of distilled water for PLA to avoid the medium solidification during pouring since this culture medium may require more preparation time.
13. This protocol is mainly applicable for Botryosphaeriaceae and Diatrypaceae fungi since the remaining group of fungi (Esca, black-foot, and Petri dishes pathogens) are able to sporulate on PDA and/or develop specific morphological characters that are enough to identify them at the family and/or genus level.
14. We recommend not sealing the Petri dishes with Parafilm® to avoid a strong condensation into the Petri dish.
15. Consider that by using PLA, it is possible to obtain conidial suspensions of enough concentration to prepare inoculum for pathogenicity tests of other experiments where large volumes with high conidia concentration are required [9, 10]. However, note that using pine needles agar successfully is often very tedious.

References

1. Bertsch C, Ramírez-Suero M, Magnin-Robert M et al (2013) Grapevine trunk disease: complex and still poorly understood. Plant Pathol 62:243–265
2. Gramaje D, Armengol J (2011) Fungal trunk pathogens in the grapevine propagation process: potential inoculum sources, detection, identification, and management strategies. Plant Dis 95:1040–1055
3. Mugnai L, Graniti A, Surico G (1999) Esca (black measles) and brown wood-streaking: two old and elusive diseases of grapevines. Plant Dis 83:404–418
4. Agustí-Brisach C, López-Moral A, Raya MC et al (2019) Occurrence of grapevine trunk diseases affecting the native cultivar Pedro Ximénez in southern Spain. Eur J Plant Pathol 153:99–625
5. Rolshausen PE, Baumgartner K, Travadon R et al (2014) Identification of *Eutypa* spp. causing Eutypa dieback of grapevine in eastern North America. Plant Dis 98:483–491
6. Trouillas FP, Pitt WM, Sosnowski MR et al (2011) Taxonomy and DNA phylogeny of Diatrypaceae associated with *Vitis vinifera* and other woody plants in Australia. Fungal Divers 49:203–223
7. Úrbez-Torres JR (2011) The status of Botryosphaeriaceae species infecting grapevines. Phytopathol Mediterr 50:S5–S45
8. Slippers B, Crous PW, Benman S et al (2004) Combined multiple gene genealogies and phenotypic characters differentiate several species previously identified as *Botryosphaeria dothidea*. Mycologia 96:83–101
9. Agustí-Brisach C, Moral J, Felts D et al (2019) Interaction between *Diaporthe rhusicola* and *Neofusicoccum mediterraneum* causing branch dieback and fruit blight of English walnut in California, and effect of pruning wounds to the infection. Plant Dis 103:1196–1205
10. Chen SF, Morgan DP, Hasey JK et al (2014) Phylogeny, morphology, distribution, and pathogenicity of Botryosphaeriaceae and Diaporthaceae from English walnut in California. Plant Dis 98:636–652



Chapter 9

Determination of De Novo Suberin-Lignin Ferulate Deposition in Xylem Tissue Upon Vascular Pathogen Attack

Weiqi Zhang, Álvaro Jiménez-Jiménez, Montserrat Capellades, Jorge Rencoret, Anurag Kashyap, and Núria S. Coll

Abstract

Plant vascular pathogens use different ways to reach the xylem vessels and cause devastating diseases in plants. Resistant and tolerant plants have evolved various defense mechanisms against vascular pathogens. Inducible physico-chemical structures, such as the formation of tyloses and wall reinforcements with phenolic polymers, are very effective barriers that confine the pathogen and prevent colonization. Here, we use a combination of classical histochemistry along with bright-field and fluorescence microscopy and two-dimensional nuclear magnetic resonance (2D-NMR) spectroscopy to visualize and characterize wall reinforcements containing phenolic wall polymers, namely, lignin, ferulates, and suberin, which occur in different xylem vasculature in response to pathogen attack.

Key words Vascular pathogens, *Ralstonia solanacearum*, Ferulate, Suberin, Lignin, 2D-NMR, Staining, Disease resistance

1 Introduction

Vascular plant pathogens cause some of the most devastating diseases in plants, ranging from annual herbaceous to big trees [1]. These pathogens adopt different strategies to make their way into xylem vessels. Once the pathogen reaches the vasculature, it multiplies profusely inside the xylem tissue and spreads vertically and horizontally to the neighboring tissues, resulting in dreadful wilting of the infected plants and eventual death [2]. However, resistant plants have evolved mechanisms in the xylem vasculature to sense invading pathogens and mount an array of defense responses against these aggressors [1]. One of the major defense mechanisms conferring resistance against vascular pathogens can be attributed to the genesis of physio-chemical blockades [3]. Plants

Weiqi Zhang and Álvaro Jiménez-Jiménez contributed equally.

Javier Agusti (ed.), *Xylem: Methods and Protocols*, Methods in Molecular Biology, vol. 2722,
https://doi.org/10.1007/978-1-0716-3477-6_9,
© The Author(s), under exclusive license to Springer Science+Business Media, LLC, part of Springer Nature 2024

have evolved effective structural defense mechanisms to prevent vessel colonization or movement between vessels once vascular colonization has occurred [4]. Structural barricades such as gels and tyloses prohibit vertical movement of xylem vascular pathogens inside the lumen of vessels. Similarly, vascular pathogen–induced reinforcements in secondary cell wall of vascular tissue act as a potent barrier against colonization [5]. Wall reinforcements with phenolic polymers such as lignin and suberin contribute toward preventing horizontal spread of the pathogens to the apoplast and the contiguous active tissues and vessels [6]. Hence, these horizontal and vertical barricades compartmentalize vascular pathogens at the site of infection [3]. Timely formation of these physicochemical vascular barriers early upon pathogen perception can lead to confinement of the vascular pathogen at the infected vessel, avoiding the spread of wilt diseases [7–9]. Also, the occurrence of these defense responses are highly intertwined, both spatial and temporally, for avoidance of deleterious repercussions (embolism and cavitation). Hence, these anatomical shifts act as a hallmark of plant defense response against xylem vascular pathogens, which can be vital while exploring resistant germplasms. Such structural defense responses vary based on the host-pathogen interaction but are conserved across the plant kingdom [3]. Hence, an in-depth histopathological characterization gives important insights on the defense responses employed by the host against a pathogen.

We present here protocols based on staining along with bright-field and fluorescence microscopy and on two-dimensional nuclear magnetic resonance (2D-NMR) spectroscopy, standardized in our laboratory, to visualize wall reinforcements with phenolic wall polymers, namely, lignin, ferulates, and suberin, that occur in xylem vasculature, in response to pathogen attack. Staining of cross sections with Phloroglucinol-HCl gives an accurate visualization of changes in lignin accumulation of xylem vasculature in response to infection. Likewise, Sudan IV staining can accurately detect deposition of aliphatic domain of suberin in walls of xylem vasculature in response to pathogen attack. Another important phenolic player in wall reinforcements is ferulate, which not only imparts strength to walls by cross-linking, but it may also act as lignin-like poly-phenolic domain of suberin. Ferulates constitute a crucial component of the suberin polyphenolic domain and are one of the first compounds deposited in a suberizing tissue, potentially acting as nucleating site for suberin matrix polymerization [10–13]. Here we also present a simple technique to detect ferulate deposition in walls of vasculature as defense response to pathogens, based on a pH-dependent blue to green color conversion of UV autofloresence. On the other hand, 2D-NMR experiments such as the Hetoronuclear Single Quantum Coherence (HSQC) can provide

additional valuable information on suberin/lignin structure. 2D-HSQC NMR is considered one of the most powerful tools for plant cell wall structural analysis providing information on the composition and linkages in lignin/suberin polymers [14, 15].

2 Materials

2.1 Plant Varieties and Plant Growth Materials

1. Use tomato (*Solanum lycopersicum*) plants cultivars Marmande and Moneymaker as susceptible controls, cultivar Hawaii as a resistant control, and the transgenic Moneymaker tomatoes overexpressing hydroxycinnamoyl-CoA:tyramine N-hydroxycinnamoyl transferase (THT), a key enzyme in the synthesis of hydroxycinnamic acid amides [16]. Grow plants in controlled growth chambers at 60% humidity, neutral day photoperiod (12 h day–12 h night), and 27 °C (when grown under light-emitting diode (LED) lighting) or 25 °C (when grown under fluorescent lighting).
2. Soil mix: 5 parts peat + 3 small parts sand + 3 small part vermiculite.

2.2 Bacterial Strains and Bacterial Culture

1. Use *Ralstonia solanacearum* strain GMI1000 (Phylotype I, race 1 biovar 3), including luminescent and fluorescent reporter strains previously described in [9].
2. Rich B medium: 10 g/L Bacteriological peptone, 1 g/L yeast extract, and 1 g/L casamino acids. For solid media, add 1.5% agar before autoclaving. Before plating, add 0.5% glucose and 0.005% triphenyltetrazolium chloride (TTC). Adjust pH to 7.0. Supplement gentamycin (10 μg/ml) in liquid and solid cultures for selection of reporter strains.
3. Sterile petri dishes.
4. Sterile 50 ml tubes.
5. Spectrophotometer.

2.3 Tissue Sectioning

1. Sterile carbon steel surgical blades.
2. Sterile 2 ml tubes.
3. 70% ethanol.

2.4 Histological Materials

1. 70% ethanol.
2. Phloroglucinol-HCl: Dissolve 100 mg of phloroglucinol in 8 ml of 95% ethanol and 8 ml of 37% HCl. Store at room temperature covered in aluminum foil.
3. 1 N potassium hydroxide (KOH) (pH above 10).

4. 5% Sudan IV solution: 2.5 g of Sudan IV in 50 ml of 70% ethanol, filtered and stored at room temperature covered in aluminum foil.
5. Microscope with ultraviolet (UV) illumination (340–380 nm excitation and 410–450 nm barrier filters).
6. HD digital microscope camera.

3 Methods

3.1 Bacterial Inoculation in Plants (Soil-Drenching Method)

1. Four- to five-week-old tomato plants are used for inoculation. Two days before inoculation, plants are transferred to a new chamber adapted for infection (27 °C, 60% RH, 12 h/12 h). Do not overwater the plants so the soil is dry enough for the plants to absorb all the inoculum through the roots.
2. One day prior inoculation, set an overnight culture of the *R. solanacearum* strain(s) of interest in Rich B medium (+antibiotics) in an Erlenmeyer flask (*see* **Note 1**). The amount of inoculum needed depends on the experiment and number of plants you want to inoculate, as well as the final bacterial concentration in the inoculum.

   Typically, a concentration of 10^8 colony forming units (CFU)/ml is used for resistant varieties and 10^7 CFU/ml for susceptible ones. Calculations can be made according to the initial concentration in the liquid culture and the fact that 40 ml of inoculum per plant is used.
3. On the day of inoculation, measure the optical density (OD_{600}) of the culture and prepare the inoculation solutions by diluting with sterile distilled water to the desired bacterial concentration (*see* **Note 2**). Poke the soil with a 1 ml pipette tip at each corner of the pot (4 punctures) to inflict root wounding, which facilitates infection.
4. Pour 40 ml of bacterial suspension in each pot, and do not water the plants until they have time to absorb the inoculum (1–2 days, depending on plant size).
5. Afterward, keep watering the plants regularly (*see* **Note 3**) and start scoring symptoms at 3 days post infection (dpi), when the susceptible backgrounds begin to show wilting symptoms.

3.2 Histochemical Analysis

1. When the desired stage of infection for analysis has come, take the plants, wash the roots with 1% v/v bleach, and eliminate the adventitious roots (*see* **Note 4**).
2. Take thin (150 μm) cross sections with a sterile razor blade or a microtome at the transition zone between the taproot and the basal hypocotyl, 1.5 cm below the soil line approximately (Fig. 1).

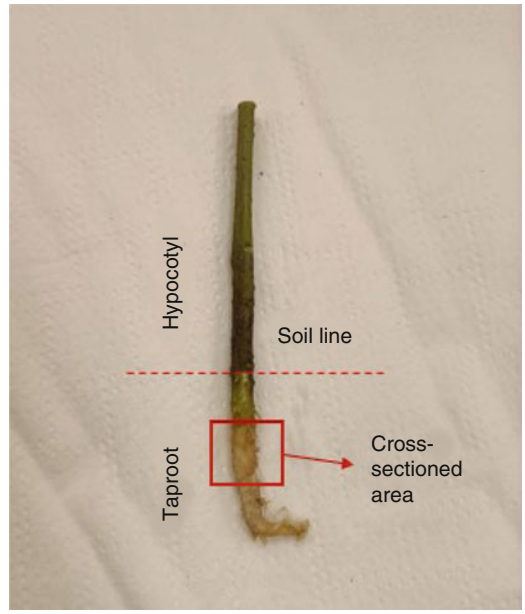


Fig. 1 Region of interest for histological analysis. The lower portion of a 4-week-old tomato plant is shown, after throughout washing and eliminating adventitious roots, specifying in red the region of interest for histochemical analysis

3. Transfer the sections to tubes containing 300–500 μl of 70% ethanol and incubate at room temperature (RT) 2–5 days (at least) before analysis. This incubation ensures that the components not bound to the cell wall become solubilized with the ethanol and are thus removed from cell wall structures.

3.3 Lignin Staining

For lignin detection, phloroglucinol (*see* **Note 5**) is used for direct visualization of lignin (cinnamaldehyde end-groups of lignin units) [17] as a red-purple coloration in the vasculature (Fig. 2).

A drop of staining solution is added to the cross sections and incubated for 5 min at room temperature, until the purple color has appeared. Then sections are mounted for microscopy using 70% ethanol and subsequently visualized under bright-field light in a stereomicroscope (*see* **Note 6**).

3.4 Detecting Ferulate Deposition

1. To detect ferulate accumulation (*see* **Note 7**), alkali treatment can be performed, adding one drop of 1 N KOH (pH = 10) in the cross sections of interest.
2. After 2 min of incubation at room temperature, samples can be mounted on microscopy slides with the KOH and ferulates can be visualized as green regions under UV light with an epifluorescence microscope. The basic pH is responsible for the blue-to-green shift in fluorescence observed specifically for ferulate deposits [18].

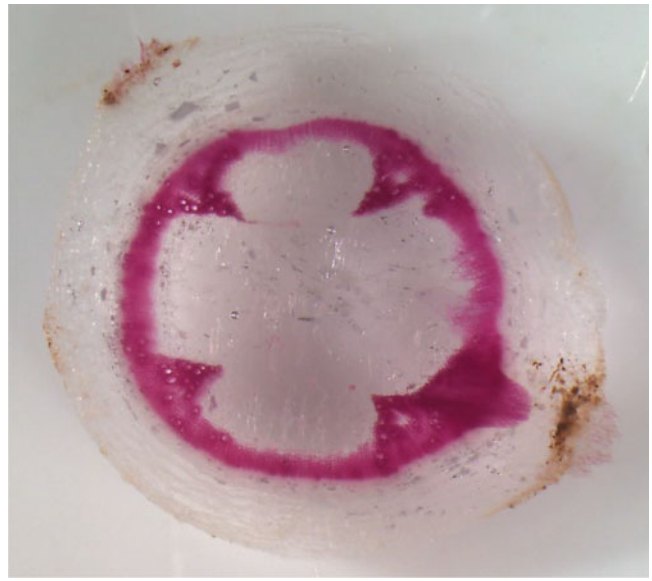


Fig. 2 Phloroglucinol-stained samples. Example cases of cross sections stained with only phloroglucinol-HCl observed under bright-field in a stereomicroscope Olympus SX16

3.5 Detecting Suberin Aliphatics

1. To detect aliphatic suberin, the Sudan IV stain is used. To prepare the samples, put the slices in a tube containing 300 μl of Sudan IV and incubate for 15 min at room temperature.
2. Perform two washes with 70% ethanol, or until the samples do not release more dye.
3. After this, samples can be mounted on slides with 70% ethanol for microscopy. Under UV light in an epifluorescence microscope, suberin deposits can be visualized as brownish regions surrounding the vessels. Alternatively, the same samples can be directly mounted with 1 N of KOH instead of ethanol to combine the techniques in order to localize both parts of suberin barriers (Fig. 3).

3.6 Deciphering the Composition and Structure of the Cell Wall–Deposited Compounds

To obtain additional information on suberin and lignin present in tomato plant cell walls, fractions enriched in both polymers were isolated and analyzed by two-dimensional nuclear magnetic resonance spectroscopy (2D-NMR), which currently represents the most powerful tool for the structural analysis of plant cell wall components [14, 15]. Prior to 2D-NMR analysis of suberin/lignin polymers, it is necessary to remove the nonstructural components of the plant cell wall, as well as the structural polysaccharides that form it.

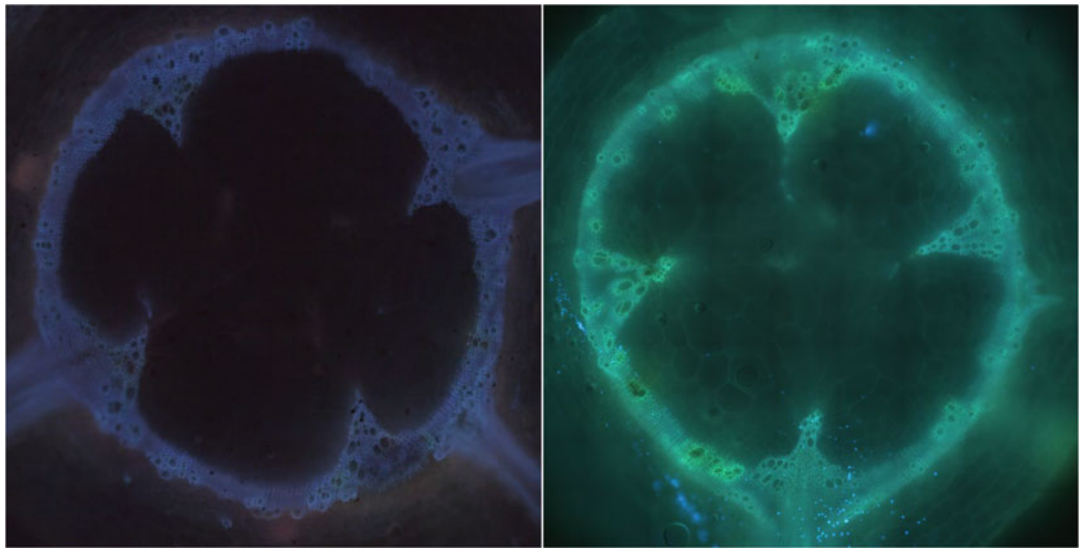


Fig. 3 Sudan IV + KOH–stained samples. Example cases of cross sections stained with only Sudan IV (left) and Sudan IV + KOH (right), observed under UV light in an epifluorescence microscopy Leica DM6

3.6.1 Solvent Extraction for Removing Nonstructural Plant Cell Wall Components

Samples of a pool of tomato plants (taproot-to-hypocotyl region), infected or water-treated, are knife-milled and extracted sequentially with distilled water, 80% ethanol, and, finally, with acetone, by sonicating in an ultrasonic bath, centrifuging, and discarding the supernatant.

1. Add ~300 mg of plant material to regular 50 ml plastic tubes.
2. Add 40 ml of distilled water and sonicate for 30 min.
3. Centrifuge the samples for 20 min at 8228 × *g* at 4 °C.
4. Remove the supernatant by decanting and discard it.
5. Repeat the water addition, sonication, centrifugation, and supernatant removal two additional times.
6. Add 40 ml of 80% (vol/vol) ethanol and sonicate for 30 min.
7. Centrifuge the samples for 20 min at 8228 × *g* at 4 °C.
8. Remove the supernatant by decanting and discard it.
9. Repeat the addition of 80% (vol/vol) ethanol, sonication, centrifugation, and supernatant removal two additional times.
10. Add 40 ml of 100% acetone and sonicate for 30 min.
11. Centrifuge the samples for 20 min at 8228 × *g* at 4 °C.
12. Remove the supernatant by decanting and then discard.
13. Oven-dry the extract-free tomato plant roots at ~45–50 C (generally, 24 h is sufficient).

3.6.2 Ball-Milling

Grind extract-free tomato plant roots (around 200 mg) using a Retsch PM100 planetary mill (Retsch, Haan, Germany) fitted with one 50 ml agate grinding jar and 10 × 10 mm ball bearings, set at 600 rpm. A total ball milling time of 3 h, alternating 20 min of grinding with 10 min of rest to avoid heating the sample, is sufficient.

3.6.3 Lignin/Suberin Isolation by Enzymatic Removal of Polysaccharides

The lignin/suberin fraction can be isolated by enzymatically hydrolyzing the structural polysaccharides that form the plant cell wall [19]. For this, cellulysin cellulase (Calbiochem), a crude cellulase preparation from *Trichoderma viride*, also containing hemicellulase activities, with activity ≥10,000 $FPUg^{-1}$ of dry weight, is used.

1. Add ~200 mg of extractives-free ball-milled tomato roots to a 50 ml PTEF Nalgene® centrifuge tube.
2. Add 30 ml of 20 mm sodium acetate (pH 5.0) buffer and 7.5 mg of Cellulysin cellulase.
3. Incubate the reaction slurry at 30 °C for 48 h, with constant agitation.
4. Centrifuge the samples (8228 × *g*, 4 °C, 20 min) and discard the solvent by decantation.
5. Repeat the process with fresh buffer (30 ml) and enzyme (7.5 mg) two additional times.
6. Finally, wash the residue (enriched lignin/suberin fraction) with distillated water, recover it by centrifugation and freeze dry it.

3.6.4 2D-NMR Analysis

Transfer approximately 20 mg of enzymatically isolated lignin/suberin preparation to a 5 mm NMR tube, and add 0.6 ml of DMSO-d_6. Sonicate the NMR tube in an ultrasonic bath for 30–60 min until complete sample dissolution. Acquire 2D ^{1}H–^{13}C Heteronuclear Single Quantum Coherence (HSQC) spectra on a cryoprobe-equipped Bruker Avance III 500 MHz instrument using a standard Bruker adiabatic-pulse program ('hsqcetgpsisp.2') that enabled a semiquantitative analysis of the different ^{1}H-^{13}C- correlation signals. 2D-HSQC spectra are acquired from 10 to 0 ppm in F2 (1H) using 1000 data points for an acquisition time (AQ) of 100 ms, an interscan delay (D1) of 1 s, and from 200 to 10 ppm in F1 (^{13}C) using 256 increments of 32 scan for a total experiment time of 2 h 34 min. The $^{1}J_{CH}$ used is 145 Hz. Processing uses typical matched Gaussian apodization in ^{1}H (LB = −0.1 and GB = 0.001) and a squared cosine bell in ^{13}C (LB = 0.3 and GB = 0.1). The central residual DMSO peak (δ_C/δ_H 39.5/2.49) is used as an internal reference.

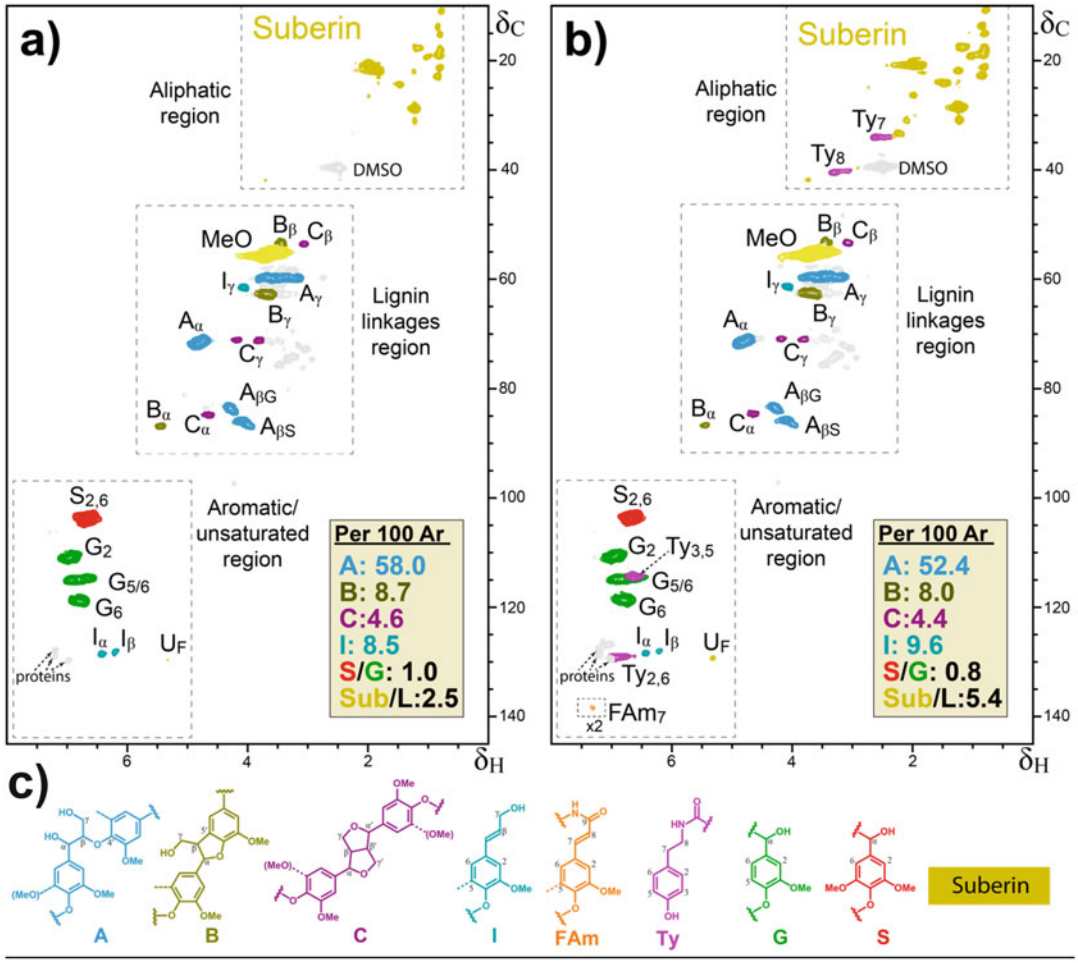


Fig. 4 2D-HSQC spectra of enzymatically isolated lignin/suberin fractions from (**a**) mock-treated and (**b**) *R. solanacearum*-infected taproots of resistant H7996 tomato. (**c**) Main lignin/suberin structures identified: β–O–4′ alkyl aryl ethers (A), β–5′ fenylcoumarans (B), β–β′ resinols (C), cinnamyl alcohols end-groups (I), feruloyl amides (FAm), amides of tyramine (Ty), guaiacyl lignin units (G), syringyl lignin units (S), as well as unassigned aliphatic signals from suberin. The structures and contours of the HSQC signals are color coded to aid interpretation To detect FAm7 signal, the spectrum scaled up to twofold (×2) intensity. The abundances of the main lignin linkages (A, B, and C) and cinnamyl alcohol end-groups (I) are referred to as a percentage of the total lignin units (S + G = 100%). (Image reproduced from Kashyap et al. [6] with permission)

3.6.5 Assignation and Quantitation of 2D-HSQC Correlation Signals

HSQC cross-signals are assigned by literature comparison [20–23]. A semiquantitative analysis of the volume integrals of the HSQC correlation peaks can be performed using Bruker's Topspin or other equivalent NMR-processing software such as MNova. The ^{1}H-^{13}C correlation signals from the aromatic/unsaturated region (δ_H/δ_C 5–8/90–150 ppm) of the spectrum are used to estimate the lignin composition in terms of guaiacyl (G) and syringil (S) units (Fig. 4). The correlation signals of G_2 and $S_{2,6}$ are used to estimate the content of the respective G- and S-lignin units (as the signal $S_{2,6}$ involves two proton-carbon pairs, its volume

integral is halved). The Cα/Hα correlation signals of the β–*O*–4′ alkyl aryl ethers (Aα), phenylcoumarans (Bα), and resinols (Cα) in the aliphatic-oxygenated region of the spectra (Fig. 4) are used to estimate their relative abundances (as per 100 aromatic units), whereas the Cγ/Hγ correlation signal of the cinnamyl alcohol end-units (Iγ) is used to estimate its relative abundance (as per 100 aromatic units); as signal Iγ involves two proton-carbon pairs, its volume integrals is also halved. Suberin/lignin (Sub/L) ratio can be roughly estimated by integration of all the HSQC signals in the aliphatic region (in which most of suberin signals appear) and referring this value to the total aromatic lignin units (G + S) integration.

4 Notes

1. Always use a bigger Erlenmeyer than the desired volume (2.5–5 times) to ensure a good aeration of bacterial culture.
2. Do not use tap water that can contain hypochlorite and other compounds toxic to bacteria.
3. It is essential to ensure proper watering of the plants during infection, as stress caused by drought interferes with the quality of the images obtained with the leica-DFC900GT-VSC07341 camera.
4. In terms of analyzing the contribution of barrier formation on resistance, always take samples where both susceptible and resistant lines carry the same bacterial load.
5. Phloroglucinol is also known as the Weisner stain.
6. Phloroglucinol is easily oxidized (green coloration starts to appear) after a couple of weeks, so always use freshly stained samples.
7. At the molecular level, suberin is generally divided into an aromatic fraction composed mainly of ferulates, metabolic derivatives from the phenylpropanoid pathway, and an aliphatic part composed of long carbon chains [24].

Acknowledgments

Research was funded through MCIN/AEI/ 10.13039/ 501100011033 and "ERDF A way of making Europe" with grants PID2019-108595RB-I00 (NSC) and PID2020-118968RB-I00 (JR) and with the fellowship PRE2020-092086 (ALJ-J). WZ is a recipient of the China Scholarship Council fellowship (CSC NO.201906990041). Research at CRAG is also funded through the "Severo Ochoa Programme for Centres of Excellence in R&D" (CEX2019-000902-S by MCIN/AEI/10.13039/501100011033) and through the CERCA Programme/Generalitat de Catalunya.

References

1. Yadeta KA, Thomma BPHJ (2013) The xylem as battleground for plant hosts and vascular wilt pathogens. Front Plant Sci 4:97
2. Bae C, Han SW, Song YR et al (2015) Infection processes of xylem-colonizing pathogenic bacteria: possible explanations for the scarcity of qualitative disease resistance genes against them in crops. Theor Appl Genet 128:1219–1229
3. Kashyap A, Planas-Marquès M, Valls M (2021) Blocking intruders: inducible physico-chemical barriers against plant vascular wilt pathogens. J Exp Bot 72:184–198
4. Beckman CH, Roberts EM (1995) On the nature and genetic basis for resistance and tolerance to fungal wilt diseases of plants. Adv Bot Res 21:35–77
5. Ferreira V, Pianzzola MJ, Vilaró FL et al (2017) Interspecific potato breeding lines display differential colonization patterns and induced defense responses after Ralstonia solanacearum infection. Front Plant Sci 8:1–14
6. Kashyap A, Jimenez-Jimenez AL, Zhang W et al (2022) Induced ligno-suberin vascular coating and tyramine-derived hydroxycinnamic acid amides restrict Ralstonia solanacearum colonization in resistant tomato. New Phytol 234:1411–1429
7. Robb J, Lee S-W, Mohan R et al (2008) Chemical characterization of stress-induced vascular coating in tomato. Plant Physiol 97:528–536
8. Zaini PA, Nascimento R, Gouran H et al (2018) Molecular profiling of pierce's disease outlines the response circuitry of Vitis vinifera to Xylella fastidiosa infection. Front Plant Sci 9:771
9. Planas-Marquès M, Kressin JP, Kashyap A et al (2019) Four bottlenecks restrict colonization and invasion by the pathogen Ralstonia solanacearum in resistant tomato. J Exp Bot 71:2157–2171
10. Negrel J, Pollet B, Lapierre C (1996) Ether-linked ferulic acid amides in natural and wound periderms of potato tuber. Phytochemistry 43:1195–1199
11. Graça J (2010) Hydroxycinnamates in suberin formation. Phytochem Rev 9:85–91
12. Graça J (2015) Suberin: the biopolyester at the frontier of plants. Front Chem 3:1–11
13. Boher P, Serra O, Soler M et al (2013) The potato suberin feruloyl transferase FHT which accumulates in the phellogen is induced by wounding and regulated by abscisic and salicylic acids. J Exp Bot 64:3225–3236
14. Ralph J, Landucci L (2010) NMR of lignins. In: Heitner JA, Dimmel C, Scmidt DR (eds) Lignin and lignans: Adv chem. CRC Press, Taylor & Francis, Boca Raton, pp 137–243
15. Correia VG, Bento A, Pais J et al (2020) The molecular structure and multifunctionality of the cryptic plant polymer suberin. Materials Today Bio 5:100039
16. Campos L, Lisón P, López-Gresa MP et al (2014) Transgenic tomato plants overexpressing tyramine N-hydroxycinnamoyltransferase exhibit elevated hydroxycinnamic acid amide levels and enhanced resistance to Pseudomonas syringae. Mol Plant-Microbe Interact 27:1159–1169
17. Pomar F, Novo M, Bernal MA et al (2004) Changes in stem lignins (monomer composition and crosslinking) and peroxidase are related with the maintenance of leaf photosynthetic integrity during Verticillium wilt in Capsicum annuum. New Phytol 163:111–123
18. Harris PJ, Trethewey JAK (2010) The distribution of ester-linked ferulic acid in the cell walls of angiosperms. Phytochem Rev 9:19–33
19. Chang H, Cowling EB, Brown W et al (1975) Comparative studies on cellulolytic enzyme lignin and milled wood lignin of sweetgum and spruce. Holzforschung 29:153–159
20. Rencoret J, Kim H, Evaristo AB et al (2018) Variability in lignin composition and structure in cell walls of different parts of macaúba (Acrocomia aculeata) palm fruit. J Agric Food Chem 66:138–153
21. del Río JC, Rencoret J, Gutiérrez A et al (2018) Structural characterization of lignin from maize (Zea mays L.) fibers: evidence for diferuloylputrescine incorporated into the lignin polymer in maize kernels. J Agric Food Chem 66:4402–4413
22. Mahmoud AB, Danton O, Kaiser M et al (2020) Lignans, amides, and saponins from Haplophyllum tuberculatum and their antiprotozoal activity. Molecules 25:2825
23. Youngsung J, Kim H, Kang M et al (2021) Pith-specific lignification in Nicotiana atenuata as a defense against a stem-boring herbivore. New Phytol 232:332–344
24. Nomberg G, Marinov O, Arya GC et al (2022) The key enzymes in the suberin biosynthetic pathway in plants: an update. Plan Theory 11:392

Part IV

Xylem Composition and Imaging



Chapter 10

Quantification of Tracheary Elements Types in Mature Hypocotyl of *Arabidopsis thaliana*

Paula Brunot-Garau, Cristina Úrbez, and Francisco Vera-Sirera

Abstract

Secondary growth is a highly relevant process for dicot and gymnosperm species development. The process relies on vascular tissue proliferation and culminates with the thickening of stems, roots, and hypocotyls. The formation of tracheary elements is a critical step during this process. Among such tracheary elements, four different cell types are distinguished depending on their secondary cell wall pattern, which is exclusive for each tracheary cell type. Here we describe a method to isolate, dye, and recognize each of these tracheary cell types. The method is optimized to be performed in the *Arabidopsis thaliana* hypocotyl. This is because, in this species, the hypocotyl is the organ undergoing the largest proportion of secondary growth. Results allow for determining the relative amounts of each of the tracheary cell types.

Key words Xylem, Hypocotyl, Secondary growth, Tracheary elements, *Arabidopsis thaliana*

1 Introduction

In general, plant vascular tissues are composed of cambium, phloem, and xylem. Each of these vascular tissues is composed of several cell types.

Xylem development has been intensively studied due to its economic importance by constituting wood in trees. The cell types present in xylem are xylem parenchyma, fibers, and tracheary elements being the tracheary elements the responsible ones for the water and minerals transport [1].

Vascular tissues, such as xylem, can grow in the longitudinal and radial axes. When growing radially, the process is known as secondary growth. Secondary growth occurs in roots, stems, and hypocotyls of gymnosperms and dicot species. The process is the result of the activity of the vascular cambium, a secondary meristem found in the form of a ring that produces secondary xylem toward the inner side and secondary phloem towards the outer side of the plant, respectively.

Javier Agusti (ed.), *Xylem: Methods and Protocols*, Methods in Molecular Biology, vol. 2722,
https://doi.org/10.1007/978-1-0716-3477-6_10,
© The Author(s), under exclusive license to Springer Science+Business Media, LLC, part of Springer Nature 2024

Xylem main functions are (i) transporting water and minerals and (ii) providing plants with mechanical support and stability. For these reasons, xylem abundance usually correlates with plant height [2].

The *Arabidopsis thaliana* hypocotyl has been proposed as a model for studding secondary growth due to several reasons:

- The hypocotyl is the organ undergoing the largest amount of secondary growth.
- The overlap on the time of the elongation and secondary growth phases is minimum, that is, the two processes are mostly uncoupled [3].
- Anatomically, the hypocotyl secondary xylem development resembles that of trees [4].

During secondary growth in *Arabidopsis thaliana* hypocotyl, xylem development occurs in two distinct subphases. In the first one, occurring before the onset of flowering, only xylem parenchyma and vessels are developed. The second one, which is coordinated with flowering, is characterized by an increased rate of xylem versus phloem development and formation of lignified xylem fibers.

The tracheary elements organize longitudinally, generating a continuous structure of connected cells in which the upper and lower sides of each cell wall are dissolved. Importantly, each individual cell is characterized by a special secondary cell wall pattern, present only in the lateral parts of the cells.

The secondary cell wall is composed of cellulose microfibrils, hemicellulose, pectin, and polymers, such as lignin; which provide impermeability as well as mechanical strength [5]. In this way, tracheary elements can resist the high pressure generated through transpiration. The deposition of cellulose is controlled by the microtubules, especially during the early stages of these process [6]. Several microtubule-associated proteins, such as AtMAP70-1 and AtMAP70-5, which inhibit the deposition of secondary cell wall [7], regulate this process.

Depending on the secondary cell wall pattern, vessel elements are categorized as annular, spiral, reticulate, or pitted [8]. While annular and spiral vessels are more abundant in the early stages of xylem development, reticulate and pitted are more abundant during secondary growth. This is because annular and spiral vessels offer less resistance to elongation and reticulate and pitted vessels display stronger longitudinal stiffness [9].

Tracheary elements differentiation culminates with the loss of all cell contents and programmed cell death, forming a hollow tube through which water and minerals are transported. Programmed cell death and the secondary cell wall pattern establishment are tightly coupled [10].

2 Materials

1. 0.01% (v/v) calcofluor white stain (Sigma Aldrich). Store at room temperature.
2. Phosphate-buffered saline (PBS; 1x): 137 mM NaCl, 2.7 mM KCl, 10 mM Na_2HPO_4, 1.8 mM KH_2PO_4. Adjust pH to 7.4.
3. pH indicator paper pH 5.5–9.0, Neutralit (MercK).
4. 1.5 ml Eppendorf tubes.
5. Thermoblock.
6. Distilled water.
7. Plunger.
8. Vortex.
9. Micropipettes: 200 μL, 1000 μL.
10. Slides.
11. Cover slips.
12. Microscope with UV filter.

3 Methods

Carry out all protocol steps at room temperature, unless otherwise specified.

3.1 Vegetal Material

1. Grow *Arabidopsis thaliana* plants to adult stage (*see* **Notes 1** and **2**).
2. Collect hypocotyls from Arabidopsis plants as follows: Remove all the leaves from the rosette using a fresh sharp razor blade, wash carefully the roots to remove the soil substrate, and cut the fragment between under the cotyledons and the first secondary root; this segment is the hypocotyl (Fig. 1).

3.2 Maceration (See Note 3)

1. Prepare 1.5 ml Eppendorf tubes filled with maceration solution (3% H_2O_2 and 50% acetic acid, *see* **Note 4**). Leave the tubes in a thermoblock at 95 °C inside a fume hood.
2. Immediately place each collected hypocotyl in a 1.5 ml Eppendorf tube with maceration solution, and leave it for 4 hours (*see* **Note 5**).
3. After the 4 hours, let the tubes temper at room temperature and remove the maceration solution.
4. Wash with distilled water, filling the whole tube, and remove the water. Repeat this step three times.

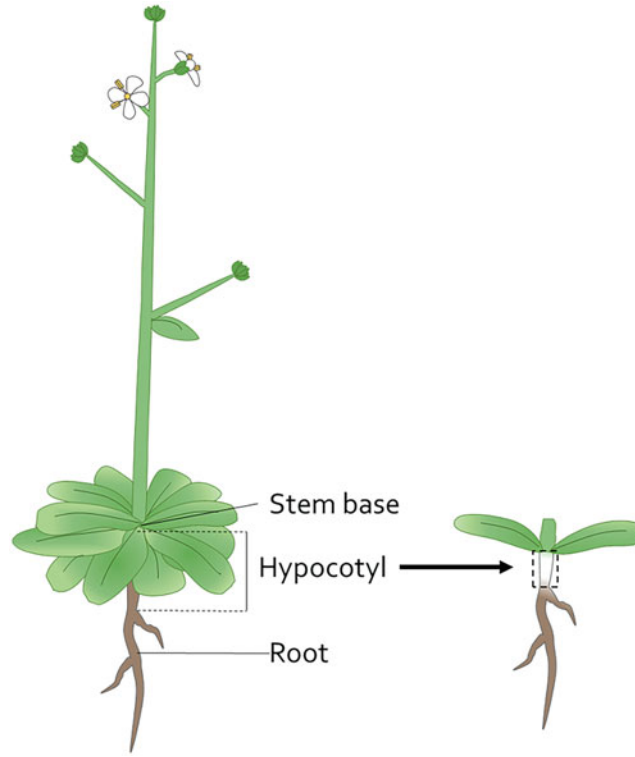


Fig. 1 Representation of an *Arabidopsis thaliana* adult plant, showing the hypocotyl

5. Add 1 ml PBS solution, and incubate 5 min at room temperature. Then remove the PBS solution. Repeat this step (*see* **Note 6**).
6. Measure pH with pH indicator paper. If the pH is lower than 7, repeat Step 5 until it is neutral.
7. Store the tubes containing the hypocotyls at 4 °C until the moment of taking the pictures (it can be stored for 1 month).

3.3 Microscope Visualization

1. Remove PBS solution, and add 50 μL of distilled water.
2. Mash the macerated hypocotyl with a plunger (*see* **Note 7**).
3. Vortex the tubes for 30 s.
4. Pipette up and down the mixture to finish breaking up the macerated hypocotyls.
5. Take 15 μL of the homogenized mixture, and put it on a slide.
6. Add 5 μL of 0.01% calcofluor solution on the slide, and mix it with the homogenized mixture with a pipette.
7. Place a cover glasses on the slide.

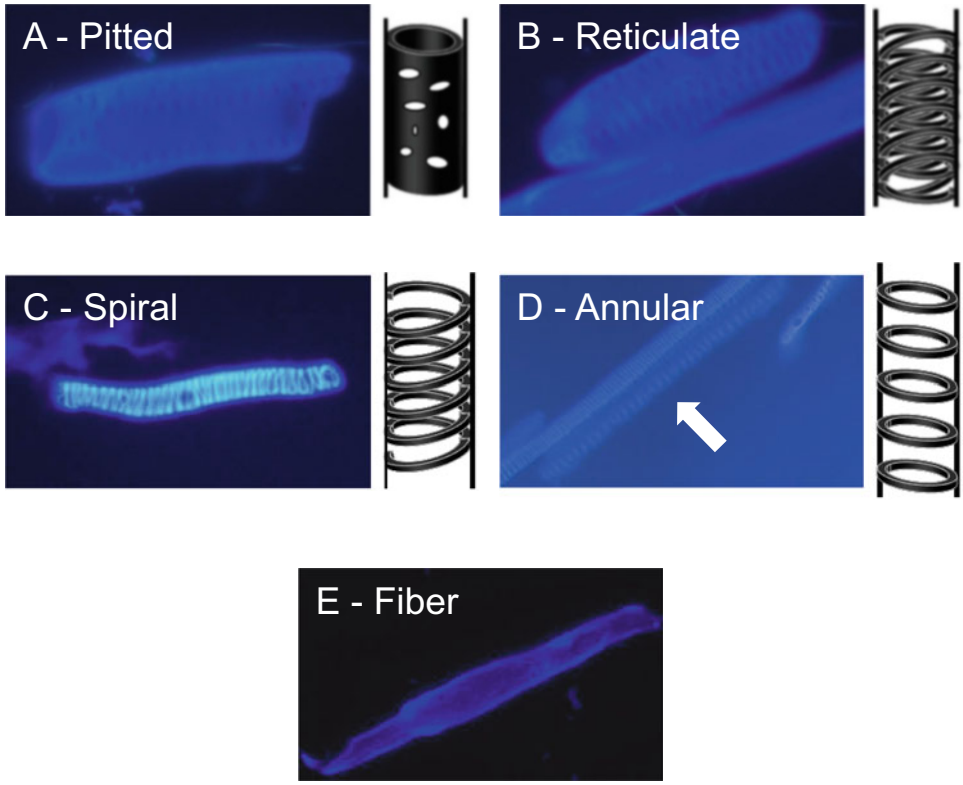


Fig. 2 Types of xylem cell types with different secondary cell wall patterns. (**a**) pitted, (**b**) reticulate, (**c**) spiral, (**d**) annular and (**e**) fiber

8. Visualize the sample with an optical microscope using the 20x objective with UV filter. Take at least 100 pictures of xylem cells for each sample (*see* **Note 8**).

3.4 Xylem Cell Types

The observed xylem elements are the tracheary elements. These structural elements are dead water-conducting cells with a lignified and thickened cell wall. The patterning of the secondary cell wall enables to differentiate between annular, spiral, reticulate, and pitted cells. In annular and spiral tracheary elements, there are large clear spaces in the secondary cell wall; while in pitted ones, the secondary cell wall covers the whole cell except in some small pits. Reticulate cells have an intermediate distribution (Fig. 2) [8, 11].

The above described differences in secondary cell wall pattern arise due to biomechanical reasons. Annular and spiral cell types have a lower cell radius compared to reticulates and pitted ones; the lower the radius, the less reinforcement is needed in the secondary cell wall [9].

It should be kept in mind that most cells in the sample correspond to xylem fibers, which contain thicker walls and more tapering ends than the tracheary elements (Fig. 2E). This xylem type cell must not be considered.

Count at least 100 tracheary elements for each sample to calculate the proportion of different cell types. The obtained values serve as a proxy to determine whether xylem develops properly or aberrantly. An example of aberrant xylem differentiation evaluated through this method can be found in reference [12] regarding the *acl5* Arabidopsis mutant.

4 Notes

1. For each condition, handle 3–6 individuals.
2. Grow the Arabidopsis plants in a soil substrate made up of peat: perlite:vermiculite (2:1:1) and under long-day conditions (16 h light and 8 h darkness).
3. The maceration process in this protocol is an adaptation from Franklin, 1945 [13].
4. Prepare at least three times the required volume.
5. The Eppendorf tubes must be opened, so the solution is evaporated during the maceration and it is necessary to add more solution frequently.
6. Use sterile PBS solution to avoid contaminations when the macerated hypocotyls are stored for a long period.
7. It is very important to completely homogenize the tissue to ensure that cells separate correctly. To that end, it is recommended to mash the tissue vigorously with a plunger that fits into Eppendorf tubes for, at least, 30 s.
8. Go over the slide systematically to avoid photographing the same field twice.

References

1. Fukuda H (2004) Signals that control plant vascular cell differentiation. Nat Rev Mol Cell Biol 5:379–391
2. Ko JH, Han KH, Park S et al (2004) Plant body weight-induced secondary growth in Arabidopsis and its transcription phenotype revealed by whole-transcriptome profiling. Plant Physiol 135:1069–1083
3. Sibout R, Plantegenet S, Hardtke CS (2008) Flowering as a condition for xylem expansion in Arabidopsis hypocotyl and root. Curr Biol 18:458–463
4. Chaffey N, Cholewa E, Regan S et al (2002) Secondary xylem development in Arabidopsis: a model for wood formation. Physiol Plant 114:594–600
5. Mark RE (1967) Cell wall mechanics of tracheids. Yale University Press, New Haven
6. Roberts AW, Frost AO, Roberts EM et al (2004) Roles of microtubules and cellulose microfibril assembly in the localization of secondary-cell-wall deposition in developing tracheary elements. Protoplasma 224:217–229

7. Pesquet E, Korolev AV, Calder G et al (2010) The microtubule-associated protein AtMAP70-5 regulates secondary wall patterning in Arabidopsis wood cells. Curr Biol 20: 744–749
8. Esau K (1977) Anatomy of the seed plants, 2nd edn. Wiley, New York
9. Karam GN (2005) Biomechanical model of the xylem vessels in vascular plants. Ann Bot 95: 1179–1186
10. Turner S, Gallois P, Brown D (2007) Tracheary element differentiation. Annu Rev Plant Biol 58:407–433
11. Evans WC (2009) Trease and Evans Pharmacognosy, 16th edn. Elsevier Inc., Edinburgh
12. Muñiz L, Minguet EG, Singh SK et al (2008) ACAULIS5 controls Arabidopsis xylem specification through the prevention of premature cell death. Development 135:2573–2582
13. Franklin GL (1945) Preparation of thin sections of synthetic resins and wood resin composites, and a new macerating method for wood. Nature 155:51



Chapter 11

Histochemical Detection of Peroxidase and Laccase Activities in Populus Secondary Xylem

Marta-Marina Pérez Alonso, Àngela Carrió-Seguí, and Hannele Tuominen

Abstract

Peroxidases (PRXs) and laccases (LACs) are enzymes involved in catalyzing the oxidation of the lignin monomers to facilitate lignin polymerization. However, due to the large number of genes composing these two families of enzymes, many details regarding their specific localization are only partially understood. Here, we present a fast and easy histochemical method that makes use of the artificial substrate 3,3′,5,5′--tetramethylbenzidine (TMB) to visualize PRX and LAC activities in the hybrid aspen (*Populus tremula* x *P. tremuloides*) xylem tissue. In addition, we describe a protocol that allows the detection of the PRX substrate, H_2O_2, using the nonfluorescent dye 2′,7′-dichlorodihydrofluorescein diacetate (H_2DCFDA) in woody tissues.

Key words Lignin, Peroxidase, Laccase, TMB, H_2DCFDA, H_2O_2, Cell wall, Xylem, Woody tissues, Populus

1 Introduction

Secondary xylem, or wood, is a specialized vascular tissue characterized by the presence of thick secondary cell walls composed of a variable mixture of cellulose, hemicellulose, and lignin polymers. Among them, lignin is an essential structural component that provides mechanical strength to upwards growth and hydrophobicity, therein enabling long-distance transport of water. The lignin polymer is primarily made of three different types of 4-hydroxycinnamyl alcohols, termed monolignols: *p*-coumaryl alcohol, coniferyl alcohol, and sinapyl alcohol, which are produced in the cytoplasm via the phenylpropanoid pathway. After their synthesis, monolignols are released into the apoplast, where they are oxidized into resonance-stabilized radicals by the action of two oxidative enzyme families, peroxidases (PRXs), and laccases (LACs). Thereafter, the resulting phenoxy radicals can be coupled in a combinatorial fashion. Once the radicals are incorporated into the growing lignin

Javier Agusti (ed.), *Xylem: Methods and Protocols*, Methods in Molecular Biology, vol. 2722,
https://doi.org/10.1007/978-1-0716-3477-6_11,
© The Author(s), under exclusive license to Springer Science+Business Media, LLC, part of Springer Nature 2024

polymer, the three classical monolignols described above form the main building blocks of lignin referred to as *p*-hydroxyphenyl (H), guaiacyl (G), and syringyl (S) units, respectively [1, 2].

Fast-growing trees, such as *Populus* and *Eucalyptus*, have emerged as valuable feedstock to produce biofuels and other lignocellulose-based materials. Nonetheless, the presence of lignin in the cell wall interferes with the extractability of fermentable sugars during the conversion of biomass to ethanol. To improve the exploitation of these woody feedstocks, substantial efforts have been made to identify and characterize enzymes involved in lignin biosynthesis [3, 4]. Unlike lignin biosynthesis, less is known about the specific PRX and LAC enzymes involved in lignin polymerization. The most remarkable problem is that both PRXs and LACs are encoded by multigene families with individual members showing functional redundancy [5, 6]. Thus, up to date, 93 PRX and 49 LAC genes have been identified in *Populus trichocharpa* [7, 8]. However, it remains uncertain which of these enzymes are responsible for monolignol oxidation. Pioneering works isolated five PRXs (PRX1, PRX2, PRX3–4, PRX5, and PRX6) and five LACs (LAC1, LAC2, LAC3, LAC90, and LAC110) from the *Populus trichocarpa* stem xylem tissue [9, 10]. Antisense suppression of either *PtrLAC3*, *PtrLAC90*, or *PtrLAC11*0 in poplar (*Populus tremula* × *Populus alba*) resulted in transgenic lines with no significant alteration in lignin content or composition, but trees with reduced *PtrLAC3* transcript accumulation showed perturbations of xylem fiber integrity [11]. More recently, a comprehensive genome-wide analysis performed in *P. trichocarpa* revealed four PRXs (*PtrPRX12*, *PtrPRX21*, *PtrPRX42*, and *PtrPRX64*) that were highly expressed in differentiating xylem. Downregulation of *PtrPRX21* translated in transgenic trees with a reduction of 20% in the lignin amount [12]. Using a similar approach, Lu et al. [8] showed the presence of 30 different LACs in *P. trichocarpa* xylem. In their work, the authors also demonstrated that the simultaneous down-regulation of 17 *PtrLACs* was accompanied by a significant decrease in the total lignin content [8]. While these studies corroborate the role of PRXs and LACs in lignin polymerization, they have not provided precise spatial information on the sites of lignin polymerization in the woody tissues of forest trees, which is hampered by the large size of gene families, incomplete genome sequences, functional redundancy, and, in case of some of the techniques, the requirement for transgene technology. Therefore, quick and easy methods are needed to reliably localize LAC and PRX activities in forest tree species.

Over the recent years, the utilization of fluorescence-tagged monolignols has appeared as a powerful method to detect the dynamics of lignification in vivo. Here, the three different monolignols, each covalently linked to a specific fluorescent reporter, are incorporated into the growing lignin polymer. After incorporation

into the cell wall, the monolignol reporter must react with exogenous molecular probes through a specific bioorthogonal reaction, followed by confocal fluorescence microscopic imaging of the fluorescent reporters [13]. Despite this technology being a step forward to study the intricacies of differential monolignol incorporation, it can be challenging due to difficulty during the chemical reporter preparation and the complexity of the data obtained. An easier and cheaper alternative is to use histochemical methods that enable the detection of the polymerizing enzymes PRXs and LACs or their substrates. However, although these methods are adequate for herbaceous plants, they are not necessarily applicable for woody tissues due to inherently poor penetration properties and extensive autofluorescence. Herein, we present a technique (Procedure 3.1) that uses the artificial substrate 3,3′,5,5′-tetramethylbenzidine (TMB) to visualize the localization of the activities of the lignin polymerization enzymes in hybrid aspen (*Populus tremula* × *P. tremuloides*) woody tissues. The chromogenic TMB substrate is oxidized both by PRXs and LACs when their respective co-substrate, H_2O_2 or O_2, is present [14, 15]. Oxidized TMB produces a blue precipitate, enabling the in situ detection of active lignin polymerization enzymes. In addition, this protocol makes use of different treatments to validate that TBM oxidation is driven by the activity of the lignin polymerization enzymes, rather than nonspecific oxidation due to external factors, for example, light exposition or the action of other apoplastic oxidases (Fig. 1). Importantly, direct inhibition of the PRX activity using salicylhydroxamic acid (SHAM) or indirect blockage using catalase as an H_2O_2 scavenger did not completely abolish the TMB staining (blue color) in newly formed xylem of hybrid aspen (Fig. 2). This blue color was visible even though we extended the incubation time or increased the concentration of the inhibitors. Therefore, the current protocol not only demonstrates the capability of LACs to oxidize TMB but also that TMB can be used to visualize simultaneously both PRX and LAC activities and specifically the LAC activities (after inhibition of the PRX activities) in the xylem cell walls of woody species. In addition, we provide a fast and simple protocol for ROS detection in woody tissues (Procedure 3.3) that has been modified on the basis of a protocol previously described in *A. thaliana* [16]. The non-fluorescent dye 2′,7′--dichlorodihydrofluorescein diacetate (H_2DCFDA) diffuses into the cell, where it is deacetylated by esterases to form 2′,7′--dichlorodihydrofluorescein (H_2DCF). In the presence of ROS, predominantly H_2O_2, the H_2DCF molecule is oxidized to 2′,7-dichlorofluorescein (DFC), leading to an intense green fluorescence that can be visualized using a confocal or epifluorescence microscope (Fig. 3). In *Arabidopsis* stems, fluorescein-diacetate staining has been reliably used to visualize the production of total ROS in lignifying cell walls [16]. Notably, both TMB and

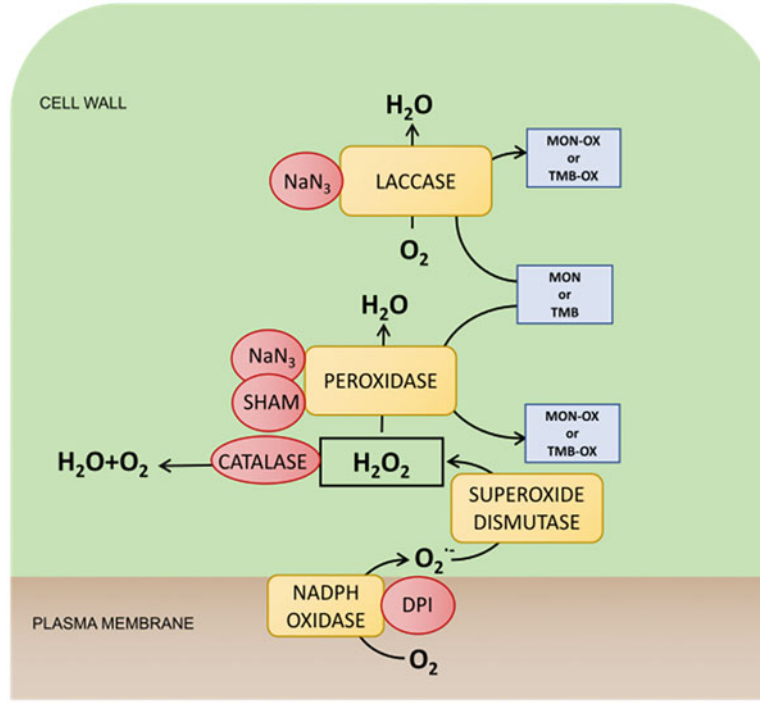


Fig. 1 Scheme showing the mechanism of monolignol oxidation in the cell wall. The NADPH oxidase-derived $O_2^{\cdot-}$ is utilized by the superoxide dismutase to catalyze oxidative reactions in the apoplast, resulting in the production of hydrogen peroxide (H_2O_2). Subsequently, peroxidases utilize H_2O_2 as a co-substrate to carry out the oxidative radicalization of monolignols (MON/MON-OX). On the other hand, laccases use O_2 to oxidase monolignols into radicals. TMB oxidation mechanism is indicated in blue (TBM/TMB-ox). Different enzyme inhibitors and H_2O_2 scavengers employed in the protocol are indicated in red. DPI; diphenyleneiodonium chloride, SHAM; salicylhydroxamic acid, NaN_3, sodium azide

H_2DCFDA methods were applied to hybrid aspen (*P. tremula* × *P tremuloides*) woody tissues, but the protocols described here can be easily transferred to other woody species.

2 Materials

2.1 General Remarks

1. Hybrid aspen trees (clone T89; *Populus tremula* × *P. tremuloides* plants) were used. For the images shown in this protocol, 1 m tall trees were grown in long-day conditions.
2. 1 cm tall pieces were collected from the tree stem and stored in separated 15 ml tubes filled with H_2O. The stem pieces were glued to a sample holder and sectioned at 30–50 μM using a Vibratome Leica VT1000 with 6 Hz frequency and program speed 4 (*see* **Note 1**).

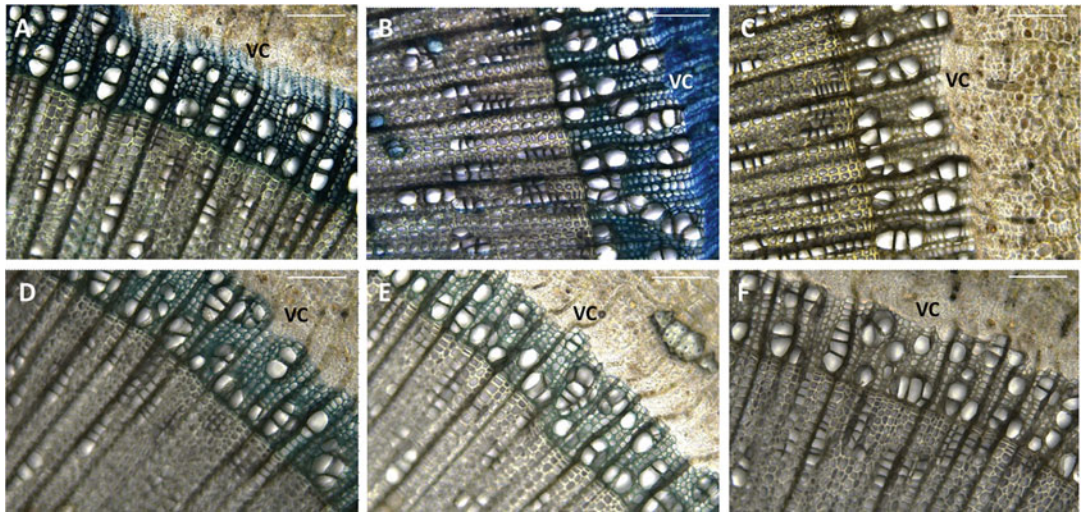


Fig. 2 Histochemical staining with tetramethylbenzidine (TMB) in cross sections of *Populus* stems. (**a**) TMB staining (without exogenous H_2O_2) reveals strong blue color specifically in the newly formed xylem cell walls, indicating the localization of the PRX and LAC activities. (**b**) TMB treatment in the presence of H_2O_2 (positive control) produces blue precipitates both in lignifying and non-lignifying tissues, indicating the presence of oxidative enzymes in these tissues. (**c**–**f**) Negative controls for the TMB staining. (**c**) TMB staining after boiling the samples for 30 min. (**d**) TMB staining after the SHAM treatment. (**e**) TMB staining after the catalase treatment. The remaining blue coloration (**d**, **e**) is indicative of LAC activity in the xylem cell walls. (**f**) TMB staining after the NaN_3 treatment. VC indicates the location of the vascular cambium. Scale bars represent 100 μM

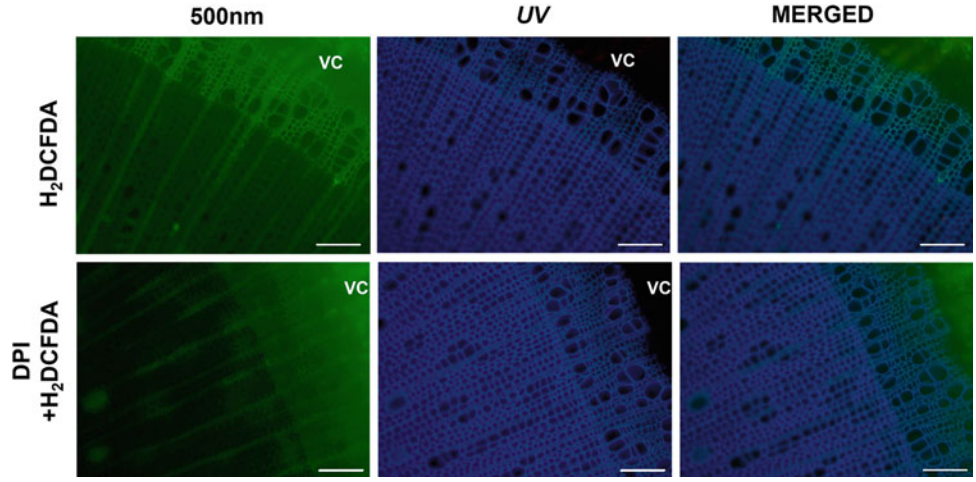


Fig. 3 Examples of H_2DCFDA staining in *Populus* stem cross sections. After the H_2DCFDA exposition, the green fluorescence product is visible in the xylem cell walls and in the living cells of the rays. DPI application substantially reduces the green fluorescence. VC indicates the location of the vascular cambium. Scale bars represent 100 μM

2.2 Equipment

1. pH meter.
2. Aluminum paper.
3. Thermo-Shaker.
4. Steril flat-bottom multiwell plates.
5. Forceps.
6. 2 ml microcentrifuge tubes.
7. Cyanocrylate glue (e.g., LOCTITE superglue).
8. Vibratome (e.g., Leica VT1000) provided with a razor blade adequated for hard tissues.
9. Microscope slides and coverslips.
10. Confocal microscope (e.g., Zeiss LSM780) or epifluorecent microscope (e.g., Leica DMi8).

2.3 Reagents

1. 3,3′,5,5′-Tetramethylbenzidine (TMB; 860336:MERCK).
2. 2′,7′-Dichlorofluorescein diacetate (H_2DCFDA; 287810: MERCK).
3. Salicylhydroxamic acid (SHAM; S607:MERCK).
4. Catalase from bovine liver (C9322:MERCK).
5. Sodium azide (NaN_3; 7128:Fluka).
6. Diphenyleneiodonium chloride (DPI; D2926:MERCK).
7. Dimethyl sulfoxide (DMSO).
8. Hydrogen peroxide (30% H_2O_2 in water (w/w); HX0640: MERCK).

2.4 Detection of Xylem Cell Wall PRXs and LACs

1. Reaction buffer: Prepare a 0.05 M phosphate-citrate buffer pH = 5.0 by mixing 27.5 ml of 0.2 M $Na_2HPO_4 \cdot 2H_2O$ (MW = 177.99 g/mol), 24.3 ml of 0.1 M citric acid (MW = 192.12 g/mol), and 50 ml distilled water. If needed, adjust the pH to 5 using HCl or NaOH.
2. TMB stock solution: Dissolve 10 mg of TMB in 10 ml DMSO to obtain a final concentration of 1 mg/ml (*see* **Note 2**).

2.5 Enzyme Inhibition and ROS Scavengers

1. SHAM stock solution (1 M): Dissolve 1.53 g of SHAM (MW = 153.14 g/mol) in 10 ml of DMSO (*see* **Note 2**).
2. DPI stock solution (10 mM): Dissolve 3.14 mg of DPI (MW = 314.55 g/mol) in 1 ml of DMSO (*see* **Note 2**).
3. NaN_3 stock solution (10 mM): Dissolve 6.5 mg of NaN_3 (MW = 65.01 g/mol) in 10 ml distilled H_2O (*see* **Notes 3** and **4**).

2.6 Monitoring ROS

1. Reaction buffer: Prepare a 50 mM NaH_2PO_4 solution (MW = 137.99 g/mol) and adjust the pH to 6 using NaOH.
2. H_2DCFDA stock solution: Dissolve 4.8 mg of 2′,7′--Dichlorofluorescein diacetate (MW = 487.29 g/mol) in 100 μl of DMSO to obtain a final concentration of 100 mM (*see* **Note 5**).

3 Methods

3.1 Detection of Xylem Cell Wall PRXs and LACs

1. Fresly prepare TMB working solutions as indicated:
   (a) TMB working solution A: For a total volume of 20 ml, mix 2 ml of the TMB stock solution, *see* Subheading 2.4, 17.990 ml of the reaction buffer, and 10 μl of 30% H_2O_2.
   (b) TMB working solution B: TMB working solution A without adding H_2O_2.
2. Prepare a negative control to confirm that the TMB oxidation is specifically mediated by proteins. Place stem cross sections in 2 ml microcentrifue tubes filled with distilled water, and place the samples in a thermoblock at 100 °C for 30 min.
3. Label one flat-bottom multiwell plate with the different treatments to be applied: TMB-A, TMB-B, and TMB boiled control. Fill the labeled wells with 2 ml of distilled water using a sterilized plastic pasteur pipette, and place stem cross sections inside each well using steril forceps (*see* **Note 6**).
4. Remove water from the wells and fill each well with 3 ml of the corresponding working solution treatment, *see* Subheading 2.4 (*see* **Note 7**). Cover the plates with aluminum foil to avoid unespecific TMB oxidation.
5. Incubate for a minimum of 30 min at RT with gently shaking.
6. Stop the reaction by rinsing the sections carefully with water. Pick up the sections on a microscope slide, and mount in water or in 50% glycerol.
7. Examine the sections immediately with a light microscope. Blue precipitates in sections exposed to TMB in the presence of H_2O_2 (TMB-A treatment) indicate on the activities of all oxidative enzymes, while blue staining in sections exposed to TMB without exogenous H_2O_2 (TMB-B treatment) indicates PRX and LAC activities in the xylem (Fig. 2a–c).

3.2 Enzyme Inhibition and ROS Scavengers

1. PRX activity inhibitor:
   (a) Prepare SHAM working solution (50 mM) by mixing 1 ml of the stock solution, *see* Subheading 2.5, and 19 ml of distilled H_2O (*see* **Note 6**).

(b) Incubate stem cross sections in 3 ml of the SHAM working solution, for 2.5 h at RT with shaking. Remove the SHAM solution, rinse twice carefully using distilled water, and stain the samples using the TMB-B working solution (*see* Subheading 3.1). Remaining blue staining is indicative of LAC activity (Fig. 2d).

2. H_2O_2 scavenger:
   (a) Prepare a catalase solution(~1000 U/ml) by dissolving 5 mg of the enzyme powder into 10 ml distilled water (*see* **Notes 8** and **9**).
   (b) Incubate cross sections in 3 ml of the catalase solution for 4 h (RT or 37 °C with continuous shaking). Remove solution and stain sections using the TMB-B working solution (*see* Subheading 3.1). Remaining blue staining is indicative of LAC activity (Fig. 2e).
3. PRX and LAC activity inhibitor:
   (a) Prepare NaN_3 working solution (1 mM) by mixing 1 ml of the stock solution, *see* Subheading 2.5, and 9 ml distilled H_2O (*see* **Note 4**).
   (b) Incubate stem cross sections using 3 ml of the above prepare solution for 1 h at RT. After incubation, rinse twice with water and perform the TMB-B staining as described in Subheading 3.1. Absence of blue coloration confirms effective inhibition of PRXs and LACs (Fig. 2f).

3.3 Monitoring ROS

1. H_2DCFDA working solution: Prior to the proceduce, prepare a fresh 50 μM H_2DCFDA solution by mixing 10 μl of the H_2DCFDA stock solution (*see* Subheading 2.6) and reaction buffer for a total volume of 20 ml. Protect the solution from light to avoid rapid H_2DCFDA oxidation.
2. Place stem cross sections in a multiwell plate prefilled with 2 ml of distilled water (*see* **Note 6**), and incubate 24 h at RT to reduce H_2O_2 derived from wounding.
3. Remove water and fill the well with 3 ml of freshly prepared H_2DCFDA working solution. Incubate 15 min at RT with continuous shaking in complete darkness.
4. Discard the solution using a sterilized plastic pasteur pipette and repeat **step 3**.
5. After incubation, rinse sections carefully with distilled water two times.
6. Examine immediately under an epifluorescence microscope using 405 nm excitation laser to observe autofluorescence associated with lignin and 488–495 nm excitation laser to observe H_2DCFDA-associated fluorescence. The green

fluorescence indicates on the localisation of the H_2O_2 (Fig. 3). Read Subheading 3.2 to perform additional control experiments.

7. To remove the newly formed H_2O_2, an NADPH oxidase inhibitor can be employed as follows:
   (a) Prepare a 1 mM DPI working solution by adding 1 ml of the DPI stock solution, *see* Subheading 2.5, to 9 ml of distilled H_2O.
   (b) Incubate stem cross sections in 3 ml of 1 mM DPI for 2 h (RT, with continuous shaking), rinse twice with distilled water and proceed with the H_2DCFDA protocol. As shown in Fig. 3, green fluorescence is not completely abolished.

4 Notes

1. We strongly recommend to keep the obtained stem sections in water or phosphate saline buffer (pH = 7.4) in order to preserve the integrity of the xylem anatomy and prevent reductions in the enzyme activities.
2. Divide the stock solution into aliquots, and store at −20 °C until needed.
3. Stock solution can be stored at RT up to 3 months.
4. NaN_3 is extemely toxic. Therefore, when working with NaN_3, gloves should be worm and solution must be prepared under fume hood.
5. The stock solution can be stored at −20 °C until further use always protected from light exposure.
6. If phosphate saline buffer was used to store the cross sections after sectioning, we recommend rinsing cross sections in water several times prior to the Procedure.
7. TMB boiled control sections have to be treated using the TMB working solution B.
8. To keep an efficient enzymatic activity, we recommend preparing fresh catalase solution prior to the Procedure. However, it can be kept at 4 °C for a maximum of 48 h.
9. Catalase from bovine liber contains 2000–5000 U/mg, and we recommend repeating this treatment with different catalase solutions to ensure the reproducibility of the results.

References

1. Wang Y, Chantreau M, Sibout R et al (2013) Plant cell wall lignification and monolignol metabolism. Front Plant Sci 4. https://doi.org/10.3389/fpls.2013.00220
2. Liu Q, Luo L, Zheng L (2018) Lignins: biosynthesis and biological functions in plants. Int J Mol Sci 19(2):335. https://doi.org/10.3390/ijms19020335
3. Carocha V, Soler M, Hefer C et al (2015) Genome-wide analysis of the lignin toolbox of *Eucalyptus grandis*. New Phytol 206(4): 1297–1313. https://doi.org/10.1111/nph.13313
4. Zhang J, Tuskan GA, Tschaplinski TJ et al (2020) Transcriptional and post-transcriptional regulation of lignin biosynthesis pathway genes in Populus. Front Plant Sci 11. https://doi.org/10.3389/fpls.2020.00652
5. Cosio C, Dunand C (2009) Specific functions of individual class III peroxidase genes. J Exp Bot 60:391–408. https://doi.org/10.1093/jxb/ern318
6. Turlapati PV, Kim K-W, Davin LB et al (2011) The laccase multigene family in *Arabidopsis Thaliana*: towards addressing the mystery of their gene function(S). Planta 233:439–470. https://doi.org/10.1007/s00425-010-1298-3
7. Ren LL, Liu YJ, Liu HJ et al (2014) Subcellular relocalization and positive selection play key roles in the retention of duplicate genes of *Populus* class III peroxidase family. Plant Cell 26:2404–2419. https://doi.org/10.1105/tpc.114.124750
8. Lu S, Li W, Wei H et al (2013) Ptr-MiR397a is a negative regulator of laccase genes affecting lignin content in *Populus trichocarpa*. Proc Natl Acad Sci 110:10848–10853. https://doi.org/10.1073/pnas.1308936110
9. Christensen JH, Bauw G, Gjesing Welinder K et al (1998) Purification and characterization of peroxidases correlated with lignification in poplar xylem. Plant Physiol 118:125–135. https://doi.org/10.1104/pp.118.1.125
10. Ranocha P, McDougall G, Hawkins S et al (1999) Biochemical characterization, molecular cloning and expression of laccases – a divergent gene family – in poplar. Eur J Biochem 259:485–495. https://doi.org/10.1046/j.1432-1327.1999.00061.x
11. Ranocha P, Chabannes M, Chamayou S et al (2002) Laccase down-regulation causes alterations in phenolic metabolism and cell wall structure in poplar. Plant Physiol 129:145–155. https://doi.org/10.1104/pp.010988
12. Lin CY, Li Q, Tunlaya-Anukit S et al (2016) A cell wall-bound anionic peroxidase, *PtrPO21*, is involved in lignin polymerization in *Populus trichocarpa*. Tree Genet Genomes 12:22. https://doi.org/10.1007/s11295-016-0978-y
13. Morel O, Lion C, Neutelings G et al (2022) REPRISAL: mapping lignification dynamics using chemistry, data segmentation, and ratiometric analysis. Plant Physiol 188:816–830. https://doi.org/10.1093/plphys/kiab490
14. Herpoël I, Moukha S, Lesage-Meessen L et al (2000) Selection of *Pycnoporus cinnabarinus* strains for laccase production. FEMS Microbiol Lett 183:301–306. https://doi.org/10.1111/j.1574-6968.2000.tb08975.x
15. Ros Barceló A (1998) The generation of H_2O_2 in the xylem of *Zinnia elegans* is mediated by an NADPH-oxidase-like enzyme. Planta 207:07–216. https://doi.org/10.1007/s004250050474
16. Hoffmann N, Benske A, Betz H et al (2020) Laccases and peroxidases co-localize in lignified secondary cell walls throughout stem development. Plant Physiol 184:806–822. https://doi.org/10.1104/pp.20.00473



Chapter 12

Lignin Analysis by HPLC and FTIR: Spectra Deconvolution and S/G Ratio Determination

Jorge Reyes-Rivera and Teresa Terrazas

Abstract

Fourier transform infrared spectroscopy (FTIR) is a simple nondestructive technique that allows the user to obtain quick and accurate information about the structure of the constituents of wood. Spectra deconvolution is a computational technique, complementary to FTIR analysis, which improves the resolution of overlapped or unobserved bands in the raw spectra. High performance liquid chromatography (HPLC) is an analytical technique useful to determine the ratio of the lignin monomers obtained by the alkaline nitrobenzene oxidation method. Furthermore, lignin content has been commonly determined by wet chemical methods; Klason lignin determination is a quick and accessible method. Here, we detail the procedures for chemical analysis of the wood lignin using these techniques. Additionally, the deconvolution process of FTIR spectra for the determination of the S/G ratio, in lignin isolated by this or other methods, is explained in detail.

Key words FTIR, Spectra deconvolution, HPLC, Lignin content, S/G ratio

1 Introduction

The chemical composition of secondary xylem (wood) has been extensively studied in economically important species [1–3]. Because lignin is the second most abundant component in wood after cellulose, it has been widely studied to determine its influence on the structural properties of wood [4–7]. A considerable number of techniques have been developed and applied to the qualitative and quantitative analysis of lignin [7]. Among the most frequently used analytical methods are Fourier transform infrared spectroscopy (FTIR) [8–26] and high performance liquid chromatography (HPLC) [22, 27, 28]; Table 1 briefly summarizes their applications. On the other hand, lignin content has been commonly determined by wet chemical methods, with Klason lignin analysis being the most frequently used [21, 22, 28, 31–35].

Javier Agusti (ed.), *Xylem: Methods and Protocols*, Methods in Molecular Biology, vol. 2722,
https://doi.org/10.1007/978-1-0716-3477-6_12,
© The Author(s), under exclusive license to Springer Science+Business Media, LLC, part of Springer Nature 2024

Table 1
Applications and complements for lignin analysis by FTIR and HPLC

Method/Analysis	Applications	References
FTIR	Lignin structure	[8–22]
	Lignin monomers	[14, 19, 21–26, 29, 30]
HPLC	Lignin structure	[27]
	Lignin monomers	[22, 28]
Klason lignin	Lignin content	[21, 22, 27, 31–35]
Nitrobenzene oxidation	Lignin monomers	[5, 13, 22, 28, 36–38]
Evolutive inference		
FTIR, HPLC, anatomy, and Klason lignin	Comparative, qualitative and quantitative: Lignin content, lignin monomers, structure–function relationship	[22]
FTIR, Py-GC/MS, 2D-RNM, anatomy, and dioxane lignin	Comparative, qualitative and quantitative: S/G ratios, wood anatomy, and structure–function relationship	[29]
Chemometrics		
FTIR, LR	Quantitative: Lignin content	[39]
FTIR, MLR	Quantitative: Lignin content, celluloses, and hemicellulose	[40]
FTIR, PLS	Quantitative: Percentage of acetyl groups Quantitative: Lignin content, celluloses, hemicellulose and extractives Quantitative: Lignin content (Kraft method)	[41] [42] [43]
FTIR, PLS, PCR	Quantitative: Hydroxyl groups content Quantitative: Lignin content prediction	[44] [45]
FTIR, PCA	Qualitative: Characterization of tropical woods Qualitative: Lignin characterization Qualitative: Separation of species	[10] [19] [46]
FTIR, PCA, HCA, PLS	Qualitative and quantitative: Lignin content prediction and characterization of woods Qualitative and quantitative: Lignocellulose degradation in hardwoods by fungi Qualitative and quantitative: Structure and monomers of various technical lignins	[47] [48] [30]

Abbreviations: *HCA* hierarchical clustering analysis, *LR* linear regression, *MLR* multiple linear regression, *FTIR* Fourier transform infrared spectroscopy, *Py-GC/MS* Pyrolysis-gas chromatography/mass spectrometry, *PCA* principal component analysis, *PCR* principal component regression, *PLS* partial less squares

FTIR spectroscopy has been used as a simple technique for obtaining quick and accurate information about the structure of the chemical constituents of wood and the changes they undergo during developmental or degradation processes [7, 22, 29, 45–50]. This nondestructive technique has multiple advantages, such as high sensitivity and selectivity, high signal/noise ratio, high accuracy, ease of data handling, simplicity of the equipment required, short analysis times (minutes, compared with several days, as required by other methods), and the use of small sample sizes (a few milligrams, compared with several grams, as required by conventional gravimetric techniques) [7, 13, 47]. In addition, the FTIR spectrum of a lignin sample provides an overview of its chemical structure [9, 21, 22, 29]. HPLC is a nondestructive analytical method that allows to separate and analyze non-volatile or thermally unstable molecules with various polarities, as well as the recovery of the fractions in the sample [22, 27, 28]. Thus, this analytical technique has also been useful to determine the Syringyl/Guaiacyl (S/G) ratio in the lignin obtained by alkaline nitrobenzene oxidation [13, 22, 28, 36–38].

The range of applications of FTIR spectroscopy is very broad. This technique is useful in the study of changes in the chemical composition of wood, that is, by tracking the peaks assigned to lignin (Table 2) or carbohydrates, as described in the literature [9, 20, 22, 42, 48–50]. Furthermore, chemometrics applied to FTIR spectra is a powerful tool for both qualitative and quantitative analysis. The structural analysis of lignin by FTIR spectroscopy, complemented with the determination of the S/G ratio by HPLC, allowed to relate the lignification of wood to developmental aspects of various succulent plants [22]. Recently, differences in lignification of several cacti with contrasting growth forms were attributed to the wood anatomy, the height of the stem, and the reduction of the oxidative damage within the stem [29] (Fig. 1a–e). Besides, the deconvolution of the FTIR spectra of lignin enabled the determination of the S/G ratio when the corresponding bands were not easily observable in the raw spectra [29]. This effect is very common in lignin analysis by infrared spectrometry and involves intrinsically overlapped bands [63] and the dominance of one band that overshadows other closer bands [29]. For example, the dominant band at 1315 cm^{-1}, assigned to S units, overshadows the band at 1267 cm^{-1}, assigned to G units (Fig. 1b), hindering the determination of the S/G ratio from the FTIR raw spectra. However, mathematical modeling of the individual components (deconvoluted peaks) allows the contour of the original infrared spectrum to be obtained by curve-fitting [64–66]. Thus, the deconvolution allows to analyze the proportions of the S and G units based on the integrated area of each individual component. The S/G ratios, obtained from deconvoluted FTIR spectra, largely correspond to those obtained by two-dimensional nuclear magnetic resonance spectroscopy (2D-NMR) [29].

Table 2
Assignment of bands in FTIR spectra of wood samples

Wave number (cm^{-1})	Assignments	References
3568–3577	Intramolecular hydrogen bond in phenolic groups	[51, 52]
3446-3455	Phenolic OH group stretching	[53]
3400-3430	O—H stretching	[7, 9, 51, 53–59]
2930-2950	CH_2 asymmetric vibration (guaiacyl-syringyl)	[49, 50, 53, 58]
2850-2920	C—H stretching in methyl and methylene groups	[51, 53, 54, 56, 59]
1734–1738	Unconjugated C=O in xylans (hemicellulose)	[7, 9, 54, 55]
1700-1715	Carbonyl stretching in conjugated ketone and conjugated carboxylic groups	[54–56, 59]
1650	Absorbed O—H and conjugated C—O	[9]
1610	C=C aromatic ring vibration	[53, 54, 56]
1594	C=C stretching of the aromatic ring (siringyl), C=O stretch, CH deformation	[52]
1501-1511	C=C aromatic ring vibration (guaiacyl-syringyl)	[7, 9, 46, 47, 49–51, 53, 55, 58, 59]
1463	CH_2 deformation stretching in lignin and xylan	[47]
1460	C—H asymmetric deformation	[13, 55]
1420-1430	Aromatic skeletal combined with C–H in-plane deforming and stretching	[47, 51, 54, 58]
1375	C—H deformation in cellulose and hemicellulose, and aliphatic C—H stretching in methyl and phenol OH	[9, 47]
1330	C—H vibration in cellulose	[9]
1320-1326	Syringyl ring breathing with C—O stretching	[9, 13, 29, 30, 56, 60]
1317-1321	Condensation of guaiacyl and syringyl units, syringyl unit and CH_2 bending stretching (softwood and hardwood, respectively)	[47]
1285	C—O and glucopyranosic cycle guaiacylic symmetric vibration	[49]
1266-1280	Guaiacyl ring breathing, C—O stretching in lignin and C—O linkage in guiacyl aromatic methoxyl groups	[9, 29, 30, 46, 47, 56, 60]
1244	Syringyl ring and C—O stretching in lignin and xylan	[9]
1225	C—O and glucopyranosic cycle syringylic symmetric vibration	[49, 54, 55]
1219–1211	C—C, C—O and C=O stretching in guaiacyl units	[58]
1170	C—O stretching in alcohol	[58]
1160	C—O—C stretching in pyranose rings, C—O stretching in aliphatic groups	[47]

(continued)

Table 2 (continued)

Wave number (cm^{-1})	Assignments	References
1158	C—O—C vibration in cellulose and hemicellulose	[9]
1151	CH stretching in aromatic ring (guaiacylic)	[7, 58]
1130	Aromatic C—H in plane deformation (guaiacylic)	[52]
1122	Aromatic skeletal and C—O stretching	[9]
1115-1116	C—O—C stretching and symmetric vibration of the ester linkage, and CH stretching in aromatic ring (syringylic)	[7, 61]
1085	C—O deformation in secondary alcohol and aliphatic ether	[54]
1048	C—O stretch in cellulose and hemicellulose	[9]
1030	C—H in-plane deformation in guaiacyl and C—O deformation in primary alcohol	[47, 54, 59, 62]
913	=CH out-of-plane deformation in aromatic ring (guaiacylic-syringylic)	[50]
898	C—H deformation in cellulose	[9, 47]
835–855	Aromatic C—H out-of-plane deformation	[13, 54, 56]

Here, we detail the procedures for determining the Klason lignin content of wood samples and their subsequent analysis by FTIR spectroscopy. The technique for the isolation of lignin subunits by nitrobenzene oxidation and their analysis by HPLC are also described. Additionally, we detail the computational process for the deconvolution of FTIR spectra in order to determine the S/G ratio in isolated lignin.

2 Materials

2.1 Sampling and Extractive-Free Wood Isolation

Use ultrapure water and analytical grade reagents to prepare all solutions.

1. Mini mill.
2. Ethanol–benzene mixture (1:2): mix together 1 volume of ethanol and 2 volumes of benzene (*see* **Note 1**).
3. Ethanol: 96% solution in distilled water.
4. Soxhlet apparatus: A heating mantle (HM), a round bottom flask (RBF), a Soxhlet extractor (SE), extraction thimbles (ET), an Allihn condenser (AC), and a cold circulator (CC). For assembly, *see* Fig. 2a.

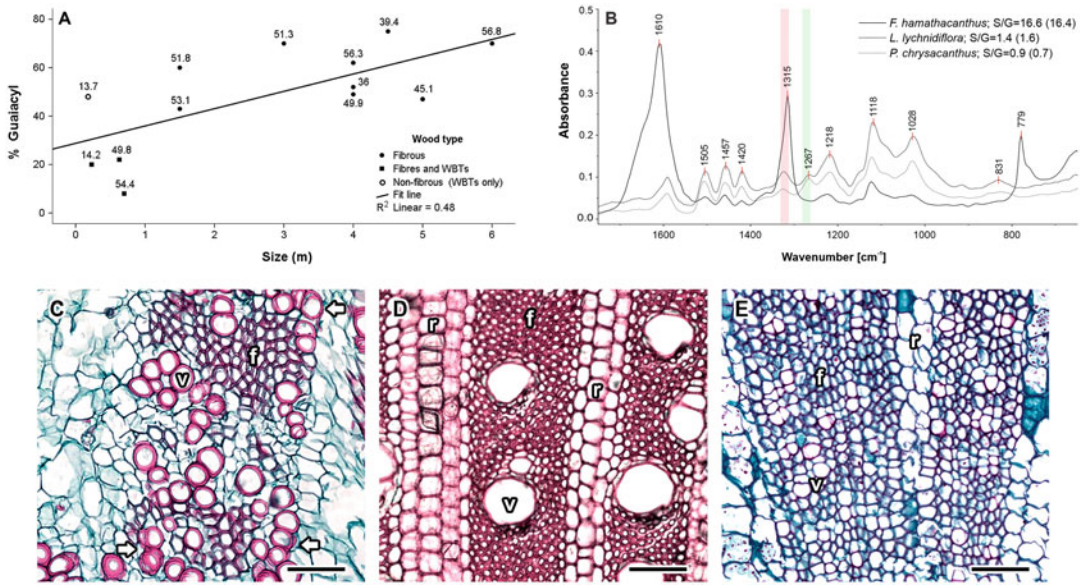


Fig. 1 (**a**) Content of guaiacyl lignin in the wood versus size of the species in Cactaceae; species with lignified rays and fast growth rates have more guaiacyl lignin. Numbers above the dots show the percentage of Klason lignin. Modified from [22]. (**b**) ATR-FTIR spectra for tree different types of wood with contrasting growth form and different S/G ratios; note that band assigned to S lignin overshadows the band assigned to G units in the raw spectrum of *Ferocactus hamatacanthus*. The S/G ratios obtained by 2D-NMR are shown in parentheses. (**c**–**e**) Cross sections of the wood in different species of Cactaceae: (**c**) *F. hamatacanthus*, dimorphic; (**d**) *Leuenbergeria lychnidiflora*, fibrous with lignified rays; (**e**) *Pylosocereus chrysacanthus*, fibrous with non-lignified rays. Bar is 100 μm; c = crystal, r = rays, v = vessels,f = fibers, arrows = wide band tracheids

5. Convection oven.
6. Desiccator.
7. Rotary evaporator.
8. Cold circulator.
9. Büchner fritted disc funnel (medium porosity: 10–15 μm pore size).
10. Amber glass bottles, capacity 10 mL.
11. Reflux apparatus: A stirring hotplate (SHp), an Erlenmeyer flask (EF), a magnetic stirrer bar (SB), an Allihn condenser (AC), and a cold circulator (CC). For assembly, *see* Fig. 2b.
12. Vacuum filtration apparatus: A trapped vacuum pump, Kitasato flasks (KF), an Erlenmeyer flask (EF), a Büchner funnel (BF), plastic tubing (PT), a rubber stopper (RS), a crucible holder (CH), a siphon tube (ST). For assembly, *see* Fig. 2c.

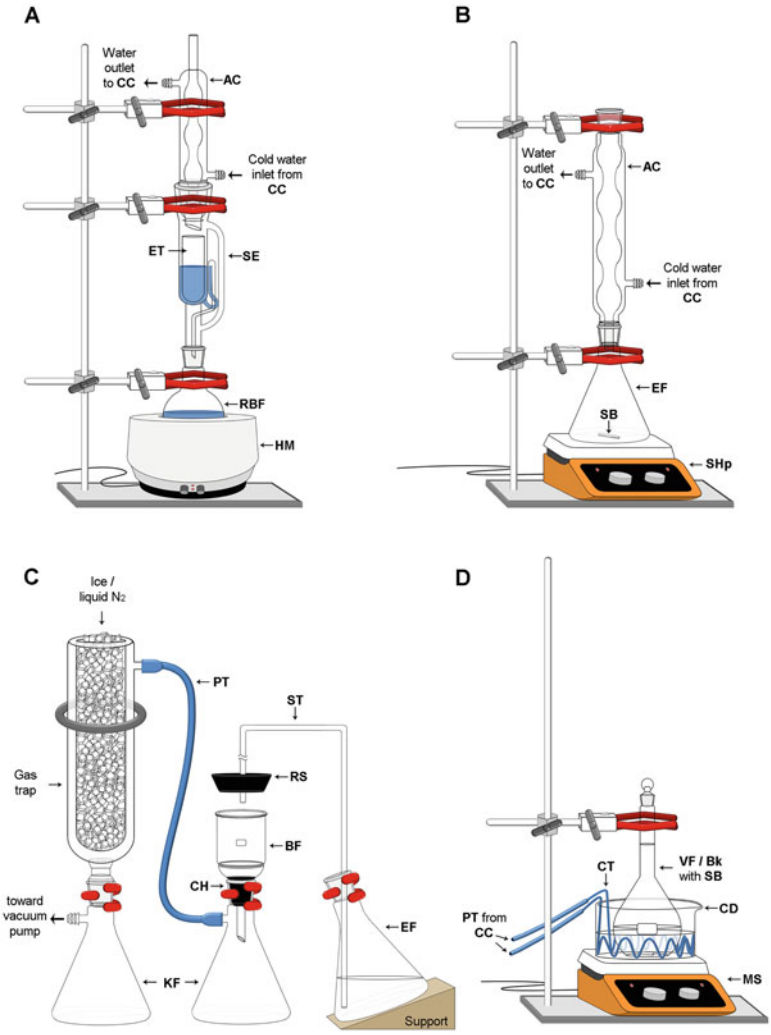


Fig. 2 Assembling of the laboratory equipment. (**a**) Soxhlet apparatus: assembly preferably in a fume hood or in a place equipped with fume extractor. (**b**) Reflux apparatus. (**c**) Vacuum filtration apparatus. (**d**) Cooling bath with stirring, for preparation of acidic or basic aqueous solutions (use a volumetric flask), and for determining Klason lignin (use a beaker). The magnetic stirrer, crystallizer dish, and magnetic stirrer bar can be replaced by an ultrasonic bath

2.2 Klason Lignin

1. Sulfuric acid: 72% H_2SO_4 solution, 24 N. Carefully and slowly pour 673.3 mL of concentrated 95% H_2SO_4 (sp gr 1.84) into a 1-L volumetric flask containing 300 mL of distilled water (*see* **Note 2**), and fill the flask up to the mark. Store at room temperature.
2. Cooling bath with stirring: magnetic stirrer (MS), magnetic stirrer bar (SB), crystallizing dish (CD), volumetric flask (VF) and/or a beaker (Bk), copper tubing (CT), plastic tubing (PT), cold circulator (CC). For assembly, *see* Fig. 2d.

3. Büchner fritted disc funnel (fine porosity: 4–5.5 μm pore size).
4. Vacuum filtration apparatus.

2.3 FTIR Spectroscopy

1. Hydraulic press, 12 tons.
2. KBr pellet die.
3. Kimwipes®.
4. Anhydrous acetone.
5. Agate mortar and pestle.
6. Potassium bromide (KBr).
7. FTIR spectrometer.
8. OMNIC™ Series Software.
9. Origin Pro 2016™ Software (OriginLab Corp., USA).

2.4 Alkaline Nitrobenzene Oxidation of Lignin

1. Reactor system, 2 L capacity.
2. Glass vials, 16 mL capacity.
3. Separatory funnels, 50 mL capacity.
4. Sodium hydroxide: 2 M NaOH solution. Carefully and slowly transfer 81.05 g of 98.7% sodium hydroxide (sp gr 2.08) into a beaker containing 250 mL of distilled water (*see* **Note 2**) and dissolve. Pour the solution into a 1-L volumetric flask, and fill the flask up to the mark. Store at room temperature until use.
5. ≥99.0% Nitrobenzene.
6. ≥99.5% Chloroform.
7. Hydrochloric acid: 4 M HCl solution. Carefully and slowly pour 328.5 mL of 37% HCl (sp gr 1.2) into a 1-L volumetric flask containing 250 mL of distilled water (*see* **Note 2**), and fill the flask up to the mark. Store at room temperature until use.
8. pH Meter.

2.5 Determination of the S/G Ratio by HPLC

1. Supelco® mobile phase filtration apparatus.
2. Vacuum pump.
3. Ultrasonic bath, capacity 2.8 L.
4. High purity grade He (can alternatively be used for degas solvents).
5. Acetonitrile-water mixture (1:1): Mix together 1 volume of acetonitrile and 1 volume of water (*see* **Note 3**).
6. Acetonitrile-water mixture (1:6): Mix together 1 volume of acetonitrile and 6 volumes of water (*see* **Note 3**).
7. MF-Millipore cellulose membrane, 0.22 μm.
8. Whatman® regenerated cellulose membrane filters, 0.45 μm.

9. Trifluoroacetic acid buffer: 0.1% TFA solution in distilled water (*see* **Note 3**).
10. pH Meter.
11. Vanillin standard. The next concentrations are suggested as a reference for the construction of calibration curves: 0.375, 0.75, 1.125, and 1.5 mM.
12. Syringaldehyde standard. The next concentrations are suggested as a reference for the construction of calibration curves: 0.825, 1.65, 2.475, and 3.3 mM.
13. Amber glass vials, 2 mL capacity.
14. Micropipettes, 100–1000 and 1000–5000 μL capacities.
15. Analytical balance.
16. HPLC System.
17. Hibar® 250–4 LiChrosorb® RP-18 (5 μm) HPLC column.
18. Manu-Cart® NT Cartridge Holder.

3 Methods

Process the samples in triplicate. Record the weight of the Büchner funnels, extraction thimbles and samples until they have reached a constant weight (moisture-free). Record each weight to the nearest 0.1 mg (e.g., 1.0001 g).

3.1 Sample Preparation

1. Obtain a wooden disk that is 10-cm thick (*see* **Note 4**). Obtain wood chips of medium size (2 cm). Dry the wood chips in a convection oven at 50 °C for 2–4 days (*see* **Note 5**).
2. When wood chips are dry, reduce the particle size using a Wiley mill and sieve the sample through a 40- or 60-mesh screen (*see* **Note 6**).
3. Dry the milled wood in a convection oven at 105 °C to a constant weight (*see* **Note 7**).

3.2 Obtaining Extractive-Free Wood

1. Prepare the Soxhlet apparatus (*see* Fig. 2a).
2. Weigh out 2 g of the sample and record the weight (*see* **Note 8**).
3. Weigh the extraction thimble and record its weight (*see* **Notes 7** and **8**). Place the sample in the extraction thimble (*see* **Note 9**). Label each thimble with a graphite pencil, and assemble the Soxhlet apparatus (*see* Fig. 2a and **Note 10**).
4. Perform the Soxhlet extraction with the ethanol–benzene mixture (1:2) for 4–5 h (not less than 24 cycles). After completing the required number of cycles, dry the extraction thimble with

the sample and record the weight (*see* **Note 11**). While the extraction thimble is drying, concentrate the extract (approximately 2 mL) contained in the distillation flask using a rotary evaporator (*see* **Note 12**) and store at 10 °C.

5. Repeat the extraction step as above but with a solution of 96% ethanol as the solvent. When finished, dry the extraction thimble with the sample and record the weight (*see* **Note 13**). Concentrate the extract and store at 10 °C (*see* **Note 12**).
6. Prepare the reflux apparatus (*see* Fig. 2b).
7. Place the dry wood in a 1 L flask, add 850 mL of distilled water, heat to a boil, and allow the sample to reflux with stirring for 1 h (*see* Fig. 2b).
8. Filter the sample through a Büchner funnel with a medium-pore fritted disk (*see* Fig. 2c and **Note 14**). Recover and store the extract (*see* **Note 15**).
9. Dry the Büchner funnel with the sample at 105 °C to a constant weight and record its weight (*see* **Note 8**).
10. Finally, calculate the percentage of wood extract according to the weight lost in each extraction (*see* **Note 16**) using the following formula:

$$\% = \frac{(A + B + C)}{W_0} \times 100$$

where:

A = weight lost (g) after extraction with the ethanol–benzene mixture (2:1).

B= weight lost (g) after extraction with 96% ethanol.

C = weight lost (g) after extraction with hot water.

W_0 = initial sample weight (g).

3.3 Klason Lignin

1. Prepare the cooling bath with stirring at a temperature of 2 °C (*see* Fig. 2d).
2. Place 1 g of extractive-free wood (record the weight to the nearest 0.1 mg; *see* **Note 8**) in a 50-mL beaker, and slowly add 15 mL of 72% sulfuric acid (previously cooled at 15 °C).
3. After the acid is added, homogenize the sample with the aid of a glass stir rod. When the sample is completely impregnated with sulfuric acid, the bath temperature can be raised to 18 °C. Then, with the aid of tweezers, place a magnetic stir bar in the beaker and turn on the magnetic stirrer at a low speed. Cover the beaker with a watch glass, and keep it in the cooling bath for 2 h (*see* **Note 17**).

4. Transfer the material to an Erlenmeyer flask containing 300 mL of distilled water, homogenize the mixture, and then add another 260 mL of distilled water (560 mL of water in total).
5. Boil the solution in the reflux apparatus for 4 h with stirring (*see* **Note 18**).
6. Allow lignin to settle to the bottom of the flask while keeping it in a tilted position (*see* **Note 19**).
7. Siphon or decant the supernatant without stirring up the precipitate. Filter through a Büchner funnel with a fine-pore fritted disk that has previously been dried to a constant weight (*see* **Note 8**).
8. Transfer the precipitated lignin directly to the Büchner filter with the aid of a rod with rubber policeman.
9. Wash the lignin fraction using 50–100 mL of distilled water, then filter with just enough vacuum to remove the excess of water.
10. Dry the Büchner filter with the sample at 105 °C, allow it to cool and record the weight (*see* **Note 8**).
11. Finally, determine the percentage of lignin with the following formula:

$$\text{Lignin } \% = \frac{W_L}{W_W} \times 100$$

where:

W_L = lignin weight (g).

W_W = weight (g) of the extractive-free wood sample.

3.4 Preparation of 1% KBr Pellets for FTIR Spectroscopy

1. Prepare the hydraulic press and KBr pellet die (*see* **Note 20**).
2. Weigh out 120 mg of dry KBr (*see* **Note 21**), and place in an agate mortar (*see* **Note 22**).
3. Weigh out 1.2 mg of dry Klason lignin (*see* **Note 8**).
4. Grind the lignin sample and the KBr until the mixture is uniform (*see* **Note 23**).
5. Transfer the mixture to the pellet die, place the remaining pieces (the upper anvil and the plunger) on top, and apply light pressure to the plunger with the press to remove any air from the sample.
6. Increase the pressure of the hydraulic press to 6–8 tons, and maintain the pressure for 2 min.
7. Slowly release the pressure from the press and remove the die.
8. Carefully disassemble the pellet die. First, remove the base and gently push the plunger to release the KBr pellet, and place in a

clean weighing dish (previously marked with the sample data). Place the dish in a desiccator until the pellet is ready for analysis in the FTIR spectrometer.

9. Measure the absorbance of the KBr pellets using an FTIR spectrometer. The recommended resolution is 2–4 cm^{-1}, in the range between 400 and 1850–4000 cm^{-1}, for 50–150 scans.
10. Normalize and analyze the obtained spectral data using scientific graphing and data analysis software, such as OMNIC™ (*see* **Notes 24** and **25**).

3.5 Alkaline Nitrobenzene Oxidation and S/G Ratio Determination by HPLC

1. Weigh out 0.2 g of dry extractive-free wood (*see* **Note 8**). Transfer the sample to a glass vial containing 7 mL of a 2 M NaOH aqueous solution and 0.5 mL of nitrobenzene (*see* **Note 26**).
2. Place the vial with the material into a pressurized reactor in an oil bath at 170 °C for 2.5 h.
3. Filter the resulting material through a 0.22 μm Millipore cellulose membrane.
4. Transfer the filtrate to a 50-mL separatory funnel. Extract three times, using 30 mL of chloroform each time (*see* **Notes 1** and **27**).
5. Acidify the aqueous phase to pH 1 with a 4 M HCl solution. Then extract three times (*see* **Note 27**).
6. Mix the organic phases resulting from the six extractions, and concentrate the mix in a rotary evaporator at 40 °C under reduced pressure.
7. Transfer the sample to a 50 mL volumetric flask, and fill the flask up to the mark with acetonitrile-water (1:1).
8. Filter the sample through a regenerated cellulose membrane with a pore size of 0.45 μm.
9. Analyze the sample on an HPLC system, preferably one equipped with a variable wavelength or UV-VIS detector, an analytical reverse phase column RP-18 type (250 × 4.6 mm, 5 μm), and a standard flow cell, at a wavelength of 280 nm with an isocratic elution. Use the acetonitrile-water mixture (1:6) as the mobile phase, and adjust to pH 2.6 using the 0.1% trifluoroacetic acid buffer solution in distilled water.
10. Make calibration curves using syringaldehyde and vanillin standards. Prepare the standards using the mixture of acetonitrile-water (1:6), and adjust the pH to 2.6 (*see* **Note 28**).
11. Finally, calculate the S/G ratio (*see* **Note 29**).

3.6 Deconvolution of FTIR Spectra for the Determination of the S/G Ratio

1. Use samples of isolated lignin to obtain the spectra by any variant of infrared spectrometry (*see* **Note 30**).
2. Weigh out 100 μg of isolated lignin, macerate in an agate mortar, and acquire the infrared spectra. Always avoid sample hydration as much as possible (*see* **Notes 23**).
3. For the acquisition of the spectra, use the native software of the spectrometer to set the suggested parameters as following: a spectral range of 650–4000 cm^{-1}, with 32 scans (15 s reading), a resolution of 4 cm^{-1}, and Happ-Genzel apodization (*see* **Note 31**).
4. Process a total of five experiments for each sample. Next, export the datasets in table format (*see* **Note 32**).
5. From here on out, use the specialized software for spectra processing with curve-fitting function to perform the spectra deconvolution. Here, the steps to be followed are described using the functions of the software Origin Pro 2016, vb9.3.226 (OriginLab Corporation, Northampton, MA, United States).
6. Using the Origin Pro software, average the five spectra through the "average multiple curves" function. Then for the spectrum deconvolution, use the "Fit peaks (Pro)" function.
7. The first step is to correct the baseline of the averaged spectrum. Valleys commonly used as baseline anchor points are at 894, 1171, 1536, and 1762 cm^{-1} [14, 29] (*see* Fig. 3a and **Note 33**). Perform the baseline correction by applying the "second derivative" and connecting the points between suggested valleys by the "Spline" interpolation (*see* **Note 34**).
8. Then perform auto baseline subtraction and auto rescaling of the resulting spectrum.
9. For peak detection, use the local maximum method and the second derivative. Other parameters suggested are as follows: auto smoothing window size, positive direction, and a minimum peak height of 4%.
10. The best start for the curve-fitting is to fix the Base (y_0) value to zero. Use a Gaussian line shape (peak type); this has been commonly used for modelling the individual components by curve-fitting [29, 65].
11. Before the first iteration, for each detected individual component, set the value of the Full Width at Half Maximums (FWHM) between 8 and 25 cm^{-1} and the value of the Areas close to 0.2 (*see* Fig. 3b and **Note 35**).
12. Once the value of FWHM and Area have been fixed for each component, iterate the Centers until their values are almost invariant (*see* Fig. 3d).

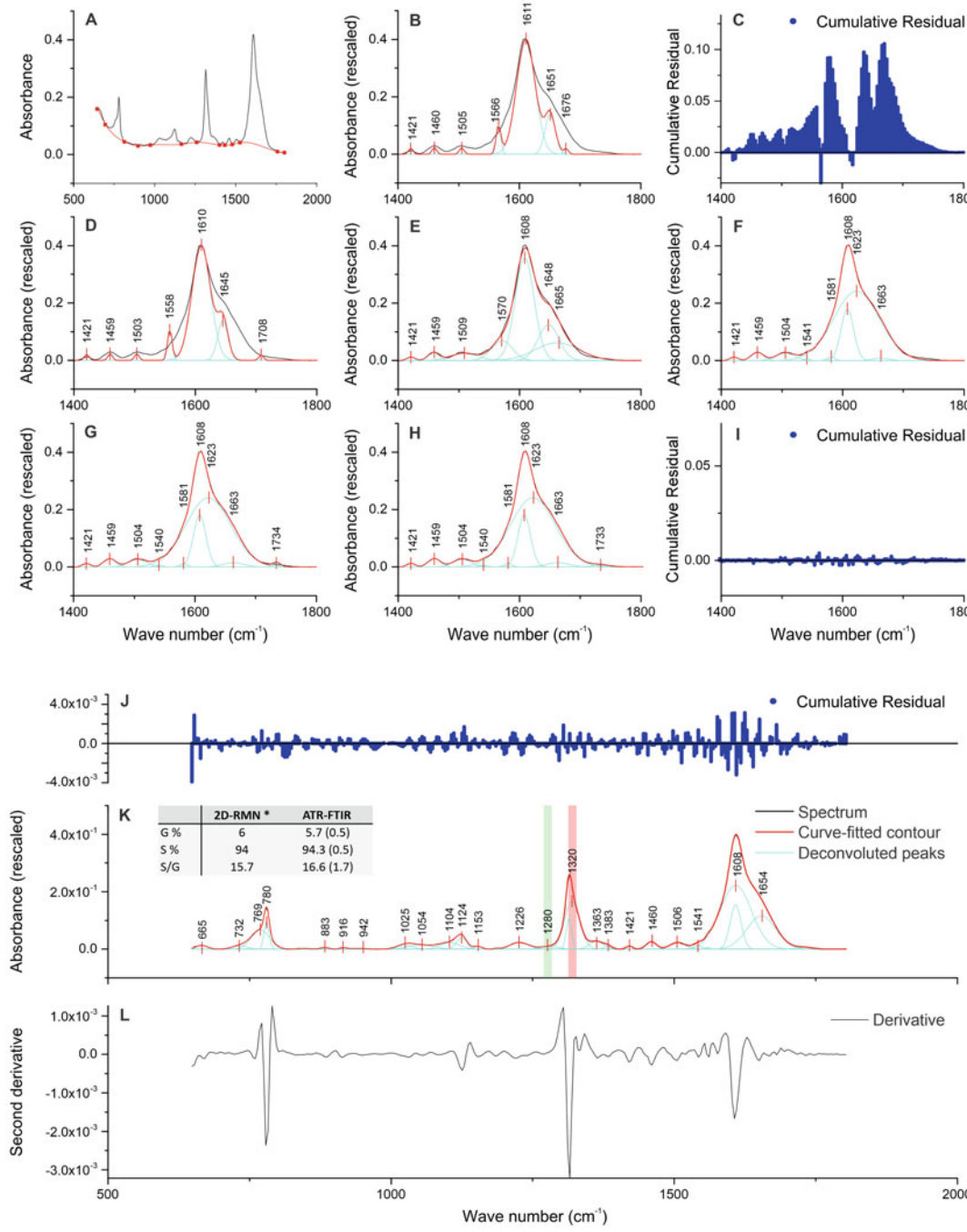


Fig. 3 Spectra deconvolution process. (**a**) Anchor points for the base-line correction of the spectrum. (**b**) FWHM and Area values initially set for detected peaks. (**c**) Cumulative residual for the curve-fitted spectrum with the initial values. (**d**) Calculated Center for each peak after some iterations, keeping the values of FWHM and Area fixed. (**e**) Curve-fitted spectrum after automatic iteration (no parameters were fixed). (**f**) Maximum fit obtained by automatic iteration when some individual components were missing. (**g**) Addition of one individual component at 1734 cm^{-1} to enhance the spectrum curve-fitting. (**h**) Preliminary curve-fitted spectrum after automatic iteration. (**i**) Reduced residual error for the preliminary curve-fitted spectrum. (**j**–**l**) Resulting parameters after deconvolution by curve-fitting. (**j**) Cumulative residual error. (**k**) Deconvoluted peaks, curve-fitted and baseline-corrected spectra. Values of the S/G ratios by 2D-RMN were published in [29]. The standard deviation for three experiments is showed in parentheses. (**l**) Second derivative initially used for peak detection

13. Now fix the obtained Center value for each component, and increase slightly the value of the Area (about half of the previous value). Then keeping fixed the Area values, release and recalculate the FWHM values through a few iterations; stop iterating when the residual cumulative is minimized (*see* Fig. 3e–i).
14. If the cumulative residual cannot be reduced to the minimum, or there is an obvious gap, add an additional component (*see* Fig. 3f, g and **Note 36**).
15. Repeat steps 10 through 14 until the curve-fit is satisfactory (*see* Fig. 3j–l and **Note 37**).
16. For the determination of the S/G ratio, use the integrated areas for the individual components: Peak Gravity Center close to 1320–1326 cm^{-1} for the S units and Peak Gravity Center close to 1266–1281 cm^{-1} for the G units (*see* bands in Fig. 3k and the respective assignments in Table 2).

4 Notes

1. Special care is recommended when handling solvents such as benzene, chloroform and other agents used in the methods described herein. These have been identified as highly carcinogenic agents under extended periods of exposure. Read the safety data sheets of each reagent before handling.
2. Because the preparation of acidic or basic aqueous solutions is a highly exothermic process, it is recommended to prepare these solutions in a cold bath at 15 °C (*see* Fig. 2d). Never add water directly to acids or bases because they may release enough heat to cause severe burns.
3. To prevent damage to the HPLC apparatus and column, filter all solvents using a mobile phase filtration apparatus and a regenerated cellulose membrane, pore size 0.45 μm. Furthermore, degas each solvent prior to use, either by an ultrasonic bath, evacuation with a vacuum pump, or with bubbling helium. The time of each degassing method depends on the total volume of solvent.
4. The age of the wood varies according to the anatomical region of the stem; cambial maturation occurs radially. The complete ontogenetic history of the wood in an individual is represented by the basal wood.
5. The drying time of the wood depends on the degree of succulence of the sample; succulent samples need to be dried for 4 days and stored in a dry, well-ventilated place to avoid fungal infestation.

6. When determination of Klason lignin is performed with a small amount of sample (<0.5 g), the homogenization of the sample with the sulfuric acid solution is most effective when working with a particle size of 0.25 mm (mesh 60).
7. It is recommended to simultaneously dry the extraction thimbles and wood samples until each reach a constant weight.
8. Always record the weight to the nearest 0.1 mg. Make sure each object (samples, extraction thimbles or Büchner funnels) has reached a constant weight by drying at 105 °C, and only weigh them under a humidity-free environment. A desiccator can be used to contain the objects and allow them to cool. To avoid burns, handle hot objects (e.g., Büchner funnels) with crucible tongs and asbestos gloves.
9. Fold the open end of the extraction thimble to prevent sample loss during reflux.
10. The volume of solvent in the distillation flask should be a little more than that in the Soxhlet extractor to ensure the continuous flow of solvent.
11. Air dry until the solvent has evaporated, then dry at 105 °C to a constant weight and record the weight of the extraction thimble with the sample.
12. Transfer the extract to an amber glass bottle, and recover the extract remaining in the distillation flask with a small amount of clean solvent. The extracts may be used to characterize the solvent extractives of the wood later.
13. Air dry until the solvent has evaporated, then dry at 105 °C to a constant weight and record the weight of the extraction thimble with the sample. Discard the extraction thimble and then record the weight (constant weight) of the sample only.
14. Dry the Büchner funnel (medium pore-size), before starting the process, at 105 °C to a constant weight and record its weight. This will be used to calculate the weight of the soluble extractives in hot water. The filtering system is shown in Fig. 2c.
15. This fraction contains substances such as tannins, gums, sugars, starches, and coloring matter. If needed, preserve by freeze-drying to prevent infestation by fungi.
16. It is important to calculate the weight of each extractive fraction independently of the weight of the extraction thimble, paper filter, or Büchner funnel.
17. During the agitation make sure that the sample does not adhere to the beaker walls. If that happens, use the glass rod to remove the sample and add it back to the solution.

18. It is not recommended to use the reflux apparatus if the content of lignin-soluble acid in the solution will be determined separately. If this is the case, keep the volume constant by adding water continuously instead of refluxing the solution.
19. The sample can be allowed to stand overnight because the settling can take several hours.
20. Completely clean the KBr pellet die before and after use, particularly the plunger and the anvil, to prevent sample contamination. Use dry acetone and Kimwipes® to avoid scratching the surfaces; a scratched surface affects the crystallinity of the KBr pellets.
21. For comparative studies, the KBr used should be of FTIR grade. In addition, the KBr should be dried previously at 105 °C to a constant weight to avoid interference in the FTIR spectra. For the normalization of FTIR spectra, the weight should be recorded to the nearest to 0.1 mg.
22. Do not use porcelain mortars because the porosity of the material can cause contamination of lignin samples.
23. Grind the mixture as quickly as possible to avoid its excessive hydration due to environmental humidity.
24. Bands that do not vary from one sample to another are used to normalize the FTIR spectra of the lignin. It is recommended to make a pellet consisting of only KBr to use as a blank; this will help in discarding bands produced by noise or bands that are not part of the sample.
25. Bands at 1501–1505 cm^{-1} are commonly used to determine the lignin content. To normalize the bands and make them quantitatively comparable, the height of the band observed in the FTIR spectrum is divided by the concentration of lignin in the KBr pellet [9, 39, 49, 50].
26. First, carefully shake the vial with the mixture of NaOH and nitrobenzene until the mixture is homogeneous, then add the sample of dry wood and ensure that it is homogeneously impregnated.
27. Constantly purge the gas formed within the separatory funnel in each extraction. The amount of gas can be considerable and can cause the funnel to open, resulting in sample loss. Work in a fume hood and wear a gas-filtering mask, protective gloves, and eye protection.
28. Concentrations suggested here were previously reported by Nunes et al. [28] and Reyes-Rivera et al. [22] with a good reproducibility.
29. For the interpretation of the results, it should be considered that, due to their high proportion of condensation,

approximately 30% of the guaiacyl units are converted to vanillin. Conversely, due to their low proportion of condensation, 90% of syringyl units are converted to syringaldehyde.

30. The use of dioxane lignin is recommended to obtain good results in the determination of the S/G ratio. Moreover, this deconvolution method, applied to the data resulting of the attenuated total reflectance-Fourier transform infrared spectroscopy (ATR-FTIR), gives S/G ratios highly comparable to those obtained by 2D-NMR [29].
31. Other authors also suggest the Boxcar apodization for FTIR spectra analysis [67].
32. Alternatively, ASCII datasets (e.g., *.asp, *.csv formats) can be used, as these are read by most deconvolution software.
33. If other valleys are preferred, it is suggested to avoid negative lobes as much as possible for obtaining the corrected baseline.
34. The number of anchor points can be set as "Same as the input" in order to improve the adjustment. If automation of the process is required, alternatively different modes (i.e., asymmetric least squares smoothing, a constant value, or end points weighted mode) can be applied to get the corrected baseline. If these features are saved in the theme, this will allow to apply the same parameters to several spectra.
35. For small peaks, or "shoulders," it is necessary that the values of Area and FWHM for the implicated components are slightly modified. In these cases, values should be half, or less, than initially suggested. Alternatively, it will be better to arbitrarily add the number of components necessary to improve the fit of the deconvoluted spectrum (to decrease the cumulative residual). This step is recommended only after auto peak detection, once a satisfactory fit has not been achieved (*see* Fig. 3f–h).
36. Alternatively, when the cumulative residual cannot be reduce, removal of some individual components is suggested.
37. A value for the cumulative residual close to $\pm 5 \times 10^{-3}$ indicates a good fit. Moreover, ensure that the coefficients of determination are never less than 0.98 (*see* Fig. 3j).

Acknowledgments

Authors thank to Santiago Duarte Aranda, Rubén San Miguel Chávez, and Domingo González Meraz for their excellent technical contributions. To Dr. Gonzalo Canché-Escamilla and Dr. Marcos Soto-Hernández for the support provided in their respective research groups for this work and to Facultad de Estudios Superiores Zaragoza, UNAM for institutional supporting.

References

1. Hon DN, Shiraishi N (eds) (2001) Wood and cellulosic chemistry. Marcel Dekker, New York
2. Pizzi A (2016) Wood products and green chemistry. Ann For Sci 73:185–203
3. Winandy JE (2017) Relating wood chemistry and strength: part II. Fundamental relationships between changes in wood chemistry and strength of wood. Wood Fiber Sci 49:2–11
4. Sarkanen KV, Ludwig CH (eds) (1971) Lignins: occurrence, formation, structure and reactions. Wiley-Interscience, New York
5. Danish M, Ahmad T (2018) A review on utilization of wood biomass as a sustainable precursor for activated carbon production and application. Renew Sust Energ Rev 87:1–21
6. Ralph J, Lapierre C, Boerjan W (2019) Lignin structure and its engineering. Curr Opin Biotechnol 56:240–249
7. Lupoi JS, Singh S, Parthasarathi R et al (2015) Recent innovations in analytical methods for the qualitative and quantitative assessment of lignin. Renew Sust Energ Rev 49:871–906
8. Colom X, Carrillo F, Nogués F et al (2003) Structural analysis of photodegraded wood by means of FTIR spectroscopy. Polym Degrad Stab 80:543–549
9. Pandey KK, Pitman AJ (2003) FTIR studies of the changes in wood chemistry following decay by brown-rot and white-rot fungi. Int Biodeterior Biodegradation 52:151–160
10. Nuopponen M, Vuorinen T, Jaemsae S et al (2004) Thermal modifications in softwood studied by FT-IR and UV resonance Raman spectroscopies. J Wood Chem Technol 24:13–26
11. Colom X, Carrillo F (2005) Comparative study of wood samples of the northern area of Catalonia by FTIR. J Wood Chem Technol 25:1–11
12. Kubo S, Kadla JF (2005) Hydrogen bonding in lignin: a Fourier transform infrared model compound study. Biomacromolecules 6: 2815–2821
13. Xu F, Sun J-X, Sun RC et al (2006) Comparative study of organosolv lignins from wheat straw. Ind Crop Prod 23:180–193
14. Del Rio JC, Gutierrez A, Rodriguez IM et al (2007) Composition of non-woody plant lignins and cinnamic acids by Py-GC/MS, Py/T-MAH and FT-IR. J Anal Appl Pyrol 79:39–46
15. Mansouri N-E, Salvadó J (2007) Analytical methods for determining functional groups in various technical lignins. Ind Crop Prod 26: 116–124
16. Müller G, Schöpper C, Vos H et al (2009) FTIR-ATR spectroscopic analysis of changes in wood properties during particle- and fibreboard production of hard- and softwood trees. Bioresources 4:49–71
17. Brebu M, Tamminen T, Spiridon I (2013) Thermal degradation of various lignins by TG-MS/FTIR and Py-GC–MS. J Anal Appl Pyrol 104:531–539
18. Hu J, Xiao R, Shen D, Zhang H (2013) Structural analysis of lignin residue from black liquor and its thermal performance in thermogravimetric-Fourier transform infrared spectroscopy. Bioresour Technol 128:633–639
19. Sammons RJ, Harper DP, Labbe N et al (2013) Characterization of organosolv lignins using thermal and FT-IR spectroscopic analysis. Bioresources 8:2752–2767
20. Xu G, Wang L, Liu J et al (2013) FTIR and XPS analysis of the changes in bamboo chemical structure decayed by white-rot and brown-rot fungi. Appl Surf Sci 280:799–805
21. Fonseca-Prieto FV, Canché-Escamilla G, Chavarria-Hernandez JC et al (2014) Characterization of lignocellulosic residues of henequen and their use as a bio-oil source. Biomass Convers Bioref 4:95–104
22. Reyes-Rivera J, Canché-Escamilla G, Soto-Hernández M et al (2015) Wood chemical composition in species of Cactaceae: the relationship between lignification and stem morphology. PLoS One 10:e0123919. https://doi.org/10.1371/journal.pone.0123919
23. Allison GG, Thain SC, Morris P et al (2008) Quantification of hydroxy cinnamic acids and ligninin perennial forage and energy grasses by Fourier-transform infrared spectroscopy and partial least squares regression. Bioresour Technol 100:1252–1261
24. Huang Y, Wang L, Chao Y et al (2012) Analysis of lignin aromatic structure in wood based on the IR spectrum. J Wood Chem Technol 32: 294–303
25. Derkacheva OY (2013) Estimation of aromatic structure contents in hardwood lignins from IR absorption spectra. J Appl Spectrosc 80:670–676
26. Lupoi JS, Singh S, Davis M et al (2014) High-throughput prediction of eucalypt lignin syringyl/guaiacyl content using multivariate analysis: a comparison between mid-infrared, near-infrared, and Raman spectroscopies for model development. Biotechnol Biofuels 7:93

27. Gora R, Hutta M, Vrska M et al (2006) Characterization of Klason lignins by reversed phase high-performance liquid chromatography using wide-pore octadecyl silica and step- wise gradient of dimethyl formamide in water. J Sep Sci 29:2179–2189
28. Nunes CA, Lima CF, Barbosa LCA et al (2010) Determination of *eucalyptus spp* lignin S/G ratio: a comparison between methods. Bioresour Technol 101:4056–4061
29. Reyes-Rivera J, Soto-Hernández M, Canché-Escamilla G et al (2018) Structural characterization of lignin in four cacti wood: implications of lignification in the growth form and succulence. Front Plant Sci 9:1518
30. Lancefield CS, Constant S, de Peinder P et al (2019) Linkage abundance and molecular weight characteristics of technical lignins by attenuated total reflection-FTIR spectroscopy combined with multivariate analysis. ChemSusChem 12:1139–1146
31. Gomes DI, Detmann E, Valadares FSC et al (2011) Evaluation of lignin contents in tropical forages using different analytical methods and their correlations with degradation of insoluble fiber. Anim Feed Sci Technol 168:206–222
32. Dence CW (1992) The determination of lignin. In: Lin SY, Dence CW (eds) Methods in lignin chemistry. Springer, Berlin
33. Ma XJ, Cao SL, Yang XF et al (2014) Lignin removal and benzene-alcohol extraction effects on lignin measurements of the hydro-thermal pretreated bamboo substrate. Bioresour Technol 151:244–248
34. Nicholson DJL, Aaron T, Francis RCA (2013) A three-stage Klason method for more accurate determinations of hardwood lignin content. Cellulose Chem Technol 48:53–59
35. Rencoret J, Gutiérrez A, Nieto L et al (2011) Lignin composition and structure in young versus adult *Eucalyptus globulus* plants. Plant Physiol 155:667–682
36. Bose SK, Francis RC, Govender M et al (2008) Lignin content versus syringyl to guaiacyl ratio amongst poplars. Bioresour Technol 100: 1628–1633
37. Sun X-F, Jing Z, Fowler P et al (2011) Structural characterization and isolation of lignin and hemicelluloses from barley straw. Ind Crop Prod 33:588–598
38. Ohra-aho T, Gomes FJ, Colodette JL et al (2013) S/G ratio and lignin structure among *Eucalyptus* hybrids determined by Py-GC/MS and nitrobenzene oxidation. J Anal Appl Pyrol 101:166–171. https://doi.org/10.1016/j.jaap.2013.01.015
39. Rodrigues J, Faix O, Pereira H (1998) Determination of lignin content of *Eucalyptus globulus* wood using FTIR spectroscopy. Holzforschung 52:46–50
40. Schultz TP, Burns DA (1990) Rapid secondary analysis of lignocellulose: comparison of near infrared (NIR) and Fourier transform infrared (FTIR). TAPPI J 73:209–212
41. Stefke B, Windeisen E, Schwanninger M et al (2008) Determination of the weight percentage gain and of the acetyl group content of acetylated wood by means of different infrared spectroscopic methods. Anal Chem 80:1272–1279
42. Toivanen TJ, Alen R (2007) A FTIR/ PLS method for determining variations in the chemical composition of birch (*Betula pendula/B. publescens*) stem wood. Appita J 60: 155–160
43. Dang VQ, Bhardwaj NK, Hoang V et al (2007) Determination of lignin content in high-yield kraft pulps using photoacoustic rapid scan Fourier transform infrared spectroscopy. Carbohydr Polym 68:489–494
44. Faix O, Bottcher JH (1993) Determination of phenolic hydroxyl group contents in milled wood lignins by FTIR spectroscopy applying partial least-squares (PLS) and principal components regression (PCR). Holzforschung 47: 45–49
45. Raiskila S, Pulkkinen M, Laakso T et al (2007) FTIR spectroscopic prediction of Klason and acid soluble lignin variation in Norway spruce cutting clones. Silva Fennica 41:351–371
46. Rana R, Langenfeld-Heyser R, Finkeldey R et al (2010) FTIR spectroscopy, chemical and histochemical characterisation of wood and lignin of five tropical timber wood species of the family of Dipterocarpaceae. Wood Sci Technol 44:225–242
47. Chen H, Ferrari C, Angiuli M et al (2010) Qualitative and quantitative analysis of wood samples by Fourier transform infrared spectroscopy and multivariate analysis. Carbohydr Polym 82:772–778
48. Rudakiya DM, Gupte A (2019) Assessment of white rot fungus mediated hardwood degradation by FTIR spectroscopy and multivariate analysis. J Microbiol Methods 157:123–130
49. Carballo AL, Igarza OU, Cordero ME (2004) Composición química de tres maderas en la Provincia del Pinar del Río, Cuba a tres alturas del fuste comercial. Parte N° 1: *Corymbia citriodora*. Rev Chapingo S Cienc Forest Amb 10:57–62
50. Orea IU, Carballo AL, Cordero ME (2004) Composición química de tres maderas en la

Provincia del Pinar del Río, Cuba a tres alturas del fuste comercial. Parte N° 2: *Eucalyptus pellita* F. Muell. Rev Chapingo S Cienc Forest Amb 10:51–55

51. Poletto M, Zattera AJ, Santana RM (2012) Structural differences between wood species: evidence from chemical composition, FTIR spectroscopy, and thermogravimetric analysis. J Appl Polym Sci 126(S1):E337–E344
52. Popescu CM, Singurel G, Popescu MC et al (2009) Vibrational spectroscopy and X-ray diffraction methods to establish the differences between hardwood and softwood. Carbohydr Polym 77:851–857
53. Pandian B, Ramalingam S, Sreeram K et al (2021) Natural pigment: preparation of brown pigment from lignin biomass for coloring application. Dyes Pigments 195:109704
54. Hergert HL (1971) Infrared spectra. In: Sarkanen KV, Ludwid CH (eds) Lignins: occurrence, formation, structure and reactions. Wiley-Interscience, New York
55. Faix O (1991) Classification of lignins from different botanical origins by FTIR spectroscopy. Holzforschung 45:21–27
56. Toledano A, Serrano L, Garcia A et al (2010) Comparative study of lignin fractionation by ultrafiltration and selective precipitation. Chem Eng J 157:93–99
57. Adel AM, Abd El-Wahab ZH, Ibrahim AA et al (2011) Characterization of microcrystalline cellulose prepared from lignocellulosic materials. Part II: Physicochemical properties. Carbohydr Polym 83:676–687
58. Pandi A, Gowthaman MK, Kamini NR (2021) Pulp bio-bleaching using a stable and scalable laccase from *Peroneutypa scoparia*. Wood Sci Technol 55:1509–1525
59. Pang Y, Sun Y, Luo Y et al (2021) Preparation of novel all-lignin microcapsules via interfacial cross-linking of pickering emulsion. Ind Crop Prod 167:113468
60. Fengel D, Wegener G (2003) Wood, chemistry and ultrastructure and reactions. Kassel Verlag, Ramagen
61. Brebu M, Cazacu G, Chirila O (2010) Pyrolysis of lignin—a potential method for obtaining chemicals and/or fuels. Cellulose Chem Technol 45:43–50
62. Derkacheva O, Sukhov D (2008) Investigation of lignins by FTIR spectroscopy. Macromol Symp 265:61–68
63. Faix O, Beinhoff O (1988) FTIR spectra of milled wood lignins and lignin polymer models (DHP's) with enhanced resolution obtained by deconvolution. J Wood Chem Technol 8:505–522
64. Kauppinen JK, Moffatt DJ, Mantsch HH et al (1981) Fourier self-deconvolution: a method for resolving intrinsically overlapped bands. Appl Spectrosc 35:271–276
65. Lórenz-Fonfría VA, Padrós E (2004) Curve-fitting of Fourier manipulated spectra comprising apodization, smoothing, derivation and deconvolution. Spectrochim Acta A Mol Biomol Spectrosc 60:2703–2710
66. Brangule A, Gross KA (2015) Importance of FTIR spectra deconvolution for the analysis of amorphous calcium phosphates. IOP Conf Ser Mater Sci Eng 77:012027. IOP Publishing Ltd.: Bristol, UK
67. Egbert S, Carpenter C (2017) Comparison of FTIR apodization functions using modeled and measured spectral data. J Appl Eng Math 4:1–4



Chapter 13

Inducible Pluripotent Suspension Cell Cultures (iPSCs) to Study Plant Cell Differentiation

Delphine Ménard, Henrik Serk, Raphael Decou, and Edouard Pesquet

Abstract

Inducing the differentiation of specific cell type(s) synchronously and on-demand is a great experimental system to understand the sequential progression of the cellular processes, their timing and their resulting properties for distinct isolated plant cells independently of their tissue context. The inducible differentiation in cell suspension cultures, moreover, enables to obtain large quantities of distinct cell types at specific development stage, which is not possible when using whole plants. The differentiation of tracheary elements (TEs) – the cell type responsible for the hydro-mineral sap conduction and skeletal support of plants in xylem tissues – has been the most studied using inducible cell suspension cultures. We herein describe how to establish and use inducible pluripotent suspension cell cultures (iPSCs) in *Arabidopsis thaliana* to trigger on-demand different cell types, such as TEs or mesophyll cells. We, moreover, describe the methods to establish, monitor, and modify the sequence, duration, and properties of differentiated cells using iPSCs.

Key words *Arabidopsis thaliana*, Habituated cell cultures, Hormone-inducible differentiation, Tracheary elements, Inducible pluripotent cell suspension cultures (iPSCs), Stable genetic transformation, Drug-treatment

1 Introduction

The inducible differentiation of specific cell type lineage(s) in plant cell suspension cultures represents a great but underused tool to study the formation and properties of specific cell types outside of tissue and physiological constraints [1]. Such experimental systems are particularly important to study xylem cells as the formation of each cell type and morphotype is unsynchronized and buried deep within plant organs. Moreover, functional studies causing important modifications of xylem cell morphology, metabolism, and/or properties due to mutations or drug treatments often lead to lethal phenotypes in whole plants. This lethality makes the inducible differentiation of cells outside of functional xylem tissues the only mean of experimental functional investigation. Whereas in whole

Javier Agusti (ed.), *Xylem: Methods and Protocols*, Methods in Molecular Biology, vol. 2722,
https://doi.org/10.1007/978-1-0716-3477-6_13,
© The Author(s), under exclusive license to Springer Science+Business Media, LLC, part of Springer Nature 2024

plant, the continuous growth juxtaposes similar cell types at different developmental state in a growing tissue, inducible differentiation in plant cell suspension cultures enables to trigger, follow, modify, and harvest large amount of synchronized cell types at a specific developmental state. Cell suspension culture systems optimized for the inducible differentiation of specific cell types in plant species have essentially enabled the on-demand formation of tracheary elements (TEs) – cells that form xylem sap conduits. TEs include multiple cell subtypes (tracheid vs. vessel element) depending on perforation plate(s): absent from tracheid but present in vessel elements. Moreover, TEs include several morphotypes differing in their morphology (cell width) and secondary cell wall organizational patterns, like annular or spiral patterns in narrow protoxylem or reticulate or pitted in wider metaxylem and secondary xylem [2–4]. Other xylem cell types like xylem parenchyma (XP) conjointly differentiate when inducing the formation of TEs at a proportion of 50:50 [5–7], but the production of xylary fibers have not been achieved yet. Since the 1980s, five distinct experimental systems have been optimized for the inducible differentiation of xylem cells using plant cell suspension cultures. These experimental systems vary by the starting biological material/plant species, their competency for differentiation and the trigger used to onset cell differentiation:

1. *Cell culture systems derived from freshly isolated living cells from tissues with a differentiation induced by adding hormones.* Such systems include the famous *Zinnia* system [8], where mesophyll cells from 14-day-old leaves of *Zinnia violacea* (formerly *Zinnia elegans*) are mechanically isolated and incubated in the presence of auxin and cytokinin to trigger their differentiation into TEs and XPs. Competency for differentiation of cells is, however, limited to 48 h after leaf isolation but does not require cell division prior to differentiation [9]. This experimental system enables the formation of all four TE morphotypes that have perforation plates [5, 10]. This is thus one of the few inducible systems enabling the triggered formation of all types of vessel elements. This *Zinnia* system was the only system extensively and independently used by multiple research teams around the world between 1980 and 2015. The *Zinnia* system led to more than 80 research publications, including several early transcriptomic studies [5, 11–13]. Although transient transformation methods have been established [14], no stable genetic transformation method has been developed for this system.
2. *Cell cultures derived from in vitro grown calli transferred to liquid media with hormones and/or anti-browning agents.* Many systems were developed for gymnosperm species like *Pinus* [15–17], *Pseudostuga* [18], as well as *Torreya* and *Cryptomeria* [19] where needle or embryo-derived calli produced

on solid media are transferred into liquid in the presence of auxin and/or anti-browning agents (polyvinylpyrrolidone or activated charcoal to adsorb the harmful substances browning the media). Most of these systems are not widely used except for the *Pinus* system for which stable genetic transformation for both silencing, and gain-of-function have been optimized and used in several research articles [20–22]. These systems enable the formation of several TE morphotypes without perforation plates.

3. *Systems derived from hormone-dependent cell suspension cultures triggered to differentiate by washing away and/or adding hormones.* They include several systems from *Arabidopsis* [23–25], *Pinus* [26] and most of the monocotyledon systems, such as banana [27], bamboo [28], and sugarcane [29]. Not widely used, they led just to one or two research publications per systems, although transcriptomic studies were performed using the *Arabidopsis* system. Stable genetic transformation method was developed for one of the *Arabidopsis* systems for gain-of-function [24]. The formation of several TE morphotypes without perforation plates was demonstrated in *Arabidopsis* systems but remained uncertain in other systems.
4. *Systems derived from hormone-habituated cell suspension cultures triggered to differentiate using hormones or other stimuli.* This technology has currently been used in *Arabidopsis* [30] where epigenetic variants of dedifferentiated cells derived from in vitro grown calli were screened for hormone-independent growth, also called hormone-habituated. In this system, cells are synchronized in G_0/G_1 using sucrose depletion, calibrated at specific density, and induced to differentiate into TEs and XPs with auxin, cytokinin, and epibrassinolides [3, 4, 6, 7, 30, 31]. Stable genetic transformation methods were developed for gain-of-function, translational, and transcriptional reporter, as well as silencing using small and artificial micro interfering RNA [6, 7, 30, 32–34]. High-throughput analyses in transcriptomic, proteomics, and chemical genomics were also performed [6, 35, 36]. This system enables the formation of all four TE morphotypes [5] with perforation plates [4]. This is, thus, one of the few inducible systems enabling to trigger all types of vessel elements.
5. *Systems derived from hormone-dependent cells in suspension genetically transformed with a chemical-inducible construct driving master transcriptional regulator for specific TE morphotypes.* These systems include hormone-dependent cell suspensions in *Arabidopsis* and *Nicotiana* stably transformed with chemically inducible promoter, responsive to estradiol or dexamethazone, driving the overexpression of the NAC master transcriptional regulator controlling specific TE morphotypes:

VND6 for metaxylem pitted TEs [37] or VND7 for protoxylem spiral TEs [38]. Cell differentiation, moreover, requires the addition of hormones, mainly epibrassinolides, to ensure high differentiation efficiency [39]. Stable genetic transformation method for gain-of-function, translational reporter, and silencing using small interfering RNA [37] were used. High throughput analyses for transcriptomics, proteomics, metabolomics, and chemical genomics have also successfully been performed using these systems [38].

Among the five experimental systems mentioned above, only the hormone-habituated cell suspension cultures have been shown to be pluripotent [1, 40]. Indeed, it enables to trigger the differentiation of distinct cell types from a common stock cell lines using different triggering conditions. The formation of lignified xylem TEs and their associated XPs can be induced by supplying auxin, cytokinin, and brassinosteroids [30], whereas photosynthetic mesophyll-like cells can be induced by reducing sugar and providing white light [40]. The use of other type of stimuli, such as changing the red to far red-light ratio [41] or changing the sugar source [35], revealed the high potencies of the hormone-habituated cell suspension culture system to trigger and understand the differentiation of other cell types and their response to changing environmental conditions. As this technology has similar properties than inducible pluripotent cell culture systems in animal species [42], it has, thus, been renamed from hormone-habituated cell suspension cultures [31] to inducible pluripotent suspension cell cultures (iPSCs) by D. Ménard in 2022 [4]. The common properties shared between animal- and plant-inducible pluripotent cell culture systems include (a) the deprogramming of somatic cells into cells that have an autonomous capacity of division in an undifferentiated state without the support of any added growth factors, (b) the capacity of cells to differentiate into specific cell type lineage in response to specific stimuli/growth factors, and (c) the capacity to lead to different cell types using distinct stimuli/growth factors. The present article will thus provide a detailed procedure on how to establish, monitor, modify and use inducible pluripotent suspension cell cultures (iPSCs) to investigate the differentiation of specific cell types in plants.

2 Materials

2.1 Equipment and Infrastructure

1. Surface sterilization and handling in sterile environment

   Every step of the handling of biological samples (explants, calli, cell suspensions, and bacteria) needs to be performed in sterile conditions using a laminar flow hood, such as a ScanLaf class 2 Mars Premium 1200 (Labogene, Denmark) (*see* **Note 1**). Small containers and manipulation tools, such as

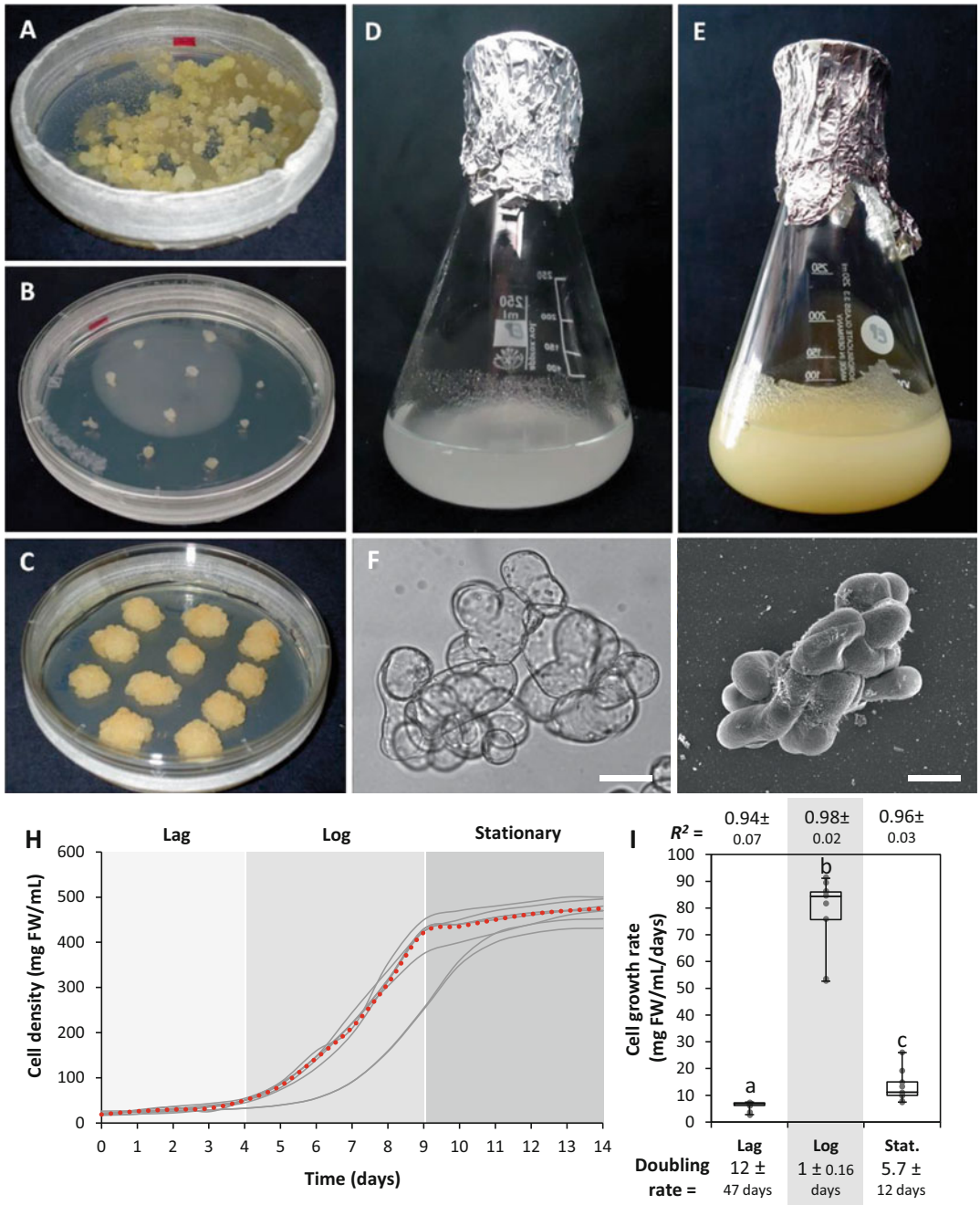


Fig. 1 Standard procedures for calli transfer to solid and liquid media during establishment, screening for habituation, titration and screening of stable transgenic transformation. (**a**) Callogenesis on solid medium after co-cultivation of habituated cells with *Agrobacterium tumefaciens* in liquid selective medium. (**b**) Sterile transfer of calli using tweezers onto fresh Petri dish for growth. (**c**) Growth of calli after 6 weeks of incubation prior to liquid transfer. (**d**) Freshly sub-cultured iPSCs at 60 mg/mL in sterile 250 mL Erlenmeyer flask. (**e**) 7-day-old iPSCs in sterile 250 mL Erlenmeyer flask. (**f**–**g**) Appearance of grouped cells in iPSCs at 7-days of culture using brightfield transmission (**f**) or scanning electron microscopy (**g**). (**h**) Characteristic growth curve of iPSCs in media devoid of any growth factor with lag, log and stationary phases. Red-dotted curve

polypropylene plastics (bottle caps, microtubes, pipette tips, etc.), metal scalpel with blades (no. 22 surgical blade), and tweezers (Bochem stainless steel 10/18), need to be enclosed either by a double layer of aluminium foil or an autoclavable containers and then sterilized by autoclaving (such as using a Tuttnauer 3870EL horizontal autoclave). Clean and dry Erlenmeyer flasks are used as containers for cell cultivation and prepared by closing the flask opening with a cotton wool ball, then covered up to the neck with a double layer of aluminium foil prior to autoclaving (*see* **Note 2**). Scalpel blades and tweezers can also be subsequently flame sterilized using a Bunsen burner (Fireboy Portable Safety Bunsen Burner, Integra, Switzerland) in between samples and left to cool on a surface-sterilized metal rack for 10–15 min (*see* **Note 1**).

2. Dark thermo-regulated growth chamber and/or incubator:

   In vitro callogenesis, cell regeneration, and transformation, as well as culture of iPSCs, are incubated in a thermo-regulated growth chamber or incubator in the dark at 24 ± 0.5 °C with ventilation to homogenize temperature and a relative humidity of 50% (*see* **Note 3**). Access and monitoring are enabled by green light to avoid any light-dependent stimulation [40, 41]. Oxygenation of cell suspension cultures is enabled by constant agitation using orbital shakers such as Orbit 1900 (Labnet, USA) placed in growth chambers or orbital shaking incubators such as INNOVA (*see* **Note 4**). Solid and liquid *Agrobacterium tumefaciens* cultures used for stable transformation of iPSCs by co-culture are incubated at 28 °C with agitation at 180 rpm before co-culture and then incubated in regular iPSC culture conditions.

3. Washing, concentrating and harvesting iPSCs:

   The washing and concentrating of cell suspension cultures to adjust cell density, to remove cell debris, to wash secreted or added compounds, or remove excess *Agrobacterium* after co-culture are made using centrifugation with a swing-out rotor with bucket adaptors for 15 and 50 mL conical tubes, such as an Eppendorf centrifuge 5804R with A-4-44 rotor.

Fig. 1 (continued) correspond to the median of 9 independent cell culture growth time-courses (shown in light grey). (**i**) Characteristic cell growth rates in the different phases showing doubling of cell amount in the log phase but plateaus for both the lag and stationary phases. Rates were determined using the slope of the linear regression for each independent growth curve in each phase (average and SD of regression coefficient R^2 are indicated). Average doubling rate and its SD corresponds to the time needed to double the quantity of cells in each phase. Different letters on top of box-plots indicated statistical significance using a one-way ANOVA coupled to a Tukey-Kramer post-hoc test ($n = 9$, $\alpha = 0.05$)

Harvesting of cell samples is made either by centrifugation (*see* **Note 5**) or by vacuum filtration (such as the Sterifil system from Millipore, USA) through two layers of 100 μm nylon mesh (*see* **Note 6**).

4. Culture containers for growing iPSCs:

   Cell suspensions are cultivated in sterile plastic or glass containers such as sterilized multi-well plates or autoclaved Erlenmeyer conical glass flasks. Specific ratios between air and cell volume depending on the culture container volume need to be respected to ensure optimal oxygenation when orbital agitation is used (*see* **Note 4**): 2–4 mL of cell suspensions per well in 6-well plates, 10–20 mL in 50 mL Erlenmeyer flasks, 30–100 mL in 250 mL Erlenmeyer flasks (Fig. 1), and 200–500 mL in 3 L Erlenmeyer flasks depending on the amount of material needed (*see* **Note 2**).

2.2 Cell Culture Media, Hormones, and Solutions

1. Surface sterilization solution

Surface sterilization solutions for *Arabidopsis* seeds or explants include 70% ethanol, autoclaved ultrapure water and 5% commercial bleach in water (Clorox, Oakland, USA) while surface sterilization of external nonsterile equipment and user's hands/gloves is performed with 70% ethanol in spray bottles (*See* **Note 7**). Other species, such as *Zinnia violacea* seeds or explants, require stronger sterilizing conditions using freshly made 1% calcium hypochlorite (211,389, Sigma-Aldrich) and 0.01% Triton X100 (T8787, Sigma-Aldrich) in water. Large volumes of sterilized water are needed to wash excess antiseptic solutions.

2. Murashige and Skoog (MS) growth media

Heterotrophic *Arabidopsis thaliana* calli and iPSCs are grown on 1× full strength Murashige and Skoog (MS) media supplemented with 3% sucrose and adjusted to pH 5.7 with a 1 M KOH solution. One liter of culture media is prepared by solubilizing 30 g of sucrose (A2211,1000, AppliChem) and 4.4 mg MS salt including vitamins (M0222, Duchefa) in 900 mL of ultrapure water under magnetic stirring in a graduated beaker. The solution pH is then adjusted to 5.7 with 1 M KOH (221,473, Sigma-Aldrich) solution and filled up to 1 L with ultrapure water. Solidified media are composed of 1× full strength supplemented with either 0.8% (w/v) Agar-agar (1.01614, Merck) or 0.4% (w/v) phytagel (F8164, Sigma-Aldrich). Growth media are sterilized by autoclaving: Solid media are poured into sterile Petri plates for plant cell cultures (such as TC10 dish standard, Sarstedt), dried under laminar flow hood for 20 min to remove water condensation, sealed with parafilm and stored at 4 °C, whereas liquid media are stored at room temperature. As autoclaving can lead to the thermal cracking

of organic molecules, filtration of liquid media through disposable 0.2 μm sterile filters can be used as an alternate sterilization method (*see* **Note 8**).

3. Growth media for triggering cell differentiation

Arabidopsis thaliana iPSCs inductive media for cell differentiation include two different media depending on the cell type desired as mineral composition/concentration, sugar source, and pH have been shown to affect cell differentiation [35]. The tracheary element (TE) differentiation media is composed of 1× full strength MS salts plus vitamins supplemented with 3% sucrose, 1 mM 2-(N-morpholino)ethanesulfonic acid (MES) (M5287, Sigma-Aldrich) and adjusted to pH 6.0. Growth media is prepared as described above in **Subheading** 2.2, **step** 2. With the addition of 195 mg of MES prior to adjusting the pH to 6.0 with 1 M KOH solution. The mesophyll differentiation media is composed of 1× full strength MS salts plus vitamins supplemented only with 1% sucrose (thus only 10g of sucrose per liter of media) and adjusted to pH 5.7. Culture media are then autoclaved and stored at room temperature (*see* **Note 8**).

4. Luria-Bertani (LB) medium for *Agrobacterium tumefaciens*

5× concentrated Luria-Bertani (LB) bacterial growth medium is prepared by dissolving 50 g tryptone, 25 g yeast extract, and 50 g NaCl in 900 mL of ultrapure water, adjusting the pH to 7.0 with 2 M NaOH (S0899, Sigma-Aldrich) and, finally, filling up to 1 L with ultrapure water. 1× working LB liquid solution is made by combining 1 volume of 5X concentrated LB solution with 4 volumes of ultrapure or distilled sterile water. Solidified media are prepared by adding 1% (w/v) Agar-agar (1.01614, Merck) to 1× working LB liquid solution. Culture media are then autoclaved: Solidified media are poured into sterile Petri plates for bacterial culture, dried under laminar flow hood for 15 min to remove water condensation, and then stored inverted at 4 °C, whereas liquid media are stored at room temperature.

5. Growth factor solutions to trigger cell differentiation

Plant growth factor solutions are generally prepared as concentrated stocks:

- 1000× concentrated solution of cytokinin-analog 6-benzylaminopurine (BAP) (B3408, Sigma-Aldrich) at 1 mg/mL (w/v corresponding to 4.4 mM)
- 166× concentrated solution of auxin-analog 1-naphthaleneacetic acid (NAA) (N0640, Sigma-Aldrich) at 10 mg/mL (w/v corresponding to 54 mM)

- 1000× concentrated solution of auxin-analog 2,4 dichlorophenoxyacetic acid (2,4D) (D7299, Sigma-Aldrich) at 1 mg/mL (w/v corresponding to 4.5 mM)
- 1200× concentrated solution of brassinosteroid epibrassinolide (EpiBL) (E1641, Sigma-Aldrich) at 5 mM.

The preparation differs for each plant growth factor solution.

- *For BAP and NAA:* 10 mg of BAP or 100 mg of NAA are placed in sterile 15 mL conical tubes supplemented with 0.5 mL of 2–3 M KOH (221,473, Sigma-Aldrich), mixed using vortex until completely dissolved, and then adjusted to 10 mL with ultrapure water.
- *For 2,4D:* 10 mg of 2,4D are transferred to a 15 mL sterile conical tube supplemented with 1 mL of 99% ethanol, mixed with vortex until completely dissolved, and adjusted to 10 mL with sterile ultrapure water.
- *For EpiBL:* 10 mg of epibrassinolide are solubilized 1 mL dimethylsulfoxide (DMSO) (0231, VWR), mixed with vortex, and transferred to a 15 mL sterile conical tube. This step is repeated with DMSO until a final volume of 4.2 mL is reached.

Growth factor solutions are filtered through 0.2 μm disposable filters under laminar flow hood and aliquoted as 0.8–1 mL fractions in 1.5 mL autoclaved microtubes. All solutions are then stored at −20 °C.

6. Antibiotic and herbicide solutions for transgenic selection

The selection of transgenic cell lines and transformed bacteria/plant cell growth depend on the selective marker associated to the transgenic construct. Usual selection markers are prepared as concentrated stocks: 1000× concentrated solution of kanamycin monosulfate (K0126, Duchefa) at 50 mg/mL in ultrapure water (w/v), 2000× solution of hygromycin B at 20 mg/mL (A2175, Applichem) in ultrapure water (w/v), 500× of spectinomycin dihydrochloride solution at 50 mg/mL (S0188, Duchefa) in ultrapure water (w/v), 2000× solution of glufosinate herbicide (Basta, Bayer CropScience) at 20 mg/mL in ultrapure water (w/v), and 500× solution of cefotaxime sodium at 200 mg/mL (C0111, Duchefa) in ultrapure water (w/v). Solutions are prepared by weighing 500 mg of kanamycin, 500 mg of spectinomycin, or 2 g of cefotaxim in sterile 15 mL conical tubes, supplemented with 10 mL of ultrapure water and mixed using vortex until complete dissolution. Hygromycin (1/2 dilution of Hygromycin B stock) and glufosinate (1/10 dilution of Basta stock) are diluted from commercially available liquid concentrated stock solutions with ultrapure water in

15 mL sterile conical tubes. All solutions are sterilized through 0.2 μm disposable syringe filters under laminar flow hood and stored at −20 °C, except for glufosinate, which is stored at 4 °C.

7. Drug or compounds solutions for media supplementation

All types of drugs and compounds can be used on iPSCs to alter specific metabolism and/or cellular processes. Previously used compounds have been solubilized either in ultrapure water or dimethylsulfoxide (DMSO), then sterilized through 0.2 μm disposable syringe filters and stored at −20 °C. 1000× concentrated stock solutions are generally made when compound solubility allows it to avoid diluting growth media. Note that a maximum of 4% volume of DMSO can be added to iPSCs without affecting cell viability [36].

8. Staining solutions to monitor cell viability

Solutions used to monitor the viability of cells in suspension cultures include (i) 0.5% (w/v) solution of fluorescein diacetate (FDA) (F7378, Sigma-Aldrich) solubilized in 100% acetone capable of fluorescently labelling living cells visible using epifluorescence microscopy with a blue filter as for FITC or GFP [43], or (ii) 1% (w/v) solution of Evans Blue (EB) (E2129, Sigma-Aldrich) solubilized in ultrapure water capable of staining in blue dead cells visible in brightfield transmission microscopy [31]. EB solution is vortexed and filtered through 0.45 μm disposable syringe filters to remove aggregates. All solutions are protected from light with aluminium foil wrapping: FDA solution is stored at 4 °C whereas EB solution is kept at room temperature.

9. Staining solutions to monitor secondary cell wall formation

Solutions to stain cell walls so that secondary cell wall patterns can be easily distinguished from the primary cell walls include (i) 0.01% (w/v) calcofluor/fluorescent brightener 28 (F3543, Sigma-Aldrich) with 5 mg solubilized first in 1 mL 2–3 M KOH and then adjusted to 50 mL with ultrapure water to stain cellulose visible using epifluorescence microscopy with a UV filter as for DAPI [3] or (ii) 1% (v/v) from commercial stock of wheat germ agglutinin coupled to Alexa488 (WGA-488, W11261, ThermoFisher) visible using epifluorescence microscopy with a blue filter as for FITC or GFP to stain secondary cell wall hemicelluloses [24, 30, 44]. Note that dead TEs accumulate autofluorescent lignin in their secondary cell walls that can be readily observed without any staining using epifluorescence microscopy with a UV filter as for DAPI [5, 13, 43]. Calcofluor solution is filtered through 0.45 μm disposable syringe filters to remove aggregates, covered with aluminium foil and stored at room temperature, whereas WGA-488 is aliquoted in smaller fractions and stored at −20 °C.

3 Methods

3.1 Initiating Cell Suspension Culture from Calli

All the experimental steps from the initiation of cell cultures to any subsequent manipulations are performed under sterile conditions using a laminar flow hood.

1. Surface sterilization of explants and sterile seedling growth

Intact seeds or excised plant organ, also called explants, are surface sterilized in sterile plastic containers (autoclaved microtubes or conical tubes) and sequentially washed with (1) sterile distilled water, two times for 5 min; (2) 70% ethanol, once for 2 min; (3) sterile water, two times for 5 min; (4) 5% Clorox solution, once for 5 min; and (5) sterile water, two times for 5 min. Seeds are then pipetted and deposited in Petri dishes filled with 0.5× half strength MS medium with 0.8% agar-agar, no sugars at pH 5.7 using sterile tips. When using seeds, plates are incubated at 4 °C for at least 2 days for seed stratification and then incubated vertically under long day conditions with 16/8-h day/night photoperiod, 22 °C/18 °C temperature, and 70% relative humidity to enable seedling to grow onto the surface of the solidified media.

2. Induction of calli formation from explants

Explant fragments (2–3 cm long) – either directly after surface sterilization of excised plant organ or derived from sectioning with sterile scalpel and tweezers in vitro grown seedlings – are transferred to the calli induction medium made of 1× MS medium with 3% sucrose, 0.8% agar-agar (or 0.4% phytogel) at pH 5.7 and supplemented with 0.5 mg / L of 2,4D (or 0.5 µl of 1000× stock per mL of media – i.e., 50 µl in 100 mL of media), and 0.05 mg/L of BAP (or 0.05 µl of 1000× stock per mL of media media – i.e., 5 µl in 100 mL of media). Samples are placed onto the surface of the solidified media and then incubated for 3–6 weeks in the dark at 24–25 °C (*see* **Note 3** and **9**). Calli generally form at the extremities of explants and damaged areas caused during the handling with tweezers (Fig. 1a, b).

3. Isolation and growth of calli

Once calli have grown and reached a diameter greater than 2 mm, these are separated from the explants using sterile scalpel and/or tweezers and then transferred to the calli growth media composed of 1× MS medium with 3% sucrose and 0.8% agar-agar (or 0.4% phytogel) at pH 5.7 and supplemented with 1 mg/L of 2,4D (or 1 µl of 1000× stock per mL of media – i.e., 100 µl in 100 mL of media) (Fig. 1b). Calli are then incubated for 3–6 weeks in the dark at 24–25 °C (*see* **Note 3**) to enable their growth (Fig. 1c).

4. Resuspending calli in liquid solution to establish hormone-dependent cell suspension cultures

Once calli have grown and reached a diameter greater than 1 cm, these are separated into two portions: One is transferred to fresh solid calli growth media, whereas the other half is placed using sterile tweezers in 6-well sterile microplates containing 2–3 mL of 1× MS medium with 3% sucrose at pH 5.7 supplemented with 1 mg/L of 2,4D (or 1 µl of 1000× stock per mL of media – i.e., 100 µl in 100 mL of media). Calli are, moreover, fragmented mechanically using sterile tweezers and gentle pipetting up and down to beak cell clumps. Cultivation plates is then sealed using micropore tape, and samples are then incubated for 1–2 weeks with agitation (120 rpm for 1.9 cm orbits) in the dark at 24–25 °C and monitored every day (Fig. 1d–e). Samples exhibiting active growth are transferred to sterile Erlenmeyer flasks, and the cell culture volume is gradually increase by 50% every 1–2 weeks (*see* **Note 10**).

5. Removing cell debris from cell suspensions

Turbid media of growing cells and calli fragments, which can cause browning and cell death, are removed by washing cell suspensions. Sterilely transfer the growing cell suspension into a 15 or 50 mL sterile conical tubes and gently centrifuge (200 g for 2 min at room temperature) using a swing out rotor centrifuge (*See* **Note 5**). Extracellular medium can then be removed under the laminar flow hood and replaced with fresh 1× MS medium with 3% sucrose at pH 5.7. Pelleted cells are then gently re-suspended by inverting the tube several times (until no pellet remains at the conical end of the tube) and subjected to two additional rounds of centrifugation and medium removal/resupply. The last medium to be supplied is 1× MS medium with 3% sucrose at pH 5.7 supplemented with 1 mg/L of 2,4D. Note that if cell clumps are large, the washing step can be performed by replacing the centrifugation step by a 10 min incubation on the bench to enable cells to sedimentate.

6. Routine cell sub-culturing

10–50% of 7-day-old cell suspension cultures (v/v) are routinely sub-cultured on a weekly basis into fresh 1× MS medium with 3% sucrose at pH 5.7, supplemented with 1 mg/L of 2,4D and incubated with agitation (120 rpm for 1.9 cm orbits) in the dark at 24–25 °C (*see* **Notes 3** and **4**) (Fig. 1d–e). Note that the relative percentage of cell to media will decrease as the cell suspension culture establishes itself, which can take from several weeks to years.

3.2 Screening of Hormone-Habituated Growth in Cell Suspension Cultures to Establish iPSCs

In contrast to immortalized cell suspensions that require a constant supply of external growth factors, iPSCs are made of undifferentiated cells actively growing in media with nutrients but without any added growth factors. This independence of hormones is called hormone-habituation, which has been already observed as early as

1942 in carrot cell lines that gradually lost their growth requirement for auxin, cytokinins, and vitamins [45]. Habituation in plant cell in vitro culture was, thus, noticed for many plant species, including *Beta vulgaris* [46], *Arabidopsis thaliana* [47], *Catharanthus roseus* [48], *Helianthus annuus* [49], *Vinca rosea* [49], and *Daucus carota* [50]. The continuous growth of hormone-habituated cell suspension cultures has been attributed to an epigenetic reprogramming [51] that, nevertheless, maintains the capacity of cells to respond to external factors such as hormones – observed for *Beta vulgaris* [46] and *Arabidopsis thaliana* [3, 23, 24, 30, 47] – and/or composition of the medium, such as the type of sugar – as observed in *Arabidopsis thaliana* between sucrose, glucose, and fructose [35, 40].

1. Screening cell suspension for hormone-habituated growth

About 2–3 L of actively growing 7-day-old cell suspension cultures (Fig. 1f) are plated onto Petri dishes containing 1× MS medium with 3% sucrose and 0.8% agar-agar (or 0.4% phytogel) at pH 5.7 without any growth factor and incubated in the dark at 24–25 °C for at least 10–18 weeks. Potentially hormone-habituated calli with diameter greater than 2 mm are transferred onto fresh solid medium (1× MS medium with 3% sucrose and 0.8% agar-agar (or 0.4% phytogel) at pH 5.7) using sterile tweezers and incubated for an additional 3–6 weeks in the dark at 24 ± 0.5 °C (*see* **Note 3**) (Fig. 1a). The resulting growing calli are then fragmented again and transferred fresh solid medium (1× MS medium with 3% sucrose and 0.8% agar-agar (or 0.4% phytogel) at pH 5.7) to ensure the hormone-habituated growth.

2. Resuspending calli in liquid solution to establish hormone-habituated cell suspension cultures

Hormone-habituated calli with diameter greater than 1 cm are separated into two: One half is transferred to fresh solidified media while the other half is placed using sterile tweezers in a 6-well sterile microplate containing 2–3 mL of 1× MS medium with 3% sucrose at pH 5.7. Calli are gently mechanically fragmented using sterile tweezers and pipetting up and down to break away cell clump. Resuspended cell samples are then incubated for 1–2 weeks with agitation (120 rpm for 1.9 cm orbits) in the dark at 24 ± 0.5 °C and monitored every day. Samples exhibiting active hormone-habituated growth are then transferred to sterile Erlenmeyer flasks and the cell culture volume is gradually increased by supplementing cell with 50% fresh liquid media (v/v) every 1–2 weeks (Fig. 1d–g).

3. Weekly sub-culturing maintenance of hormone-habituated cell line

Hormone-habituated cell suspension cultures are maintained by weekly sub-culturing 10–20% of 7-days old cells into fresh 1×

MS medium with 3% sucrose (or another sugar source) at pH 5.7 and incubated with 120 rpm agitation in the dark at 24 ± 0.5 °C (*see* **Notes 3** and **4**) (Fig. 1d–g).

4. Platting of diluted cell suspension to maintain hormone-habituation

Hormone-habituation and their differentiation potency can be gained or lost with the successive weekly cell sub-culturing that can introduce and stabilize mutations leading to chimeric cell suspension cultures. Hormone-habituated cell suspension cultures are, therefore, routinely screened to confirm hormone-habituation by plating 2–3 mL of 7-day-old cell at different titer 50%, 20%, and 10% dilution in fresh 1× MS medium with 3% sucrose at pH 5.7 onto Petri dishes containing 1× MS medium with 3% sucrose and 0.8% agar-agar (or 0.4% phytogel) at pH 5.7 and incubated 3–6 weeks in the dark at 24 ± 0.5 °C. Resulting actively growing calli reaching diameter greater than 1 cm are then transferred back to solid medium as in 3.2.1 or to liquid medium as in 3.2.2 (Fig. 1a–c).

3.3 Stable Genetic Transformation of Habituated Cell Suspensions

Stable transgenic transformation of hormone-habituated cell suspension cultures are made using the horizontal gene transfer capacity of transgenic *Agrobacterium tumefaciens*, having both the helper plasmid and the modified gene construct, co-cultivated with plant cell suspensions to be stably and randomly insert the transgene (Fig. 2). Multiple types of genetic transformation have been successfully reported, including (i) targeted silencing constructs using small double strand RNA and artificial microRNA [3, 30–34], (ii) targeted overexpression of fluorescently fused proteins [3, 7, 30–32], and (iii) transcriptional reporter driving β-glucuronidase (GUS). All experimental to achieve the stable genetic transformation of plant cell suspension cultures are performed under sterile conditions (*see* **Subheading** 2.1). The resulting transgenic lines are very stable in time with some transgenic cell suspension cultures established more than 7 years ago still used today, capable of TE differentiation and with good fluorescent fusion expression [3, 7, 30–34].

1. Co-culture of *Arabidopsis* hormone-habituated cells with transgenic *Agrobacterium tumefaciens*

About 5 mL of 3–5 days hormone-habituated plant cell suspension cultures are transferred to a 50 mL sterile Erlenmeyer flask, supplemented with 5 mL of fresh 1× MS medium with 3% sucrose at pH 5.7 and 200 μL of 2 days grown transgenic *Agrobacterium tumefaciens* (cultivated in 1× LB medium with selection antibiotics like spectinomycin until O.D. 600 nm ~1). The co-cultures are incubated for 2 days in the dark with agitation at 24 ± 0.5 °C. Both

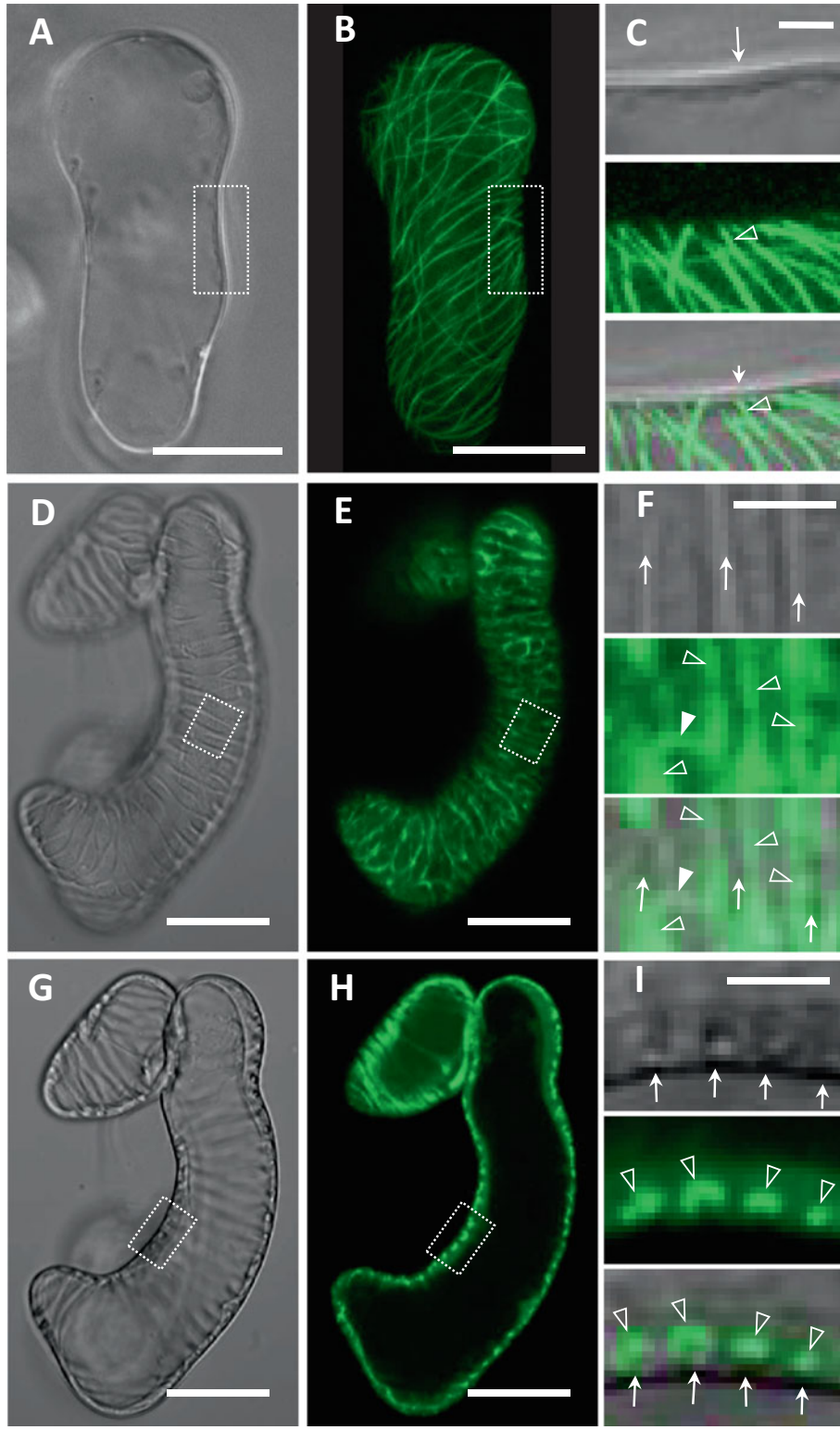


Fig. 2 Examples of live-cell imaging showing the reorganization of the cortical microtubule array in stably transformed iPSCs overexpressing tubulin-α6-GFP fusions during TE formation. (**a**) Tangential focal plan of

LB4404 and GV3101 strains of *Agrobacterium* have been used successfully for the stable transformation of *Arabidopsis* cell cultures [3, 30–34].

2. Removal of excess *Agrobacterium tumefaciens* and damaged plant cells

The co-culture is transferred to a 15 mL Falcon conical tube and gently pelleted at 200 g for 2 min at room temperature by centrifugation using a swing out rotor (*see* **Note 5**). The extracellular medium is then removed delicately without disturbing the cell pellet (generally, the pellet is between 1–2 mL packed cells) and 10 mL of fresh 1× MS medium with 3% sucrose at pH 5.7 are added to resuspend cells by inverting the tube several times (until no pellet remains at the conical end of the tube). The washing step is repeated three additional times until the extracellular medium shows no turbidity.

3. Screening for transgenic cell suspension on selective medium

At the last centrifugation step, the volume of the pelleted cells is supplemented with 1.5 to 2 volumes of fresh 1× MS medium with 3% sucrose at pH 5.7 and resuspended by gentle inversion and/or pipetting up and down. Total 2–3 mL of resuspended cell suspensions are then poured and spread on the surface of Petri plates with solidified 1× MS medium with 3% sucrose and 0.8% agar-agar (or 0.4% phytogel) at pH 5.7 supplemented with 200–250 μg/mL of cefotaxim (as a general antibiotic to target remaining *Agrobacterium*) as well as the selective antibiotic/herbicide present in the transgenic construct – generally, either 50 μg/mL of

Fig. 2 (continued) cell induced to become TE at $t = 0$ days observed in brightfield transmission, bar = 20 μm. (**b**) Image of half-cell maximal projection of cell induced to become TE at $t = 0$ days observed using confocal microscopy to detect GFP, bar = 20 μm. (**c**) Close-up of boxed region in A and B to show from top to bottom, brightfield transmission, GFP fluorescence and merged images, bar = 5 μm. White arrows indicate primary cell walls and hollow arrow head indicates microtubules. (**d**) Tangential focal plan of cell induced to become TE at $t = 4$ days observed in brightfield transmission, bar = 20 μm. Note that secondary cell wall patterns can be easily distinguished. (**e**) Image of half-cell maximal projection of cell induced to become TE at $t = 4$ days observed using confocal microscopy to detect GFP, bar = 20 μm. (**f**) Close-up of boxed region in **c** and **d** to show from top to bottom, brightfield transmission, GFP fluorescence and merged images, bar = 7 μm. White arrows indicate secondary cell wall thickenings, filled arrow heads show cortical microtubules in-between secondary cell wall thickenings and hollow arrow heads indicate microtubules flanking the secondary cell wall thickenings. (**g**) Middle focal plan of cell induced to become TE at $t = 4$ days observed in brightfield transmission, bar = 20 μm. Note that secondary cell wall patterns can be easily distinguished. (**h**) Image of median optical sections maximal projection of cell induced to become TE at $t = 4$ days observed using confocal microscopy to detect GFP, bar = 20 μm. (**i**) Close-up of boxed region in **g** and **h** to show from top to bottom, brightfield transmission, GFP fluorescence and merged images, bar = 7 μm. White arrows indicate secondary cell wall thickenings, and hollow arrow heads indicate microtubules cortically delimiting the secondary cell wall thickenings as U-shape cups

kanamycin, 5 μg/mL of hygromycin, or 20 μg/mL of Basta herbicide. Plates are sealed using surgical Millipore tape and then incubated for 5–12 weeks in the dark at 24–25 °C (Fig. 1a).

4. Transgenic calli selection

Clearly separated calli of diameter greater than 2–3 mm growing on the selective media are then transferred using sterile tweezers onto the surface of new Petri plates filled with 1× MS medium with 3% sucrose and 0.8% agar-agar (or 0.4% phytagel) at pH 5.7 supplemented with 200–250 μg/mL of cefotaxim and selective antibiotic/herbicide markers. The new selective media is used to confirm transgenic cell lines, each individual calli, made of clonal cells, are separated by at least 1 cm to check for any satellite resistance. Plates are then incubated for 2–5 weeks in the dark at 24 ± 0.5 °C (Fig. 1b–c).

5. Resuspending and screening in liquid culture transgenic lines

Freshly developed calli of diameter greater than 1 cm are placed in 2–4 mL of fresh liquid 1× MS medium with 3% sucrose at pH 5.7 with selective compound and incubated in sterile 6-wells plate or 25 ml Erlenmeyer flasks for 1 week in the dark with agitation at 24–25 °C (*see* **Notes 3** and **4**) (Fig. 1d–e). To maximize resuspension, transferred calli are mechanically fragmented gently into smaller pieces using tweezers and/or pipetting up and down to break down cellular clumps. The actively growing cell lines are then screened according to the activity of the genetic construct stably inserted, such as the overexpression of GFP fusion proteins (Fig. 2) or promoter driving β-glucuronidase (GUS) reporter gene [31].

3.4 Triggering the Differentiation of iPSCs into Specific Cell Types

The induction of cell differentiation from actively dividing parenchyma cells in iPSCs depends on (i) the cell cycle phase and (ii) the cell density of the iPSC cell initial stock, (iii) the inductive media, and (iv) the presence of specific hormones or stimuli (light, sugar source) (Fig. 3). To date, *Arabidopsis* iPSCs have been shown to differentiate into two distinct cell types from the same common iPSC cell stock, including TE/XP [1, 3, 4, 7, 31–34] and photosynthetic mesophyll cells [40]. Other cell culture systems enable the differentiation of TEs from parenchymatic cells in *Zinnia elegans* [5], *Lactuca sativa* [52], *Helianthus tuberosus* [53], and *Arabidopsis thaliana (14–15, 18)*, but unlike iPSCs, these other experimental systems have not been shown to be pluripotent.

1. Cell cycle synchronization of initial iPSC cell stock

To ensure highest differentiation efficiency, cell cycles of the iPSCs need to be synchronized to G_1/G_0 to be the most responsive to cell differentiation and limit cell division. Similarly to the *Zinnia* system that used the S-phase DNA replication inhibitor aphidicolin

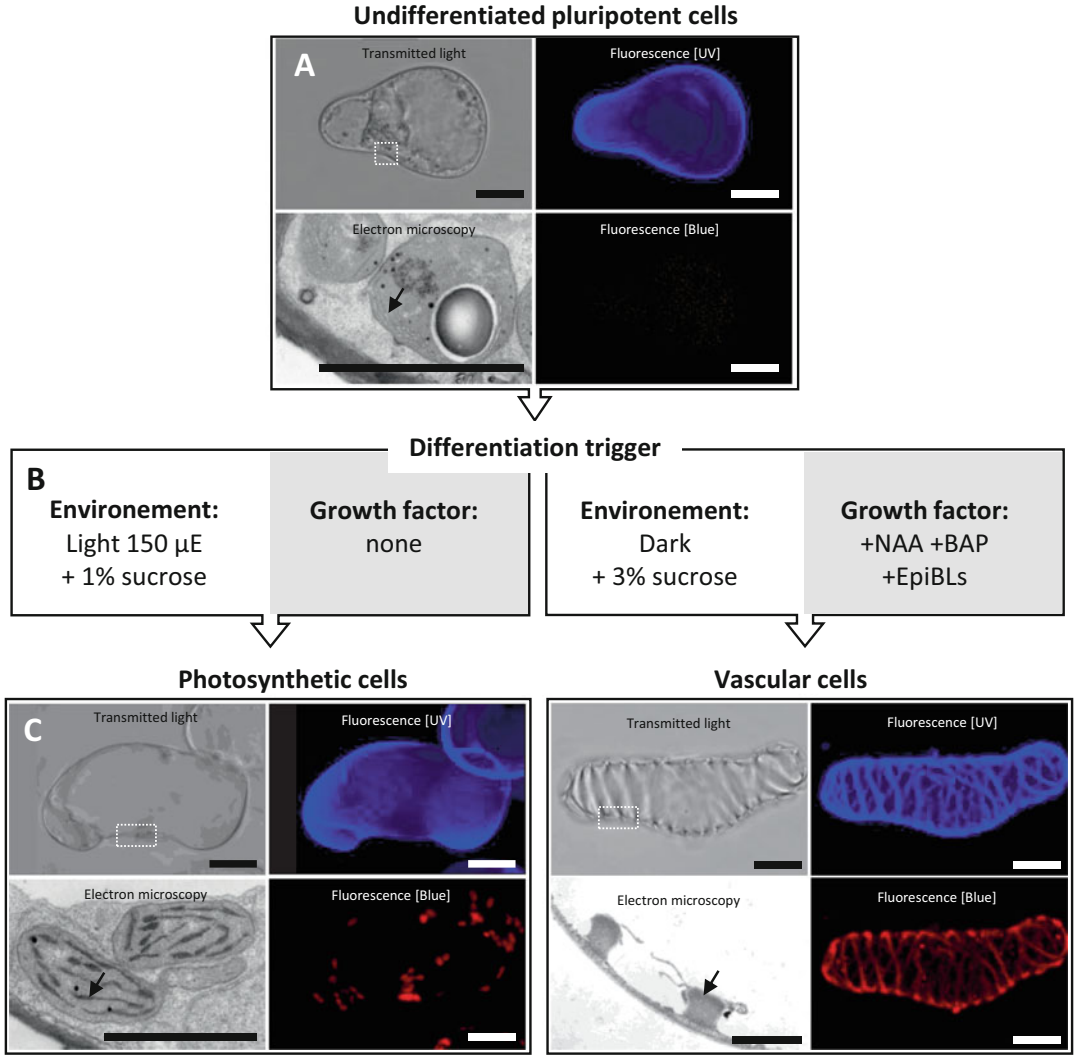


Fig. 3 General scheme presenting the use of plant inducible pluripotent cell suspension cultures (iPSCs) in *Arabidopsis thaliana* to trigger the differentiation specific cell types. (**a**) Image of undifferentiated actively dividing parenchyma cell without any hormones at $t = 0$ days observed in brightfield transmission and epifluorescence to observed calcofluor-stained cell walls (under UV excitation) and chlorophyll/lignin autofluorescence (under blue light excitation). Transmission electron microscopy image (in the bottom left) shows the state of characteristic organelles of the cell, with here proplastids with starch granule and their characteristic prolamellar body indicated by arrow, bar $= 4$ µm. (**b**) Difference in triggers induce the differentiation of specific cell types. These include both modification of the cellular environment (sugar concentration and illumination) as well as changes in the supplied growth factors. (**c**) Image of differentiated photosynthetic parenchyma cell at $t = 7$ days observed in brightfield transmission and epifluorescence to observed calcofluor-stained cell walls (under UV excitation) and chlorophyll autofluorescence (under blue light excitation). Transmission electron microscopy image (in the bottom left) shows the state of characteristic organelles of the cell, with here chloroplasts with thylakoids and grana indicated by arrow, bar $= 4$ µm. (**d**) Image of differentiated tracheary element cell at $t = 7$ days observed in brightfield transmission and epifluorescence to observed calcofluor-stained cell walls (under UV excitation) and lignin autofluorescence (under blue light excitation). Transmission electron microscopy image (in the bottom left) shows the state of characteristic organelles of the cell, with here the secondary cell wall thickenings indicated by arrow, bar $= 4$ µm

for cell cycle synchronization [9], *Arabidopsis* iPSCs are gently synchronized using sucrose/nutrient depletion, an important regulator of the G_1 to S transition [54]. In order to synchronise the cell cycle of iPSCs using sucrose/nutrient depletion, an initial density of 60 mg/mL of 7-day-old dividing iPSCs are cultivated several days beyond the plateau phase of the growth for a total of 9–11 days.

2. Cell density adjustment

To ensure optimal cell differentiation, the density of iPSCs is adjusted to 30 mg/mL. In sterile conditions, 10 mL of 9–11-day-old G_1/G_0 synchronised cell suspensions are transferred to a sterile 15 mL Falcon conical tube (weighed empty beforehand) and gently centrifuged at 200 g for 2 min at room temperature using a swing out rotor. The extracellular medium in excess is then carefully removed using a controllable suction pipette (i.e. using Eppendorf pipetboy) until the pellet is not covered by any liquid and then weighted again. The pelleted and weighed cells are then resuspended in 5 mL fresh 1× MS medium with 3% sucrose and 1 mM MES at pH 6.0 and inverted until no pellet remains at the conical end of the tube – this sample corresponds to the concentrated iPSC stock to dilute at the desired cell density. The newly re-suspended and concentrated cells are then transferred to the cultivation containers (6-well plates, Erlenmeyer) containing fresh 1× MS medium with 3% sucrose and 1 mM MES at pH 6.0 so that the final cell density reaches 30 mg of cells/mL of medium (final volume depends on the pellet weight; *see* **Note 11**).

3. Hormonal triggering of TE differentiation

Freshly G_1/G_0 synchronised iPSCs at a density of 30 or 60 mg of cells/mL are induced to differentiate into TEs by specific combination of plant growth factors. To do so, media are supplemented with 6 µg/mL of NAA (0.6 µL of the 166x stock/mL of culture medium), 1 µg/mL of BAP (1 µL of the 1000x stock/mL of culture medium), and 4 µM of epibrassionolide (0.8 µL of the 1200x stock/mL of culture medium). Induced iPSCs are then incubated in the dark, under agitation at 24 ± 0.5 °C for up to 50 days [4] if needed (*see* **Note 11**). Any changes to the cell age, cell density, pH of the medium and the hormone concentrations will lead to a reduction of TE differentiation efficiency [31, 33].

4. Light triggering of mesophyll differentiation

As iPSCs are pluripotent, G_1/G_0 synchronised iPSCs at a density of 60 mg of cells /mL can be induced to differentiate into photosynthetic mesophyll cells [40] using the sugar-depleted media composed of 1× MS medium with 1% sucrose at pH 5.7 and illuminated by continuous light at the intensity of 150 µmol

photons m^{-2} s^{-1} with agitation for 7 days. Light-induced iPSCs are then sedimentate, excess extracellular media is replaced by fresh 1× MS medium with 1% sucrose at pH 5.7 and cells are then incubated for another 7 days under continuous light at the intensity of 150 μmol photons m^{-2} s^{-1} with agitation.

5. Sampling of cells during the differentiation time course

The iPSCs at specific time-point or following specific treatment are harvested either (i) by centrifugation at 200 g for 5 min at room temperature using a swing-out rotor and removing the excess culture medium by pipetting or (ii) by vacuum-filtration through a double 100 μm nylon mesh and transferring the cells with a clean spatula to an aluminium foil folded sheet. The resulting cell pellets or filtrates are immediately flash frozen in liquid nitrogen and stored at −80 °C until their processing.

3.5 Monitoring Cell Culture Growth, Viability, and Differentiation

Cell suspension cultures composed of both isolated cells and clumps of 3 to 10 cell clusters can be directly monitored using microscopic analysis to assess the state of individual cells within the entire cell population at each time points during the cell division or differentiation time-course. Following changes in cell density, cell viability and/or cell differentiation (by the presence of secondary cell walls for TEs or autofluorescent chloroplasts for mesophyll cells) are essential steps to be performed during the establishment, screening and use of iPSCs, such as described in **Subheadings** 3.1, **step** 6, 3.2, **step** 3, 3.3, **step** 5, and 3.4, **step** 3 and 4.

1. Measuring cell growth

Changes in the cell density of iPSCs is measured either by: (i) by the *packed cell volume* (PCV), a percentage that corresponds to the volume of cells pelleted by 2 min centrifugation at 200 g in 10 mL of cell suspension determined using a graduated conical tube [35]; (ii) by the fresh weight density, the cell mass of fresh cells after vacuum filtering (described in **Subheading** 3.4, **step** 5) in 10 mL of cell suspensions and expressed in mg of cells per volume of media (Fig. 1a) [35]; or (iii) by the dry weight density, the cell mass after vacuum filtering 10 mL of cell suspensions, transferred to an aluminium sheet and dried in an oven overnight at 60−70 °C [35] and expressed in mg of cells per volume of media. Generally, the fresh weight density to PCV relationship is around 11.4 ± 0.2 mg of pelleted fresh cells per % PCV, thus requiring the pelleted cells to be adjusted to 25% PCV with fresh media to reach 60 mg/mL fresh cell density.

2. Measuring cell viability

Changes in cell viability between individual cells during the differentiation time-course and/or in response to specific treatment is measured using viability stains such as (i) fluorescently staining living cells by incubating 100 µl cell suspension with 2 µL of 0.5% FDA solution [31, 36, 43] or (ii) chromogenically staining dead cells by incubating 1:1 (v/v) cell volume with 1% EB solution. Cells are then incubated 1–3 min at room temperature and observed between glass and coverslip using light microscopy: EB staining colors dead cells in blue in brightfield transmission (*see* **Note 13**), whereas FDA stains living cells with fluorescein (green fluorescence) under blue light excitation (excitation filter 450–490 nm; emission filter 515 nm) (*see* **Note 14**) [31, 36, 43]. Cell viability can also be directly determined without any staining in stably transformed cells, such as monitoring the presence of intact nuclei per cells using constitutively driven HISTONE2B-RFP fusions [7]. Representative measures are obtained by counting from 200 to 500 individual cells per sample. The proportion of living cells are then expressed as percentage of either all cells in the sample or specific cell types or morphotypes.

3. Key morphological aspects of cell differentiation

The measurement of cell differentiation efficiency at the single cell level during the differentiation time-course is estimated using the key differentiated traits of each cell types, such as the patterned secondary cell walls in TEs [3, 4, 14, 23, 30, 33, 41] or the presence of chloroplasts in mesophyll cells [40, 41]. TE differentiation efficiency is, thus, followed and estimated using (i) brigthfield microscopy due to the birefringence of TE secondary cell walls [3, 4, 14, 23, 30, 33, 41], (ii) fluorescent staining of cellulose using 10 µL of 0.01% calcofluor solution for 100 µL of cell suspensions (Fig. 3–4) [3, 4, 14, 23, 30, 33, 41], or (iii) autofluorescence of lignin [5, 30, 36] or chloroplasts [40, 41] (Fig. 3). Cells are incubated 2–5 min at room temperature and observations are performed using light microscopy by placing 50 µL of the stained samples between microscopy glass slides and coverslips. Calcofluor-stained cells, which can be combined with FDA, are observed with UV filter, such as the ones used for DAPI. TE lignin autofluorescence is visualized without any staining with UV filter, such as the ones used for DAPI [5, 30, 36, 55]. Mesophyll cell differentiation is mainly followed by the formation of chloroplast, which can be easily detected using autofluorescence without any staining with blue filter, such as the ones used for FITC [40, 41]. Approximatively 400–500 individual cells are counted to obtain representative results, and cell differentiation efficiency is expressed as a percentage of all cells in the population (Fig. 4).

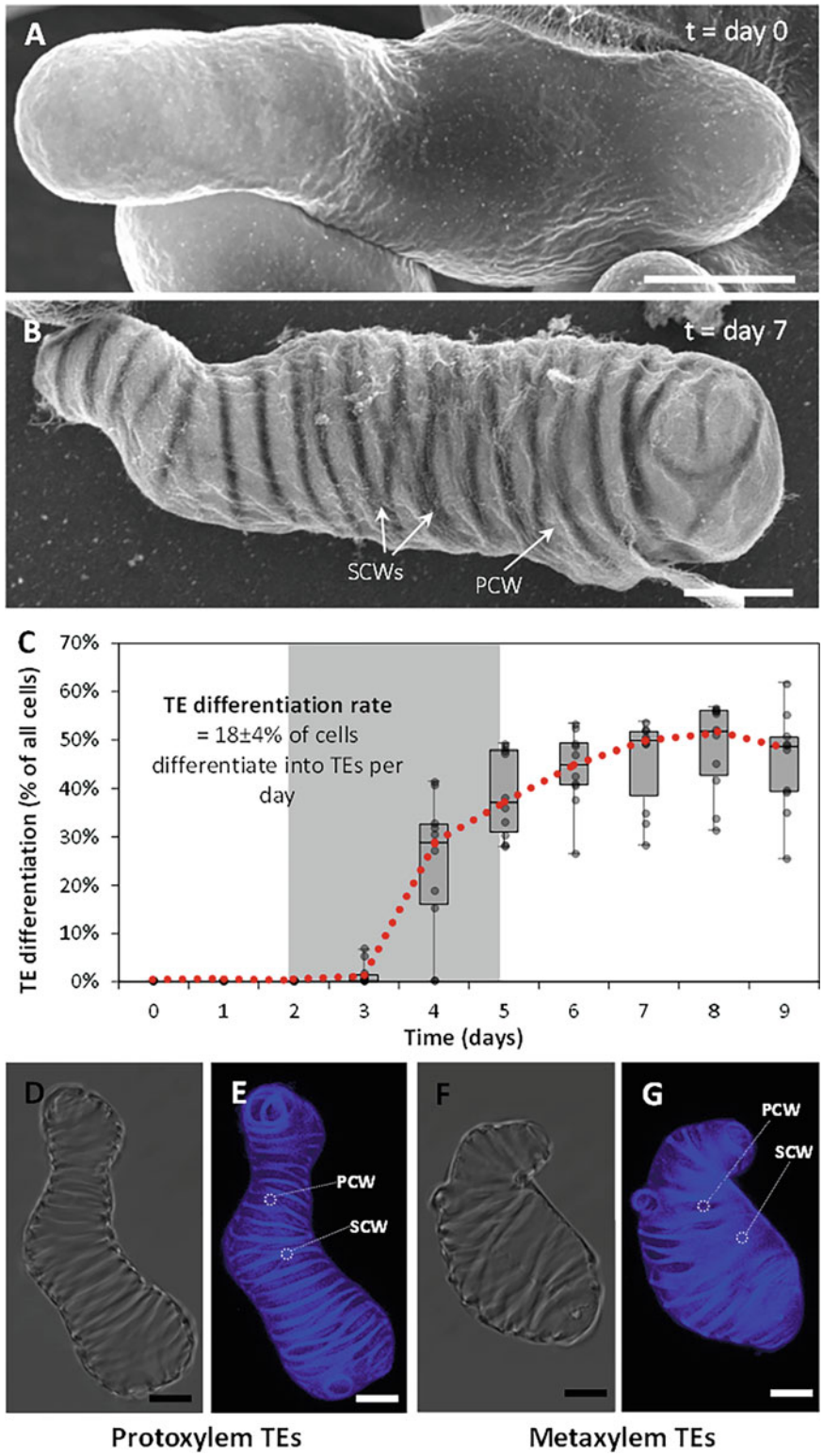


Fig. 4 Triggering TE differentiation in iPSCs of *Arabidopsis thaliana*. (**a**) Scanning electron microscopy image of cell induced to become TE at $t = 0$ days, bar = 15 μm. (**b**) Scanning electron microscopy image of cell fully

3.6 Real-Time Live Cell Imaging of Cell Differentiation in iPSCs

Each cell in *Arabidopsis thaliana* iPSCs is either isolated or in small cellular clump of 3 to 9 cells, this property is ideal for real-time live imaging either of short term (minutes to few hours) or long term (up to 3 days) [3, 30–32, 56]. Such techniques enable to directly monitor the chronological progression of cell differentiation and/or defect in metabolism or morphology following genetic changes and/or drug treatment in three to multiple dimensions using light, confocal, or light-sheet microscopies. Examples of real-time live cell three dimensional imaging were made to determine the duration of TE xylan/cellulose secondary cell wall deposition [3, 30, 31], the duration of nuclear degradation [30, 31, 56] and vacuole implosion [56] during TE programmed cell death, and the timing of lignin deposition during TE differentiation [3, 30]. The main difficulty of real-time live imaging is to maintain oxygenation and humidity and immobilize cells during the imaging period.

1. Sample mounting in microscopy bio-chamber

   Total 200 μL of cell suspension culture are transferred into separate wells of a bio-chamber (one for the control and one for the treatment), onto the poly-lysine coated cover-slip delimiting the bottom part of the 3 mm thick acrylic plastic bio-chamber. Design and assembly of the bio-chamber have been described previously in [57]. The cell suspension is then spread all over the cover-slip surface, and excess culture medium and nonadherent cells are removed by pipetting. This step is repeated twice to fully saturate the poly-lysine surface of the bottom of each well in the bio-chamber with cells.

2. Immobilization of cells in microscopy bio-chamber

   Total 500 μL of 0.5% low melting point agarose (A9639, Sigma-Aldrich) in 1× MS medium with 3% sucrose at pH 5.7 are slowly added from one corner of the well until a meniscus is formed

Fig. 4 (continued) differentiated in TE at $t = 7$ days, bar = 15 μm. Note the characteristic secondary cell pattern of TEs alternating unthickened regions with only primary cell wall (PCW) and thickened regions with secondary cell walls (SCWs). (**c**) Progression of TE differentiation in iPSCs during culture time-course ($n = 10$ independent cell cultures). Note that the active phase of differentiation for secondary cell wall formation is shaded in grey and occurs at the linear rate of 18 ± 4% of all cells per days to reach a differentiation plateau of ~50% of all cells. (**d**) TE at 7-days with a protoxylem secondary cell wall pattern observed using brightfield transmission, bar = 10 μm. (**e**) TE at 7-days with a protoxylem secondary cell wall pattern stained with calcofluor and observed using epifluorescence, bar = 10 μm. Note the characteristic annular/sprial pattern of TEs alternating unthickened regions with only primary cell wall (PCW) and thickened regions with secondary cell walls (SCWs). (**f**) TE at 7-days with a metaxylem secondary cell wall pattern observed using brightfield transmission, bar = 10 μm. (**g**) TE at 7-days with a metaxylem secondary cell wall pattern stained with calcofluor and observed using epifluorescence, bar = 10 μm. Note the characteristic pitted pattern of TEs alternating unthickened regions with only primary cell wall (PCW) and thickened regions with secondary cell walls (SCWs)

at the top of the well. Upper surface of each well in the bio-chamber is flattened using a microscopy slide to temporally seal the bio-chamber. Medium is incubated 10–15 min on a flat surface of a laboratory bench for the low melting point agarose to solidify thus immobilizing cells in the bio-chamber.

3. Mounting of the bio-chamber on the upright or inverted microscope

The sealing microscopy slide is removed delicately without damaging the agarose surface prior to the imaging and replaced with a microscope cover-slip separated from the bio-chamber by two spacing strips of Whatmann paper 3 mm (3–4 mm wide) and sealed using double sided tape. The assembled bio-chamber is then mounted in the holding brackets of an upright or inverted microscope (i.e., Zeiss Aixoplan II with automated xyz stage equipped with Axiocam camera and controlled with Axiovision software) for real-time live cell imaging observations (Fig. 3). Real-time acquisition is then performed as described in the detailed protocol described in [57].

3.7 Drug-Induced Modulation of Cell Differentiation or Uncoupling of Distinct Specialization Stage

The timely supply or removal of drugs represents a great tool to test the importance of a cellular component (i.e. microtubules), a hormonal pathway and/or an enzyme during the chronological progression of the differentiation in iPSCs. Drug treatment affecting enzyme activity can, moreover, be chemically complemented to restore and even redirect the metabolism [5, 36]. Delayed drug supply and/or removal from the cell culture media, thus, enable to determine which process is altered by the drug treatment and when it starts during cell differentiation as well as its duration. Drug treatments have, thus, been successfully used during TE formation for metabolic regulation of lignin biosynthesis, chemical genomic analysis of novel interfering molecules for lignin biosynthesis, and hormonal intervention of ethylene biosynthetic inhibitor aminovinylglycine (AVG) [43], the ethylene perception inhibitor silver thiosulfate (STS) [5, 56], the microtubule-destabilizing compound oryzalin, and the microtubule-stabilizing drug taxol [3, 34].

1. Dose toxicity (can be performed on both 6-well microplates and larger Erlenmeyer flasks): Increasing concentrations of drug as well as the corresponding of solvent used to solubilize the drug need to be tested to define the maximal non-lethal dose of drug that can be supplied to iPSCs. Following the effect of concentration of drug between the different wells or flasks, by monitoring cell viability after a certain time, depending on the drug and its targets, needs to be performed using the methods described in **Subheading** 3.5, **step** 2.
2. Dose-dependency (can be performed on both 6-well microplates and larger Erlenmeyer flasks): Nonlethal drug treatments are then provided at different concentration to each

independent well or flask at a defined time after the hormonal induction of cell differentiation in iPSCs. One example is the dose-dependent effect of aminovinylglycine (AVG) on TE differentiation efficiency [43], of oryzalin on TE secondary cell wall organization [3], or of piperonylic acid (PA) on TE secondary cell wall lignification [4, 5, 36].

3. Delayed drug treatments to determine which process is affected (can be performed on both 6-well microplates and larger Erlenmeyer flasks): The nonlethal drug treatments are made at a defined time lapses after the hormonal induction of cell differentiation in iPSCs to define whether modifications occur. One example is the impact of the delayed oryzalin treatment on TE secondary cell wall organization [3] or of silver thiosulfate (STS) on TE programmed cell death [56].
4. Removal of the drug inhibition by washing (can be performed on both 6-well microplate and larger Erlenmeyer flasks): Cells are transferred to a 15 mL or 50 mL Falcon conical tube and gently pelleted using centrifugation with a swing out rotor at 200 g for 2 min at room temperature. The total volume is recorded, the extracellular medium is removed delicately without disturbing the cell pellet with a pipette and replaced with the same volume of fresh TE induction medium (1× MS medium with 3% sucrose and 1 mM MES at pH 6.0). Cells are then re-suspended by gentle inversion and optionally subjected to additional rounds of centrifugation and medium removal if needed. Cells are, thereafter, incubated either into fresh medium or the extracellular medium from cells at the same developmental stages, which were not treated with the drug. One example is to test the lignin-compatibility of the phenolic secreted in the extracellular medium of STS-treated cells by supplying them to PA-treated cells of the same age [5, 56].

3.8 Extracting Biomolecules During Cell Differentiation Time-Course

Due to the chronological progression sequence of cell differentiation, one can readily sample cells at different time points during the cell culture time-course to follow changes in biomolecules during the distinct chronological stages of cell specialization. Previous analysis have shown a ~ 8 h delay between the first and last TE committing programmed cell death [5], thereby showing that sampling at a minimal of 12 h delays suffices to isolate distinct stages of cell differentiation. Harvested cell samples, collected as described in **Subheading** 3.4, **step** 5, are ground in ceramic mortar with pestle (*see* **Note 15**). Powdered samples are then transferred to new autoclaved microtubes, filled halfway, to be either stored at − 80 °C or directly processed. Powdered cells can then be processed using any standard protocol to extract specific cellular components or biomolecules, such as previously described for RNAs [3, 5, 7, 13, 40], soluble proteins [3, 30], cell walls [4], or metabolites [40].

4 Notes

1. The use of accessory flame sterilization with a Bunsen burner under laminar flow hood is not advised, as it will increase local temperature, causing heat-shock-induced cell damages and cell death during handling.
2. Cleaning of Erlenmeyer flask for cell cultivation is essential as any cell debris left in the flask from previous cultures can be perceived by the cells to induce morphogenic response. Thus to avoid undesired cell responses, Erlenmeyer flasks are first cleaned manually with warm water with household detergent (i.e., Nila, Nørdex) and glassware brush, well rinsed, and then washed again in dish washer with laboratory detergent (i.e., A285 Solid pF, RBA) using hot wash and drying program. Glassware is then immediately covered with a cotton wool ball- Ensure that the cotton ball is neither humid nor too compacted, otherwise cell oxygenation during cultivation will be compromised.
3. Ideal temperature for iPSC cultivation is from 23.8 to 24.2 °C; below 23.5 °C will slow down cell division and cell growth, and above 24.5 °C will stress cells, causing browning and oxidation, leading to cell death. Note that white light contamination will also affect the growth and differentiation of habituated cell suspensions; green safety light is, therefore, recommended for handling cells in the growth room. Additionally, black painted wall and a safety lock delimited by black curtains to enter the growth room represent additional features limiting white light contamination in the cell culture growth room.
4. Note that orbital agitation speed (in rpm) depends on the rotation diameter of the orbital shaker: 120 rpm are used for effective nondamaging agitation using an Orbit 1900 (Labnet, USA) with a 1.9 cm rotation diameter.
5. Note that centrifugation of cell suspensions needs to be made at room temperature or close to the growth incubation temperature of 24 ± 0.5 °C, and heat-shocks will induce changes in the growth and sensitivity of the habituated cell suspensions.
6. Note that vacuum filtering is the most efficient way to remove excess water from the collected cell suspension samples.
7. Note that the external surface of containers and the user's arms are surface sterilized by spraying with a solution of 70% ethanol or using alcogel when appropriate.
8. Note that autoclaving will cause a slight drop of the pH in the MS medium due to thermal cracking of the sucrose into small organic acid and simpler sugars. Thermal cracked derivatives from sucrose can be avoided by mixing 1 volume of autoclaved

2x MS solution at pH 5.7 without any sugar with 1 volume of 6% sucrose in water (w/v) at pH 5.7 sterilized through a 0.2 μm filter [35].

9. Note that the sealing of Petri plates for calli production and growth is best made with micro-pore tape rather than parafilm, which becomes brittle and cracks.
10. Note that cell suspension cultures should remain for a maximum of 1 h without any agitation. Longer absence of agitation will lead to hypoxia/anoxia, causing browning from stress then death of the cell suspensions.
11. The weight of the cell pellet is determined by subtracting the weight of the tube with dried pellet minus the weight of the empty tube. The volume of medium to be added to reach 30 mg/mL is calculated by dividing the pellet weight (in mg) by 30.
12. The exact time and date need to be recorded, as it will correspond to the initiation time or t_0 of the cell differentiation time course.
13. Note that EB exhibits affinity for cellulose and will stain TE secondary cell walls in blue.
14. Note that long incubation with FDA will lead to an extracellular release of fluorescein, which will prevent efficient numeration of cell viability.
15. Large flash frozen samples will require hammering if placed in a collection tube before transfer in mortar and pestle. Mechanical extraction in the containing tubes using vortexing with tungsten carbide beads and freeze/thawing cycles only works for small cell pellets of 10–50 mg [5].

Acknowledgments

We thank Prof. Åsa Strand and Dr. Alain Jauneau for electron microcopy images. This work was supported by Vetenskapsrådet VR (grant 2010-4620 and 2016-04727), the SFO TD/IP (to DM and EP), the Kempe Foundation (Gunnar Öquist Fellowship to EP), by the Carl Tryggers Foundation CTS 16:362/17:16/18:306/21:1201 (to EP), the Stiftelsen för Strategisk Forskning (ValueTree) to EP, and the Bolin Centre for Climate Research RA3, RA4 and RA5 "seed money" and "Engineering Mechanics for Climate Research" (to EP). We also thank Bio4Energy (a strategic research environment appointed by the Swedish government), the UPSC Berzelii Centre for Forest Biotechnology, the Department of Ecology, Environment and Plant Sciences (DEEP) and the Bolin Centre for Climate Research of Stockholm University (SU).

References

1. Pesquet E, Wagner A, Grabber JH (2019) Cell culture systems: invaluable tools to investigate lignin formation and cell wall properties. Curr Opin Biotechnol 56:215–222
2. Pesquet E, Lloyd CW (2011) Microtubules, MAPs and xylem formation. In: Liu B (ed) The plant cytoskeleton, advances in plant biology. Springer, New York
3. Derbyshire P, Ménard D, Green P et al (2015) Proteomic analysis of microtubule interacting proteins over the course of xylem tracheary element formation in Arabidopsis. Plant Cell 27:2709–2726
4. Ménard D, Blaschek L, Kriechbaum K et al (2022) Plant biomechanics and resilience to environmental changes are controlled by specific lignin chemistries in each vascular cell type and morphotype. Plant Cell 34:4877–4896
5. Pesquet E, Zhang B, Gorzsás A et al (2013) Non-cell autonomous post-mortem lignification of tracheary elements in Zinnia elegans. Plant Cell 25:1314–1328
6. Ménard D, Pesquet E (2015) Cellular interactions during tracheary elements formation and function. Curr Opin Plant Biol 23:109–115
7. Blaschek L, Murozuka E, Serk H et al (2023) Different combinations of laccase paralogs nonredundantly control the amount and composition of lignin in specific cell types and cell wall layers in Arabidopsis. Plant Cell 35(2):889–909
8. Fukuda H, Komamine A (1980) Establishment of an experimental system for the study of tracheary element differentiation from single cells isolated from the mesophyll of Zinnia elegans. Plant Physiol 65:57–60
9. Mourelatou M, Doonan JH, McCann MC (2004) Transition of G1 to early S phase may be required for zinnia mesophyll cells to transdifferentiate to tracheary elements. Planta 220: 172–176
10. Nakashima J, Takabe K, Fujita M et al (2000) Autolysis during in vitro tracheary element differentiation: formation and location of the perforation. Plant Cell Physiol 41:1267–1271
11. Milioni D, Sado PE, Stacey NJ et al (2002) Early gene expression associated with the commitment and differentiation of a plant tracheary element is revealed by cDNA-amplified fragment length polymorphism analysis. Plant Cell 14:2813–2824
12. Demura T, Tashiro G, Horiguchi G et al (2002) Visualization by comprehensive microarray analysis of gene expression programs during transdifferentiation of mesophyll cells into xylem cells. Proc Natl Acad Sci U S A 99: 15794–15799
13. Pesquet E, Ranocha P, Legay S et al (2005) Novel markers of xylogenesis in zinnia are differentially regulated by auxin and cytokinin. Plant Physiol 139:1821–1839
14. Endo S, Pesquet E, Tashiro G et al (2008) Transient transformation and RNA silencing in Zinnia tracheary element differentiating cell cultures. Plant J 53:864–875
15. Ramsden L, Northcote DH (1987) Tracheid formation in cultures of pine (Pinus sylvestris). J Cell Sci 88:467–474
16. Möller R, McDonald AG, Walter C et al (2003) Cell differentiation, secondary cell-wall formation and transformation of callus tissue of Pinus radiata D. Don Planta 217:736–747
17. Möller R, Steward D, Phillips L et al (2005) Gene silencing of cinnamyl alcohol dehydrogenase in Pinus radiata callus cultures. Plant Physiol Biochem 43:1061–1066
18. Pillai KV, McDonald AG, Wagner FG (2011) Developing a model system in vitro to understand tracheary element development in Douglas-fir (Pseudostuga mensziesii). Maderas, Cienc tecnol 13:3–18
19. Yamagishi Y, Sato T, Uchiyama H et al (2012) Tracheary elements that resemble secondary xylem in calli derived from the conifers, Torreya nucifera and Cryptomeria japonica. J Wood Sci 58:557–562
20. Wagner A, Donaldson L, Kim H et al (2009) Suppression of 4-coumarate-CoA ligase in the coniferous gymnosperm Pinus radiata. Plant Physiol 149:370–383
21. Wagner A, Tobimatsu Y, Goeminne G et al (2013) Suppression of CCR impacts metabolite profile and cell wall composition in Pinus radiata tracheary elements. Plant Mol Biol 81: 105–117
22. Wagner A, Tobimatsu Y, Phillips L et al (2015) Syringyl lignin production in conifers: proof of concept in a pine tracheary element system. Proc Natl Acad Sci USA 112:6218–6223
23. Kubo M, Udagawa M, Nishikubo N et al (2005) Transcription switches for protoxylem and metaxylem vessel formation. Genes Dev 19:1855–1860
24. Oda Y, Mimura T, Hasezawa S (2005) Regulation of secondary cell wall development by cortical microtubules during tracheary element differentiation in Arabidopsis cell suspensions. Plant Physiol 137:1027–1036
25. Yamamura M, Wada S, Sakakibara N et al (2011) Occurrence of guaiacyl/p-

hydroxyphenyl lignin in Arabidopsis thaliana T87 cells. Plant Biotech 28:1–8

26. Eberhardt TL, Bernards MA, Lanfang H et al (1993) Lignification in cell suspension cultures of Pinus taeda. J Biol Chem 268:21088–21096
27. Negi S, Tak H, Ganapathi TR (2015) In vitro xylem vessel elements formation from banana embryogenic cells and expression analysis of vessel development-related genes. Plant Biotechnol Rep 9:47–54
28. Ogita S, Nomura T, Kishimoto T et al (2012) A novel xylogenic suspension culture model for exploring lignification in Phyllostachys bamboo. Plant Method 8:40
29. Simões MS, Ferreira SS, Grandis A et al (2020) Differentiation of Tracheary elements in sugarcane suspension cells involves changes in secondary wall deposition and extensive transcriptional reprogramming. Front Plant Sci 11:617020
30. Pesquet E, Korolev AV, Calder G et al (2010) The microtubule-associated protein AtMAP70-5 regulates secondary wall patterning in Arabidopsis wood cells. Curr Biol 20: 744–749
31. Ménard D, Serk H, Decou R et al (2017) Establishment and utilization of habituated cell suspension cultures for hormone-inducible Xylogenesis. In: De Lucas M, Etchells P (eds) Methods in molecular biology, vol 1544. Springer, Cham
32. Pesquet E, Korolev AV, Calder G et al (2011) Mechanisms for shaping, orienting, positioning and patterning plant secondary cell walls. Plant Signal Behav 6:843–849
33. Escamez S, André D, Zhang B et al (2016) METACASPASE9 modulates autophagy to confine cell death to the target cells during Arabidopsis vascular xylem differentiation. Biol Open 5:122–129
34. Schneider R, Tang L, Lampugnani ER et al (2017) Two complementary mechanisms underpin Cell Wall patterning during xylem vessel development. Plant Cell 29:2433–2449
35. Kunz S, Pesquet E, Kleczkowski L (2014) Functional dissection of sugar signals affecting gene expression in Arabidopsis thaliana. PLoS One 9:e100312
36. Van de Wouwer D, Vanholme R, Decou R et al (2016) Chemical genetics uncovers novel inhibitors of lignification, including p-Iodobenzoic acid targeting CINNAMATE-4-HYDROXYLASE. Plant Physiol 172:198–220
37. Oda Y, Iida Y, Kondo Y et al (2010) Wood cell-wall structure requires local 2D-microtubule disassembly by a novel plasma membrane-anchored protein. Curr Biol 20:1197–1202
38. Goué N, Mortimer JC, Nakano Y et al (2013) Secondary cell wall characterization in a BY-2 inductive system. Plant Cell Tissue Organ Cult 115:223–232
39. Oda Y (2017) VND6-induced xylem cell differentiation in Arabidopsis cell cultures. In: De Lucas M, Etchells P (eds) Methods in molecular biology, vol 1544. Springer, Cham
40. Dubreuil C, Jin X, Barajas-López JD et al (2018) Establishment of photosynthesis through chloroplast development is controlled by two distinct regulatory phases. Plant Physiol 176:1199–1214
41. Botterweg-Paredes E, Blaakmeer A, Hong SY et al (2020) Light affects tissue patterning of the hypocotyl in the shade-avoidance response. PLoS Genet 16:e1008678
42. Zweigerdt R, Olmer R, Singh H et al (2011) Scalable expansion of human pluripotent stem cells in suspension culture. Nat Protoc 6:689–700
43. Pesquet E, Tuominen H (2011) Ethylene stimulates tracheary element differentiation in Zinnia cell cultures. New Phytol 190:138–149
44. Hogetsu T (1990) Detection of hemicelluloses specific to the cell wall of tracheary elements and phloem cells by fluorescein-conjugated lectins. Protoplasma 156:67–73
45. Meins F (1989) HABITUATION: heritable variation in the requirement of cultured plant cells for hormones. Annu Rev Genet 23:395–408
46. Kevers C, Filali M, Petit-Paly G et al (1996) Habituation of plant cells does not mean insensitivity to plant growth regulators. In Vitro Cell Dev Biol – Plant 32:204–209
47. Pischke MS, Huttlin EL, Hegeman AD et al (2006) A transcriptome-based characterization of habituation in plant tissue culture. Plant Physiol 140:1255–1278
48. Eilert U, Deluca V, Kurz WG et al (1987) Alkaloid formation by habituated and tumorous cell suspension cultures of Catharanthus roseus. Plant Cell Rep 6:271–274
49. Sogeke AK, Butcher DN (1976) The effect of inorganic nutrients on the hormonal requirements of Normal, habituated, and crown-gall tissue. J Exp Bot 27:785–793
50. Smith DL, Krikorian AD (1990) Low external pH replaces 2,4-D in maintaining and multiplying 2,4-D-initiated embryogenic cells of carrot. Physiol Plant 80:329–336
51. Tanurdzic M, Vaughn MW, Jiang H et al (2008) Epigenomic consequences of immortalized plant cell suspension culture. PLoS Biol 6: 2880–2895

52. Dalessandro G (1973) Hormonal control of Xylogenesis in pith parenchyma explants of Lactuca. Ann Bot 37:375–382
53. Phillips R, Dodds JH (1977) Rapid differentiation of tracheary elements in cultured explants of Jerusalem artichoke. Planta 135:207–212
54. Riou-Khamlichi C, Menges M, Healy JMS et al (2000) Sugar control of the plant cell cycle: differential regulation of Arabidopsis D-type cyclin gene expression. Mol Cell Biol 20: 4513–4521
55. Decou R, Serk H, Ménard D et al (2017) Analysis of lignin composition and distribution using fluorescence laser confocal microspectroscopy. In: de Lucas M, Etchells P (eds) Methods in molecular biology, vol 1544. Springer, Cham
56. Ménard D, Escamez S, Tuominen H et al (2015) Life beyond death: the formation of xylem sap conduits. In: Gunawardena A, McCabe P (eds) Plant programmed cell death, Advances in plant biology. Springer, Cham, pp 55–76
57. Buschmann H, Sambade-Zumoffen A, Pesquet E et al (2010) Microtubule dynamics in plant cells. Methods Cell Biol 97:373–400



Chapter 14

Bulk and In Situ Quantification of Coniferaldehyde Residues in Lignin

Edouard Pesquet, Leonard Blaschek, Junko Takahashi, Masanobu Yamamoto, Antoine Champagne, Nuoendagula, Elena Subbotina, Charilaos Dimotakis, Zoltan Bascik, and Shinya Kajita

Abstract

Lignin is a group of cell wall localised heterophenolic polymers varying in the chemistry of the aromatic and aliphatic parts of its units. The lignin residues common to all vascular plants have an aromatic ring with one *para* hydroxy group and one *meta* methoxy group, also called guaiacyl (G). The terminal function of the aliphatic part of these G units, however, varies from alcohols, which are generally abundant, to aldehydes, which represent a smaller proportion of lignin monomers. The proportions of aldehyde to alcohol G units in lignin are, nevertheless, precisely controlled to respond to environmental and development cues. These G aldehyde to alcohol unit proportions differ between each cell wall layer of each cell type to fine-tune the cell wall biomechanical and physico-chemical properties. To precisely determine changes in lignin composition, we, herein, describe the various methods to detect and quantify the levels and positions of G aldehyde units, also called coniferaldehyde residues, of lignin polymers in ground plant samples as well as in situ in histological cross-sections.

Key words Lignin, Xylem cell types, In situ quantitative chemical imaging, Coniferaldehyde residues, Wiesner test, Raman microspectroscopy, Pyrolysis-GC/MS, Thioacidolysis-GC/MS

1 Introduction

The polyphenolic cell wall polymer lignin is essential to the cellular function and cohesion of vascular plants by providing specific biochemical, biomechanical, and water-repelling properties, such as between the different cell wall layers of each cell type and morphotype in xylem tissues [1]. Lignin is mainly composed of C_6C_3 phenylpropanoid units that can be linked by -C–O–C- ether and -C–C- bonds in between their C_6 aromatic and/or C_3 aliphatic parts depending on their chemical structure (Fig. 1) [2, 3]. Lignin

Javier Agusti (ed.), *Xylem: Methods and Protocols*, Methods in Molecular Biology, vol. 2722,
https://doi.org/10.1007/978-1-0716-3477-6_14,
© The Author(s), under exclusive license to Springer Science+Business Media, LLC, part of Springer Nature 2024

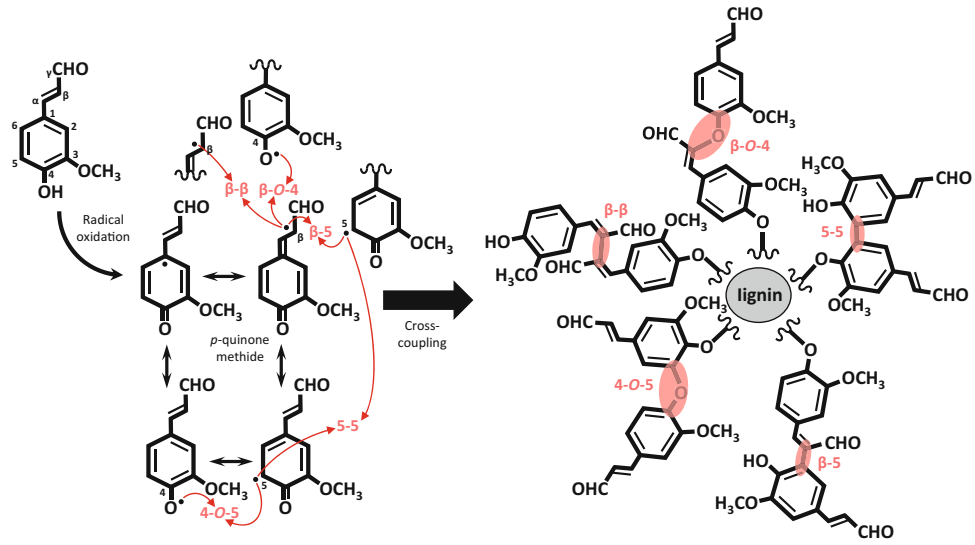


Fig. 1 Coniferaldehyde and inter-unit linkages in lignin polymers. Coniferaldehyde, presenting a C_6 aromatic part with C numbered from 1 to 6 as well as a C_3 aliphatic part with C labelled from α to γ, are oxidized by phenoloxidases and resonate into various mesomers including several *p*-quinone methides that can react with other mesomers to make different linkages between the aromatic and/or aliphatic parts of two monomers. These linkages include uncondensed β-*O*-4 and condensed β-β, β-5, 5–5 and 4-*O*-5 linkages

unit chemistry, thus, varies in their C_6 ring substitution levels with the *para* position baring a hydroxy group and each *meta* positions having either hydrogen, hydroxy, or methoxy groups, as well as in their C_3 terminal aliphatic chain presenting either an alcohol, aldehyde, carboxylic acid, or ester function (Fig. 1) [2, 3]. The accumulation of chemically distinct C_6C_3 residues is conserved between plant species for the different cell wall layers of each cell types [4]. This includes differences in lignin quantities between primary cell walls, cell corners, and secondary cell walls in xylem cells [5, 6], but also differences in chemical composition between xylem cell types with enrichment in mono-*meta* methoxylated C_6 in xylem sap conducting cells (also called guaiacyl or G) compared to enrichment in di-*meta* methoxylated C_6 in xylem fibers (also called syringyl or S) [6, 7]. Compositional specificities also affect the C_3 aliphatic end functions between cell wall layers, G residues including both the very abundant C_3 alcohols, also called coniferyl alcohol units (although the polymerized residues form dihydroconiferyl alcohols), and lower proportions of C_3 aldehyde, also called coniferaldehyde units. In contrast to coniferyl alcohol units abundance in secondary cell walls, coniferaldehyde units accumulate mostly in primary cell walls and cell corners [8] but also differently between cell types and morphotypes, with higher accumulation of coniferaldehyde units in xylem sap conducting cells compared to xylem fibers [6, 7]. These C_3 compositional differences, moreover, vary

during the maturation of each cell types, with G aldehyde units increasing gradually with the maturation of xylem sap conducting cells [1, 6, 9]. Although the majority of lignin residues have alcohol end functions, coniferaldehyde residues represent from 0.1% to 12% of lignin depending on developmental and environmental constraints and plant species [7]. Differences in C_3 end function have huge impact on lignin biochemical, biomechanical, and water-repelling properties depending on the position of the monomer within the polymer: Internal coniferaldehyde units will extend lignin oligo/polymers, whereas coniferyl alcohol units will increase the compactness of lignin [1]. Increases in coniferaldehyde units will also improve cell wall dismantling during digestion [10, 11], increase cell wall water repulsion properties [12], and modify cell wall biomechanics by increasing flexibility but lowering stiffness compared to coniferyl alcohol units [1]. The adjustment of the cell wall properties during the maturation of xylem cells, thus, depends on the precise spatio-temporal accumulation of lignin units with similar C_6 ring substitutions but specific C_3 functions, shifting from more alcohol initially to more aldehyde with aging [1]. As these chemical adjustments vary with cell wall layers, cell types, developmental and environmental conditions for each plant species, precise and reliable methods are needed to estimate these changes. The following article describes the various bulk and in situ methods enabling the precise quantification of coniferaldehyde residues at different position and/or differently linked in lignin polymers from μg to mg amounts for ground samples or at subcellular levels in whole plant biopsies.

2 Materials

2.1 Equipment and Infrastructure

1. Light microscopy:

   Any upright or inverted light microscopes can be used, we have successfully used both an Olympus BX60 upright microscope [1, 6, 11] and a Zeiss Axiovert 200 M inverted microscope [7]. Imaging systems used require a microscope equipped with (i) long-working distance 40x objectives, (ii) a color camera, and (iii) color correction. Additionally, microscope equipped with an automated stage can ease the acquisition of full cross sections. For each used objective, optimize irradiance and gamma correction to fully exploit the dynamic range of the camera. Adjust the red/green/blue correction to represent natural colors. During the experiment, keep those settings constant to facilitate unbiased comparison between samples.

2. Raman microspectroscopy:

   Any Raman microspectrometer can be used, we have successfully used both a Raman Touch-VIS-NIR (Nanophoton, Japan) [1, 11, 13] and a LabRAM HR 800 Raman spectrometer (Horiba, France) [1, 7]. Raman microspectrometry systems require (i) a Nd:YAG laser operating at 532 nm with variable power (0.5–12 mW) and (ii) long-working distance 50x objectives (NA 0.42 to 0.8). Spectrometer parameters included a diffraction grating with 600–1200 grooves mm^{-1} to resolve the spectra. Typically, several hundred scans were accumulated with 1–2 s exposure times from 100 to 2000 cm^{-1} waveband range with a spectral resolution of 1.6–2 cm^{-1}. Note that the optimal parameters (laser power, accumulation number, exposure time) were set to obtain the best quality spectra without causing thermal decomposition of the samples.

3. Gas chromatography and mass spectrometry (GC/MS):

   Any gas chromatography coupled to mass spectrometry (GC/MS) equipment can be used, we have successfully used both a Shimadzu GC-2010 Plus equipped with a HP-5 MS capillary column (30 m × 0.25 mm × 0.25 μm) and a Shimadzu GC/MS QP2020 (Shimadzu, Japan) [1, 11], as well as an Agilent GC/MS 7890A/5975C (Agilent Technologies AB, Sweden) equipped with a pyrolyzer (PY-2020iD or EGA/PY-3030D, Frontier Lab, Japan), and an autosampler (AS-1020E, Frontier Lab, Japan) [1, 6, 7, 11, 13].

2.2 Chemical Solutions

1. Sectioning mounting media

   Mounting media to enable sectioning of plant samples is made of 5–10% (w/v) low-melting point agarose in water. The solution is heated to 70–90 °C using microwave to solubilize the agarose and then kept at 60 °C ready to be added to plant samples.

2. Wiesner test or phloroglucinol/HCl solution:

   Ready-to-use Wiesner test solution is made with 0.5–2% (w/v) phloroglucinol in 1:1 (v/v) 99.5% ethanol: 37%/12.1 M HCl, although lower concentrations of HCl and other acids, such as formic acid, can be used. The solution will turn from translucid to yellow/orange with time, but this color change will not affect staining, background, nor sensitivity. Renewing the solution regularly is recommended, and long-term storage can be made if no acid is added to the ethanolic solution of phloroglucinol (*see* **Note 1**).

3. Solutions for extractive-free cell wall preparation and thioacidolysis:

   Solutions for the cell wall isolation can be prepared and stored long in advance in contrast to solutions for the thioacidolysis, which should be prepared fresh prior to usage,

specifically for the main thioacidolysis solution composed of (v/v/v) 1,4-dioxane:ethanethiol:boron trifluoride diethyl ether (87.5:10:2.5). Note that proper handling of solvents under a chemical hood is necessary for thioacidolysis.

3 Methods

3.1 Producing Synthetic Lignin with Only Coniferaldehyde Units

1. Principles behind synthetic lignin or dehydrogenation polymers (DHPs)

   Dehydrogenation polymers (DHPs) are synthetic lignin polymers made directly in test tubes by co-incubating purified phenoloxidase enzymes, such as peroxidase or laccase, which are capable of radically oxidizing phenolic compounds, with phenylpropanoids of specific chemistry, such as coniferaldehyde monomers, as well as other co-substrates necessary for each type of phenoloxidase (H_2O_2 for peroxidases or O_2 for laccases). The in vitro oxidative polymerization will then occur during the incubation time by the combinatorial cross-coupling of two resonating radical coniferaldehyde monomers (Fig. 1), and the resulting polymer property/structure is fine-tuned by the way/rate coniferaldehyde monomers are supplied to the phenoloxidase: either all at once in a process called *zulauf* [7] or gradually by dripping coniferaldehyde during the incubation time in a process called *zutropf* [13]. Additional factors such as the concentration of phenoloxidase [14], the type of phenoloxidase used [15], and the pH of the reaction buffer [15] can also alter lignin polymer characteristics. DHPs can then be used as references in bulk and in situ analyses [7, 11, 13].

2. Sequential steps to synthesize DHPs

   (a) *Preparing enzyme solution:* Solution of 0.1 mg/mL horseradish peroxidase (HRP) is prepared in 0.1 M sodium phosphate buffer at pH 6 and placed in a 50 mL clean Erlenmeyer flask with a magnetic stirring bar (Fig. 2) (*see* **Note 2**).

   (b) *Preparing substrate and co-substrate solutions:* A 10 mL solution of 12 mM of monomer (coniferaldehyde MW = 178.18 g/mol) is prepared in 3:7 (v/v) methanol:phosphate buffer (0.1 M, pH 6) (*see* **Note 3**) and a 10 mL solution of 14 mM H_2O_2 is prepared in H_2O (*see* **Note 4**).

   (c) *Polymer synthesis:* Polymers are synthetized for 24 h at 25 °C under constant stirring using a magnetic stirrer inside a temperature-controlled cabinet (Fig. 2). For *zulauf* synthesis, all solutions are mixed together and the Erlenmeyer flask is sealed with five layers of parafilm. For

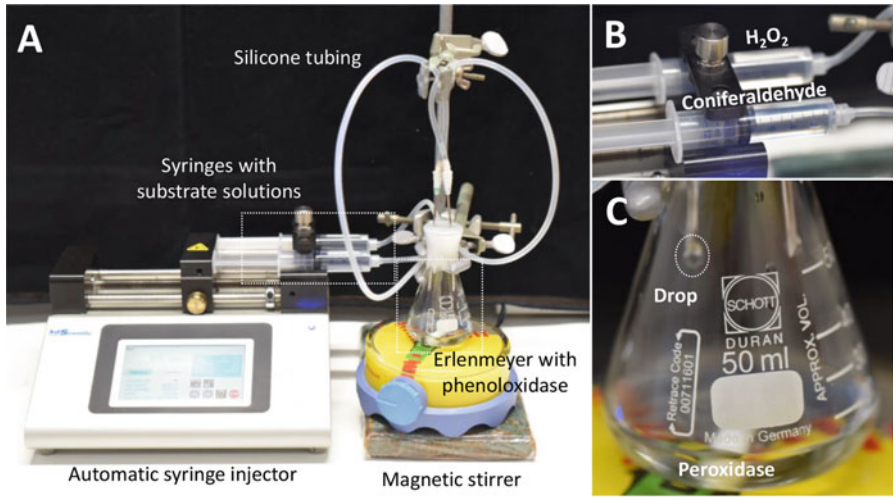


Fig. 2 Set-up for the gradual or *zutropf* synthesis of dehydrogenation polymers (DHP) or synthetic lignins. (**a**) Organisation of the set-up with an automatic syringe injector controlling the rate of drop addition to the HRP enzyme solution in an Erlenmeyer flask under agitation. Note that syringes dispense their content directly into the agitating Erlenmeyer using silicone tubing. (**b**) Close-up on the two syringes with the different substrates to enable the oxidative activity of peroxidases. (**c**) Close-up of Erlenmeyer flask with agitated peroxidase solution. Note that substrates drip as drops in the agitating solution

zutropf synthesis, monomer and H_2O_2 solutions are transferred to 10 mL syringes (Fig. 2), the Erlenmeyer flask with the enzyme solution is sealed with five layers of parafilm, and two silicon tubes (diameter 2–3 mm) are used to connect the end of syringes to a syringe needle piercing the parafilm cap (Fig. 2) (*see* **Note 5**). Dripping of solutions from syringes in the Erlenmeyer is set at the rate of 0.5 mL/h using a Legato 200 syringe pump.

(d) *Polymer purification:* The solution from the 50 mL Erlenmeyer flask is transferred to a 50 mL conical centrifugation tubes. Precipitation is enhanced by adding 150 µL of 12 M HCl and incubating the solution for 30 min at 4 °C. DHPs are then pelleted by centrifugation at 10,000 g using fixed angle rotor. The pellet is then washed with butanol, then twice with ultrapure water, and subsequently freeze-dried.

3.2 Total Coniferaldehyde Unit Quantification in Lignin Using Pyrolysis-GC/MS

1. Principles behind coniferaldehyde unit quantification using pyrolysis

   Pyrolysis enables the thermal degradation of polymers under a limited amount of oxygen, cleaving the weakest links by hemolysis (for C–C and C–O) within lignin polymers and releasing pyrolyzates, mostly phenol-alkenes like coniferaldehyde and coniferyl alcohol residues, independently of the type

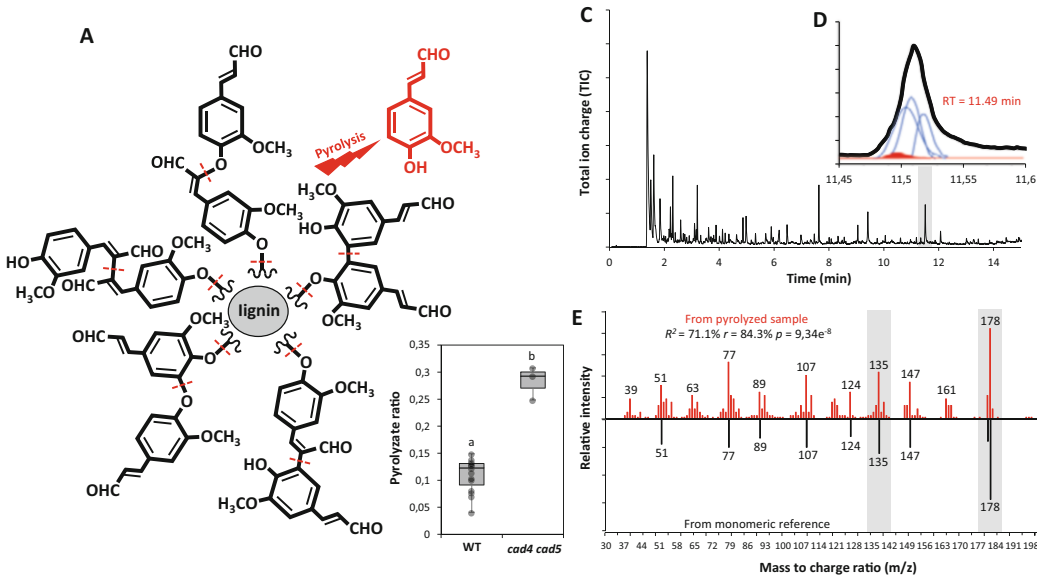


Fig. 3 Pyrolysis-GC/MS for total coniferaldehyde unit quantification in lignin polymers. (**a**) General principle of pyrolysis of lignin polymer through the hemolytic cleavage (shown by dotted red lines) of inter-monomeric linkages to release smaller phenyl-alkene pyrolyzates. (**b**) Relative proportion of coniferaldehyde to coniferyl alcohol unit pyrolyzates from stems of wild-type (WT) and *cad4 cad5* double loss-of-function *Arabidopsis thaliana* plants. Comparison included n = 5–9 independent stem samples through one-way ANOVA with a Tukey-Kramer post hoc test ($\alpha = 0.05$) where significance was presented using different letters. (**c**–**d**) Pyrogram of *Arabidopsis thaliana* WT stems – overall pyrogram is presented in (**c**) and close-up is presented in (**d**) where the different pyrolyzate contributions are deconvoluted (in red coniferaldehyde and in blue coniferyl alcohol). Note that no correction for differences in response factors are made. (**e**) Mass to charge (m/z) fragmentation profile of lignin coniferaldehyde unit pyrolyzate from *Arabidopsis thaliana* stems (in red) compared to reference chemical standards (in black), regression analysis is presented between both profiles as well as key ions shaded in grey for the identification of coniferaldehyde pyrolyzates

of linkage binding them to the polymer (Fig. 3a) [17]. The resulting pyrolyzates are separated using gas chromatography (Fig. 3c, d) and identified with mass spectroscopy – coniferaldehyde residues have specific mass to charge (m/z) signatures with diagnostic 178 and 135 ions (Fig. 3e) [18–21]. The chemical structure of lignin residues from pyrolysis depends on both primary thermal cleavage and secondary thermal reorganization reactions once cleaved when performed in the temperature range of 400–450 °C [17]. Primary pyrolytic cleavage (occurring up to 400 °C) enables the release from lignin of G residues with unsaturated alkyl groups, like coniferaldehyde residues. Additional chemical processes such as oxidation/reduction of alcohols into aldehydes will also occur at low pyrolysis temperature (around 250 °C) but not at higher temperature [17]. Secondary pyrolytic reorganisation (from 400 to 450 °C) can then alter the chemical structure of pyrolyzates by

either demethylating aromatic groups and/or shortening the length of aliphatic chains, leading to the increased release of the G benzaldehyde called vanillin. Coniferaldehyde residues released from the pyrolysis of lignin at high temperature, thus, include mostly *bona fide* coniferaldehyde units freed from primary pyrolysis of lignin but also some unspecific products derived from the oxidation of the terminal aliphatic function of coniferyl alcohols [17]. High temperatures ~450 °C and rapid pyrolysis of several seconds are, thus, recommended to limit the formation of unspecific products and enable the release of *bona fide* lignin fragments. Coniferaldehyde residues can thus be accurately measured and compared in plant samples of different genotypes, such as between *Arabidopsis thaliana* stems of wild-type (WT) and loss-of-function in *CINNAMYL ALCOHOL DEHYDROGENASEs* (*CAD*) *4* and *5*, blocking the conversion of coniferaldehyde into coniferyl alcohol monomers (Fig. 3b) [7, 11]. Pyrolysis-GC/MS, thus, represents a rapid micro-scaled method to accurately estimate changes in the proportion of total coniferaldehyde residues in lignin polymers.

2. Sequential steps to perform pyrolysis-GC/MS analyses
   (a) Frozen samples are first freeze dried, using for example a ScanVac CoolSafe Pro110-4 (LABOGENE, Denmark) freeze drier, for at least overnight, to ensure to removal of any residual water (*see* **Note 6**).
   (b) Freeze-dried samples are then ball-milled to reach diameter of fine particle below ca. 300 μm. For soft materials like *Arabidopsis* stems, samples are placed in 1.5 mL metal small jars with 1 small bead of 7 mm diameter and milled at 30 Hz for 1–2 min in a standard ball mill (such as Retsch MM400). Hard materials like poplar wood are preferably first fragmented into smaller fragment of around 500 μm, using a centrifugal mill (such as Retsch ZM200), and then placed in 10 mL metal containers with a large metal bead (13 mm diameter) and milled at 30 Hz for 1–2 min in a standard ball mill (*see* **Note 7**).
   (c) About 50–70 μg (optimally 60 μg) of milled plant sample are weighted using a microbalance and aliquoted into a pyrolysis cup. Each aliquot is then stored in a 96-well plate in a desiccator until pyrolysis.
3. Pyrolysis of samples and analysis of pyrograms

   Aliquoted ball-milled samples are delivered to a pyrolyzer equipped with an auto sampler connected to a GC/MS, as described in Subheading 2.1, item 3. After 20 sec of pyrolysis at 450 °C, pyrolysates are separated on a J&W DB-5MS

capillary column (30 m length, 0.25 mm diameter, 0.25 μm film thickness). The following oven program is used for the chromatographic separation: 40 °C, followed by a temperature increase of 32 °C/min to 100 °C, then 6 °C/min to 120 °C, then 15 °C/min to 250 °C, and, finally, 32 °C/min to 320 °C, which was kept for additional 3 min. The total run time is 19 min, and scanned spectra were recorded in the range 35–250 m/z [18]. Pyrograms are then analyzed by any analytical software, such as OpenChrom (http://www.openchrom.net/), to identify each pyrolyzate based on their m/z and retention time. R can also be used to deconvolute the contribution of each pyrolyzate in the pyrogram, enabling one to determine the contribution of each overlapping pyrolyzate peak, such as the ones between coniferaldehyde and coniferyl alcohol residues in lignin (Fig. 3d) [18]. The proportion of each pyrolyzate is then expressed as percentage of the overall pyrogram, the sum of the pyrolyzates with phenolic rings or compared to other pyrolyzates with the same phenolic ring substitution (Fig. 3b) (*see* **Note 8**).

3.3 Terminal and Internal Ether-Linked Coniferaldehyde Unit Quantification in Lignin Using Thioacidolysis-GC/MS

1. Principles behind coniferaldehyde unit quantification using thioacidolysis

   Thioacidolysis restrictively cleaves glycerol aryl ether linkages in between the C_6 *para* hydroxy group of one lignin unit and the C_3 β carbon of another, known as β-*O*-4 (Fig. 1). The detailed chemical reactions enabling the β-*O*-4 cleavage of coniferaldehyde units in lignin using thioacidolysis is presented in Fig. 4. Depending on the position of coniferaldehyde units in the lignin polymer, thioacidolysis products will lead to either thioethylated products for terminal residues with free aliphatic part (terminal residues with free aliphatic part linked only by one β-*O*-4, labeled A in Fig. 4) or indenes for internal and terminal residues with free aromatic part (internal residues interlinked by two β-*O*-4 and terminal residues with free aromatic part linked by one β-*O*-4, labeled B in Fig. 4) (*see* **Note 9**). Both trithioketals and indene dithioketals have distinct retention times (Fig. 5a, b) and specific mass spectrum, enabling their clear identification (Fig. 5e, g). Representative yields in *Arabidopsis* and poplar always show detectable amounts of terminal thioethylated products (representing between 1% and 2% of the total chromatogram area) in all genotypes tested [7], but indenes are less abundant and mostly accumulated in knock-out or knock-down plants in *CINNAMYL ALCOHOL DEHYDROGENASEs* (*CADs*) [11]. Internal coniferaldehyde thioacidolised products, moreover, result in two regioisomers with the int.1 form 8–10 fold more abundant than int.2 form in both poplar and *Arabidopsis* (Fig. 5c) [22]. Comparison between stems of *Arabidopsis* wild-type

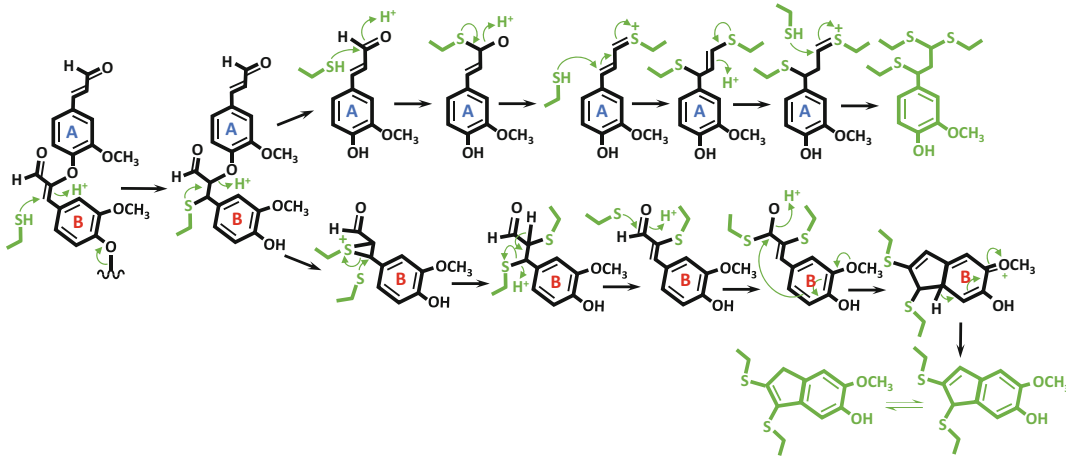


Fig. 4 Schematic representation of the chemical reactions behind the thioacidolysis of β-*O*-4 linked coniferaldehyde residues depending on their position in lignin polymers. Two coniferaldehyde units are presented linked by β-*O*-4 with one in terminal position with a free aliphatic chain (labelled A) and another internal or terminal with a free aromatic ring (labelled B). Sequential reactions occurring during thioacidolysis produce distinct thioethylated products depending on the position of coniferaldehyde monomers in the lignin polymers – one thioethylated product for terminal residues with free aliphatic chain and two regioisomeric indenes for internal or terminal residues with free aromatic ring. *See* references [22, 27, 28]

(WT) and loss-of-function in *CAD4* and *5*, named *cad4 cad5* [1, 11], illustrates differences in both coniferaldehyde residue content and changes of coniferaldehyde unit position in lignin polymers between genotypes (Fig. 5d). Thioacidolysis-GC/MS represents a highly reliable milli-scaled method to accurately estimate the proportion and position of β-*O*-4-linked coniferaldehyde units in lignin polymers.

2. Preparation of extractive-free cell wall material

   Extract-free cell wall materials are isolated from plant samples ground in liquid nitrogen using ceramic mortar and pestle and then transferred using spatula to fill half of 2 mL sterile microtubes. Samples are then sequentially treated with 1 mL of solutions, vortex mixed for 15–20 sec, and cell wall isolates pelleted with centrifugation (10,000 g, 10 min) to discard the supernatant removing (i) first proteins with three washes of 140 mM Tris-base, 105 mM Tris-acetate, 0.5 mM ethylenediamine tetraacetic acid, and 8% w/v lithium dodecyl sulfate; (ii) then two washes of water; (iii) two washes of 100% methanol; (iv) one wash of chloroform:methanol (1:1); and, finally, (v) one wash of acetone. Pellets are then air-dried overnight.

3. Sequential steps to perform thioacidolysis

   (a) Dried isolated extractive-free cell walls are weighted and 5–10 mg are transferred to a 1 mL vial. Internal standard

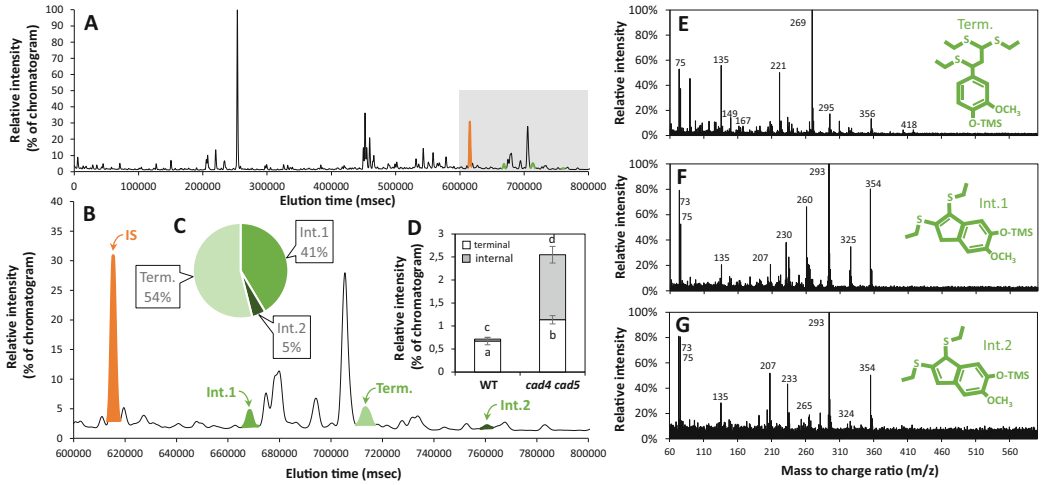


Fig. 5 Thioacidolysis of β-*O*-4 linked coniferaldehyde residues in lignin polymers. (**a**–**b**) Gas chromatogram of the thioacidolyis products of lignin including internal standard (IS in orange - tetracosane) and coniferaldehyde thioacidolysed products (in green) – overall chromotagram is presented in (**a**) and close-up is presented in (**b**) where each thioacidolysis product is clearly separated. (**c**) Relative proportion of the summed chromatogram area comprised by the different thioacidolysis products of coniferaldehyde. Note that similar response factors have been assumed between these thioacidolysed products. (**d**) Relative proportion of the different coniferaldehydes in stem thioacidolysed products for terminal and internal monomers in wild-type (WT) and *cad4 cad5* double loss-of-function *Arabidopsis thaliana* plants. Comparison included n = 3–4 independent stem samples through one-way ANOVA with a Tukey-Kramer post hoc test ($\alpha = 0.05$) where significance was presented using different letters. (**e**–**g**) Mass to charge (m/z) fragmentation profiles of the different thioacidolysed products of coniferaldehyde depending on their position in lignin with terminal (Term.) producing thioethylated product (**e**) and internal (Int.) producing two types of indene regioisomers (**f-g**)

tetracosane (100 µg, 10 µL of 10 mg/mL) is then added to each sample, and the vials are dried overnight with a vacuum pump.

(b) Total 800 µL of (v/v/v) 1,4-dioxane: ethanethiol: boron trifluoride diethyl ether complex (87.5:10:2.5) are added to each vial, which are then closed and tightened using screw-on caps and sealed with Teflon tape.

(c) Vials are mixed using strong vortexing for 10–20 sec, wrapped in aluminum foil and heated at 100 °C for 4 h in a sand bath (*see* **Note 10**).

(d) Vials are removed from the sand bath and cooled on ice for several minutes.

(e) Total 200 µL of the sample solution are then transferred to a 1.5 mL microtube, supplemented with 100 µL of 1 M sodium bicarbonate in water, mixed by vortexing, and then centrifuged for 2–5 sec using a benchtop minicentrifuge.

(f) Total 130 μL of 1 M hydrochloric acid are then added to adjust the pH of the solution to 3–4 (checked using pH-test paper).

(g) About 250 μL of diethyl ether are added, and the solution is mixed by vortexing and then centrifuged for 10–30 sec using a benchtop minicentrifuge to separate aqueous and organic phases. The upper organic phase is then transferred to a new microtube. This step is repeated three times to ensure that all of the thioacidolysed products are recovered.

(h) About 100 μL of saturated saline solution is added to the organic phase, mixed by vortexing and centrifuged. The upper phase is then transferred to a new 1.5 mL microtube containing 100–150 mg sodium sulfate. The new solution is then mixed by vortexing and centrifuged briefly using a benchtop minicentrifuge.

(i) Samples are then transferred to a 1 mL vial, air dried with a nitrogen stream, then closed and tighten using screw-on caps and stored at −20 °C until analysis (*see* **Note 11**).

4. Chromatographic analyses of thioacidolysis

About 250 μL of diethyl ether are added to each vial, vortexed and left to stand on the bench for at least 5 min. Then 10 μL of the supernatant is transferred to an insert in a GC vial and supplemented with 50 μL of N,O- Bis (trimethylsilyl)trifluoroacetamide and 50 μL of anhydrous pyridine, then heated at 60 °C for 1 h. Finally, 100 μL of dichloromethane is added and mixed thoroughly, and the vial is closed and placed in the GC autosampler for analysis. The remaining part of the samples are dried again and stored at −20 °C. Chromatographic analysis is performed on a standard GC/MS, as described in Subheading 2.1, **step 3**, with an injector at 250 °C. The column temperature program used include 60 °C (2 min), from 60 to 260 °C (15 °C min^{-1}), 260 °C (18 min), from 260 to 300 °C (5 °C min^{-1}), and 300 °C (10 min). Mobile phase used helium at a rate of 1.46 mL/min. Chromatograms are finally analyzed by any analytical software, such as OpenChrom (http://www.openchrom.net/), to identify each trimethylsilyl (TMS) thioacidolysed product based on their retention time and m/z profile, and to quantify their contribution to the total chromatogram peak area normalized by the internal standard tetracosane (Fig. 5).

3.4 Total Coniferaldehyde Unit Quantification in Lignin In Situ Using the Wiesner Test

1. Principles behind coniferaldehyde unit quantification using Wiesner test

Probably the oldest and most used histochemical test in plant sciences, the Wiesner test enables the quantitative chemical imaging of total coniferaldehyde units in lignin with

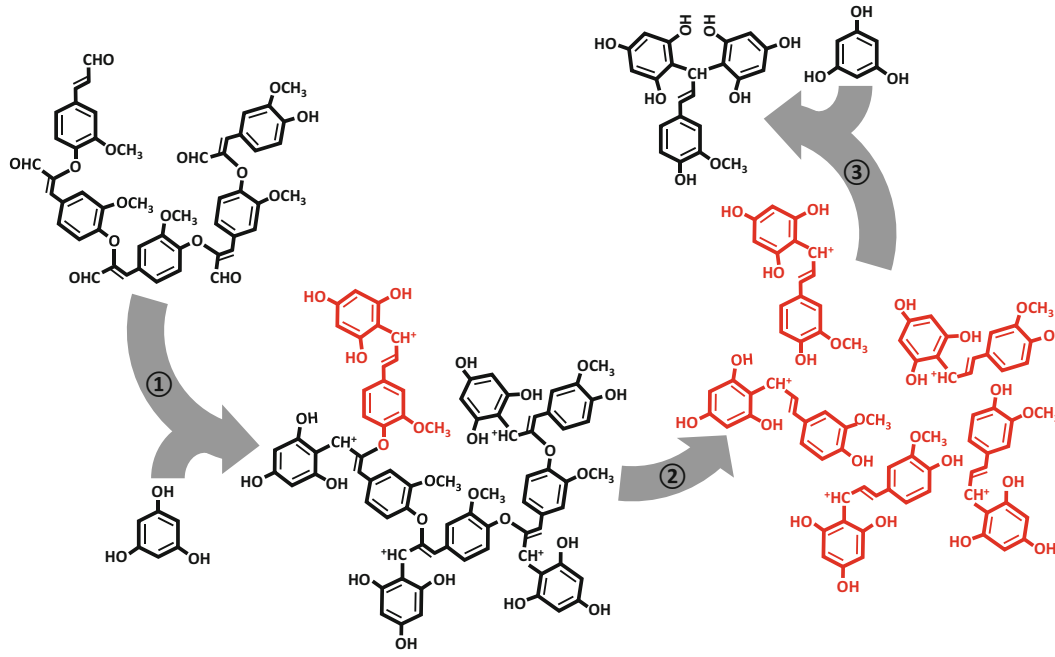


Fig. 6 Schematic representation of the sequential chemical reactions behind the Wiesner test for coniferaldehyde unit quantification in lignin. The Wiesner test sequentially reacts with the coniferaldehyde units of lignin independently of their position in the polymer by (1) forming mono-phloroglucinol conjugate carbocations in acidic conditions where only terminal residue exhibit chromogenic activity, followed by (2) the gradual fragmentation through ethanoacidolysis of lignin polymers into smaller fragments that proportionally free more terminal mono-phloroglucinol conjugates with chromogenic activity, and finally leading (3) to a second conjugation with another phloroglucinol in acidic conditions to form di-phloroglucinol conjugates that are not chromogenic

subcellular resolution levels [7, 11]. The Wiesner test staining chemical reactions occur sequentially with (i) acid-dependent conjugation of coniferaldehydes with phloroglucinol into monophloroglucinol-coniferaldehyde carbocations, which are chromogenic in low pH; (ii) ethanoacidolysis of lignin polymers into shorter oligo/monomers, enabling internal conjugates to become terminal; and (iii) a second acid-dependent conjugation with phloroglucinol, forming diphloroglucinol-coniferaldehyde conjugates that are not chromogenic (Fig. 6). The monophloroglucinol-coniferaldehyde carbocations resonate in acid conditions to produce a chromogene absorbing at λ of 547 nm with a red to purple hue (Fig. 7a–c). The staining reaches its peak after 5–15 min when it releases all the terminal monophloroglucinol-coniferaldehyde conjugates during the ethanoacidolysis (Fig. 7d, e) and faints afterward as diphloroglucinol-coniferaldehyde conjugates form [7, 22, 23]. The intensity and sensitivity of the Wiesner test chromogenic reaction depends both on the local levels of

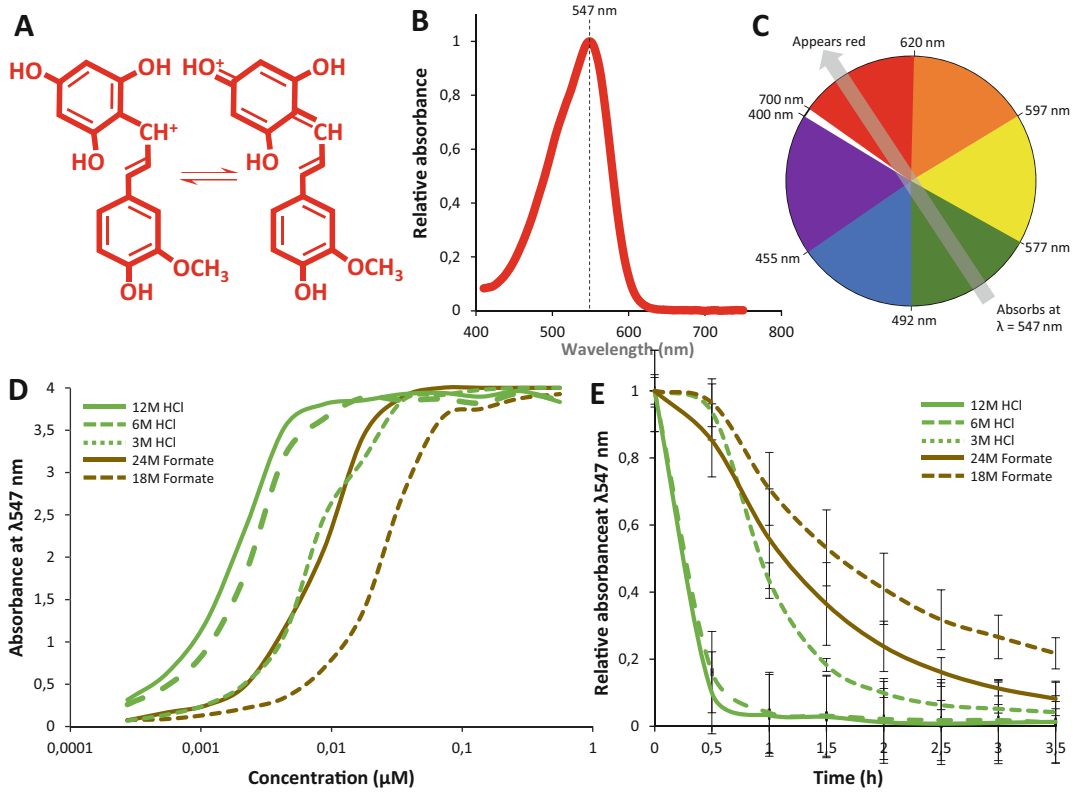


Fig. 7 Identity, absorbance and stability of the Wiesner test chromophore. (**a**) Mesomeric resonance forms of the chromogenic mono-phloroglucinol conjugate carbocations of the Wiesner test. (**b**) UV-Vis absorbance spectra of the Wiesner test mono-phloroglucinol conjugate carbocations in acidic conditions with a single maximum absorbance peaking at 547 nm. (**c**) Color wheel representation of the chromophore color based on its absorbance maximum. (**d**) Effect of the 1 volume acid concentration added to the 2% phloroglucinol ethanol solution for the formation of mono-phloroglucinol conjugate carbocations and its quantitative relationship with coniferaldehyde concentration. Note that 1 volume of 24 M formic acid resulted in similar detection sensitivity than 1 volume of 3 M HCl. (**e**) Effect of the 1 volume acid concentration added on the lifetime of mono-phloroglucinol conjugate carbocations. Note that strong acid condition with 12 or 6 M HCl cause rapid conversion into di-phloroglucinol conjugates

coniferaldehyde units in lignin and on the pH of the solution (Fig. 7d, e). Although the Wiesner test is also often called phloroglucinol/HCl, other acids, such as formic acid, can be used to reach similar intensity and sensitivity (Fig. 7d, e). The Wiesner test, thus, represents a rapid and highly reliable method to accurately estimate the total coniferaldehyde unit content in lignin polymers with subcellular resolutions in plant histological samples.

2. Mounting samples and imaging

   (a) *Sample preparation and sectioning:* Cellular content, interfering pigments and extractives are removed by incubating plant samples in 70% ethanol for several days before

staining [6, 7]. Samples are then embedded in warm 5–10% agarose, described in Subheading 2.2, **step 1**, using the cap of 1.5 or 2 mL microtubes as a cast support. Samples are first oriented vertically in the warm agarose and then left on the bench to settle for 10–15 min. Solidified agarose plugs with embedded samples are then removed from their cast support with tweezers, glued using ethylcyanoacrylate (ECA) glue onto the sample holder of a vibratome (such as a Leica VT1000S), and the glue is left to set for 10–15 min. The sample holder is then mounted in the vibratome and the sectioning tray filled with distilled water to cover the agarose plug. Sectioning parameters to make 50 μm histological cross sections are performed at a speed of 0.20 mm/s (4 on the speed dial), 70 Hz frequency (7 on the frequency dial), with half of a razor blade tilted at ~5° from the horizontal (using angle level in blade mounting bracket). These parameters should be adjusted by the user to the properties of each plant sample depending on its hardness and size.

(b) *Sample imaging:* 50 μm thick cross sections from cleared plant samples are imaged between 1 mm thick glass slide and 150 μm thick coverslip before staining in water only and after staining just a few minutes after adding 40–50 μL of Wiesner test solution (Fig. 8). Acid concentration can be lowered or replaced by weaker acids, but this will both lower the detection sensitivity and increase the chromogene lifetime (Fig. 7d, e). The removal of the coverslip after imaging the unstained sample can lead to damages, leaving a nonoverlapping portion of the coverslip over the microscopy slide to grab with tweezers will ease the removal of the coverslip and reduce damages. Imaging is performed using standard brightfield microscopes, as described in Subheading 2.2, **step 2** [6, 7].

(c) *Image processing prior to analysis:* All image handlings are made using open-source image analysis software Fiji/ImageJ [24–26].

  (i) *Image correction for uneven illumination:* If necessary, uneven background illumination during image acquisition is corrected by first taking an image of an empty area of the glass slide and cover slip with identical illumination and acquisition parameters. This image is then subtracted from a plain white image using the Fiji image calculator (in "Process/Image Calculator…" tab, and selecting images and using the operation "subtract"). The result of this subtraction can then, again using the image calculator, be added to the images of samples, resulting in an evenly white background between images.

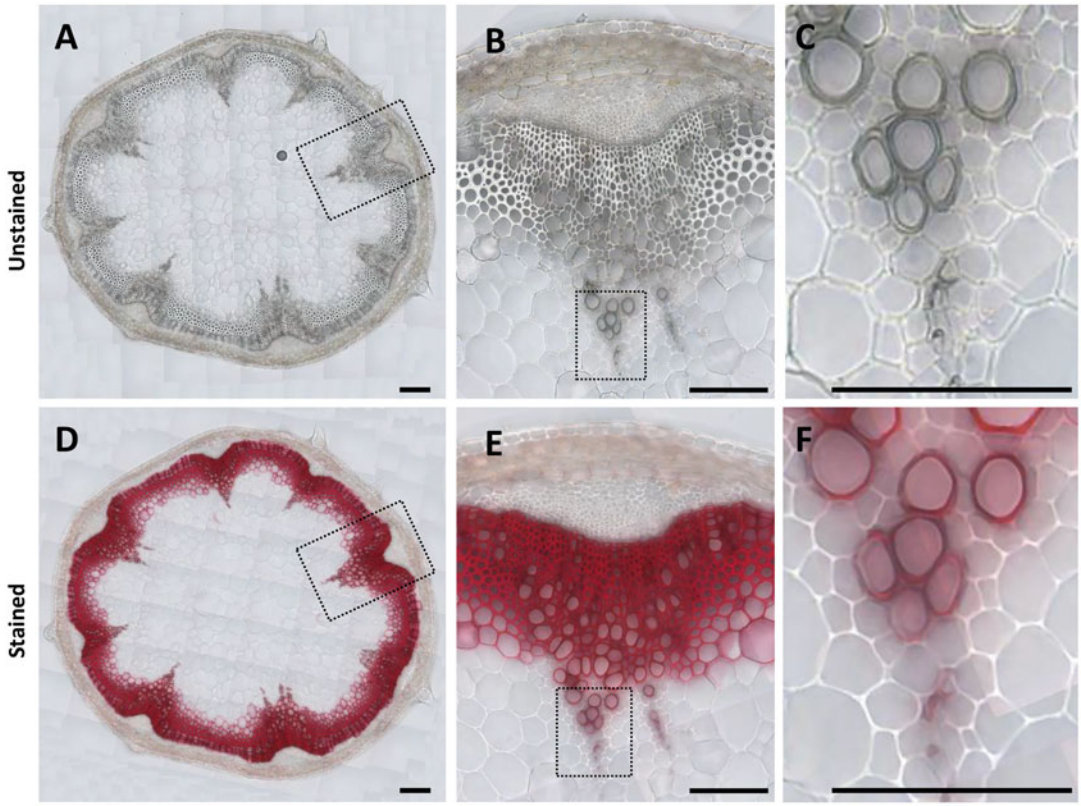


Fig. 8 Wiesner test staining of coniferaldehyde in whole plant cross-sections assembled using image stitching with 10% overlaps. (**a**–**c**) Unstained stem cross-sections of *Arabidopsis thaliana* WT prior to the Wiesner test staining observed as a whole (**a**), close-up of vascular bundle (**b**) and meta- and proto-xylem vessels (**c**), bars = 75 μm. (**d**-**f**) Stained stem cross-sections of *Arabidopsis thaliana* WT after 3 min of Wiesner test staining observed as a whole (**d**), close-up of vascular bundle (**e**) and meta- and proto-xylem vessels (**f**), bars = 75 μm

(ii) *Stitching images together to form full sections:* Overlapping images of a larger sample (background corrected if necessary) can be stitched together into a larger image (Fig. 8) using the "Grid/Collection stitching" plugin [24]. Images need to be acquired with at least a 10% overlap between each other to enable proper stitching. Increasing the overlap can, moreover, improve the probability of successful stitching.

(iii) *Assembling and aligning RGB image stack:* Images (single images or stitched mosaics) of the same sample before and after staining are then assembled into a stack of images using the "Image/Stack" tab and selecting "Images to stack." Make sure that the unstained and stained images have the same

dimensions in pixels; otherwise, use the "Image/Scale" tab to adjust image size. Finally, the stacked images are aligned to each other using image registration, such as the "Linear Stack Alignment with SIFT" plugin. If the alignment is not satisfactory, possibilities for troubleshooting are using the "bUnwarpJ alignment" plugin or cutting the images to a smaller sizes before aligning.

(d) *Processed image analysis:* Wiesner test signal measurements include determining (i) the hue of unstained and/or stained region-of-interest (ROI) by converting the RGB image stack into the hue/saturation/brightness (HSB) color space and (ii) the optical density or absorbance of unstained and/or stained ROIs by converting the RGB image stack into 8-bit image stack. To ease the understanding of the image processing steps, both color and intensity scales have been added to Figs. 9 and 10 below each image and submitted to the same image conversion steps to show how each image is affected and how reproducible measurements are obtained. The measured areas are either defined by ROIs using "Oval" or the "Line" selection tools of ImageJ that are drawn at specific positions in the aligned image stack, and then measured using "Analyze/measure" for "Oval" ROIs to obtain average, median, area, minimal and maximum values (defined using "Analyze/Set Measurements...") or using "Analyze/Plot profile" for "Line" ROIs to obtain y values along the x distance (data is obtained using "Data >> Copy all data").

(i) *Measuring hue:* Hue measurements are obtained by transforming the aligned images stacks from the RGB into the HSB color space. This conversion is made using the "Image/Adjust" tab and selecting "HSB," which will convert each single RGB image into an image stack of three distinct images for hue, saturation, and brightness (Fig. 9). Note that hue, saturation, and brightness images will still be in an 8-bit scale. The hue values are obtained using the hue image of the HSB stack. The average hue values on 8-bit scale (ranging from 0 to 255), measured by the ROIs, are then divided by 255 and multiplied by 360 to have the hue degree values of the hue scale (ranging from 0° to 360°). Changes in hue due to Wiesner staining for specific cell types or cell wall layer can, thus, be reliably measured and statistically tested (Fig. 9). Measure single pixels, not ROIs, to avoid the averaging of pixels with 8-bit values close to 0 or

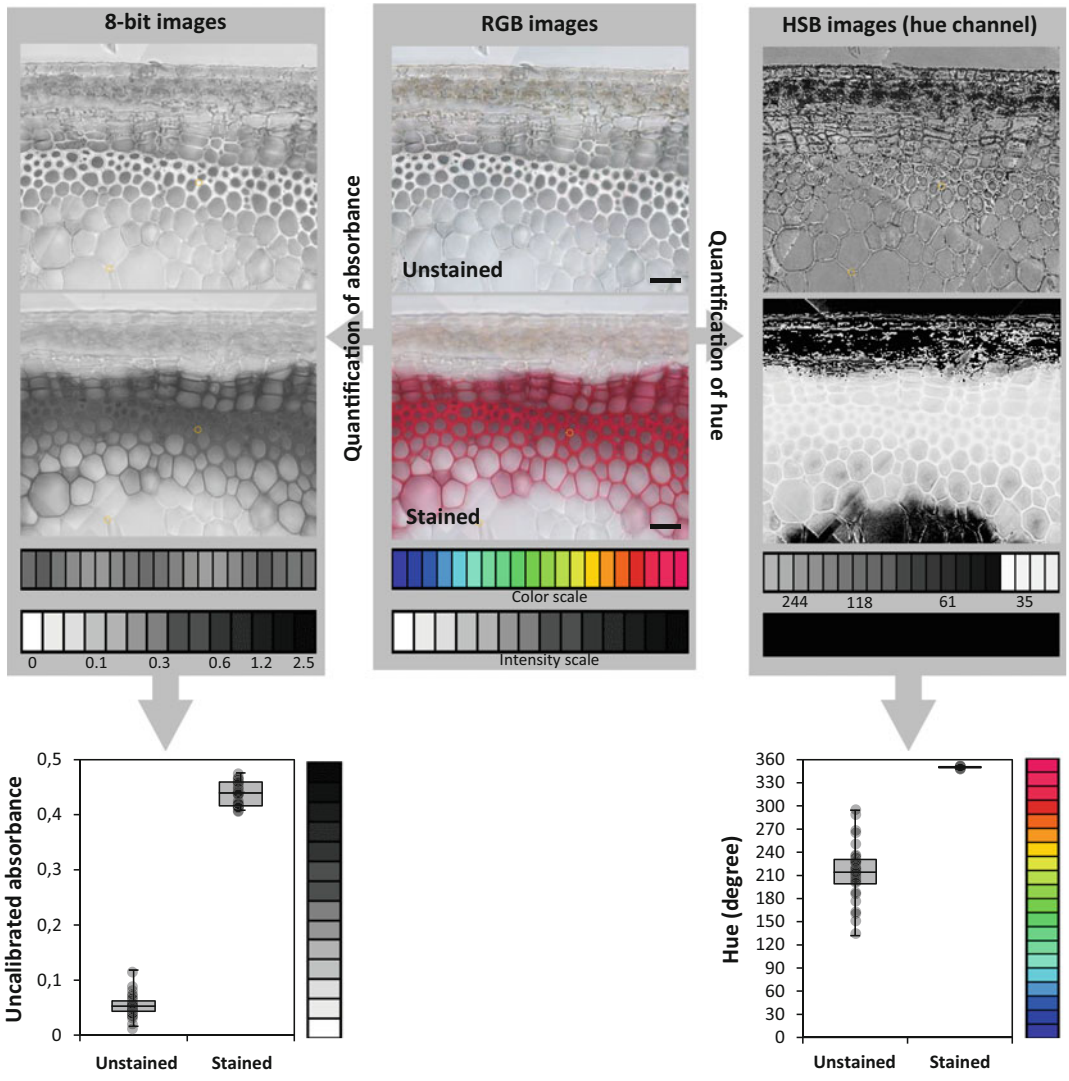


Fig. 9 Determination of Wiesner test absorbance and hue using oval region-of-interests (ROIs). Different image processings lead to different parameters that can be quantified. Two scales, one color scale and another grey-scale intensity, are also presented below each images to show the impact of each image conversion step. For absorbance measurements, images from the initial RGB images (color images in the center of the figure, bars $= 50\mu m$) before and after staining are converted in 8-bit scale (left hand side that only affects the intensity and neglects the color) and converted in "uncalibrated absorbance" to show difference in absorbance for the same position of oval ROIs (red dotted circles) between unstained and stained cell walls of interfascicular fibers of *Arabidopsis thaliana* stems. For hue measurements, images from the initial RGB images before and after staining are converted in HSB (left hand side that only affects the color as hue and neglects the intensity) and converted to a hue degree scale to show color differences for the same position of oval ROIs between unstained and stained cell walls of interfascicular fibers of *Arabidopsis thaliana*

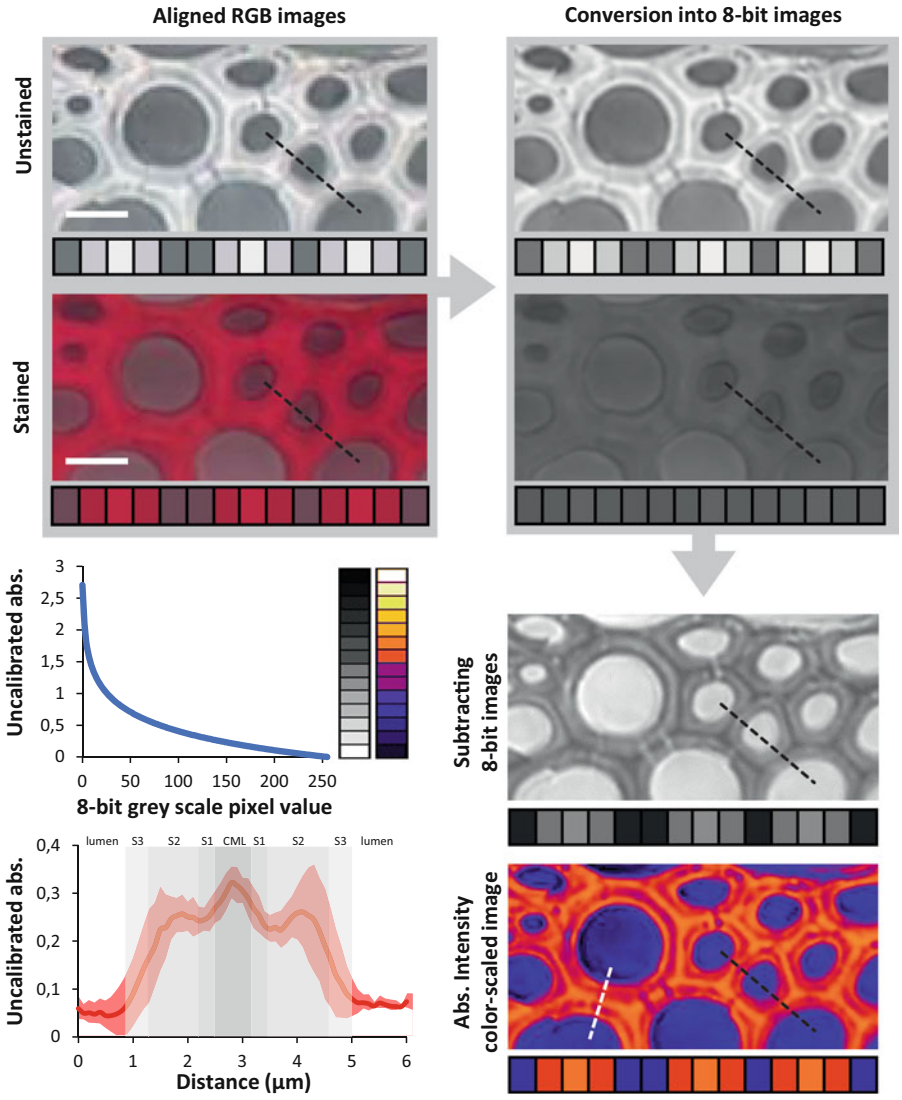


Fig. 10 Image processing and determination of Wiesner test absorbance using line profiles across cell walls to monitor changes between layers. The sequential image processing steps are presented using boxed arrows from the initial RGB images (bars = 8 µm) before and after staining (as well as their schematic representation in boxes showing changes along the segmented black lines), which are then converted into 8-bit scale, then subtracted using "Image Calculator" and converted into artificial intensity color using the "Fire" on "Image/ Look-up tables". Absorbance are obtained by converting the 8-bit subtracted image in "uncalibrated absorbance" (and the exponential relationship between 8-bit and absorbance is presented) and then using line profiles (such as the segmented white line) to determine the change in absorbance across cell wall layers between two neighboring interfascicular fibers of *Arabidopsis thaliana d*

255. As both 0 and 255 are shades of red on the circular hue scale (around 360°), their average on the linear 8-bit scale results in shades of green hue (around 127.5 or 180°).

(ii) *Measuring absorbance:* Unlike in fluorescence images, the intensity in bright field microscopy RGB images is not linearly but exponentially proportional to the pixel value (Fig. 10). To transform pixel values into an approximation of absorbance (still referred to optical density or OD, although nowadays the use of this term is discouraged), the "calibration" function of ImageJ/Fiji is used. The RGB aligned image stack is converted into 8-bit image stack using the "Image/Adjust" tab and selecting "8-bit." Subtracting the aligned unstained image from its corresponding stained image using the "Process/Image Calculator…" tab will enable to obtain the Wiesner test absorbance independently of the background (Fig. 10) (*see* **Note 12**). The 8-bit grey scale values are then converted into absorbance by using the "Analyze/Calibrate..." tab and selecting "Uncalibrated OD." The image will not change visually, but any pixel value measured will change from grey scale intensity to absorbance, which have an exponential relationship (Fig. 10). The absorbance of unstained and stained areas can then be measured using oval ROIs for fixed cell type position (Fig. 9) or between the different cell wall layers of neighboring cells using line ROIs (Fig. 10) (*see* **Note 13**). Changes in absorbance due to Wiesner staining for specific cell types or cell wall layers can, thus, be reliably measured and statistically tested (Figs. 9 and 10).

3.5 Terminal Coniferaldehyde Unit Quantification in Lignin In Situ Using Raman Spectroscopy

1. Principles behind coniferaldehyde unit quantification using Raman spectroscopy

Raman microspectroscopy is a microscopy-based method using Raman scattering or the inelastic scattering of photons from a monochromatic laser at 766 or 1064 nm by the molecular vibrations, varying with linkages and elemental composition of each molecules, and leading to scattered photon with energy shifted up or down, also called a Raman waveband shift (Fig. 11a). The relative scattering intensity of each Raman band shift depends on the chemistry of the compound, the solvent, the spatial orientation of the molecule, and its conformational degree of freedom (Fig. 11c) [11, 13]. Raman microspectroscopy thus enables to discriminate between the chemistry as well as the position of specific monomers in lignin compared to

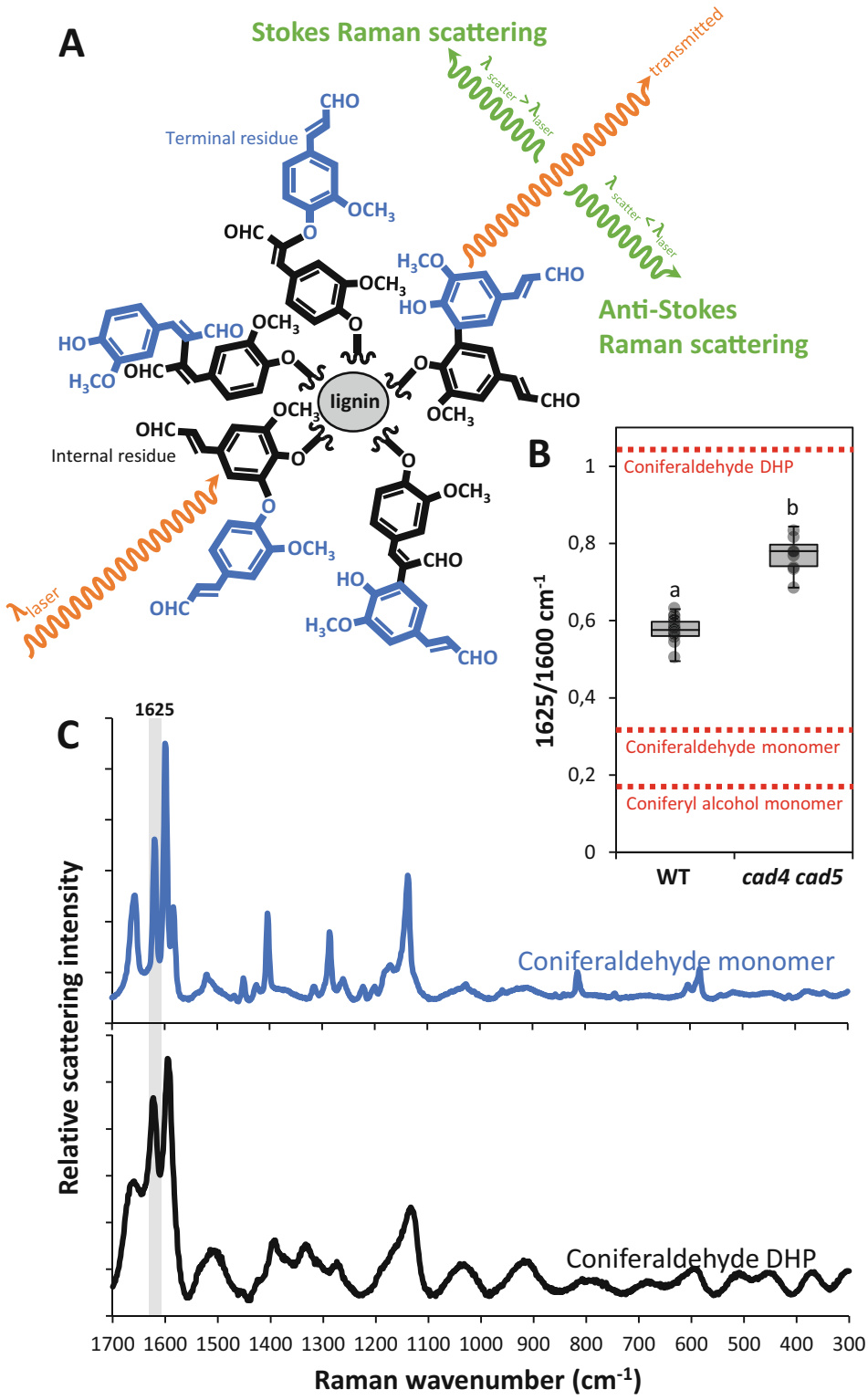


Fig. 11 Determination of coniferaldehyde unit content in cross-section using Raman microspectroscopy. (**a**) Schematic principle of Raman scattering in lignin polymers where coniferaldehyde units have both different position (blue terminal and black internal) and inter-monomeric linkage types. The Raman effect is

other cell wall components made of polysaccharides [1, 6, 13]. The semi-quantitative capacity of Raman spectroscopy for lignin levels and part of its chemistry are now well-established [1, 6, 7, 11, 13], and coniferaldehyde units with free aliphatic chain in terminal positions in lignin polymers can be easily measured using the 1625 cm^{-1} Raman waveband [1, 6, 11, 13]. Comparison between xylem sap conducting cells of *Arabidopsis* wild-type (WT) and loss-of-function in *CAD4* and *5* illustrates differences in terminal coniferaldehyde unit content in lignin polymers in situ compared to synthetic polymers made only of coniferaldehyde units and isolated coniferaldehyde and coniferyl alcohol monomers (Fig. 11a). Raman microspectroscopy, thus, represents a rapid and highly reliable method to accurately estimate the terminal coniferaldehyde unit content in lignin polymers at subcellular resolutions in plant histological samples. Samples can be then processed using the Wiesner test to estimate total coniferaldehyde residue content in lignin to determine relative terminal to total coniferaldehyde unit content with subcellular resolutions [1, 6, 11].

2. Mounting samples and imaging
   (a) *Calibration of spectrometer to silicon standard:* Ensure that the Raman microspectrometer is calibrated with crystalline silicon standard (main waveband at 520 cm^{-1}) prior to acquisition of plant samples.
   (b) *Sample imaging:* 50 μm thick cross sections from cleared plant samples are prepared, as described in Subheading 3.4, **step 2a**, and imaged in water between 1 mm thick glass slide and 150 μm thick coverslip. Imaging at high laser intensity will cause the mounting water to evaporate quickly therefore requiring to top up samples with water between acquisitions.
3. Spectral processing (baseline correction and normalization)
   The acquired Raman spectra are first baseline corrected using an asymmetric least squares algorithm available in the

Fig. 11 (continued) schematized by the photons of a monochromatic laser (wavy orange lines of specific wavelength λ_{laser}) being scattered to higher or lower wavelengths (wavy green lines of λ different than λ_{laser}). (**b**) Relative ration of 1625 cm^{-1} (for coniferaldehyde) to 1603 cm^{-1} (for G type lignin) in lignin in situ of sap conducting cells from stem cross-sections of wild-type (WT) and *cad4 cad5* double loss-of-function *Arabidopsis thaliana* plants. Comparison included $n = 7–12$ independent cells from multiple plants through one-way ANOVA with a Tukey-Kramer post hoc test ($\alpha = 0.05$) where significance was presented using different letters. Note that dotted red lines are added to show 1625 cm^{-1} to 1603 cm^{-1} ratios of DHPs made only of coniferaldehyde as well as coniferaldehyde and coniferyl alcohol monomers. (**c**) Raman scattering spectra of coniferaldehyde as monomer (in blue) or incorporated in homopolymers as DHPs (in black) with the common characteristic 1625 cm^{-1} Raman waveband

"baseline" R package with the following parameters: smoothness $\lambda = 100{,}000$ and asymmetry $p = 0.01$. Differences can be readily observed in the Raman scattering spectra between isolated monomers and their polymerized forms, thus confirming that the position and interlinkage type both affect the Raman scattering of coniferaldehyde units (Fig. 11c). The baseline corrected spectra can then be normalized and analyzed differently:

Normalisation to the area under the curve (AUC): This normalization determines the proportion that each Raman band represents in the overall Raman scattering spectrum of the sample and, thus, postulates that the Raman scattering spectra is proportional to its cell wall polymer content/composition [13]. The AUC of the entire Raman scattering spectra is, thus, first determined between 300–1700 cm^{-1} after baseline correction and the coniferaldehyde unit proportion is determined by dividing the 1625 cm^{-1} band intensities by the AUC.

Ratios to either lignin ~1600 cm^{-1} or cellulose ~380 cm^{-1} wavebands: This normalization determines the ratio of each Raman band relatively to a reference Raman waveband in the sample and, thus, determines ratios of Raman scattering bands that are proportionally dependent on cell wall polymer content/composition [6, 13]. The intensities of the 1625 cm^{-1} band in spectra are, thus, divided by a reference band in the same spectrum either the lignin 1603 cm^{-1} band (Fig. 11b) [13] or by the cellulose 378 cm^{-1} [6].

4 Notes

1. The Wiesner test solution only works when using an acidified ethanolic solution of phloroglucinol or 1,3,5-benzenetriol and will not work if using pyrogallol or 1,2,3-benzenetriol. Note that protecting the solution from light with aluminum foil will decrease the yellowing of the solution with time.
2. Enzyme used for making DHP is not limited to peroxidase and, other phenoloxidase such as laccase can be used [15].
3. Other organic solvents can be used for the solubilisation of phenylpropanoid monomer, such as acetone:phosphate buffer [16].
4. When using laccase enzymes, either air bubbling should be used to increase oxygenation instead of dripping a solution H_2O_2 or adding catalase to the enzyme solution to release O_2 from the breaking down of H_2O_2.

5. Plumbing or Teflon sealing tape can be used to ensure that the fit between syringe needle and silicon tubing is tight (Fig. 2).
6. The freeze-drying is essential for the GC column as any residual water molecules in the sample will damage the lifetime of GC columns.
7. The uses of more beads increases friction and will burn the sample, causing both loss of materials and contaminating artefacts.
8. No readjustment for difference in the relative response factor are generally performed, although they differ quite significantly between pyrolyzates [21].
9. Distinction in thioacidolysis between internal and terminal residues with free aromatic part can be performed by permethylating lignin prior to thioacidolysis (Fig. 4). This permethylation step will change the *para* hydroxy group of terminal residues with free aromatic part into methoxy group, which can then be distinguished from internal indenes.
10. 100 °C is not the set temperature of the sand bath but the actual temperature in the sand near the sample, measured using a thermometer.
11. Put containers used for thioacidolysis in sodium hypochlorite aqueous solution for several days, and wash when there is no smell.
12. Note that calibration to "Uncalibrated OD" will inverse the scale, thus requiring the "Image/Lookup tables/invert LUT".
13. Press on "Alt" key to ensure that the line ROI does not change size when moved at different location in the image so that average profile can be measured for the same length ROIs (Fig. 10).

Acknowledgments

We thank Prof. Yasuyuki Matsushita (TUAT, Japan), Prof. Catherine Lapierre (INRA Versailles, France) and Prof. John Ralph (Univ. Wisconsin-Madison, USA) for comments and help on the chemical processes associated with thioacidolysis and its quantification. We thank Kevin Rein for help with the acid dependency of the Wiesner test. This work was supported by Vetenskapsrådet VR (grant 2010-4620 and 2016-04727), the BioImprove FORMAS (to EP), the Kempe Foundation (Gunnar Öquist Fellowship to EP), the Stiftelsen för Strategisk Forskning (ValueTree to EP), the Bolin Centre for Climate Research RA3, RA4 and RA5 "seed money" and "Engineering Mechanics for Climate Research" (to EP), and the Carl Trygger Foundation CTS 16:362/17:16/18:306/21:1201

(to EP). We also thank Bio4Energy (a strategic research environment appointed by the Swedish government), the UPSC Berzelii Centre for Forest Biotechnology, and the Departments of Materials and Environmental Chemistry (MMK), of Organic Chemistry (OK), of Ecology, Environment and Plant Sciences (DEEP), and the Bolin Centre for Climate Research of Stockholm University (SU).

References

1. Ménard D, Blaschek L, Kriechbaum K et al (2022) Plant biomechanics and resilience to environmental changes are controlled by specific lignin chemistries in each vascular cell type and morphotype. Plant Cell 34:4877–4896
2. Boerjan W, Ralph J, Baucher M (2003) Lignin biosynthesis. Ann rev. Plant Biol 54:519–546
3. Barros J, Serk H, Granlund I et al (2015) The cell biology of lignification in higher plants. Ann Bot 115:1053–1074
4. Pesquet E, Wagner A, Grabber JH (2019) Cell culture systems: invaluable tools to investigate lignin formation and cell wall properties. Curr Opin Biotechnol 56:215–222
5. Serk H, Gorzsás A, Tuominen H et al (2015) Cooperative lignification of xylem tracheary elements. Plant Signal Behav 10:e1003753
6. Blaschek L, Murozuka E, Serk H et al (2023) Different combinations of laccase paralogs nonredundantly control the amount and composition of lignin in specific cell types and cell wall layers in Arabidopsis. Plant Cell 35:889–909
7. Blaschek L, Champagne A, Dimotakis C et al (2020) Cellular and genetic regulation of coniferaldehyde incorporation in lignin of herbaceous and woody plants by quantitative Wiesner staining. Front Plant Sci 11:109
8. Peng F, Westermark U (1997) Distribution of coniferyl alcohol and coniferaldehyde groups in the cell wall of spruce fibers. Holzforschung 51:531–536
9. Kutscha NP, Gray JR (1972) The suitability of certain stains for studying lignification in balsam fir, Abies balsamea (L.). Mill Tech Bull Univ Maine 53:1–51
10. Van Acker R, Vanholme R, Storme V et al (2013) Lignin biosynthesis perturbations affect secondary cell wall composition and saccharification yield in Arabidopsis thaliana. Biotechnol Biofuels 6:46
11. Yamamoto M, Blaschek L, Subbotina E et al (2020) Importance of lignin coniferaldehyde residues for plant properties and sustainable uses. ChemSusChem 13:4400–4408
12. Holmgren A, Norgren M, Zhang L et al (2009) On the role of the monolignol gamma-carbon functionality in lignin biopolymerization. Phytochemistry 70:147–155
13. Blaschek L, Nuoendagula BZ et al (2020) Determining the genetic regulation and coordination of lignification in stem tissues of Arabidopsis using semiquantitative Raman microspectroscopy. ACS Sustain Chem Eng 8: 4900–4909
14. Méchin V, Baumberger S, Pollet B et al (2007) Peroxidase activity can dictate the in vitro lignin dehydrogenative polymer structure. Phytochemistry 4:571–579
15. Kishimoto T, Hiyama A, Toda H et al (2022) Effect of pH on the Dehydrogenative polymerization of Monolignols by laccases from Trametes versicolor and Rhus vernicifera. ACS Omega 7:9846–9852
16. Tobimatsu Y, Chen F, Nakashima J et al (2013) Coexistence but independent biosynthesis of catechyl and guaiacyl/syringyl lignin polymers in seed coats. Plant Cell 25:2587–2600
17. Kawamoto H (2017) Lignin pyrolysis reactions. J Wood Sci 63:117–132
18. Gerber L, Eliasson M, Trygg J et al (2012) Multivariate curve resolution provides a high-throughput data processing pipeline for pyrolysis-gas chromatography/mass spectrometry. J Anal Appl Pyrolysis 95:95–100
19. Faix O, Meier D (1989) Pyrolytic and hydrogenolytic degradation studies on lignocellulosics, pulps and lignins. Holz als Roh-und Werkstoff 47:67–72
20. Ralph J, Hatfield RD (1991) Pyrolysis–GC–MS characterization of forage materials. J Agric Food Chem 39:1426–1437
21. Van Erven G, de Visser R, Merkx DWH et al (2017) Quantification of lignin and its structural features in plant biomass using 13C lignin as internal standard for pyrolysis-GC-SIM-MS. Anal Chem 89:10907–10916
22. Kim H, Ralph J, Lu F et al (2002) Identification of the structure and origin of thioacidolysis marker compounds for cinnamyl alcohol

dehydrogenase deficiency in angiosperms. J Biol Chem 277:47412–47419

23. Pomar F, Merino F, Barceló AR (2002) O-4-linked coniferyl and sinapyl aldehydes in lignifying cell walls are the main targets of the Wiesner (phloroglucinol-HCl) reaction. Protoplasma 220:17–28
24. Preibisch S, Saalfeld S, Tomancak P (2009) Globally optimal stitching of tiled 3D microscopic image acquisitions. Bioinformatics 25: 1463–1465
25. Schindelin J, Arganda-Carreras I, Frise E et al (2012) Fiji: an open-source platform for biological-image analysis. Nat Methods 9: 676–682
26. Schroeder AB, Dobson ETA, Rueden CT et al (2021) The ImageJ ecosystem: open-source software for image visualization, processing, and analysis. Protein Sci 30:234–249
27. Lapierre C, Pilate G, Pollet B et al (2004) Signatures of cinnamyl alcohol dehydrogenase deficiency in poplar lignins. Phytochemistry 65(3):313–321
28. Ito T, Kawai S, Ohashi S et al (2002) Characterization of new thioacidolysis products of sinapyl aldehyde and coniferyl aldehyde. J Wood Sci 48:409–413



Chapter 15

Clearing of Vascular Tissue in *Arabidopsis thaliana* for Reporter Analysis of Gene Expression

Antonio Serrano-Mislata and Javier Brumós

Abstract

To study the gene regulatory mechanisms modulating development is essential to visualize gene expression patterns at cellular resolution. However, this kind of analysis has been limited as a consequence of the plant tissues' opacity. In the last years, ClearSee has been increasingly used to obtain high-quality imaging of plant tissue anatomy combined with the visualization of gene expression patterns. ClearSee is established as a major tissue clearing technique due to its simplicity and versatility.

In this chapter, we outline an easy-to-follow ClearSee protocol to analyze gene expression of reporters using either β-glucuronidase (GUS) or fluorescent protein (FP) tags, compatible with different dyes to stain cell walls. We detail materials, equipment, solutions, and procedures to easily implement ClearSee for the study of vascular development in *Arabidopsis thaliana*, but the protocol can be easily adapted to a variety of plant tissues in a wide range of plant species.

Key words ClearSee, Vasculature, Fluorescent proteins, GUS staining, Gene expression patterns, *Arabidopsis thaliana*

1 Introduction

To better understand the molecular and cellular bases underpinning plant development, we need to visualize gene expression patterns in their native context. To this end, it is required not only a precise three-dimensional view of plant anatomy but also a simple way to image gene expression in diverse organs/tissues and through different developmental stages. Reporter analyses using β-glucuronidase (GUS) or fluorescent proteins (FPs) have been instrumental to match gene expression patterns to quantitative information about cell number, size, and shape in diverse genetic backgrounds, contributing to our understanding of gene function during different developmental processes.

GUS staining, together with differential interference contrast (DIC) microscopy – also known as Nomarski interference contrast or Nomarski microscopy, is a common methodology that provides

Javier Agusti (ed.), *Xylem: Methods and Protocols*, Methods in Molecular Biology, vol. 2722,
https://doi.org/10.1007/978-1-0716-3477-6_15,
© The Author(s), under exclusive license to Springer Science+Business Media, LLC, part of Springer Nature 2024

remarkable information at the tissue level. Reporter analyses using GUS are extensively employed due to its high sensitivity, enzyme stability, and simplicity of detection. The GUS enzyme cleaves the 5-Bromo-4-chloro-3-indolyl β-D-glucuronide cyclohexylammonium salt (X-Gluc) substrate into two indoxyl derivatives that compose the characteristic blue pigment of GUS staining. This blue pigment is observed in cells where *GUS* is expressed, defining the location where the reporter gene is active. The use of GUS exhibits some advantages compared to FPs. GUS-staining protocol is simple and does not require expensive confocal microscopy. The GUS enzyme is extraordinarily stable, remaining active after several days. In addition, a single GUS enzyme is able to catalyze many X-Gluc molecules, resulting in strong signals that allow the visualization of very low expressed reporters. All these features make GUS an extremely sensitive reporter that enables the analysis of large samples at the tissue/organ level.

Expression patterns of genes of interest can also be analyzed by tagging them with FPs and then imaging the expression of the resulting reporter genes using confocal microscopy. The use of FPs is a powerful technique that can also offer several advantages over GUS staining. FPs can be live-imaged to monitor gene expression patterns over time with high cellular resolution. By using FPs emitting at different wavelengths, we can examine multiple genes simultaneously in the same tissue/developmental process. However, working with chlorophyll-rich plant tissues is challenging due to their high background auto-fluorescence that can mask the FPs signal. In addition, the plant cell wall opacity can also hamper the detection of FPs emission from deep tissues.

Trying to overcome some of the challenges offered by the use of different reporter genes, tissue-dissecting techniques have been developed. However, these techniques are usually time- and labor-intense. Moreover, when using sectioning approaches, it is difficult to obtain a complete series of sections that represents an entire tissue, limiting the observation to discrete 2D images. These drawbacks are partially addressed by fixing and clearing the plant tissues. Clearing agents such as chloral hydrate can be successfully used to clear tissues before DIC observations. The depth and resolution of the plant tissue imaging is notably improved, but clearing agents generally present some limitations. Staining details deep in the cleared sample may still be difficult to visualize, tissue integrity is often altered, and most importantly, these clearing techniques may impair FPs activity.

In the last few years, different approaches have addressed many of the mentioned drawbacks refining the current clearing protocols [1–3]. These approaches have improved not only the plant tissue clearing and penetration but also the cellular resolution of fluorescence microscopy [4–6]. Among all of them, ClearSee [7] stands

out for its simplicity and quick implementation. ClearSee allows imaging of plant deep tissues being compatible with FPs and with different cell wall dyes for simultaneous tissue visualization. Importantly, ClearSee removes chlorophyll autofluorescence, which can interfere with FPs imaging. ClearSee can also be employed to improve the visualization of GUS reporters staining. For all these reasons, ClearSee has become one of the most employed clearing methods, providing researchers the possibility of visualizing gene expression patterns using a variety of reporters combined with an unprecedented increase in tissue morphology resolution.

ClearSee preparation is easy. It is just composed of urea, xylitol, and sodium deoxycholate. In the last years, ClearSee has been used in a wide range of plant species, such as *Arabidopsis thaliana*, *Physcomitrium patens* [7], *Glycine max* [8], *Zea mays* [9], *Astragalus sinicus* [10], *Oryza sativa* [11], *Allium ochotense* [12], *Wolffiella hyalina* [13], *Marchantia polymorpha* [14], *Triticum aestivum* [15], *Fragaria* × *ananassa* [16], *Persea americana* [17], *Hordeum vulgare* [18], *Brassica rapa* [19], *Eucalyptus brachyphylla* and *Eucalyptus x trabutii* [20], *Monophyllaea glabra* [21], or *Petunia hybrida* [22]. As shown, ClearSee is a popular clearing technique to easily examine plant development beyond the model plant *Arabidopsis thaliana* (Arabidopsis) [23].

ClearSee has been successfully applied to whole seedlings and different plant tissues, including roots, leaves, and floral organs [7]. Several days to weeks are required to achieve an optimal tissue transparency for imaging, especially in tissues embedded deep within plant organs, such as the vasculature. Vasculature is key to transport water, nutrients, hormones, and other signaling molecules, as well as to provide mechanical support for the plant. Vasculature morphology depends on species, organ and developmental stage, but essentially consists of xylem and phloem – transport – and cambium – meristematic – tissues. In Arabidopsis, a combination of anticlinal and periclinal cell divisions during embryogenesis gives rise to all cell types that comprise the vascular system. After germination, cambium cells divide asymmetrically to maintain a pool of stem cells while continuously providing precursor cells of either xylem or phloem. These oriented cell divisions occur in both sides of the cambium throughout secondary plant growth to radially expand the number of vascular cell files and to maintain the bilateral symmetry with a central xylem axis and two phloem poles, one at each side. As a result, secondary xylem and secondary phloem are formed in the inner and outer side of the vascular structure respectively. Due to the localization and nature of the vascular tissue, its imaging has proven to be challenging. ClearSee, however, offers now easy-to-implement approaches to study and analyze the vasculature development.

2 Materials

2.1 Plant Lines and Growth Conditions

1. *Arabidopsis thaliana* (Arabidopsis) Col-0 ecotype was used as the wild type. *DR5p:GUS*, recombineering *TAA1p:GUS-TAA1*, and double *RGAp:GFP-RGA KNAT1p:KNAT1-2xeCFP* reporter lines were previously described [24–27].
2. Seed surface-sterilization. 50% commercial bleach supplemented with 0.01% Triton X-100. Autoclaved double distilled water (ddH_2O).
3. Plating and in vitro culture. 0.7% low-melting-point agarose. Murashige and Skoog basal medium (MS medium): 4.33 g/L Murashige and Skoog salts, 10 g/L sucrose, pH is raised to 5.8 using 1 M KOH, 7 g/L phytoagar.
4. Laminar flow hood is required for sterile work.
5. Air-permeable paper tape to seal plates.
6. Ethanol 70%.
7. Growth cabinet and plant growth chamber. Standard Arabidopsis growth conditions are long-day photoperiod (16 h light/8 h darkness), 22 °C, and 100–150 μmol m^{-2} sec^{-1} light intensity.
8. Fine sphagnum peat moss, perlite, and vermiculite (2:1:1) mixture to grow plants on soil.
9. Plastic pots and trays.
10. Wrapping transparent film.
11. Paclobutrazol (PAC). Prepare a 10 mM stock solution in dimethyl sulfoxide (DMSO): Dissolve 29.4 mg of PAC powder (Duchefa Biochemie) in 10 mL of DMSO. Make 1 mL aliquots and store at −20 °C until use [27].

2.2 Solutions

2.2.1 GUS Stock Solutions

- Ice-cold 90% acetone.
- 100 mM Potassium ferrocyanide, dissolve 4.22 g of $K_4Fe(CN)_6 \cdot 3H_2O$ in 100 mL in ddH_2O.
- 100 mM Potassium ferricyanide, dissolve 3.29 g of $K_3Fe(CN)_6$ in 100 mL ddH_2O.
- 1 M Disodium phosphate, dissolve 134.03 g of $Na_2HPO_4 \cdot 7H_2O$ in 500 mL ddH_2O.
- 1 M Monosodium phosphate, dissolve 39 g of $NaH_2PO_4 \cdot H_2O$ in 250 mL ddH_2O.

GUS rinse solution:
GUS-staining solution:

X-Gluc (5-Bromo-4-chloro-3-indolyl β-D-glucuronide cyclohexylammonium salt) is a substrate for GUS (beta-glucuronidase)

enzyme. Prepare just the required amount to be used, X-Gluc stock solution 100 mg/mL in DMF (N, N, dimethylformamide) or DMSO (Dimethyl sulfoxide) (*see* **Note 1**). Although X-Gluc stocks can be stored in the freezer (−20 °C) for a few weeks, the stock solution should be fresh to obtain better results.

The staining solution is the rinse solution supplemented with X-Gluc 1 mg/mL. So, 100 μL of X-Gluc stock solution (100 mg/mL) should be added to 9.9 mL of GUS rinse solution to obtain 10 mL of staining solution with a final X-Gluc concentration of 1 mg/mL.

2.2.2 Fixing Solution for Imaging Fluorescent Protein Tags

Fixing solution: 4% PFA (paraformaldehyde) in 1x PBS (Phosphate Buffered Saline) solution.

10x PBS solution is composed of: 70 mM Na_2HPO_4, 30 mM NaH_2PO_4, 27 mM KCl and 1.37 M NaCl. To prepare 1 L of 10x PBS solution: 70 mL 1 M Na_2HPO_4, 30 mL 1 M NaH_2PO_4, 2 g KCl and 80 g NaCl. Dissolve these reagents in 800 mL ddH_2O. Adjust pH to 7.2–7.4 and fill with ddH_2O up to 1 L. Autoclave. To prepare 1x PBS, dilute 1 volume of 10x PBS in 9 volumes of ddH_2O. Store at room temperature (RT).

To prepare 100 mL of 4% PFA, add 4 g PFA powder to 90 mL 1x PBS solution. For this, place a glass Erlenmeyer flask on a stir plate into the fume hood (*see* **Note 2**). Heat while stirring the solution to approximately 60 ° C. It is important to keep the solution from boiling. PBS can be preheated in a microwave though it is not essential. To dissolve the powder, slowly raise the pH by adding 1 M NaOH dropwise until the solution clears (a drop of a 1 M NaOH solution is enough for 100 mL). Alternatively, NaOH pellets can be used (1 pellet is enough for 100 mL of PFA solution). Allow the solution to cool down to room temperature and adjust PFA solution final volume to 100 mL by adding 1x PBS. Store at 4 ° C for no longer than 1 month. For long storage (up to a year), the solution can also be aliquoted and frozen at −20 ° C.

2.2.3 Clearing Solution

ClearSee solution is composed of 10% w/v xylitol, 15% w/v sodium deoxycholate, and 25% w/v urea in water. To prepare 10 mL of ClearSee solution, start adding 2.5 g urea to 7 mL of ddH_2O. Make sure the urea is well dissolved in the water; it can take a while. Application of mild heat (37 ° C to 42 ° C) short pulses can help dissolving the urea in water. Then add 1 g of xylitol powder; let it dissolve. Finally, add 1.5 g of sodium deoxycholate (*see* **Note 3**). Add ddH_2O to complete the 10 mL volume while stirring continuously. Store at RT in darkness for up to a week. For optimum results, ClearSee needs to be prepared and used fresh.

2.2.4 Staining Solutions

To prepare 0.1% Direct Red solution, dissolve 0.01 g of Direct Red 23 powder dye content 30% (Sigma-Aldrich) in 10 mL of ClearSee solution. Store at RT in darkness.

2.3 Materials for Sample Processing and Microscopy

1. Vacuum pump to infiltrate solutions.
2. Plastic tubes (1.5 mL) and/or 12 wells tissue culture plates to process the samples.
3. Cover slips, regular (flat) microscope slides, and 0.3 mm cavity microscope slides (these ones are recommended for confocal analysis of thick samples, as in the case of hand-sectioned hypocotyl slices).
4. Tweezers, razor blades, and a thin brush to manipulate samples.
5. For DIC observations, a Leica DFC550 digital camera mounted on a Leica DM5000B microscope was used.
6. For FP observation, images were acquired with an Axio Observer LSM 780 (Zeiss) confocal microscope equipped with a C-Apochromat 40x/1.20 W Korr FC5 M27 objective.

3 Methods

3.1 Plant Cultivation In Vitro

1. Seeds need to be sterilized before plating them. To this end, first the seeds are surface-sterilized for 15 min using 50% bleach supplemented with 0.01% Triton X-100 to avoid seed clumping. Next, seeds are washed six times with autoclaved ddH_2O to remove any bleach traces. Alternatively, seeds can be washed with 70% ethanol supplemented with 0.01% Triton X-100 for 3 min, followed by a 1 min wash with 100% ethanol (*see* **Note 4**).
2. Seeds are resuspended in melted pre-cooled 0.7% low-melting-point agarose and plated on the surface of MS medium plates. Then plates are sealed with air-permeable paper tape (*see* **Note 5**).
3. Seeds are stratified for at least 3 days at 4 ° C to obtain a uniform germination.
4. Plates are moved to an in vitro growth cabinet at 22 ° C, under long day photoperiod (16 h of light and 8 h of dark), and light intensity of approximately 120 μmol m^{-2} sec^{-1}.

3.2 Plant Cultivation on Soil

1. For the analysis of fluorescent reporters in the hypocotyl of adult plants, seeds are germinated in vitro as described above. Seven-day-old seedlings are transferred to soil-containing pots (2:1:1 mixture of sphagnum:perlite:vermiculite) and moved to plant growth chambers with the described conditions of

temperature, photoperiod and light intensity. Pots are sealed with transparent wrapping film to help seedlings adapt to the lower relative humidity in the growth chamber compared to the in vitro conditions. Wrapping film is punctured after a couple of days and completely removed 2–3 days later.

2. To promote DELLA accumulation, and hence visualization of the *RGAp:GFP-RGA* reporter, 10 μM PAC was supplied with the irrigation water once plants had developed the first pair of true leaves, about 1 week after the seedlings were transferred to the growth chamber (*see* **Note 6**). Four-week-old plants were used for the analysis.

3.3 Seedlings GUS Staining and Clearing

1. Seedlings samples harboring the *DR5p:GUS* or *TAA1p:GUS-TAA1* are harvested and fixed in ice-cold 90% acetone and can be stored at −20 ° C overnight or longer.
2. Fixed seedlings are washed twice with GUS rinse solution (*see* Table 1) to remove any traces of acetone.
3. Then samples are vacuum-infiltrated with the GUS-staining solution (*see* Table 2 and **Note 7**).
4. Seedlings are stained at 37 °C for 1–14 h until staining is noticeable (*see* **Note 8**).

Table 1
GUS rinse solution for a final volume of 100 mL

Stock solution	For 100 mL	Working concentration
1 M Na_2HPO_4 1 M NaH_2PO_4	3.42 mL 1.58 mL	50 mM
100 mM $K_4Fe(CN)_6$	0.5 mL	0.5 mM
100 mM $K_3Fe(CN)_6$	0.5 mL	0.5 mM
ddH_2O	94 mL	

Table 2
GUS-staining solution for a final volume of 10 mL

Stock solution	For 10 mL	Working concentration
1 M Na_2HPO_4 1 M NaH_2PO_4	342 μL 158 μL	50 mM
100 mM $K_4Fe(CN)_6$	50 μL	0.5 mM
100 mM $K_3Fe(CN)_6$	50 μL	0.5 mM
100 mg/mL X-Gluc	100 μL	1 mg/mL
ddH_2O	9.3 mL	

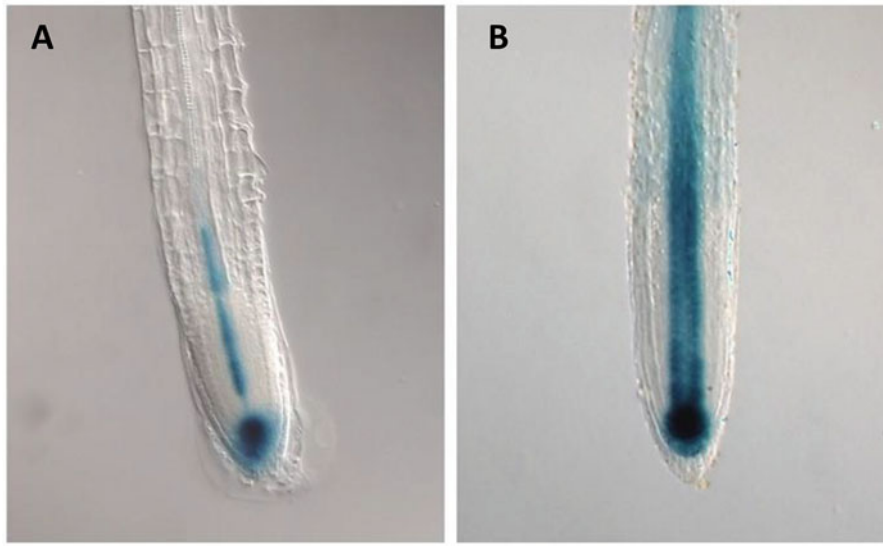


Fig. 1 Expression patterns of *DR5p:GUS* (**a**) and recombineering *TAA1p:GUS-TAA1* (**b**) in roots treated with ClearSee for 7 days after GUS staining

5. GUS-staining reaction is stopped by adding ethanol to a final concentration of 15%.
6. Seedlings are tapped dry on a paper towel to remove most of the ethanol and staining solution.
7. Seedlings are optically cleared by submerging them in freshly made ClearSee solution for 5–7 days (Fig. 1). Samples in ClearSee must be kept always at RT in the dark (*see* **Notes 9** and **10**).

3.4 Hypocotyls Clearing for FP Visualization Combined with Cell Wall Staining

1. The hypocotyl is defined as the region between the oldest true leaf and the shoot–root junction. To assess the expression of FPs in hypocotyls, plants expressing *RGAp:GFP-RGA* and *KNAT1p:KNAT1-2xeCFP* reporters are carefully pulled up from soil, including their roots, and washed with tap water to remove all traces of soil.
2. Under a magnifying glass, hypocotyl slices are hand-cut with a razor blade. The thinner the slices, the better for downstream processing. PAC treatment reduces hypocotyl growth. Thus, just a couple of sections can be usually obtained per PAC-treated plant.
3. Hypocotyl slices are carefully transferred with a brush to a 12 wells plate containing a few milliliters of 4% PFA in PBS 1x.
4. Fixation is initially carried out under vacuum for 1 h at RT (*see* **Note 11**). Then replace PFA with fresh 4% PFA and continue fixation without vacuum for an additional hour at RT with gentle shaking.

5. Fixed samples are washed three times with 1x PBS at RT with gentle shaking to remove any traces of PFA.
6. Transfer washed samples to freshly prepared ClearSee solution. Samples are left submerged in ClearSee for a week at RT and protected from light. Exchange ClearSee every 2–3 days (*see* **Note 10**).
7. To visualize cell walls, samples are transferred to 0.1% (w/v) Direct Red solution in ClearSee and stained for 3 h at RT with gentle shaking (*see* **Note 12**).
8. To completely eliminate Direct Red excess, wash twice with ClearSee for 5 min, followed by an additional 30 min incubation with ClearSee. All steps at RT with gentle shaking [28].

3.5 Imaging

3.5.1 Imaging of Cleared GUS Stained Seedlings

1. Place samples on a microscope slide, add some drops of fresh ClearSee, and cover the samples carefully to prevent bubble-formation with the cover slip (*see* **Notes 13** and **14**).
2. To improve visualization, GUS-stained samples are imaged using DIC microscopy to enhance the contrast of transparent tissues.

3.5.2 Imaging of FPs Combined with Cell Wall Staining in Cleared Hypocotyl Sections

1. To help imaging deep tissues without squeezing the sample, it is required to generate some space between hypocotyl slices and the coverslip. To this end, 0.3 mm cavity slides can be used. Alternatively, 2–3 layers of stickers can be added to the longitudinal sides of a regular slide. It is important to fill the cavity with the right amount of ClearSee solution. Overfilling may cause drifting of the sample during image acquisition. Incomplete filling favors bubble formation and sample squeezing. Approximately, 90–100 μl of ClearSee work well for 0.3 mm cavity slides (Fig. 2).
2. Samples with FPs and cell wall staining are imaged using confocal microscopy. eCFP and GFP/Direct Red 23 are sequentially visualized after excitation with 405 and 488 nm laser lines, respectively. Emission filters must be set to 466–481 nm for eCFP, 503–517 nm for GFP, and 594–613 nm for Direct Red 23. Emission spectra for eCFP and GFP can be verified within individual nuclei with the "lambda scan" mode of the microscope. Images were analyzed using the Fiji (ImageJ2) software [29] https://imagej.net/software/fiji/.

4 Notes

1. X-Gluc is light sensitive. Keep X-Gluc stock and GUS-staining solutions in the dark.

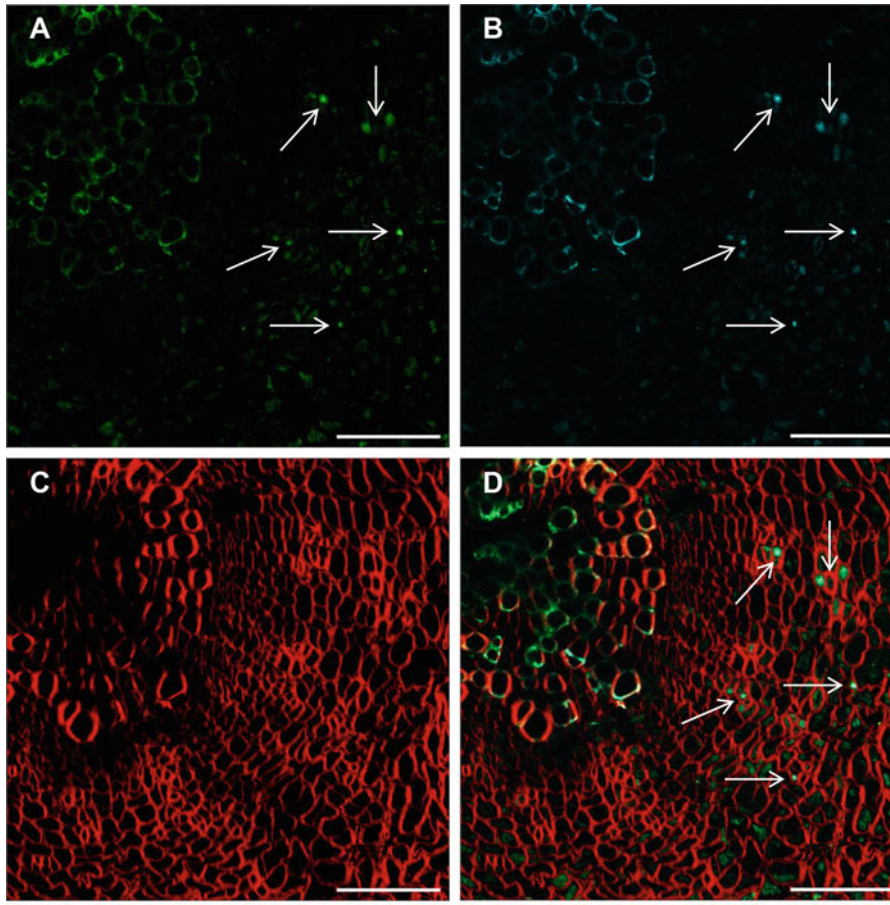


Fig. 2 *RGAp:GFP-RGA* and *KNAT1p:KNAT1-2xeCFP* reporter activity in the vascular tissue of cleared hypocotyls from 4 weeks-old Arabidopsis plants. (**a**) *RGAp:GFP-RGA* reporter. (**b**) *KNAT1p:KNAT1-2xeCFP* reporter. (**c**) Cell-walls staining with Direct Red. (**d**) Composite image of panels (**a**) to (**c**). Arrows point to cell nuclei with co localization of the GFP-RGA and KNAT1-2xeCFP proteins. Scale bars, 50 μm

2. PFA powder is harmful by inhalation and contact skin. Use mask and gloves. Work in a fume hood. Once the PFA solution has been prepared, clean thoroughly all material with detergent and water.
3. Wear a mask and gloves to handle ClearSee reagents (sodium deoxycholate is irritant by inhalation). Dissolving urea can take up several hours; it is an endothermic reaction that makes the container feel cold when handled.
4. For plant in vitro growth, it is key to maintain all plant culture media and materials under strictly sterile conditions. All media and materials must be autoclaved/sterilized prior to their use.

5. To seal the plates, it has been shown that the employment of air-permeable paper tape works better than parafilm. Paper tape allows gas exchange and minimizes media contamination without triggering seedling stress.
6. PAC is a triazole plant growth inhibitor that, among other effects, inhibits GA biosynthesis. Use always the same set of pots, trays, etc. for PAC treatments. PAC traces are hard to remove from plastic surfaces by conventional washing.
7. For GUS staining, samples should be placed under vacuum for 3–4 pulses of 2 min each to improve the penetration of the solution into the plant tissue. Break the vacuum carefully to prevent sample loss. Samples soaked in solution sink to the bottom of the tubes; if samples float, apply additional vacuum pulses.
8. GUS staining is usually performed at 37 ° C, but the incubation time depends on gene expression levels. Staining should be checked regularly to prevent overstaining. GUS activity also depends on potassium ferro- and ferricyanide concentration in the staining solution [30]. There is a range of concentrations, from 0 to 10 mM, that may work well depending on reporter activity. Higher concentrations result in weaker GUS signals but more restricted to the cells and tissues where the reporter is active. Lower concentrations result in stronger signals that trend to diffuse to neighboring tissues where the reporter is not active. Thus, it is convenient to first optimize the ferro/ferricyanide concentration for each experiment. Concentrations between 0.5 and 2 mM represent a standard starting point.
9. The volume of the sample should not be higher than 20% of the total volume of the fixing or ClearSee solution.
10. The ClearSee solution can darken over time. If it is not transparent, replace it for fresh ClearSee, as many times as necessary. Depending on plant species and tissue type, incubation times vary. Clearing Arabidopsis seedlings roots can take from 3 to 5 days, leaves up to 7 days, and pistils 2 to 4 weeks. If clearing is not optimal, samples can be kept in fresh ClearSee for longer times until desired clearing is obtained.
11. For hypocotyls fixation, gentle vacuum needs to be applied for longer times, such as 1 h. Check regularly the process. Do not apply heavy vacuum which can cause bubble formation and sample-loss by jumping from the wells. It is important that 4% PFA fixing solution penetrates well the tissue, otherwise FPs may weaken during the clearing process.
12. Different fluorescent dyes for staining cell walls, with specific excitation and emission (Em) wavelength spectra, are compatible with ClearSee (check [28] for a complete list). Direct Red

23 (Em λmax ≈ 600 nm) is the right choice for FPs with emission peaks in the blue or green region of the spectrum like CFP or GFP. In turn, other dyes like Calcofluor White (Em λmax = 432 nm) should be used for imaging of FPs whose emission peaks are in the red region of the spectrum, like mCherry (Em λmax = 610 nm) or tdTomato (Em λmax = 581 nm).

13. Handle gently cleared samples to minimize damage. They are especially soft and fragile after clearing and usually hardly visible to the eye. Cleared samples can be stored in ClearSee solution (at least for 6 months) after visualizations are done. These samples can be imaged as many times as needed.
14. Cleared samples should be image on the same day as the samples are mounted on the optical slides. After some hours, the ClearSee used to mount the samples dries, forming crystals that impair the sample visualization.

Acknowledgments

Work in JB's group is funded by a grant from the Spanish Ministry of Science PID2021-1274610B-I00. JB is sponsored by a Ramon y Cajal contract RYC2019-026537-I. Research in ASM's group is funded by a grant from the Valencian Government (CISEJI/2022/28, Plan GenT).

References

1. Warner CA, Biedrzycki ML, Jacobs SS et al (2014) An optical clearing technique for plant tissues allowing deep imaging and compatible with fluorescence microscopy. Plant Physiol 166:1684–1687
2. Hasegawa J, Sakamoto Y, Nakagami S (2016) Three-dimensional imaging of plant organs using a simple and rapid transparency technique. Plant Cell Physiol 57:462–472
3. Musielak TJ, Slane D, Liebig C et al (2016) Versatile optical clearing protocol for deep tissue imaging of fluorescent proteins in Arabidopsis thaliana. PLoS One 12:e0161107
4. Palmer WM, Martin AP, Flynn JR et al (2015) PEA-CLARITY: 3D molecular imaging of whole plant organs. Sci Rep 5:1–6
5. Timmers AC (2016) Light microscopy of whole plant organs. J Microsc 263:165–170
6. Littlejohn GR, Gouveia JD, Edner C et al (2010) Perfluorodecalin enhances in vivo confocal microscopy resolution of Arabidopsis thaliana mesophyll. New Phytol 1:1018–1025
7. Kurihara D, Mizuta Y, Sato Y, Higashiyama T (2015) ClearSee: a rapid optical clearing reagent for whole-plant fluorescence imaging. Development 142:4168–4179
8. Okuda A, Matsusaki M, Masuda T et al (2017) Identification and characterization of GmPDIL7, a soybean ER membrane-bound protein disulfide isomerase family protein. FEBS J 284:414–428
9. Kelliher T, Starr D, Richbourg L et al (2017) MATRILINEAL, a sperm-specific phospholipase, triggers maize haploid induction. Nature 542:105–109
10. Ohtsu M, Sato Y, Kurihara D et al (2017) Spatiotemporal deep imaging of syncytium induced by the soybean cyst nematode Heterodera glycines. Protoplasma 254:2107–2115
11. Chu TT, Hoang TG, Trinh DC et al (2018) Sub-cellular markers highlight intracellular dynamics of membrane proteins in response to abiotic treatments in rice. Rice 11:1–8

12. Tanaka E, Ono Y (2018) Whole-leaf fluorescence imaging to visualize in planta fungal structures of victory onion leaf rust fungus, Uromyces japonicus, and its taxonomic evaluation. Mycoscience 59:137–146
13. Isoda M, Oyama T (2018) Use of a duckweed species, Wolffiella hyalina, for whole-plant observation of physiological behavior at the single-cell level. Plant Biotechnol 35:387–391
14. Aki SS, Mikami T, Naramoto S et al (2019) Cytokinin signaling is essential for organ formation in Marchantia polymorpha. Plant Cell Physiol 60:1842–1854
15. Wu J, Mock HP, Giehl RF et al (2019) Silicon decreases cadmium concentrations by modulating root endodermal suberin development in wheat plants. J Hazard Mater 364:581–590
16. Kim DR, Cho G, Jeon CW et al (2019) Mutualistic interaction between Streptomyces bacteria, strawberry plants and pollinating bees. Nat Commun 10(1):4802
17. Duman Z, Hadas-Brandwein G, Eliyahu A et al (2020) Short de-etiolation increases the rooting of VC801 avocado rootstock. Plan Theory 11:1481
18. Ho WW, Hill CB, Doblin MS et al (2020) Integrative multi-omics analyses of barley rootzones under salinity stress reveal two distinctive salt tolerance mechanisms. Plant Commun 1: 100031
19. Arsovski AA, Zemke JE, Hamm M et al (2020) BrphyB is critical for rapid recovery to darkness in mature Brassica rapa leaves. bioRxiv
20. Eliyahu A, Duman Z, Sherf S et al (2020) Vegetative propagation of elite eucalyptus clones as food source for honeybees (Apis mellifera); adventitious roots versus callus formation. Isr J Plant Sci 67:83–97
21. Kinoshita A, Koga H, Tsukaya H (2020) Expression profiles of ANGUSTIFOLIA3 and SHOOT MERISTEMLESS, key genes for meristematic activity in a one-leaf plant Monophyllaea glabra, revealed by whole-mount in situ hybridization. Front Plant Sci 11:1160
22. Chen M, Bruisson S, Bapaume L et al (2021) VAPYRIN attenuates defence by repressing PR gene induction and localized lignin accumulation during arbuscular mycorrhizal symbiosis of Petunia hybrida. New Phytol 229:3481–3496
23. Kurihara D, Mizuta Y, Nagahara S et al (2021) ClearSeeAlpha: advanced optical clearing for whole-plant imaging. Plant Cell Physiol 62: 1302–1310
24. Brumos J, Zhao C, Gong Y et al (2020) An improved recombineering toolset for plants. Plant Cell 32:100–122
25. Brumos J, Bobay BG, Clark CA et al (2020) Structure–Function Analysis of Interallelic Complementation in ROOTY Transheterozygotes. Plant Physiol 183:1110–1125
26. Silverstone AL, Jung HS, Dill A et al (2001) Repressing a repressor: gibberellin-induced rapid reduction of the RGA protein in Arabidopsis. Plant Cell 13:1555–1566
27. Felipo-Benavent A, Úrbez C, Blanco-Touriñán N et al (2018) Regulation of xylem fiber differentiation by gibberellins through DELLA-KNAT1 interaction. Development 145: dev164962
28. Ursache R, Andersen TG, Marhavý P et al (2018) Protocol for combining fluorescent proteins with histological stains for diverse cell wall components. Plant J 93:399–412
29. Schindelin J, Arganda-Carreras I, Frise E et al (2012) Fiji: an open-source platform for biological-image analysis. Nat Methods 9: 676–682
30. Sessions A, Weigel D, Yanofsky MF (1999) The Arabidopsis thaliana MERISTEM LAYER 1 promoter specifies epidermal expression in meristems and young primordia. Plant J 20: 259–263

INDEX

A

Acer 4
Acetone 123, 156, 165, 180, 210, 223, 230, 233
Activated charcoal 173
Adigor 5, 7, 11–13
Adjuvant 5, 6, 11
Agar 4–7, 11, 13, 68, 108, 111–113, 115, 119
Agarose 193, 194, 204, 215, 230, 232
Agrobacterium tumefaciens 80, 83, 175, 176, 178, 184, 186
Air-permeable paper tape 230, 232, 237
Alkaline nitrobenzene oxidation 156, 160
Aminovinylglycine (AVG) 194, 195
Anti-browning agents 172, 173
Aphidicolin 187
Arabidopsis 4–8, 11, 13, 68, 75, 76, 84, 133, 136, 141, 173, 177, 184, 186, 187, 189, 208, 209, 222, 229, 230, 236, 237
Artificial interfering RNA 173
Aspen 141, 142
Assay for transposase-accessible chromatin (ATAC) 68, 70, 74–76
Autofluorescence 141, 146, 188, 191, 229
Auxin 38, 172–174, 178, 179, 183

B

Bacteria 83, 126, 174, 179
Bamboo 173
Banana 173
Basic Fuchsin 6, 10
Basta 179, 187
Beaker 110, 111, 155, 156, 158, 164, 177
6-benzylaminopurine (BAP) 178, 179, 181, 188, 189
β-glucuronidase (GUS) 184, 187, 227–231, 233–235, 237
Beta vulgaris 183
Black-foot disease 107–109
Botryosphaeria dieback 107–109
5-Bromo-4-chloro-3-indolyl β-D-glucuronide cyclohexylammonium salt (X-Gluc) 228, 230, 231, 233, 235
Bundle 36, 38, 39, 45, 46, 52, 81, 216

C

Cadophora luteo-olivacea 108
Calcium hypochlorite 177
Calcofluor 6, 10, 12, 133, 134, 180, 188, 191, 193, 238
Calli 172–175, 177, 181–184, 187, 197
Cambium 38, 59, 79, 91, 131, 143, 229
5(6)-carboxyfluorescein diacetate (CFDA) 4–14
Carrot 183
Catalase 141, 143, 144, 146, 147, 223
Catharanthus roseus 183
Cavitation 18, 45, 118
Cefotaxime sodium 179
Cell suspension culture 171–174, 176, 181–184, 188, 190, 193, 197
Cellulase 82, 124
Cellulose 10, 132, 139, 149, 150, 152, 153, 156, 160, 163, 180, 191, 193, 197, 223
Cenozoic 90, 94–99
Chemical genomics 173, 174, 194
Chloral hydrate 228
Chromatin 67–77
ClearSee 6, 9, 10, 228, 229, 231, 232, 234–238
Clonal cells 187
Clorhydric acid (HCl) 68, 70, 75, 118, 119, 122, 144, 156, 160, 204, 206, 214
Clorox 177, 181
Cohesion-tension 36
Confocal 5, 6, 10, 141, 144, 186, 193, 228, 232
Conical tubes 84, 176, 179–182, 186, 189, 195
Conidial suspensions 115
Coniferaldehyde 201–225
Coniferyl alcohol 139, 202, 203, 206–209, 221, 222
Cotton wool ball 176, 196
Cotyledons 4, 7–9, 11, 13, 14, 133
Cryptomeria 172
Cuscuta 4
Cylindrocarpon 108, 109, 115
Cytokinin 38, 172–174, 178, 183

Javier Agusti (ed.), *Xylem: Methods and Protocols*, Methods in Molecular Biology, vol. 2722,
https://doi.org/10.1007/978-1-0716-3477-6,

© The Editor(s) (if applicable) and The Author(s), under exclusive license to Springer Science+Business Media, LLC, part of Springer Nature 2024

D

DAPI 68, 69, 76, 180, 191
Darcy's law 38
Daucus carota 183
ddH_2O, *see* Double distilled water (ddH_2O)
Deconvolution 149–166
De-differentiated 4, 188
Dehydrogenation polymers (DHPs) 205, 206, 221–223
Deprogramming 174
Dexamethazone 173
2',7'-dichlorodihydrofluorescein (H_2DCF) 141
2',7'-dichlorodihydrofluorescein diacetate (H_2DCFDA) 141–147
Differential interference contrast (DIC) 227, 228, 232, 235
Differentiation 4, 41, 79, 132, 136, 171–197
Dihydroconiferyl alcohol 202
Dimethylformamide (DMF) 231
Dimethyl sulfoxide (DMSO) 5, 11, 12, 124, 144, 145, 179, 180, 230, 231
Diphenyleneiodonium chloride (DPI) 142–144, 147
Direct Red solution 232, 235
Disease 107–109, 114, 118
Disodium phosphate 230
Double distilled water (ddH_2O) 5, 11, 12, 230–233
Dual luciferase reporter 79–86

E

Earlywood 30, 31
Embolism 17–32, 44, 45, 51–62, 118
Embryo 172
Epibrassinolides 173, 174, 179
Epifluorescence 6–9, 13, 122, 123, 141, 146, 180, 188, 193
Epigenetic 173, 183
Erlenmeyer flask (EF) 108, 110–112, 115, 120, 154, 159, 175, 177, 182–184, 187, 194–196, 205, 206, 231
Esca 107–109, 115
Estradiol 173
2-(N-morpholino)ethanesulfonic acid (MES) 81, 82, 178, 189, 195
Ethanoacidolysis 213
Ethanol 69, 70, 73, 74, 84, 86, 110, 111, 119–123, 140, 153, 157, 158, 177, 179, 181, 196, 204, 214, 230, 232, 234
Ethylenediamine tetraacetic acid 68, 210
Eucalyptus 140
Eutypa dieback 107–109
Explant 174, 177, 181

F

Ferulate 117–126
Field of view (FOV) 54–57, 61
Fiji (software) 215, 235
Fine sphagnum peat moss 230
FITC 180, 191
Flow cytometry 69, 77
Fluid 38–40, 59, 76
Fluorescein diacetate (FDA) 141, 180, 191, 197
Fluorescein sodium salt 4
Fluorescence-activated nucleus sorting (FANS) 68
Fluorescent dye 3–14, 141, 237
Fluorescent protein 75, 227, 231
Fomitiporia mediterranea 108
Fossil 89–99
Fourier transform infrared spectroscopy (FTIR) 149–166
Fraxinus excelsior 30, 313

G

Gas chromatography coupled to mass spectrometry (GC/MS) 150, 204, 206–212
Gene expression patterns 227–229
Glufosinate 179, 180
Grafting 4, 9, 13
Grapevine 41, 107–115
Grapevine trunk diseases (GTDs) 107–109
Gravimetric techniques 151
Guaiacyl (G) 125, 140, 151–154, 166, 202
GUS staining 227, 228, 230, 233–235, 237

H

Habituated cell cultures 173, 174, 182–184
Helianthus annuus 52, 183
Helianthus tuberosus 187
Hetoronuclear Single Quantum Coherence (HSQC) 118, 119, 124–126
High performance liquid chromatography (HPLC) 149–166
Hormone 37, 45, 172, 174, 177–180, 182–184, 187–189, 229
Hormone habituated 173, 174, 182–184
Hormone habituation 182, 184
Hormone inducible differentiation 184, 189, 195
Host plant 4
Hydraulic 18, 19, 22, 23, 30, 35–40, 42, 43, 45, 46, 51–53, 56, 59, 60, 62, 156, 159
Hydrogen peroxide (H_2O_2) 133, 141–147, 205, 206, 223
Hygromycin 179, 187

I

Ilyonectria liriodendri 108
ImageJ (software) 6, 13, 53, 59, 62, 217, 220, 235
Inducible differentiation 171, 172
Inducible pluripotent suspension cell cultures (iPSCs) 171–197
In vitro 108, 112, 113, 172, 173, 176, 181, 183, 205, 230, 232, 233, 236

K

Kanamycin 179, 187
Klason lignin 149, 150, 153–156, 158–159, 164

L

Laccase (LAC) 139–147, 205, 223
Lactic acid 114
Lactuca sativa 187
Laminar flow hood 108, 110–112, 174, 178–182, 196, 230
Lateral root 5, 7, 8, 11, 12
Latewood 30, 31
Leaves 4, 5, 8, 12, 13, 17, 35, 37, 40, 44, 56–58, 61, 76, 80–84, 86, 90, 97, 98, 110, 114, 133, 172, 229, 233, 237
5'-leader 80–83
Lignin 117–126, 132, 139–141, 146, 149–166, 180, 188, 191, 193–195, 201–224
Liquid-metal-jet anode (MetalJet) 55
Liquid nitrogen 84, 190, 210
Lithium dodecyl sulfate 210
L phytoagar 230
L sucrose 230
Luciferase 79–86
Luria-Bertani (LB) 178, 184

M

Magnetic stirring bar 205
Malt extract agar (MEA) 108, 110, 111
Mesophyll 44, 80–82, 174, 178, 187, 189–191
Mesozoic 90, 92–94
Metaxylem 4, 10, 172, 174, 193
Methanol:phosphate buffer 205
Micro-computed tomography (micro-CT) 51–62
Micrografting 13
Microscopy 4, 5, 76, 118, 121–123, 175, 180, 186, 188, 191–193, 203, 215, 220, 227, 228, 232, 235
MMG solution 82, 84
Model 4, 20, 22–24, 26–32, 35, 36, 39–45, 94, 98, 132, 229
Modeling ..... v, 17–32, 35–46, 151
Monolignols 139–142
Monosodium phosphate 230
Morphotypes 171–173, 191, 202
Murashige and Skoog (MS) 6, 11, 177, 181–184, 186, 189, 190, 193, 195, 196, 230
Mutant 4, 8, 81, 136
Mycelial agar plug 113
Mycelial growth rate (MGR) 108, 111, 114

N

1-naphthaleneacetic acid (NAA) 178, 179, 188, 189
Network 8, 21–24, 28, 31, 36, 38, 40, 43, 52
Nicotiana 173
N,O-Bis(trimethylsilyl)trifluoroacetamide 212
Nomarski 227
Nucleus sorting 69, 72
Nylon mesh 72, 84, 86, 177, 190

O

Oryzalin 194, 195

P

Paclobutrazol (PAC) 230, 233, 234, 237
Paleozoic 90–92, 99
Parafilm 4–9, 11, 13, 53, 56, 110, 111, 114, 115, 177, 197, 205, 206, 237
Paraformaldehyde (PFA) 6, 9, 231, 234–237
Parasitic plant 4
Pathogen ..... vi, 25, 107–115, 117–126
Peat 92, 95, 119, 136, 230
Percent loss of conductivity (PLC) 19, 30
Perforation plate 36, 172, 173
Perlite 136, 230, 232
Peroxidase (PRX) 139–147, 205, 206, 223
Petri disease 107, 108, 114
Petri dish 6, 9, 11, 13, 68, 71, 75, 84, 110–115, 119, 175, 181, 183, 184
Phaeomoniella chlamydospora 108
Phase contrast imaging (PCI) 53, 55, 58
Phloem 5, 11, 36–38, 44, 45, 131, 132, 229
Phloroglucinol 118, 119, 121, 122, 126, 204, 213, 214, 223
Phosphate-buffered saline solution (PBS) 6, 9, 10, 69, 76, 133, 134, 136, 231, 234, 235
Phosphate-citrate 144
p-hydroxyphenyl 140
Phytogel 181, 183, 184, 186
Pine 40, 41, 110, 112–115
Pinus 172, 173
Piperonylic acid (PA) 195
Pistachio 110
Pistachio leaf agar (PLA) 112, 113, 115
Pistacia vera 110

Polyamine 79
Polypropylene 176
Polyvinylpyrrolidone 173
Populus 4, 52, 139–147
Potassium ferricyanide 230, 237
Potassium ferrocyanide 230, 237
Prepared potato dextrose agar (PDA) 108, 110–112, 115
Primary root 4, 7, 8, 10, 11
Programmed cell death 132, 193, 195
Proteomics 173, 174
Protoplast 67, 80–82, 84–85
Protoxylem 4, 10, 172, 193
Pseudostuga 172
Pycnidia 108, 112–113
Pyrogram 207–209
Pyrolysis-GC/MS 206–209
Pyrolytic 207
Pyrolyzates 206, 207, 209, 224

R

Ralstonia solanacearum 119, 120, 125
Raman microspectroscopy 3, 204, 220–222
Raman spectrometer 204, 222
Reactive oxygen species (ROS) 141, 144–147
Regeneration 4, 176
Renilla 80, 81, 85
Rhodamine B 4
Rhodamine WT 5–8, 10, 12
RNA 69–70, 72–74, 76, 173, 174, 184
Root ..... v, 3–14, 35, 37, 42, 44, 45, 52, 53, 56, 61, 90, 96, 97, 107, 110–112, 114, 115, 120, 121, 123, 124, 131, 133, 229, 234, 237

S

Salicylhydroxamic acid (SHAM) 141–146
Secondary cell wall (SCW) ..... v, 10, 118, 132, 135, 172, 180, 186, 188, 190, 191, 193, 195, 197, 202
Secondary growth 38, 91, 95, 131, 132
Seedlings 3–14, 68, 75, 181, 229, 232–235, 237
Seeds 90, 96, 98, 177, 181, 230, 232
Sequoia sempervirens 20, 27
Shoot 4, 5, 8, 9, 11, 13, 14, 37, 39, 54
Shootward transport 3, 4, 8, 12
Silver thiosulfate (STS) 194, 195
SIR model 20, 24–31
Sodium azide (NaN_3) 142–144, 146, 147
Sodium bicarbonate 211
Sodium deoxycholate 229, 231, 236
Sodium hypochlorite 110, 114, 224
Software 42, 53, 56, 58–60, 76, 125, 156, 160, 161, 166, 194, 209, 212
Somatic cells 174
Spectinomycin dihydrochloride 179
Spectra deconvolution 149–166
Spectroscopy 118, 207
Spruce 42
Stable genetic transformation 172–174, 184–187
Staining 10, 18, 68, 69, 71, 118, 121, 141, 143, 145, 146, 180, 191, 204, 213, 215–220, 228, 229, 231–237
Stem ..... v, 38, 40, 52, 53, 56–61, 93, 96, 97, 140, 142, 143, 145–147, 151, 163, 207, 211, 216, 222, 229
Sterile filter paper 110, 112
Streptomycin sulphate 110, 111, 114
Suberin 118, 119, 121, 124–126
Sucrose 173, 177, 178, 181–184, 186, 187, 189, 190, 193, 195–197, 230
Sugarcane 173
Synchrotron 51–62
Synchrotron radiation (SR) 53, 55, 56, 58, 60
Syringyl 125, 140, 152, 166
Syringyl/Guaiacyl (S/G) ratio 149–166

T

Taxol 194
Teflon bar magnetic stirrer 112
3,3',5,5'-tetramethylbenzidine (TMB) 141–147
Texas Red (sulforhodamine 101 acid chloride) 4
Thermospermine 79–86
Thioacidolysis 204, 205, 209–212, 224
Torreya 172
Tracheary elements (TE) 131–136, 172, 173, 185–189, 191–195, 197
Tracheid 27, 36, 39, 95, 154, 172
Transcriptional reporter 173, 184
Transcriptome 67, 68
Transcriptomics 67–77, 172–174
Transpiration 36, 43, 44, 132
Transport ..... v, 4, 6, 8–9, 11–14, 17, 36, 37, 43–45, 131, 139, 229
Triphenyltetrazolium chloride (TTC) 119
Triton X-100 ..... 230, 232
Tungsten carbide beads 197
Two-dimensional nuclear magnetic resonance spectroscopy (2D-NMR) 118, 122, 124, 151, 154, 166
2,4 dichlorophenoxyacetic acid (2,4D) 179, 181, 182
Tylose 92, 93, 118

U

Upstream open reading frame (uORF) 80
Urea 6, 229, 231, 236

V

Vanillin 157, 160, 208
Vascular development 4
Vasculature 11, 117, 118, 121, 229
Vermiculite 119, 136, 230, 232
Vessels 18, 28–31, 35–37, 39, 52, 56, 60, 79, 107, 117, 118, 122, 132, 154, 172, 173, 216
Vinca rosea 183
Vitamins 81, 177, 178, 183
Vulnerability curves (VC) 18–21, 28, 30–32, 45, 52, 60, 143

W

Water flow ..... v, 36, 40, 42
Whatman paper 5, 9, 11, 13
Wiesner test 204, 212–220, 222, 223
Wood ..... v, 18, 20, 21, 23, 27, 30, 37, 57, 89–99, 107–115, 131, 139, 149–154, 157–160, 163–165, 208

X

X-Gluc 228, 230, 231, 233, 235
X-ray 51–62
Xylan 152, 193
Xylem axis 229
Xylem connections 4
Xylem differentiation 4, 136
Xylem fibers 132, 136, 140, 202
Xylem necrosis 107–115
Xylem parenchyma (XP) ..... v, 131, 172
Xylem reconnection 4, 9
Xylem sap 17, 36, 45, 172, 202, 203, 222
Xylem transport ..... v, 3–14, 37
Xylitol 6, 229, 231

Z

Zinnia elegans 172, 187
Zinnia violacea 172, 177
Zulauf 205
Zutropf 205, 206